Title
Understanding Snow Process Uncertainties and Their Impacts

Author
Jeong, Seongeun

Publication Date
2009

Understanding Snow Process Uncertainties and Their Impacts

by

Seongeun Jeong

A dissertation submitted in partial satisfaction of the
requirements for the degree of
Doctor of Philosophy

in

Engineering - Civil and Environmental Engineering

in the

Graduate Division
of the
University of California, Berkeley

Committee in Charge:
Professor John A. Dracup, Co-chair
Professor Xu Liang, Co-chair
Professor Peng Gong
Professor Fotini K. Chow

Fall 2009

Understanding Snow Process Uncertainties and Their Impacts

To My Family

Contents

List of Tables

List of Figures

Acknowledgments

It is a great pleasure to acknowledge those who supported my Ph.D. study. My teachers and mentors at UC Berkeley have helped me forge new knowledge foundations that will lead my academic journey. I appreciate Professor Xu Liang for her incredible guidance and encouragement with every due respect. Her support is where my Ph.D. study started. Her continued trust in me enabled me to finish this Ph.D. work. I thank Professor John Dracup for his support through my whole progression at Berkeley. I also thank Professor Peng Gong and Professor Fotini Chow for serving on my qualifying exam committee and reading this dissertation, Professor Raja Sengupta for serving on my qualifying exam committee, and Professor William Nazaroff and Mark Stacey for serving on my preliminary exam committee. I also thank Professor Michael I. Jordan for his valuable class that helped me conduct the data assimilation work.

Thanks to the many members of the Liang and Dracup labs who provided so much guidance, support, and insight. These include Laura Parada, Maoyi Huang, Jianzhong Guo, and Ian Ferguson. I especially thank Ben Runkle for his wonderful companionship during these years. Without Ben, many of the joys I appreciated at Berkeley would not have been possible. He was a great friend and sometimes a mentor. I also thank Shugong Wang who provided the data assimilation code. I am amazed and delighted by the constructive support and intelligence provided by fellow students and dear friends.

I also thank the various funders of my work. My stipends were paid variously by the the Consortium of Universities for the Advancement of Hydrologic Science (CUAHSI), the National Oceanic and Atmospheric Administration (NOAA), Maybelle B. Tucker and John T. Tucker Fellowship, and the Department of Civil and Environmental Engineering.

I would like to thank my church members. They have been always with me throughout my Ph.D. study. Their prayers and support were a cornerstone for my endurance while meeting all the requirements for my Ph.D. I give my special thanks to Pastor Daniel Cho and his wife Dr. Maria Cho. They helped my family settle down and provided everything we need during the last seven years. When I was preparing for the comprehensive exam, the preliminary exam, and the qualifying exam, they encouraged me to pass them with every prayer. I also would like to thank Pastor Chungwon Chai and his family. He has been my friend for 17 years, and we worked together to build His Kingdom wherever we are. Regarding my Ph.D. study, he volunteered to be my study partner for my comprehensive exam. He stayed up late with me at the Doe Library main stack. I cannot think of my continued study at Berkeley without him. I give thanks to Pastor Chungnam Kim and his family for his love and encouragement. Like my father, he always believed and encouraged me with warm words.

I thank the deacons at my church: Deacon Sang Lee, Deacon Lucia Kang, Deacon Jack Kim, Deacon Youjin Choung, Deacon Eugene Lee and his wife Rose Lee, and Deacon Jinwoo Kim and his wife Grace Chung. They are incredible people. They supported me and my family with loving hearts as if my concerns were theirs. I thank my spiritual children in my Mokjang, the current and former ones. The current people include Jongsoo, Soyoun, Eun Hae, Myungki, Youmee, Shinae, and Shinhye. For the former members, I give special thanks to Sungwhan Hong and his family and Jihwi Kim and his family among many, who try to live the same life as me. They have been with me many times every week and became my joy all the time. I also thank many other church members who supported me in prayer.

There are a few more people to whom I cannot thank enough. My father-in-law and mother-in-law were always in the first place to support me. They called us almost every day to express their love and support. Simply I cannot find ways to give them back. I also thank my

sister-in-law, her family, and brother-in-law for their encouragement and prayer. My special thanks go to my brother and his family, my cousin, Shincheol, and my youngest uncle, Professor Johngseok Bae.

Thanks finally to my wife and children. My wife, Hye Jin, spent seven years at a chemistry lab in Berkeley and sacrificed her career for me. We had lunch together almost everyday, and I enjoyed listening to her research progress. She developed her ideas while talking to me, and I learned what science is from her advanced research. My children, Ha Young, Chanhee (David), and Hamin (Jonathan), were a well of joy during my Ph.D. study, which never dried up. Because of them, I was able to reach the finish line.

Above all, special thanks to my parents on the earth and the One above in the heaven. My parents could have given me their lives to support me. The heavenly Father has already done it for me. Sola Gratia!

Abstract

Understanding Snow Process Uncertainties and Their Impacts

by

Seongeun Jeong
Doctor of Philosophy in Engineering - Civil and Environmental Engineering

University of California, Berkeley

Professor John A. Dracup, Co-chair
Professor Xu Liang, Co-chair

Prediction of snow in regional and global hydrological models has been a difficult task due to errors in the forcing data, subgrid-scale variability in the snowpack, and uncertain model physics. This dissertation conducts thorough studies of uncertainties that are concerned with snow modeling, in particular for high mountain areas. First, an in-depth analysis of uncertainties associated with meteorological forcing data in the Sierra Nevada was performed. The use of ensemble forcing data with a reasonable degree of uncertainty and model parameter adjustments did not overcome the low-bias in simulating snow states using a simple two-layer (2-L) snow model in the Variable Capacity Infiltration (VIC) land surface model (LSM). To reveal the uncertainty related to model parameterization, a multi-layer (M-L) soil-snow model with more complexity has been developed. This dissertation examines the impact of model complexity on snow simulations in high mountains by comparing the M-L model and the 2-L model. While the current VIC LSM solves state variables for soil and snow separately, the new M-L model solves state variables for the integrated soil-snow system simultaneously. This dissertation has found that the complex M-L model performs better than the 2-L model overall, in particular during the melting season, but the added complexity did not significantly remove the uncertainty, which is similar to some other researchers' findings. This conclusion has led this dissertation research to data assimilation work to investigate the uncertainty problem from a different angle.

The data assimilation approach was taken to discover the hidden facets of uncertain land surface processes that could not be explained by the complex M-L soil-snow model. This research uses a multiscale data assimilation scheme that allows for incorporation of data with different scales. As an extension of the traditional state space model (e.g., Kalman filtering), the multiscale data assimilation incorporates data at different scales by computing their conditional probabilities in a scale-recursive way. The multiscale assimilation scheme has been embedded into the M-L soil-snow model of the VIC LSM. This dissertation applies the new assimilation system to the West Coast region to examine the impact of snow data assimilation at the regional scale as well as at the local scale. The assimilation at the local and regional scales showed promise by reducing biases in simulating snow states in the region. In addition, this research shows the impact of snow data assimilation on energy flux and streamflow simulations.

Chapter 1

Introduction

The existence of snow cover significantly changes the land surface processes governing the energy and water cycles. Change in surface albedo due to snow cover affects the overall energy balance of the snow-covered area, leading to reduced surface temperature and cooling of the lower boundary of the atmosphere [1]. Simulations of surface climate by General Circulation Models (GCMs) have large feedbacks with snow cover whose magnitude depends on the snow process representation of GCMs [2] [3]. In the western United States snow is an important water supply source for both urban and agricultural uses. In the region, mountain snowmelt accounts for about 75% of the annual streamflow [4]. In addition to supporting water resources predictions, long-term snow cover monitoring can provide a record of atmospheric climate change of the region [5] [6]. Using data supported process-oriented models creates more accurate prediction of snow processes during winter and helps provide better water resources services to the region [7] [8].

Prediction of snow in regional and global hydrological models has been a difficult task due to errors in the forcing data, subgrid-scale variability in the snowpack, and uncertain model physics [9]. In particular, simulating snow processes in high mountains such as the Sierra Nevada is challenging due to additional uncertainties associated with high subgrid-scale variations of landscape and hydrologic variables (e.g., precipitation) with altitude [10]. Therefore, in mountainous regions addressing uncertainty is necessary in preparing simulations and analyzing simulation results. When forcing data and model parameters are prepared for simulations in high mountains, it is necessary to know the nature of meteorological forcing data and parameters for the area of interest. When necessary, modelers should consider sources of uncertainty such as the undercatch of precipitation to avoid unreasonable simulation results. In addition, ignoring uncertainties in the analysis of simulation results will likely contribute to errors in the state variables under study.

This dissertation conducts thorough studies of uncertainties that are concerned with snow modeling, in particular for high mountain areas. Many studies have focused on either the forcing data or model physics to understand uncertain land surface processes [11] [12]. This dissertation research considers uncertain factors from both forcing data and model physics, and further presents a method to reduce the uncertainty. First, forcing data, which are the input to the snow model, are investigated by answering the following questions: (1) why are forcing data problematic in high mountains? (2) how do the uncertain input data translate to simulation results? and (3) how much does forcing-induced uncertainty compare relative to other uncertainty factors. The answers to these questions from this study indicate that forcing data is the dominant contributor to the uncertainty in simulating snow state variables in a mountain basin of the Sierra Nevada. But this uncertainty associated with forcing data does not explain everything. For instance, even though quality forcing data that are believed to represent the model grid cell are used, there exists a large discrepancy between simulated and observed snow states. In addition, as will be discussed later, the snow albedo scheme can change simulation results in magnitude as much as precipitation-induced uncertainty for certain environments. This incomplete understanding of snow process uncertainty leads this dissertation to its second subject: development of a more complex snow model. This dissertation focuses on understanding how adding physical process complexity to an existing simple model can reduce the uncertainty associated with model physics.

Finally, this dissertation discusses how the uncertainties associated with forcing data and model physics can be alleviated. The data assimilation approach was taken to discover the hidden facets of uncertain snow processes that could not be explained by greater understanding of meteorological forcing data and more complex modeling techniques. In particular, the data assimilation study employs a multiscale process to consider the complex terrain and high spatial gradient of hydrologic variables with altitude in mountainous areas.

The subsections that follow introduce each of the subjects related to snow process uncertainties.

1.1 Uncertainty in Forcing Data

This dissertation investigates the response of snow-related state variables to uncertain forcing data as the first step to understanding snow process uncertainties. In high mountains, the uncertainty associated with meteorological forcing data is conspicuous [13] [14], and the precipitation error is measurably large [15]. A recent study using NLDAS data has shown that significant underestimations of snow water equivalent (SWE) by land surface models (LSM) exist for mountainous regions [16]. Most of the low-biases for SWE result from precipitation underestimates due to spatial heterogeneity, wind blowing, and scarce measurement gages. As shown in studies such as [17] using large low or high-biased forcing data cannot produce simulation results comparable to ground observations even through complex modeling. In this regard, this dissertation sets as its starting point the use of quality data that represent model grid cells better than normally available forcing data. The Distributed Hydrologic Model Intercomparison Project - Phase 2 (DMIP2) provides specially derived precipitation and temperature data that reduce low biases in high mountain sites of the Sierra Nevada. Based on these datasets and other secondary forcing data from the North America Land Data Assimilation System (NLDAS) [18] and North American Regional Reanalysis (NARR) [19], this dissertation aims at understanding the impacts of uncertain forcing data to snow state variables.

The measure of uncertainty for forcing data is the uncertainty range in noisy ensemble datasets. The basic approach to the generation of noisy ensemble data is the state space model approach. For precipitation data, other methods such as an autoregressive model are used due to the intermittent nature of precipitation events. We compute the moments of the posterior distribution for the data and use them to generate ensemble data with reasonable levels of noise. By adding measurement noises to the quality gridded data (i.e., DMIP2 data) at reasonable levels, this study investigates the impact of these perturbed forcing data on snow variables. This dissertation focuses on learning whether the simulated ensemble SWE values based on the perturbed forcing can explain the underestimation of SWE that frequently occurs in the Sierra Nevada. The detailed methods and results are presented in Chapter 2. This chapter also explains how data from different sources are combined.

1.2 Development of Multi-layer Soil-Snow Model

A new multi-layer soil-snow model is developed and validated to understand the contribution of model physics to uncertain snow processes. The fundamental approach to this understanding is to investigate how added model complexity affects the simulation of snow state variables and the energy budget. Quite a few snow model intercomparison studies have been conducted to address the complexity issue [20] [21]. It is fairly easy to determine whether a new model is better than an old model or whether one model is better than the other. However, it is often more complex to identify which snow process makes a difference in terms of the state variable (e.g., snow depth) of interest than to develop a complex snow model itself. In many snow model comparison projects including [20] and [22], it is not easy to define which process is the dominant cause of discordant results among models because descriptions of snow processes for each model are different.

The development of a new soil-snow model focuses on examining the uncertainty associated with model physics. With this goal, the model developed in this dissertation investigates the effect of more complex descriptions of heat transfer in the snow layers. By adding complexity of physical processes to the existing model, we want to know how this complexity reduces or increases uncertainty and what additional effort is required by the complex model to reduce the uncertainty. As will be discussed in later chapters and sections, increasing model complexity requires more work in terms of computational cost and parameter adjustment as well as more understanding of physical processes. For easy identification of contributing processes to the reduction of uncertainty, we focus on representations of heat transfer in the soil and snow systems while leaving snow surface boundary conditions the same between the existing model and the new complex model. We build upon the subcomponent two-layer snow model of the Variable Infiltration Capacity (VIC) land surface model (LSM) and develop a new multi-layer model within the framework of the VIC LSM. The existing snow model successfully simulates snow variables in various environments, implying that processes at the surface such as latent heat transfer are well described by the model. Therefore, it is reasonable to focus on the heat transfer process through the snow and soil layers and its related processes, which the current simple model does not have. The details of model development and its results are the subject of Chapter 3.

1.3 Multiscale Data Assimilation

The previous two major efforts to study uncertainties in model forcings and other factors in complex model development cannot overcome the majority of the large SWE underestimation found between the model and SNOpack TELemetry (SNOTEL) observations for mountainous regions. The main reason for this problem is due to underestimation of areal precipitation. Even though we used a precipitation product that incorporated the point-scale observations from SNOTEL stations, there is a large discrepancy between model simulations and the ground observation. Even when model-data scale differences are considered, the magnitude seems to be large. Two simple solutions to this problem are to adjust precipitation data locally and to run the model at fine scales. In this dissertation study, a data assimilation method is instead used to reduce the uncertainty related to snow processes.

Assimilation of remotely sensed retrievals into a snow model is an important method to reduce uncertainties associated with the estimates of snow states. To use data assimilation in an advantageous way it is critical that the data assimilation scheme account for the uncertainty structure of both the physical model and observations. To this end, this dissertation study employs a multiscale data assimilation scheme. Many studies (e.g., [12]) related to snow modeling uncertainty have focused on characterizing the uncertainty related to the temporal evolution of the snow variable of interest. However, in high mountains where land surface environments vary sharply in space, many factors that cause uncertainty are hidden in scale. We therefore present a method to relate the variable of interest at one scale to another scale to overcome the unfavorable conditions for physical snow models in high mountains. Moreover, this method allows us to obtain estimates of snow variables at different scales by getting optimal parameters for the multiscale process. Chapter 4 introduces the methodology for the multiscale process and presents the results from an uncertainty experiment based on this method.

This study extends its study scale for the application of the multiscale process from grid cells to a region that includes states of Washington, Oregon, California, and part of Nevada. This regional application work is used to understand the impact of the multiscale data assimilation on hydrological variables at different scales. More efforts are made in the simulation of streamflow that represents the characteristics of hydrological states including snow within a watershed. This work is presented in Chapter 5.

Chapter 2

Understanding of Uncertainty in Forcing Data

2.1 Introduction

Snow processes are affected by various uncertainties such as model physics and meteorological forcing data. In high mountains, the uncertainty associated with meteorological forcing data is large [13] [14]. In particular, the precipitation error is dominant. Precipitation gauge measurement errors involve several processes, including catch errors due to wind-blowing and losses from evaporation [15]. In this chapter, we investigate the basic response of the land surface model to the uncertain forcing data. This dissertation focuses on the response of snow-related state variables to uncertain forcing data.

Many current land surface models simulate hydrological variables using distributed modeling techniques. Their meteorological forcing data are provided for each modeling unit, usually known as a model grid cell. An areal mean value represents the model grid cell and is inherently different from point scale data. Throughout this chapter we use the areal mean data to represent model grid cells and investigate their uncertain behavior.

NLDAS provides publicly available areal mean forcing data that cover the continental US in 1/8th degrees [18]. A recent study using NLDAS data has shown that significant underestimations of snow water equivalent (SWE) by land surface models (LSM) exist for mountainous regions [16]. Most of the low-biases for SWE result from precipitation underestimation in the dataset. For the same reason, all four land surface models that participated in the NLDAS project underestimated the mean annual runoff in the northern Rocky Mountains [17]. NLDAS hourly precipitation data are generated by combining daily gauge-based precipitation and hourly radar-based (Doppler radar with gauge bias correction) precipitation data [18]. One of the reasons for such low-bias is that the ability to obtain accurate precipitation data from ground-based radar or gauge measurement for mountain areas is very limited [23]. Note that version 2 of NLDAS products shows some improvement in precipitation data, which will be presented in Chapter 5.

An effort to provide more accurate meteorological forcing data for distributed modeling has been initiated in the Sierra Nevada via the Distributed Hydrologic Model Intercomparison Project - Phase 2 (DMIP2) data. The DMIP2 experiment in the Sierra Nevada intends to test various models in areas of complex hydrology, where accurate forcing data are not available and model simulations are affected by terrains with high spatial gradients. DMIP2 data are provided in a finer resolution (i.e., approximately 4 km) than NLDAS data. Its precipitation data incorporate estimates from three different sources to provide more accurate areal mean precipitation for the Sierra Nevada [24]. Because the DMIP2 precipitation estimation method uses ground gage measurements and SNOw pack TELemetry (SNOTEL), it reduces the undercatch problem that is conspicuous in NLDAS precipitation data. DMIP2 also provides hourly temperature grids that are derived from daily minimum and maximum temperature records of gages. Our experiment in this chapter takes advantage of the resolution and quality of DMIP2 data. For example, its temperature data are comparable to the point measurement at the SNOTEL station. Figure 2.1 shows the temperature comparison between the point measurement at the Ebbetts Pass SNOTEL station and its corresponding areal mean values for the 1/8th degree model grid cell (For precipitation data see Figure 2.7).

Using gridded data comparable to point measurements provides an ideal environment to examine how uncertain forcing data affect snow-related state variables. This chapter aims to examine the effect of uncertain forcing data on snow water equivalent simulations using the DMIP2 data for precipitation and temperature that represent model grid cells better than the existing NLDAS data. By adding measurement noise to the quality gridded data at reasonable levels, we investigate the effect of these perturbed forcing data on snow variables. For this purpose, we generate perturbed ensemble forcing data and analyze their effect. In particular, this chapter focuses on learning whether the simulated ensemble SWE values based on the perturbed forcing can explain the underestimation of SWE that frequently occurs in the Sierra Nevada. For other energy forcing data such as shortwave radiation we combine data from NLDAS [18] and North American Regional Reanalysis (NARR) [19]. This chapter also explains how data from different sources are combined.

2.2 Representation of Forcing Uncertainty

2.2.1 Study Site and Data

The study site is the East Fork Carson River Basin in the Sierra Nevada. Figure 2.2 shows the basin boundary and two SNOTEL stations within the basin. This basin is used for the Distributed Hydrologic Model Intercomparison Project - Phase 2 (DMIP2). The basin outlet at East Fork Carson River near Gardnerville, NV covers 922 km^2 and is located at latitude 38.845 and longitude -119.70361. We will revisit this basin in Chapter 5 for streamflow simulation. We use two SNOTEL stations as shown in Figure 2.2. The Ebbetts Pass SNOTEL station is located at latitude 38.549550 and longitude -119.804650 and the Blue Lake station at latitude 38.607800 and longitude -119.924433. Both of these stations are located in high altitudes with elevations 8765 feet and 8057 feet, respectively.

DMIP2 provides hourly precipitation and temperature data for the period of 1987 - 2002. DMIP2 hourly precipitation data use three data sources: 1) hourly cooperative observer gauges,

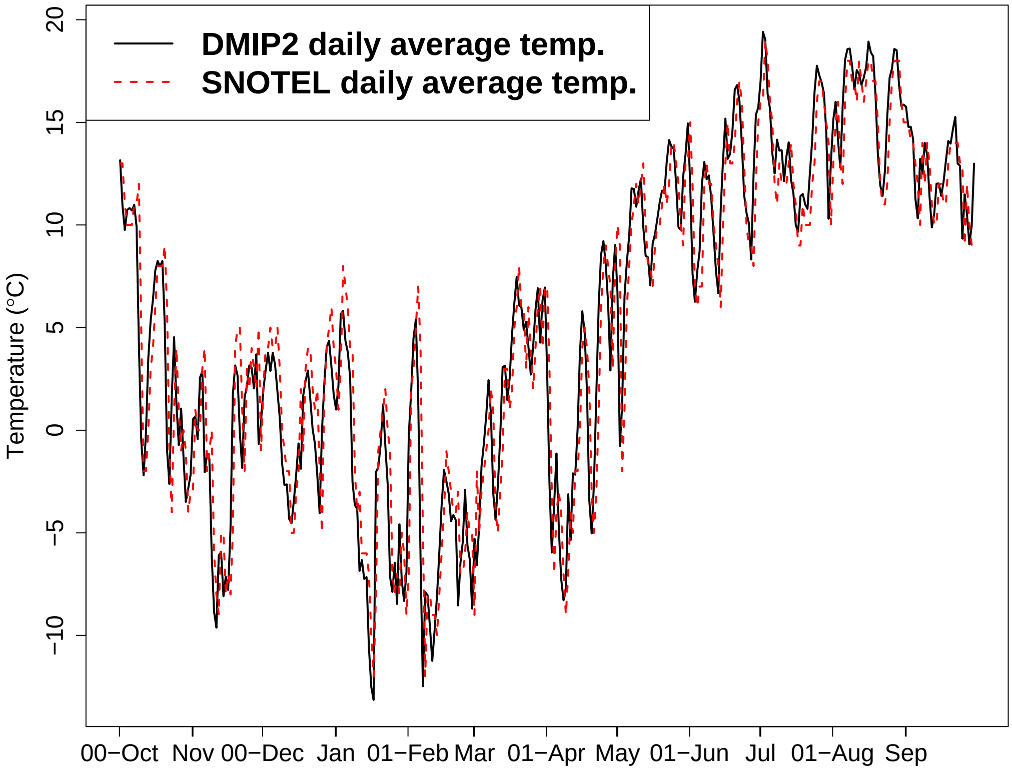

Figure 2.1: Temperature comparison between point measurements at the Ebbetts Pass station and areal mean values at the corresponding grid cell for the 2001 water year.

2) daily total cooperative gauges, and 3) SNOTEL daily precipitation gauges. The daily values are disaggregated to hourly estimates using the nearest hourly gauge values. The estimated hourly data are interpolated to approximately 4 *km* Hydrologic Rainfall Analysis Project (HRAP) grids [25] using an inverse-distance method [24]. The HRAP grid in 4 *km* x 4 *km* resolution was regridded into 1/8th degrees using a weighted spatial averaging algorithm, which is presented in Appendix D. The hourly temperature grids are estimated from daily minimum and maximum temperature records of gages.

Other secondary forcing data such as shortwave radiation and pressure are prepared by combining NARR [19] and NLDAS products. The 3-hourly NARR data are provided in a resolution of 32 *km* and regridded into our model grid, which is 1/8th degree. Using the state space model described in the following subsection, the two datasets are combined to generate smoothed estimates and related statistics. We use the 2-layer (2-L) snow model of the VIC LSM for simulations throughout this chapter.

2.2.2 Generation of Ensemble Forcing Data

2.2.2.1 State space approach

A linear state-space model is used to perturb meteorological forcing data. The basic idea is to obtain the posterior distribution of the sequence of data of interest. For temperature, we have only one observation from DMIP2 and use it in the observation equation. For other secondary

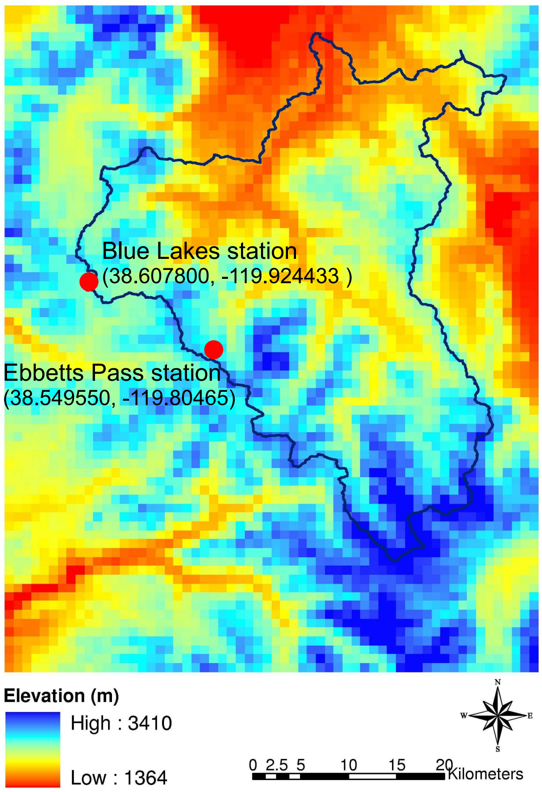

Figure 2.2: Study site in the East Fork Carson River Basin.

forcing data (e.g., longwave radiation), we use two observations from NARR and NLDAS products. Depending on the forcing variable, the trend of each time series shows different behavior. For example, pressure data behaves like a random walk process (see Figure 2.9) while radiation data have cyclic behavior. Temperature data show a trend over the water year. The ideal approach to obtaining the posterior distribution is to prescribe the best model for each forcing variable. In this study, we use a simple linear model to represent all the variables. However, we use the Expectation Maximization (EM) algorithm [26] to estimate optimal model parameters (e.g., noise term covariances) for the model that differ from one forcing variable to another. For the details of the EM algorithm see Appendix G. For every case, we use the same observations as the hidden state we want to estimate without data transformation. Thus, our linear assumption is especially true for the observation equation in the state-space model.

The state space model can be represented by:

$$x_{t+1} = Ax_t + w_t \tag{2.1}$$

$$y_t = Cx_t + v_t \tag{2.2}$$

where t is time index, x_t and y_t are the state and observation at time t, respectively, A and C are linear operators, $w_t \sim N(0, Q)$, and $v_t \sim N(0, R)$. As usual, we assume that v_t and w_t are white and independent of the state x_t. Because we are modeling the same state variable as the observation, C is set to 1.

From the Markov property and the Bayes rule, the posterior density can be expressed as

$$\begin{aligned}
p(x_{t+1}|y_{t+1}, y_0, ..., y_t) &\propto p(y_{t+1}|x_{t+1}, y_0, ..., y_t)p(x_{t+1}|y_0, ..., y_t) \\
&= p(y_{t+1}|x_{t+1})p(x_{t+1}|y_0, ..., y_t) \\
&= p(y_{t+1}|x_{t+1}) \int p(x_{t+1}, x_t|y_0, ..., y_t)dx_t \\
&= p(y_{t+1}|x_{t+1}) \int p(x_{t+1}|x_t, y_0, ..., y_t)p(x_t|y_0, ..., y_t)dx_t \\
&= p(y_{t+1}|x_{t+1}) \int p(x_{t+1}|x_t)p(x_t|y_0, ..., y_t)dx_t \qquad (2.3)
\end{aligned}$$

where $p(\cdot)$ is a general Gaussian density function and we use conditional independences from the Markov property to convert the integrand into an easy form for integrating out x_t.

As in Blight [27], the posterior density in the final form of Equation 2.3 can now be solved analytically. The full derivation is available in Appendix F. Using notations in [28] we define

$$\hat{x}_{t|t} \equiv E[x_t|y_0, ..., y_t] \qquad (2.4)$$

$$P_{t|t} \equiv E[(x_t - \hat{x}_{t|t})(x_t - \hat{x}_{t|t})^T|y_0, ..., y_t] \qquad (2.5)$$

The posterior density can now be written as

$$x_{t+1}|y_{t+1}, y_0, ..., y_t \sim N(\hat{x}_{t+1|t+1}, P_{t+1|t+1}) \qquad (2.6)$$

with

$$\begin{aligned}
\hat{x}_{t+1|t+1} &= \hat{x}_{t+1|t} + K_{t+1}(y_{t+1} - \hat{x}_{t+1|t}) \\
P_{t+1|t+1} &= P_{t+1|t} - K_{t+1}CP_{t+1|t} \qquad (2.7)
\end{aligned}$$

where K_{t+1} is the quantity known as Kalman gain.

Once we have these posterior mean and covariance for a sequence of data, we can use the posterior distribution to generate Gaussian random numbers. For our experiment, we generate 100 perturbed ensemble datasets.

2.2.3 Ensemble Precipitation

Precipitation data have intermittent properties showing a sequence of wet and dry days for a given period. Therefore, it is difficult to use the general approach to generating ensemble forcing data based on the posterior distribution of the time series without transformation of the original data. One thing to note is that we can still use the general state space model approach for precipitation perturbation by transforming the original data into cumulative format. While the general approach is possible, we use two different methods to perturb precipitation data. The first approach is concerned with sampling-related uncertainty of precipitation data. The sampling-related error is one of the main sources of errors in estimating precipitation [29]. Even though DMIP2 precipitation data are produced by interpolating ground-based observations, it is provided in a spatially gridded format similar to radar or satellite precipitation. Therefore, in this synthetic experiment we assume the underlying interpolation errors as equivalent to radar or satellite sampling errors. For the second approach an autoregressive (AR) model is used to generate error time series by assuming some statistics.

First, we use a simple scaling law proposed by Steiner et al. [30]. The sampling error E is calculated as:

$$E = 0.008(\frac{R_0}{R})^{0.20}(\frac{L_0}{L})^{0.70}(\frac{T_0}{T})^{0.35}(\frac{\Delta t}{\Delta t_0})^{1.05} \tag{2.8}$$

where R is the rainfall rate in mm/h, L is the length scale of the domain in km, T is the accumulation period in days, and Δt is the sampling interval in hours. The constants have values $R_0 = 1\,mm/h$, $L_0 = 500\,km$, $T_0 = 30$ days, and $\Delta t_0 = 1$ hour. In our study, L is taken as the length of one side of the model grid cell. For T we use 1 day considering the method of DMIP2 data generation.

Nijssen and Lettenmaier [11] applied the sampling error to produce synthetic precipitation sequences. Assuming a log-normal distribution, the perturbed precipitation values are produced as:

$$P_t = \left(\frac{1}{\sqrt{E^2+1}} e^{\sqrt{ln(E^2+1)}\epsilon(0,1)}\right) P \tag{2.9}$$

where P_t is the perturbed hourly precipitation, P is the hourly DMIP2 precipitation, E is the sampling error in Equation 2.8, and $\epsilon(0,1)$ is the error from normal distribution with zero mean and unit variance.

In this experiment, hourly precipitation values were perturbed to generate 100 ensemble precipitation data for each grid cell independently. Precipitation was perturbed only when precipitation occurs, keeping the original wet and dry sequence. We use Equation 2.8 for solid precipitation during cold seasons. Because there is no information about the spatial correlation of sampling errors and we use only a small number of grid cells, it is assumed that the sampling errors are spatially uncorrelated.

Following the notation in Shumway and Stoffer [31], the AR model for the error time series is written as:

$$\epsilon_t = \phi\epsilon_{t-1} + w_t \tag{2.10}$$

where w_t is the white noise with zero mean and variance σ_w and ϕ a scalar parameter. The details for this model are introduced in Appendix E.

The AR model needs a prescribed error standard deviation to generate random numbers. A different number of error standard deviations can be used but in this experiment we use 0.6, based on initial tests which show reasonable results comparable to the sampling error approach.

2.3 Effect of Uncertainty

Figures 2.3, 2.4, and 2.5 show the ensemble simulation of SWE for the grid cell corresponding to the Ebbetts Pass SNOTEL station for the water years 2000, 2001, and 2002, respectively, using the perturbed precipitation data based on the sampling method. Figure 2.6 shows the effect of ensemble precipitation on SWE simulation for the water year 2002 using the AR method. Compared to the water year 2002, the ensemble simulation based on the sampling method shows a wider uncertainty range than that of the AR method. However, the uncertainty ranges of SWE from both methods do not explain the underestimation of SWE values. Because our simulation is conducted for gridded cells, it is not easy to directly compare the model simulated SWE with the observed point-scale SWE. Considering that the DMIP2 precipitation and temperature data represent the model grid cell very well, however, the magnitude of the underestimation for the Ebbetts Pass station is large.

To understand this underestimation of SWE even with perturbed precipitation, we have calculated the cumulative precipitation from DMIP2 and solid precipitation from the snow model and compared them with SWE from the Ebbetts Pass station. Figure 2.7 shows this comparison for the water year 2002. As shown in the figure, at the beginning of the accumulation period the DMIP2 precipitation and calculated solid snow show similar values to the observed SWE, but diverge as intermittent melting occurs. Moreover, the cumulative solid snow is less than the observed SWE. In fact, in order to match the model simulated SWE to observed SWE, the solid snow should be more than the measured SWE because of the intermittent melting. This comparison implies that the DMIP2 precipitation should be much higher than the current value to reduce the underestimation of SWE even though the areal mean value does not necessarily have to be matched with the point-scale observation. Note that the temperature values from DMIP2 were very close to those of the SNOTEL observation.

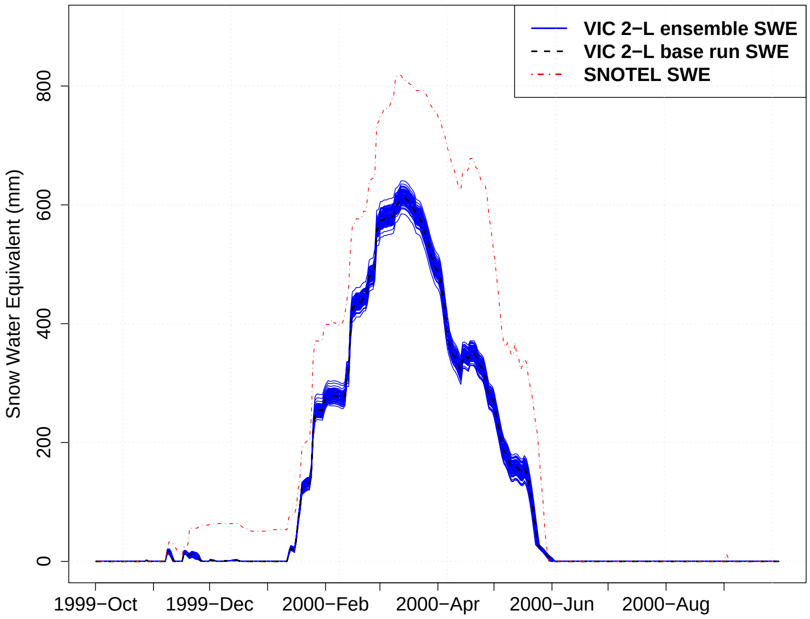

Figure 2.3: Ensemble simulation of SWE using the sampling method for water year 2000.

Precipitation is known as the most dominant forcing in simulating SWE [32]. Compared to the precipitation effect on SWE simulations, we also examined the effects of other forcing data. Figure 2.8 shows ensemble simulations of SWE using the 100 perturbed DMIP2 temperature data. In comparison with the effect of precipitation, its uncertainty range is very small. Because of the strong nonlinearities in land surface hydrological processes, temperature effect may be increased in some cases and reduced in others, depending on the location. For example, when the temperature is very low and the downward radiation is weak during the accumulation season, it is likely that temperature uncertainty may not play a big role. In Figure 2.8, the temperature uncertainty is amplified when melting occurs even though the overall uncertainty magnitude is much less than that of precipitation.

Figures 2.9 and 2.10 show the smoothed pressure and longwave radiation driving data, respectively, using NLDAS and NARR products. These smoothed estimators were computed

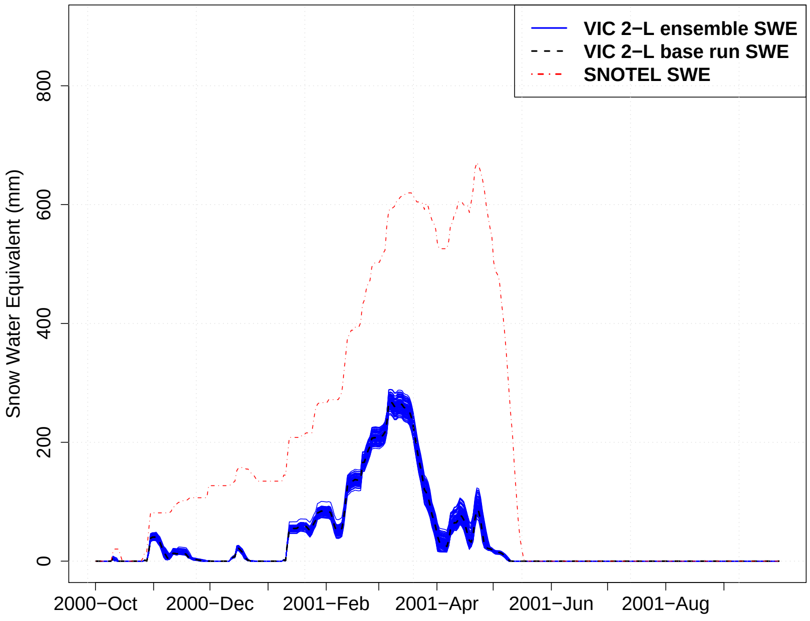

Figure 2.4: Ensemble simulation of SWE using the sampling method for water year 2001.

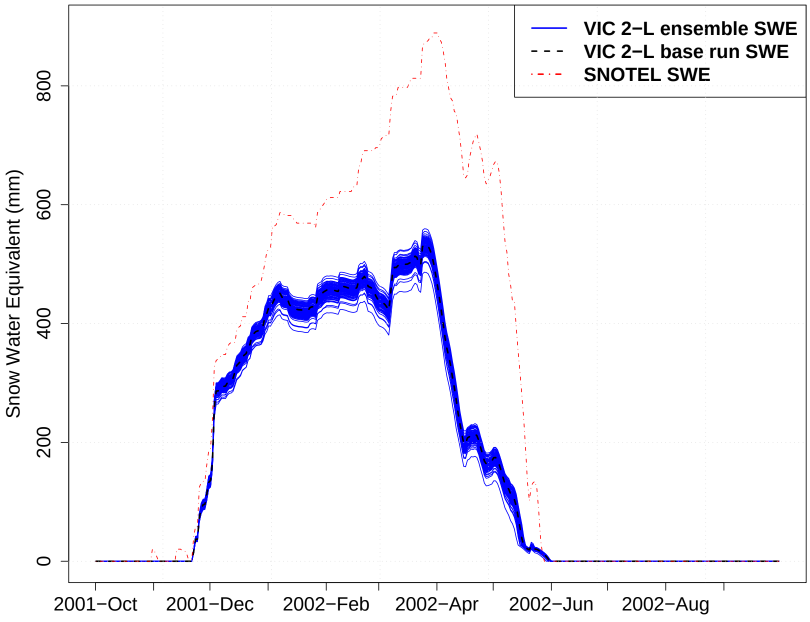

Figure 2.5: Ensemble simulation of SWE using the sampling method for water year 2002.

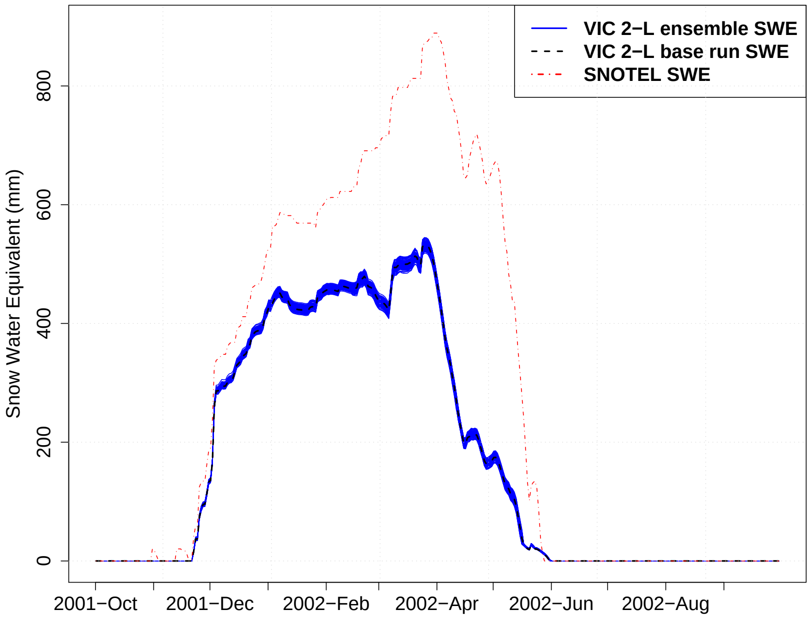

Figure 2.6: Ensemble simulation of SWE using the AR method for the water year 2002.

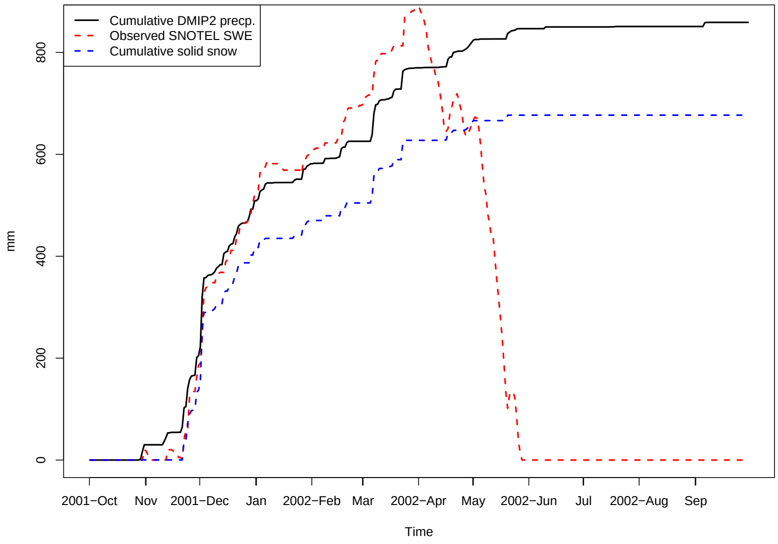

Figure 2.7: Comparison of cumulative DMIP2 precipitation, cumulative solid snow from the snow model, and SNOTEL SWE.

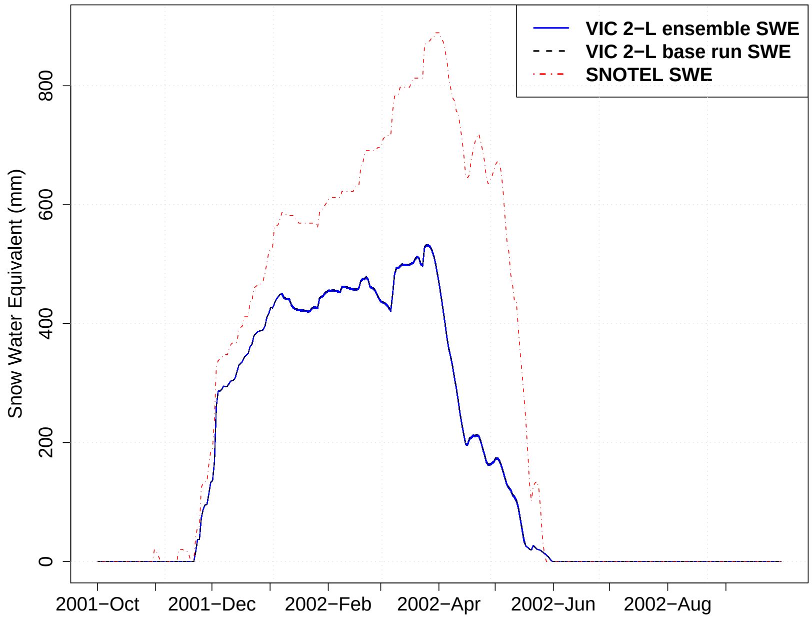

Figure 2.8: SWE simulations based on ensemble temperature data for the water year 2002.

by the state space approach described in Section 2.2. Based on the smoothing and EM-based parameter estimation, we computed the posterior distribution, which is then used to generate 100 ensemble datasets. As discussed earlier, the pressure data from NLDAS and NARR behave like a random walk process and can be well modeled by our simple linear state space model. Figures 2.11 and 2.12 show the difference between the baserun simulation and each of the ensemble simulations for longwave and shortwave radiation, respectively (for convenient comparison, the differences are plotted). The baserun simulation is forced with DMIP2 gridded precipitation and temperature and smoothed secondary energy forcings from NLDAS and NARR. Compared with the effect of precipitation perturbations, the effects by longwave and shortwave are much smaller. In the comparison between longwave and shortwave radiations, the effect of perturbed shortwave radiation is larger than that of longwave radiation due to the larger magnitude of shortwave radiation fluxes, particularly during the cold season.

2.4 Conclusion

The results from ensemble simulations show that perturbed forcing data with reasonable uncertainty cannot reduce the underestimation of SWE. Considering that the gridded precipitation and temperature data are from the DMIP2 product that represents the grid cell very well, these results show that more uncertainty factors need to be addressed. One of the factors was found in the comparison between the calculated solid precipitation (i.e., snow) and the observed SNOTEL SWE. In comparison, the solid precipitation was less than the observed SWE, which led to underestimation of SWE in the model simulations. Among the forcing variables used, the effect of precipitation uncertainty was the largest. Temperature followed precipitation and other secondary forcing variables were smaller than these two.

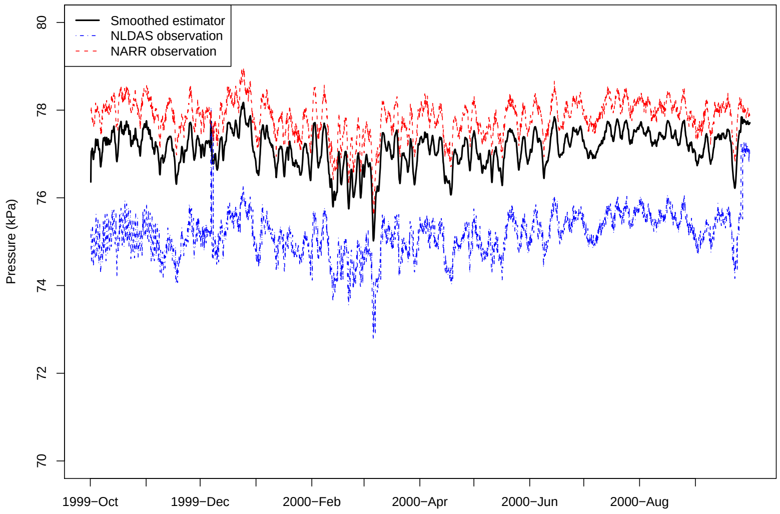

Figure 2.9: Smoothed estimator for pressure during October 1999.

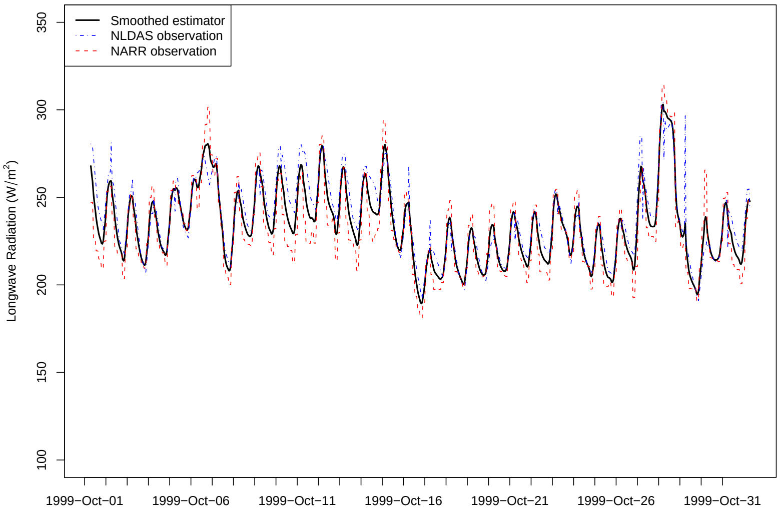

Figure 2.10: Smoothed estimator for longwave radiation during October 1999.

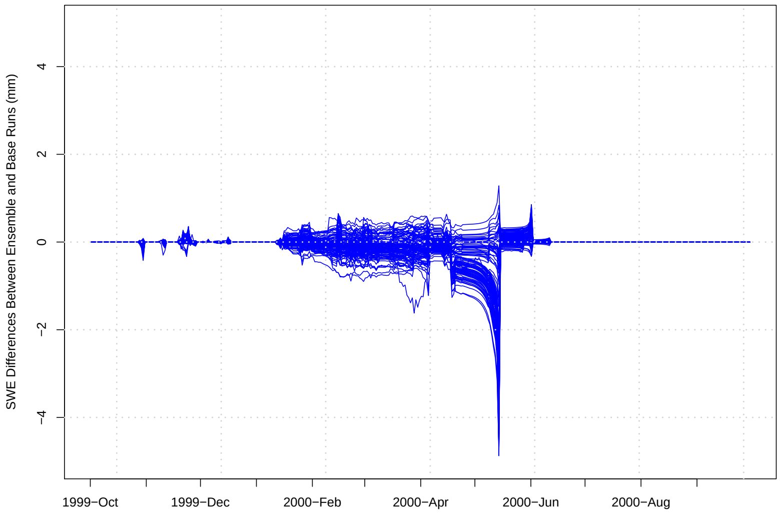

Figure 2.11: Difference in SWE between the baserun and 100 ensemble simulation using the perturbed longwave radiation for the water year 2000 at the Ebbetts Pass SNOTEL station.

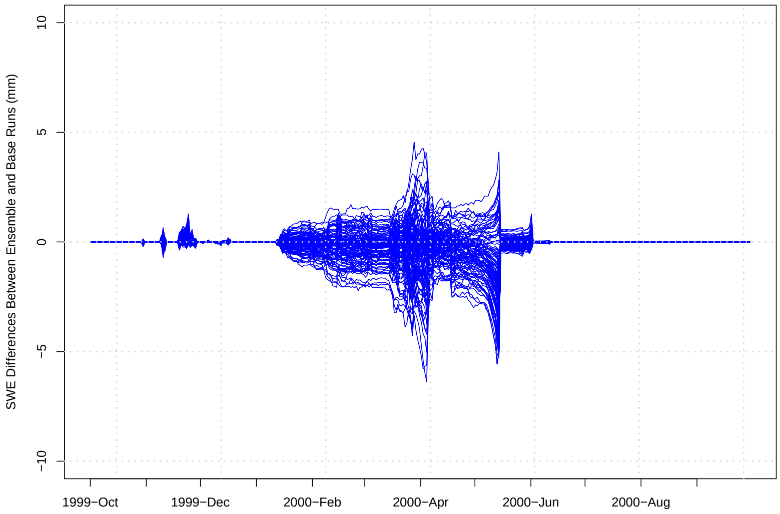

Figure 2.12: Difference in SWE between the baserun and 100 ensemble simulation using the perturbed shortwave radiation for the water year 2000 at the Ebbetts Pass SNOTEL station.

DMIP2 precipitation data are bias-corrected in a sense, at least by removing the systematic low bias of NLDAS for a subdomain of the Sierra Nevada. It is likely that DMIP2 precipitation and temperature data are the most accurate ones we could use for distributed modeling unless we use point-scale adjustments for gridded data. However, our results indicate that there are still undercatch problems in the raw precipitation data (e.g., cooperative rain gage data) on which the DMIP2 precipitation product is based. This situation leads us to a question of snow model physics. We are interested in learning how a more complex model combined with quality forcing data would help improve the underestimation problem and the degree to which it would help. At this moment, it seems that at least a more thorough examination of snow processes is needed to understand the underestimations, which may not be explained by uncertainties in the forcing data. The underestimation problem is a result of the combination of uncertain forcing and model physics. Underestimation of SWE due to forcing data with a large undercatch may not be overcome by any snow model. But we may need to learn how new snow parameterizations could change the underestimation problem with quality forcing data such as DMIP2 precipitation and temperature to fully understand the uncertain processes of snow. In the following chapter, we develop a new snow model and investigate its impact on simulating snow states.

Chapter 3

Model Complexity and Its Impact

3.1 Introduction

Snow models have been developed for a wide range of purposes from point scale to global scale applications. Because of the importance of snow physics in global circulation modeling, many snow models were developed as components of global circulation models (GCMs) [1]. Snow models were also designed and implemented to monitor snow states at the point scale. At the local scale, snow models are used for hydrological applications and avalanche studies. The results from the previous chapter showed that simulations with perturbed ensemble forcing data did not explain the low bias problem in high mountain sites of the Sierra Nevada. In this chapter, we are concerned with understanding what portion of this uncertainty a snow model can explain by developing a more complex snow model.

One of the issues regarding snow model development is the impact of snow model complexity on simulation of snow state variables and energy budget. A small number of snow model intercomparison studies have been done to address the complexity issue [20] [21]. Many model intercomparison studies have attempted to discover whether more complicated snow models with more complete snow processes perform better than simple models. An important study objective for them is to identify which internal processes play a dominant role in explaining uncertainties associated with snow model physics and how the identified processes can improve model performance.

Intercomparison studies of snow models can be classified into: 1) comparison of snow models using different land surface parameterizations and 2) comparison of snow models using the same parameterization but with different internal processes. The former includes studies done by Schlosser et al. [33], Jin et al. [34], Pan et al. [16], Bowling et al. [21], Nijssen et al. [35], Etchevers et al. [20], and Feng et al. [22]. The latter is well represented by Boone and Etchevers [36]. Etchevers et al. [20] implemented the SnowMIP project for a more general comparison of snow models and found that more sophisticated models do not necessarily perform better than simpler models. In some cases, simple models simulate snow states better than sophisticated models.

Depending on study methods, data and study locations, the impacts of snow model complexity are evaluated differently. Model complexity itself is not easy to define because snow internal processes for each model are different [20]. Moreover, the difference in land surface parameterization into which a snow model is incorporated increases the overall complexity for modeling and analysis. For this reason, a simple criterion for complexity classification such as the number of snow layers is often used. An array of snow model complexity studies have been conducted focusing on intercomparison of snow models under different land surface parameterization schemes. When many different models with different levels of complexity are involved in an intercomparison study, it is often hard to interpret the results because of the complexity of land surface parameterization [35].

This study aims to address the issue of snow model complexity with a specific goal. Our experiment focuses on examining the effect of model complexity when we add complexity to an existing LSM (i.e., VIC LSM). The benefit of this experiment is that we can understand which physical processes make a difference and which processes do not contribute to model performance more clearly. The snow model component of the VIC LSM has been evaluated to simulate snow states (e.g., SWE) relatively well. Feng et al. [22] showed that VIC simulations are in good agreement with those of SNTHERM [37], which is one of the most complex snow models. The 2-layer snow model of VIC performed equivalently or sometimes better than the Community Land Model version 3 (CLM3), which uses five snow layers. Pan et al. [16] showed that VIC simulated SWE relatively well compared with the other snow models used in the NLDAS project. VIC also participated in the Project for Intercomparison of Land-surface Parameterization Schemes (PILPS) Phase 2(e), and the 2-L snow model in the VIC LSM captured the overall dynamics of snow accumulation and ablation [35]. Even though the 2-L snow module of the VIC LSM has been evaluated favorably in many simulations, we hypothesize that there are more internal processes to be added to improve snow processes at a reasonable level of computational cost. In this regard, we develop a new snow model by adding more complexity to the existing snow model of the VIC LSM and compare the effect of complexity between the two models. The fundamental change in complexity is moving from a 2-L structure to a multi-layer one. This internal process comparison can be done more effectively when using the same land surface boundary conditions under the same LSM.

Processwise, the snow model developed in this study focuses on a more complete description of heat transfer in the snow layers. In snow model intercomparison studies, both different boundary conditions and different complexity levels inside the snow layers are used to compare snow models. This is one of the reasons that snow models show great variability during ablation processes. Even a simple snow model may contain many parameters. In order to make our comparison experiment reasonably affordable, we limit our experiment to the effect of the heat transfer through the snow and soil layers and its associated physical processes, including density changes across the layer. Therefore, we focus on the thermal process in the soil and snow with the boundary condition in the snow surface having the same formulation between the two models. For the snow-air boundary condition, we use the formulation used in [38].

One thing to be cautious about complex model development is the expense of running the model. Since the new multi-layer model allows an unlimited number of vertical layers as in SNTHERM [37], its computational cost is larger than the existing 2-L model. In order to reduce the computational cost, we changed some structure of the VIC LSM for cold processes (see the following section for details). As a result, we combine snow and soil layers into one single system to solve hydrological variables simultaneously. This simultaneous processes saves some computational cost by consolidating two numerical non-linear solving process for snow and frozen soil into one process, created by a new soil-snow model.

3.2 Development of Multi-layer Soil-Snow Model

3.2.1 Change in Model Structure

The new soil-snow model accounts for direct interactions of thermal fluxes between the soil and snow systems, combining them as one system. The most significant feature is that the main variables (e.g., temperature and water content) for the soil and snow layers are simulated as one system simultaneously. Thus, the heat fluxes through soil and snow layers are calculated seamlessly. The new model adopts a multiple-layer approach to describe the changes of variables over time and layer depths more precisely. For example, snow density changes are simulated over time and depth following Anderson [39]. The new soil-snow model can be embedded in land surface models (LSM) or run as a stand-alone system when the necessary input and output for the new model are provided. The new soil-snow model has significantly changed the framework of the VIC LSM for cold season processes.

Figure 3.1 shows the layer structure of the new soil-snow system, which includes the snow layers, the soil moisture layers, and the soil thermal nodes. During the cold season, the temperature profile of the frozen soil is computed, and subsequently the water content for each soil node is obtained. Then the calculated water content is redistributed over the three soil moisture layers in the same way as in Cherkauer and Lettenmaier [38]. Even though the soil and snow systems are shown separately to demonstrate the details of each system, they are treated as one system in the solution processes. That is, the bottom layer of the snow system communicates with the top layer of the soil system directly in terms of heat fluxes when snow is present on the ground. When the number of the snow layers is N, the zero-based index for the top soil thermal node is N (Figure 3.1). Since the top 30 cm of the snow layers are sensitive to changes in snow thermal conductivity, a shallow thickness (e.g., 5 cm) is applied for these layers. For the other layers, the thickness of each layer increases as the depth from the surface increases for numerical efficiency. The number of layers and their thicknesses can be changed by the user due to the model's flexible structure.

For the soil system, the top two layers are shallow (e.g., 10 cm) to be consistent with the structure of the soil moisture layers from the VIC LSM. As shown in Figure 3.1, the bottom of the soil system is fixed as an annual average temperature at the damping depth. This fixed temperature is used as a Dirichlet boundary condition for the whole snow-soil system. Note that in Figure 3.1 we assume the number of soil thermal nodes as seven for illustration purposes but any number of nodes can be given by the user. For the soil moisture layers, we use the same structure as that of the original VIC LSM. The number of soil moisture layers is taken as three with the top layer being very thin (e.g., 10 cm) by default [40].

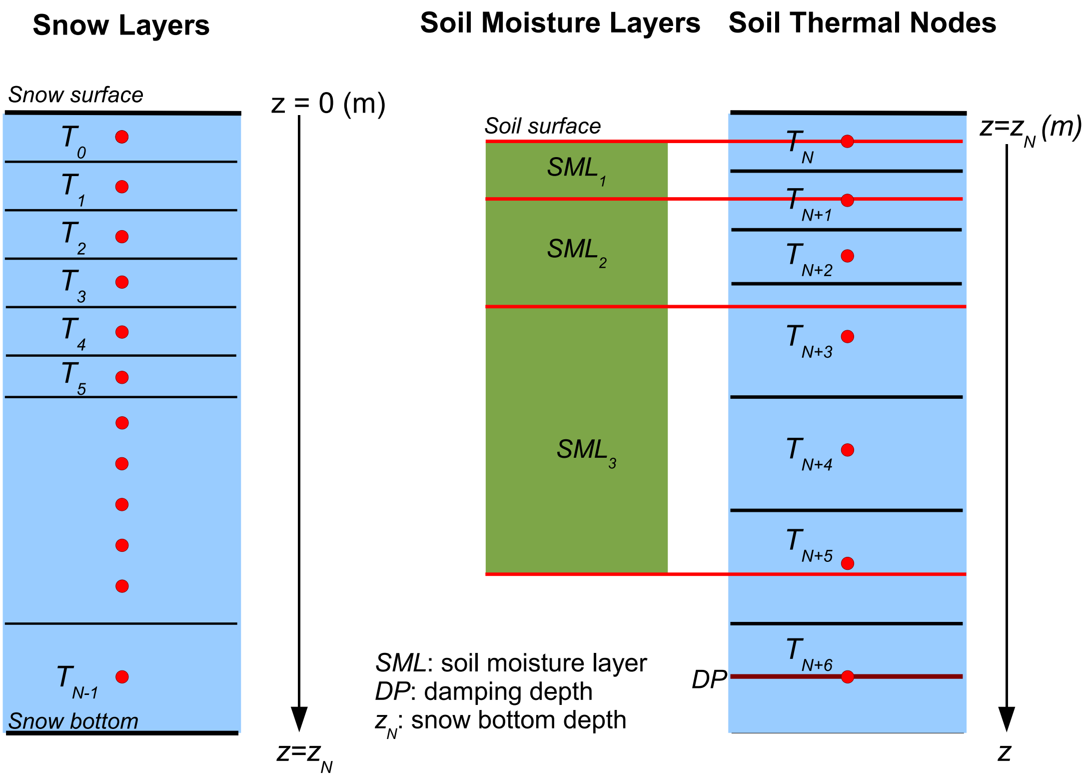

Figure 3.1: New soil-snow model structure

3.2.2 Soil Model

3.2.2.1 Governing equation

The general governing equation for heat flux in the soil column can be written as:

$$
\begin{aligned}
C_s \frac{\partial T}{\partial t} &= -\frac{\partial G}{\partial z} + \rho_i L_f (\frac{\partial W_i}{\partial t}) \\
G &= -\kappa \frac{\partial T}{\partial z}
\end{aligned}
\tag{3.1}
$$

where G is the soil heat flux in the z direction, C_s is the volumetric specific heat of soil ($Jm^{-3}K^{-1}$), κ is the soil thermal conductivity ($Wm^{-1}K^{-1}$), ρ_i is the density of ice (kgm^{-3}), L_f is the latent heat of fusion (Jkg^{-1}), and W_i is the ice content of the layer (m^3m^{-3}). Each term in Equation 3.1 has a unit of Wm^{-3}. If we let κ change each time step, we can write the equation in the following form:

$$
C_s \frac{\partial T}{\partial t} = \frac{\partial \kappa}{\partial z}\frac{\partial T}{\partial z} + \kappa \frac{\partial^2 T}{\partial z^2} + \rho_i L_f (\frac{\partial W_i}{\partial t}) \tag{3.2}
$$

Flerchinger and Saxton [41] use the following equation to express the frozen soil moisture in terms of the layer temperature and other known values:

$$
W_l = W^c_{max} \left[\left(\frac{1}{g\psi_e} \right) \left(\frac{L_f T}{T + 273.15} \right) \right]^{-1/b} \tag{3.3}
$$

where W_l is the liquid water content (i.e., fraction of unfrozen water) (mm), W^c_{max} is the maximum (or saturated) water content (mm), g is acceleration due to gravity (ms^{-2}), L_f is the latent heat of fusion (Jkg^{-1}), T is temperature (^oC), and b is the pore-size distribution index. The above equation relates the amount of unfrozen soil moisture (i.e., liquid water in the soil) to soil properties, temperature, and maximum water content, and is also used in the current VIC LSM [38].

3.2.2.2 Numerical solutions

The new soil-snow model solves temperature and water content simultaneously as one system. However, we present the numerical solution for each system separately for convenience. We use the Crank-Nicholson scheme where θ, the weight between explicit and implicit schemes, is 0.5 by default. The Crank-Nicholson method has second-order accuracy in both time and space. Now the governing equation can be represented by:

$$\begin{aligned} C_s\frac{T_j^{n+1}-T_j^n}{\Delta t} &= \theta\left(\frac{\partial\kappa}{\partial z}\right)_j^n\left(\frac{\partial T}{\partial z}\right)_j^{n+1}+(1-\theta)\left(\frac{\partial\kappa}{\partial z}\right)_j^n\left(\frac{\partial T}{\partial z}\right)_j^n+ \\ &\quad \theta(\kappa)_j^n\left(\frac{\partial^2 T}{\partial z^2}\right)_j^{n+1}+(1-\theta)(\kappa)_j^n\left(\frac{\partial^2 T}{\partial z^2}\right)_j^n+ \\ &\quad \rho_i L_f\left(\frac{(W_i)_j^{n+1}-(W_i)_j^n}{\Delta t}\right) \end{aligned} \tag{3.4}$$

where j is the layer index, and n is the time index.

Equation 3.4 is a system of equations when used for multiple layers and thus can be summarized as a matrix equation. We use a multi-dimensional version of the Newton Raphson (NR) method to solve the system of equations. In this case, the NR method is a multi-dimensional version. For a macroscale land surface model we need a fast nonlinear solving algorithm, and the NR method is known to be efficient. To be used for the NR method, we rearrange Equation 3.4 and equate it to f_j to get:

$$\begin{aligned} f_j &= T_j^{n+1}-T_j^n-\theta\frac{\Delta t}{C_s}\left(\frac{\partial\kappa}{\partial z}\right)_j^n\left(\frac{\partial T}{\partial z}\right)_j^{n+1}-(1-\theta)\frac{\Delta t}{C_s}\left(\frac{\partial\kappa}{\partial z}\right)_j^n\left(\frac{\partial T}{\partial z}\right)_j^n \\ &\quad -\theta\frac{\Delta t}{C_s}(\kappa)_j^n\left(\frac{\partial^2 T}{\partial z^2}\right)_j^{n+1}-(1-\theta)\frac{\Delta t}{C_s}(\kappa)_j^n\left(\frac{\partial^2 T}{\partial z^2}\right)_j^n \\ &\quad -\frac{\rho_i L_f}{C_s}\left((W_i)_j^{n+1}-(W_i)_j^n\right) \end{aligned} \tag{3.5}$$

Note that f_j is the governing equation in a finite-difference form for layer j.

The following numerical scheme is used for the first derivative:

$$\left(\frac{\partial T}{\partial z}\right)_j^n = 0.5\left(\frac{T_j^n-T_{j-1}^n}{z_j^n-z_{j-1}^n}+\frac{T_{j+1}^n-T_j^n}{z_{j+1}^n-z_j^n}\right) \tag{3.6}$$

Note that the first derivative at layer j for time n is the average of the fluxes at the upper and lower interface of layer. This configuration of numerical differentiation can reduce the numerical error in a layer structure where each layer has a different thickness.

In a simpler form, Equation 3.6 can be expressed as:

$$\left(\frac{\partial T}{\partial z}\right)_j^n = \frac{1}{2}\frac{F1_{soil}}{\Delta z_1 \Delta z_2} \tag{3.7}$$

where:

$$\begin{aligned}
F1_{soil} &= \Delta z_{j,j-1}^n T_{j+1}^n + (\Delta z_{j+1,j}^n - \Delta z_{j,j-1}^n)T_j^n - \Delta z_{j+1,j}^n T_{j-1}^n \\
&= \Delta z_1 T_{j+1}^n + (\Delta z_2 - \Delta z_1)T_j^n - \Delta z_2 T_{j-1}^n \\
\Delta z_1 &= \Delta z_{j,j-1}^n = z_j^n - z_{j-1}^n \\
\Delta z_2 &= \Delta z_{j+1,j} = z_{j+1}^n - z_j^n
\end{aligned}$$

The second derivative can be expressed in the following finite-difference form:

$$\left(\frac{\partial^2 T}{\partial z^2}\right)_j^n = \frac{2}{z_{j+1}^n - z_{j-1}^n}\left(\frac{T_{j+1}^n - T_j^n}{z_{j+1}^n - z_j^n} - \frac{T_j^n - T_{j-1}^n}{z_j^n - z_{j-1}^n}\right) \tag{3.8}$$

In the similar way, Equation 3.8 can be expressed in a simpler form:

$$\left(\frac{\partial^2 T}{\partial z^2}\right)_j^n = 2\frac{F2_{soil}}{\Delta z_1 \Delta z_2(\Delta z_1 + \Delta z_2)} \tag{3.9}$$

where $F2_{soil}$ can be expressed as:

$$F2_{soil} = \Delta z_1 T_{j+1}^n - (\Delta z_1 + \Delta z_2)T_j^n + \Delta z_2 T_{j-1}^n$$

The NR method requires derivatives for each finite-difference form with respect to the unknowns. The unknowns include T_{j-1}^{n+1}, T_j^{n+1}, and T_{j+1}^{n+1} in the soil system.

First we define the first derivative as follows:

$$[U]_x \tag{3.10}$$

where U is the variable we are taking the derivative of and x is the variable we take the derivative with respect to.

Based on the definition above, we have the following derivatives for the time $t = n$:

$$\left[\left(\frac{\partial T}{\partial z}\right)_j^n\right]_{T_{j-1}^{n+1}} = 0 \tag{3.11}$$

$$\left[\left(\frac{\partial T}{\partial z}\right)_j^n\right]_{T_j^{n+1}} = 0 \tag{3.12}$$

$$\left[\left(\frac{\partial T}{\partial z}\right)_j^n\right]_{T_{j+1}^{n+1}} = 0 \tag{3.13}$$

For time $t = n + 1$, we have the following:

$$\left[\left(\frac{\partial T}{\partial z}\right)_j^{n+1}\right]_{T_{j-1}^{n+1}} = -\frac{1}{2\Delta z_1} \tag{3.14}$$

$$\left[\left(\frac{\partial T}{\partial z}\right)_j^{n+1}\right]_{T_j^{n+1}} = \frac{\Delta z_2 - \Delta z_1}{2\Delta z_1 \Delta z_2} \tag{3.15}$$

$$\left[\left(\frac{\partial T}{\partial z}\right)_j^{n+1}\right]_{T_{j+1}^{n+1}} = \frac{1}{2\Delta z_2} \tag{3.16}$$

Now we take derivatives for terms with the second derivatives. First for time $t = n$ we have:

$$\left[\left(\frac{\partial^2 T}{\partial z^2}\right)_j^{n}\right]_{T_{j-1}^{n+1}} = 0 \tag{3.17}$$

$$\left[\left(\frac{\partial^2 T}{\partial z^2}\right)_j^{n}\right]_{T_j^{n+1}} = 0 \tag{3.18}$$

$$\left[\left(\frac{\partial^2 T}{\partial z^2}\right)_j^{n}\right]_{T_{j+1}^{n+1}} = 0 \tag{3.19}$$

For time $t = n + 1$ we have the follow set of results:

$$\left[\left(\frac{\partial^2 T}{\partial z^2}\right)_j^{n+1}\right]_{T_{j-1}^{n+1}} = \frac{2}{\Delta z_1(\Delta z_1 + \Delta z_2)} \tag{3.20}$$

$$\left[\left(\frac{\partial^2 T}{\partial z^2}\right)_j^{n+1}\right]_{T_j^{n+1}} = -\frac{2}{\Delta z_1 \Delta z_2} \tag{3.21}$$

$$\left[\left(\frac{\partial^2 T}{\partial z^2}\right)_j^{n+1}\right]_{T_{j+1}^{n+1}} = \frac{2}{\Delta z_2(\Delta z_1 + \Delta z_2)} \tag{3.22}$$

The final step for the derivatives is to take derivatives of f_j with respect to T_{j-1}^{n+1}, T_j^{n+1}, and T_{j+1}^{n+1}.

In the governing equation for the soil system (i.e., Equation 3.1), we have the ice content term W_i, which can be expressed as

$$W_i = W_t - W_l \tag{3.23}$$

where W_t is the total moisture of a given layer. Therefore, the derivative of W_i for layer j can be written as:

$$[W_i]_{T_j} = -[W_l]_{T_j} \tag{3.24}$$

3.2.3 Snow Model

3.2.3.1 Governing equation

The governing equation for the snow layers is expressed as:

$$\begin{aligned}\frac{\partial H}{\partial t} &= -\frac{\partial F}{\partial z} - \frac{\partial R_s}{\partial z} \\ &= \frac{\partial}{\partial z}\left(K_e \frac{\partial T}{\partial z} - R_s\right) \qquad (3.25)\end{aligned}$$

where H is the volumetric heat content (Jm^{-3}), F is the heat flux (Wm^{-2}), K_e is the effective heat conductivity ($J\ s^{-1}\ m^{-1}\ K^{-1}$) and R_s is net (downward) solar radiation (Wm^{-2}). We follow Verseghy [3] who used the following expression for volumetric heat content:

$$H = C_v(T - 273.15) - f_s L_f \rho_{sl} \qquad (3.26)$$

where C_v is $1.9 \times 10^6 \rho_{sl}/920$, f_s is mass fraction of the solid portion of the layer, L_f is latent heat of fusion (Jkg^{-1}), and ρ_{sl} ($kg\ m^{-3}$) is the snow density, which includes both solid and liquid portions.

3.2.3.2 Numerical solutions

The surface layer of the snow system involves fluxes at the snow-atmosphere interface. Thus, we explicitly treat the fluxes at the upper and lower interfaces of the first layer of the snow system. Now Equation 3.25 can be written as:

$$\begin{aligned}\frac{H_0^{n+1} - H_0^n}{\Delta t} &= -\frac{F^n_{0+\frac{1}{2}} - F^n_{0-\frac{1}{2}}}{\Delta z_{j=0}} - \frac{(R_s)^n_{0+\frac{1}{2}} - (R_s)^n_{0-\frac{1}{2}}}{\Delta z_{j=0}} \\ &= \frac{F^n_{0-\frac{1}{2}} - F^n_{0+\frac{1}{2}}}{\Delta z_{j=0}} + \frac{(R_s)^n_{0-\frac{1}{2}} - (R_s)^n_{0+\frac{1}{2}}}{\Delta z_{j=0}} \qquad (3.27)\end{aligned}$$

where $F^n_{0-\frac{1}{2}}$ and $F^n_{0+\frac{1}{2}}$ are the fluxes at the upper interface and lower interface of the first layer, respectively. Similarly, $(R_s)^n_{0-\frac{1}{2}}$ is the shortwave radiation at the snow-atmosphere interface, and $(R_s)^n_{0+\frac{1}{2}}$ is the solar radiation flux at depth $z = \Delta z_{j=0}$. Thus, the solar radiation flux that contributes to the first layer is $(R_s)^n_{0-\frac{1}{2}} - (R_s)^n_{0+\frac{1}{2}}$.

If we do not specifically define the index for space, we consider it as at the snow-atmosphere interface. That is, we can write as

$$(R_s)_{0-\frac{1}{2}} = (R_s)$$

First, we need to define the flux at the snow-atmosphere interface. If we use $j = 0$ for the surface layer, we can define the net flux at the interface as $F_{0-\frac{1}{2}}$, which can be expressed as

$$F_{0-\frac{1}{2}} = R_n + LE + H + M_p \qquad (3.28)$$

where R_n is net radiation, LE is the latent heat, H is sensible heat, and M_p is the advected heat by precipitation. The unit of each flux term is Wm^{-2}. Each of these terms is explained in Liang et al. [42] and we briefly introduce them in the multi-layer perspective.

The net radiation R_n is computed as:

$$R_n = f_{sa}R_s + R_L - \varepsilon\sigma T_{j=0}^4 \tag{3.29}$$

where f_{sa} is surface attenuation factor due to vegetation coverage, R_s is incoming solar (shortwave) radiation(Wm^{-2}), R_L is the downward longwave radiation (Wm^{-2}), ε is the emissivity, and σ is the Stefan-Boltzmann constant ($Wm^{-2}K^{-4}$).

The latent heat is computed as:

$$LE = L_s \frac{0.622\rho_a}{P} \frac{1}{r_a}(e_a - e_s) \tag{3.30}$$

where L_s is the latent heat of sublimation ($J\ kg^{-1}$), ρ_a is the mass density of air ($kg\ m^{-3}$), e_a is actual vapor pressure of air (Pa), P is the atmospheric pressure (Pa), and e_s is snow surface vapor pressure (Pa). e_s is assumed to be equal to the saturation vapor pressure at the snow surface temperature. When the snow surface temperature is equal to or greater than 0 $°C$, the latent heat of vaporization L_v is used instead of the latent heat of sublimation. The saturated vapor pressure over water is computed as:

$$e_{s,water} = 610.8exp\left(\frac{17.27(T - 273.15)}{237.3 + (T - 273.15)}\right) \tag{3.31}$$

where T is in K.

However, the saturated vapor pressure over ice or snow is different from that over water. e_s is approximated by [43]

$$e_s = e_{s,water}\left(1 + 0.00972(T - 273.15) + 0.000042(T - 273.15)^2\right) \tag{3.32}$$

where T is in K.

The latent heat of sublimation is also a function of the layer temperature and written as [43]:

$$L_s = (677.0 - 0.07T) \times 4.1868 \times 10^3 \tag{3.33}$$

The latent heat of vaporization (Jkg^{-1}) is calculated as:

$$L_v = (2.501 - 0.002361(T - 273.15)) \times 10^6 \tag{3.34}$$

where T is in K. We use L_v when the snow surface temperature is 0 $°C$. Therefore, L_v is $2.501 \times 10^6\ Jkg^{-1}$.

The sensible heat H is written as:

$$H_s = \frac{\rho_a c_p}{r_a}(T_a - T_{j=0}) \tag{3.35}$$

where c_p is the specific heat of air at constant pressure ($Jkg^{-1}K^{-1}$), r_a is aerodynamic resistance (s/m), and T_a is the air temperature (K).

The advected heat is written as:

$$M_p = \rho_w c_w T_a P_l \frac{1}{\Delta t} \tag{3.36}$$

where c_w is the specific heat of water (i.e., 4186 $Jkg^{-1}K^{-1}$), P_l is the amount of liquid rain (m) during the model time step, and Δt is the model time step. Note we divided the right-hand side of Equation 3.36 by Δt to use consistent units for the flux terms.

If we combine all the terms related to the upper flux of the snow surface layer, we obtain

$$\begin{aligned}
F^n_{0-\frac{1}{2}} &= f_{sa}R_s + R_L - \varepsilon\sigma(T^n_{j=0})^4 \\
&\quad + L_s\frac{0.622\rho_a}{P}\frac{1}{(r_a)^n_0}(e_a - (e_s)^n_0) \\
&\quad + \frac{\rho_a c_p}{(r_a)^n_0}(T_a - T^n_{j=0}) \\
&\quad + \rho_w c_w T_a P_l\frac{1}{\Delta t}
\end{aligned} \tag{3.37}$$

Since we derived the equation for the upper flux of the surface layer, we need to find the flux from the bottom interface $F_{0+\frac{1}{2}}$. We write an equation for the flux at the interface between layer $j = 0$ and layer $j = 1$ following [44] as:

$$F_{0+\frac{1}{2}} = -(DK_e)^n_{0,1}(T_{j=1} - T_{j=0}) \tag{3.38}$$

where $(DK_e)^n_{0,1}$ can be expressed as:

$$(DK_e)^n_{0,1} = \frac{1}{\left(\frac{\Delta z^n_{j=0}}{2} + \frac{\Delta z^n_{j=1}}{2}\right)}\left(\frac{\Delta z^n_{j=0} + \Delta z^n_{j=1}}{\frac{\Delta z^n_{j=0}}{(K_e)^n_{j=0}} + \frac{\Delta z^n_{j=1}}{(K_e)^n_{j=1}}}\right) \tag{3.39}$$

Note that n denotes the previous time as usual.

Then we obtain

$$\begin{aligned}
F^n_{0+\frac{1}{2}} &= -(DK_e)^n_{0,1}(T^n_{j=1} - T^n_{j=0}) \\
F^{n+1}_{0+\frac{1}{2}} &= -(DK_e)^n_{0,1}(T^{n+1}_{j=1} - T^{n+1}_{j=0})
\end{aligned} \tag{3.40}$$

Now we need to find derivatives for each term with respect to the unknowns. First, the derivatives of $F^n_{0-\frac{1}{2}}$ are expressed as:

$$\begin{aligned}
\left[F^n_{0-\frac{1}{2}}\right]_{T^{n+1}_{j=0}} &= 0 \\
\left[F^n_{0-\frac{1}{2}}\right]_{T^{n+1}_{j=1}} &= 0 \\
\left[F^{n+1}_{0-\frac{1}{2}}\right]_{T^{n+1}_{j=0}} &= -4\varepsilon\sigma(T^{n+1}_{j=0})^3 \\
&\quad + L_s\frac{0.622\rho_a}{P}\left[\frac{1}{r_a}(e_a - (e_s)^{n+1})\right]_{T^{n+1}_{j=0}} \\
&\quad + \rho_a c_p\left[\frac{1}{r_a}(T_a - T^{n+1}_{j=0})\right]_{T^{n+1}_{j=0}} \\
\left[F^{n+1}_{0-\frac{1}{2}}\right]_{T^{n+1}_{j=1}} &= 0
\end{aligned} \tag{3.41}$$

The derivatives of $F^n_{0+\frac{1}{2}}$ are given as

$$\begin{aligned}
\left[F^n_{0+\frac{1}{2}}\right]_{T^{n+1}_{j=0}} &= 0 \\
\left[F^n_{0+\frac{1}{2}}\right]_{T^{n+1}_{j=1}} &= 0 \\
\left[F^{n+1}_{0+\frac{1}{2}}\right]_{T^{n+1}_{j=0}} &= (DK_e)^n_{0,1} \\
\left[F^{n+1}_{0+\frac{1}{2}}\right]_{T^{n+1}_{j=1}} &= -(DK_e)^n_{0,1}
\end{aligned} \tag{3.42}$$

Finally we combine all terms to yield:

$$\begin{aligned}
f_0 &= H^{n+1}_0 - H^n_0 - \theta\frac{\Delta t}{\Delta z_{j=0}}F^{n+1}_{0-\frac{1}{2}} - (1-\theta)\frac{\Delta t}{\Delta z_{j=0}}F^n_{0-\frac{1}{2}} \\
&\quad +\theta\frac{\Delta t}{\Delta z_{j=0}}F^{n+1}_{0+\frac{1}{2}} + (1-\theta)\frac{\Delta t}{\Delta z_{j=0}}F^n_{0+\frac{1}{2}} \\
&\quad +\frac{\Delta t}{\Delta z_{j=0}}(R_s)^n_{0+\frac{1}{2}}
\end{aligned} \tag{3.43}$$

where we removed $\frac{1}{\Delta z_{j=0}}(R_s)^n_{0-\frac{1}{2}}$ because it is included in $F_{0-\frac{1}{2}}$.

Now, we derive numerical solutions for the intermediate layers of the snow system. By assuming the effective heat conductivity K_e as a function of z, we obtain:

$$\frac{\partial H}{\partial t} = \frac{\partial K_e}{\partial z}\frac{\partial T}{\partial z} + K_e\frac{\partial^2 T}{\partial z^2} - \frac{\partial R_s}{\partial z} \tag{3.44}$$

If we use the Crank-Nicholson method as we did for the soil system, Equation 3.44 can be expressed as:

$$\begin{aligned}
\frac{H^{n+1}_j - H^n_j}{\Delta t} &= \theta\left(\frac{\partial K_e}{\partial z}\right)^n_j\left(\frac{\partial T}{\partial z}\right)^{n+1}_j + (1-\theta)\left(\frac{\partial K_e}{\partial z}\right)^n_j\left(\frac{\partial T}{\partial z}\right)^n_j \\
&\quad +\theta(K_e)^n_j\left(\frac{\partial^2 T}{\partial z^2}\right)^{n+1}_j + (1-\theta)(K_e)^n_j\left(\frac{\partial^2 T}{\partial z^2}\right)^n_j \\
&\quad -\left(\frac{\partial R_s}{\partial z}\right)^n_j
\end{aligned} \tag{3.45}$$

Rearranging Equation 3.45 and letting it be f_j yields:

$$\begin{aligned}
f_j &= H^{n+1}_j - H^n_j - \theta\Delta t\left(\frac{\partial K_e}{\partial z}\right)^n_j\left(\frac{\partial T}{\partial z}\right)^{n+1}_j - (1-\theta)\Delta t\left(\frac{\partial K_e}{\partial z}\right)^n_j\left(\frac{\partial T}{\partial z}\right)^n_j \\
&\quad -\theta\Delta t(K_e)^n_j\left(\frac{\partial^2 T}{\partial z^2}\right)^{n+1}_j - (1-\theta)\Delta t(K_e)^n_j\left(\frac{\partial^2 T}{\partial z^2}\right)^n_j \\
&\quad +\Delta t\left(\frac{\partial R_s}{\partial z}\right)^n_j
\end{aligned} \tag{3.46}$$

The derivatives for each term of Equation 3.46 are similar to those we derived from the soil system. The only difference is for the derivatives of the volumetric heat content H, which is expressed as:

$$\begin{aligned} H_j^n &= (C_v)_j^n (T_j^n - 273.15) - (f_s L_f \rho_{sl})_j^n \qquad (3.47) \\ H_j^{n+1} &= (C_v)_j^n (T_j^{n+1} - 273.15) - (f_s)_j^{n+1} (L_f \rho_{sl})_j^n \qquad (3.48) \end{aligned}$$

The derivatives of H with respect to the unknown temperatures are:

$$\begin{aligned} \left[H_j^n\right]_{T_{j-1}^{n+1}} &= 0 \\ \left[H_j^n\right]_{T_j^{n+1}} &= 0 \\ \left[H_j^n\right]_{T_{j+1}^{n+1}} &= 0 \\ \left[H_j^{n+1}\right]_{T_{j-1}^{n+1}} &= 0 \\ \left[H_j^{n+1}\right]_{T_j^{n+1}} &= (C_v)_j^n \\ \left[H_j^{n+1}\right]_{T_{j+1}^{n+1}} &= 0 \end{aligned} \qquad (3.49)$$

3.2.3.3 Snow density

Snow density change over depth is one of the key features of the new soil-snow model. In the 2-L model, a single density accounts for the state of the entire snowpack. In the new model, we compute snow density for each layer to describe this property more explicitly. The representation of density change in the multi-layered setting is based on Anderson's work [39]. We begin with the basic physical relationship between snow water and snow layer thickness to derive density change equations based on Anderson's work. The relationship between the solid portion density of the snow layer and its depth can be expressed as:

$$\Delta z = \frac{W_s \rho_w}{\rho_s} \qquad (3.50)$$

where Δz is the thickness of the layer (m), W_s is the snow water equivalent (m), ρ_w is the water density, and ρ_s is the density of the solid portion.

We can take derivative on both sides with respect to time to yield:

$$\begin{aligned} \frac{\partial \Delta z}{\partial t} &= W_s \rho_w \frac{\partial (\rho_s)^{-1}}{\partial t} \\ &= -W_s \rho_w \frac{1}{(\rho_s)^2} \frac{\partial \rho_s}{\partial t} \end{aligned} \qquad (3.51)$$

If we rearrange equation 3.51, we have

$$\frac{1}{\rho_s} \frac{\partial \rho_s}{\partial t} = -\frac{\partial \Delta z}{\partial t} \frac{1}{W_s \rho_w} \rho_s \qquad (3.52)$$

If we substitute Equation 3.50 into Equation 3.52, we obtain:

$$\frac{1}{\rho_s}\frac{\partial \rho_s}{\partial t} = -\frac{\partial \Delta z}{\partial t}\frac{1}{W_s\rho_w}\frac{W_s\rho_w}{\Delta z} \tag{3.53}$$

$$= -\frac{1}{\Delta z}\frac{\partial \Delta z}{\partial t} \tag{3.54}$$

The multi-layered snow model requires snow density to change over depth as well as in time. We consider two-phase density changes: (1) snow settling and (2) compaction.

During destructive metamorphism of snow (e.g., from star-shaped crystals to rounded aggregates), snow settling occurs, causing an increase in density. The influence of snow settling is primarily important in the initial stages (i.e., new snow) following snowfall. For the estimation of snow density changes due to settling, Anderson [39] suggested the following relationship as a function of temperature and snow density:

$$\frac{1}{\rho_s}\frac{\partial \rho_s}{\partial t} = -\frac{1}{\Delta z}\frac{\partial \Delta z}{\partial t} = \begin{cases} C_3 e^{-C4(T_0-T)} & \rho_s \leq \rho_d, \\ C_3 e^{-C4(T_0-T)} e^{-0.046(\rho_s-\rho_d)} C_6 & \rho_s > \rho_d \end{cases} \tag{3.55}$$

where C_3 is the fractional settling rate at $0°C$ for densities less than ρ_d, C_4 and ρ_d are constants to be determined by calibration. Yen [45] reports that the effect of snow settling is not significant for densities greater than 250 $kg\,m^{-3}$. Therefore, ρ_d is set as 150 $kg\,m^{-3}$. The constant C_3 assumes a value of 0.01 hr^{-1} or 2.78 × 10^{-6} s^{-1}. C_4 is assigned a value of 0.04 K^{-1}. The value of C_6 depends on the bulk density of liquid water, ρ_l:

$$C_6 = \begin{cases} 2 & \rho_l > 0 \\ 1 & \rho_l = 0 \end{cases} \tag{3.56}$$

Equation 3.56 indicates that the density change increases by a factor of 2 when liquid water is present in the snow layer.

According to Anderson [39], the density change due to compaction can be expressed as:

$$\frac{1}{\rho_s}\frac{\partial \rho_s}{\partial t} = -\frac{1}{\Delta z}\frac{\partial \Delta z}{\partial t} \tag{3.57}$$

$$= \frac{P_s}{\eta_c} \tag{3.58}$$

where P_s is snow load pressure (Nm^{-2}) and η_c is the viscosity coefficient ($m \cdot hr$) related to snow density, temperature and snow type.

Kojima [46] found the following relationship between the compactive viscosity factor η_c and the snow solid bulk density ρ_s:

$$\eta_c = \eta_t e^{C_2\rho_s} \tag{3.59}$$

where η_t is the viscosity ($m \cdot hr$) at a temperature T, and C_2 is a constant to be determined by observed data. Mellor [47] further indicated that the relationship between η_t and η_0, which is the viscosity coefficient at 0 $°C$ and $\rho_s = 0$ $kg\ m^{-3}$, can be expressed as:

$$\eta_t = \eta_0 e^{0.08(T_0-T)} \tag{3.60}$$

Considering the dependence of density on temperature, the density change due to compaction can be expressed as

$$\frac{1}{\Delta z}\frac{\partial \Delta z}{\partial t} = -\frac{1}{\eta_0} e^{-C_2 \rho_s} e^{-0.08(T_0 - T)} P_s \tag{3.61}$$

Based on Kojima [46] and Mellor [47], Anderson suggested a value of 0.021 $m^3 kg^{-1}$ for C_2 and 3.6× 10^6 $Nm^{-2}s^{-1}$ for η_0. These values are also used by Loth et al. [1].

3.2.3.4 Other parameters

The 2-L snow model considers solar radiation in the surface layer only. However, solar radiation may penetrate below the surface layer and has a gradient over depth. Since shortwave radiation flux intensity decreases over depth, we consider this process in a multi-layered manner. The shortwave radiation flux can be expressed as:

$$R_s(z) = R_{ir}(1 - \alpha)\exp(-\nu z) \tag{3.62}$$

where $R_s(z)$ is the net solar radiation flux ($Js^{-1}m^{-2}$) at a depth z, R_{ir} is the incoming shortwave radiation at the snow surface, α is surface albedo, and ν is the extinction coefficient. The value of ν depends on the snow density and grain size. Bohren and Barkstrom [48] derived an equation for ν as an approximate solution for solar radiation penetration into a snowpack:

$$\nu = 0.0038\frac{\rho_s}{\sqrt{d}} \tag{3.63}$$

where ρ_s is snow density ($kg\,m^{-3}$), and d is grain diameter (m), and thus the scaling factor 0.0038 has units of $m^{2.5}\,kg^{-1}$. Loth et al. [1] uses a parameterization for d following Anderson [39]:

$$d = a + b\rho_s^4 \tag{3.64}$$

with the coefficients $a = 1.6 \times 10^{-4} m$, and $b = 1.1 \times 10^{-13} m^{13}\,kg^{-4}$.

The concept of liquid water holding capacity is used to describe the gravitational flow of liquid water. The liquid water holding capacity, C_r is parameterized as a function of the snow density as used in Anderson [39], Loth et al. [1] and Jin et al. [34]

$$C_r = \begin{cases} C_r^{min} & \rho_s \geq \rho_e, \\ C_r^{min} + (C_r^{max} - C_r^{min})\frac{\rho_e - \rho_s}{\rho_e} & \rho_s < \rho_e \end{cases} \tag{3.65}$$

where $C_r^{min} = 0.03$, $C_r^{max} = 0.1$, and ρ_e is 200 $kg\,m^{-3}$.

3.2.3.5 Soil snow interface scheme

The model validation process in this dissertation research found that model results are sensitive to the numerical scheme for the soil-snow interface (see the results on soil temperature simulations for details). Therefore, we implemented an alternative scheme for the interface used in [44].

First, we reintroduce the governing equation for the snow system:

$$\frac{\partial H}{\partial t} = -\frac{\partial F}{\partial z} - \frac{\partial R_s}{\partial z} \tag{3.66}$$

where H is the volumetric heat content (Jm^{-3}), F is the heat flux (Wm^{-2}), and R_s is net (downward) solar radiation (Wm^{-2}).

The term $-\frac{\partial F}{\partial z}$ can be expressed explicitly as follows:

$$\begin{aligned} -\frac{\partial F}{\partial z} &= -\frac{F_{j,j+1} - F_{j-1,j}}{\Delta z_j} \\ &= -\frac{(-(DK_e)_{j,j+1}(T_{j+1} - T_j)) - (-(DK_e)_{j-1,j}(T_j - T_{j-1}))}{\Delta z_j} \\ &= \frac{(DK_e)_{j,j+1}(T_{j+1} - T_j) - (DK_e)_{j-1,j}(T_j - T_{j-1})}{\Delta z_j} \end{aligned} \tag{3.67}$$

where $F_{j,j+1}$ is the heat flux between layers j and $j+1$, and DK_e is defined as:

$$(DK_e)^n_{j-1,j} = \frac{1}{\left(\frac{\Delta z^n_{j-1}}{2} + \frac{\Delta z^n_j}{2}\right)} \left(\frac{\Delta z^n_{j-1} + \Delta z^n_j}{\frac{\Delta z^n_{j-1}}{(K_e)^n_{j-1}} + \frac{\Delta z^n_j}{(K_e)^n_j}}\right)$$

Using the semi-implicit numerical method, the governing equation can be differentiated as:

$$\begin{aligned} \frac{H^{n+1}_j - H^n_j}{\Delta t} &= (1-\theta)\left(-\frac{F^n_{j,j+1} - F^n_{j-1,j}}{\Delta z^n_j}\right) + \\ &\quad \theta\left(-\frac{F^{n+1}_{j,j+1} - F^{n+1}_{j-1,j}}{\Delta z^n_j}\right) - \\ &\quad \frac{(R_s)_j}{\Delta z^n_j} \end{aligned} \tag{3.68}$$

If we use the expression for F in Equation 3.67, Equation 3.68 becomes:

$$\begin{aligned} \frac{H^{n+1}_j - H^n_j}{\Delta t} &= (1-\theta)\left(\frac{(DK_e)^n_{j,j+1}(T^n_{j+1} - T^n_j) - (DK_e)^n_{j-1,j}(T^n_j - T^n_{j-1})}{\Delta z^n_j}\right) + \\ &\quad \theta\left(\frac{(DK_e)^n_{j,j+1}(T^{n+1}_{j+1} - T^{n+1}_j) - (DK_e)^n_{j-1,j}(T^{n+1}_j - T^{n+1}_{j-1})}{\Delta z^n_j}\right) - \\ &\quad \frac{(R_s)_j}{\Delta z^n_j} \end{aligned} \tag{3.69}$$

The solution for temperature profiles requires a system of equations in the form of a tridiagonal matrix. First we simplify the expressions as:

$$\begin{aligned} F_n &= \frac{(DK_e)^n_{j,j+1}(T^n_{j+1} - T^n_j) - (DK_e)^n_{j-1,j}(T^n_j - T^n_{j-1})}{\Delta z^n_j} \\ I_1 &= \Delta t \frac{(DK_e)^n_{j,j+1}}{\Delta z^n_j} \\ I_2 &= \Delta t \frac{(DK_e)^n_{j-1,j}}{\Delta z^n_j} \end{aligned}$$

If we rearrange Equation 3.68 using the above expression and set it equal to f_j, we obtain the following:

$$\begin{aligned} f_j &= H_j^{n+1} - H_j^n - (1-\theta)\Delta t F_n \\ &\quad -\theta I_1 (T_{j+1}^{n+1} - T_j^{n+1}) + \theta I_2 (T_j^{n+1} - T_{j-1}^{n+1}) \\ &\quad -\frac{(R_n)_j}{\Delta z_j^n} \end{aligned} \tag{3.70}$$

where $(R_n)_j$ is the amount of net solar radiation penetrated into the layer j during the given time step.

We have unknowns: T_{j-1}^{n+1}, T_j^{n+1}, and T_{j+1}^{n+1}. Therefore, as in our original scheme we need to take derivatives of f_j with respect to the unknowns to yield:

$$[f_j]_{T_{j-1}^{n+1}} = -\theta I_2 \tag{3.71}$$

$$\begin{aligned} [f_j]_{T_j^{n+1}} &= [H_j^{n+1}]_{T_j^{n+1}} + \theta I_1 + \theta I_2 \\ &= (C_v)_j^n + \theta(I_1 + I_2) \end{aligned} \tag{3.72}$$

$$[f_j]_{T_{j+1}^{n+1}} = -\theta I_1 \tag{3.73}$$

3.3 Study Sites and Data

The M-L soil-snow model is validated and evaluated at a shallow snowpack site and deep snowpack sites. The Valdai water balance research station in Russia was chosen for the shallow snowpack site. The Valdai water balance research station is located at 57.6 $^\circ N$ and 33.1 $^\circ E$ in the forest zone of Russia. This study uses data collected from the Usadievskiy (hereafter Usad) catchment within the research site. The Usad catchment has a small area of 0.36 km^2 and is mostly grassland. Therefore, it has ideal conditions for model validation. It also has 18-year long meteorological forcing data and snow observation data for the period of 1966 - 1983 [49]. For model validation long-term forcing and observation datasets are important because they provide the ability to study interannual variability of model performances. As will be discussed later, the good performance of a model during a short period does not guarantee a consistent long-term performance.

The forcing data for the Valdai station is provided at 3-hour interval and aggregated into daily values. We also interpolated the dataset into hourly intervals, but the results of the hourly data are similar to those from the daily data. Thus, we use the daily forcing data to probe numerical stability and accuracy of the M-L model. The station also provides observed data including snow water equivalent, snow depth, and soil temperature. Details of this dataset are provided in [49].

SNOTEL stations in the Sierra Nevada are used for deep snowpack sites for model validation and comparison. Figure 3.2 shows the East Fork Carson River Basin and the location of SNOTEL stations within the basin. We use SWE data from these SNOTEL station for model comparison, and the basic information of these stations is shown in Table 3.1. Among the information about the SNOTEL stations, we need to note their different elevations to understand that stations at lower elevation tend to have less SWE accumulation. As in Chapter 2, hourly precipitation and air temperature data from DMIP2 are also used to investigate the model performance for water years 2000 - 2002. Other forcing data are from NLDAS [50] and NARR [19]. For the East Fork Carson River Basin, we conduct hourly simulations.

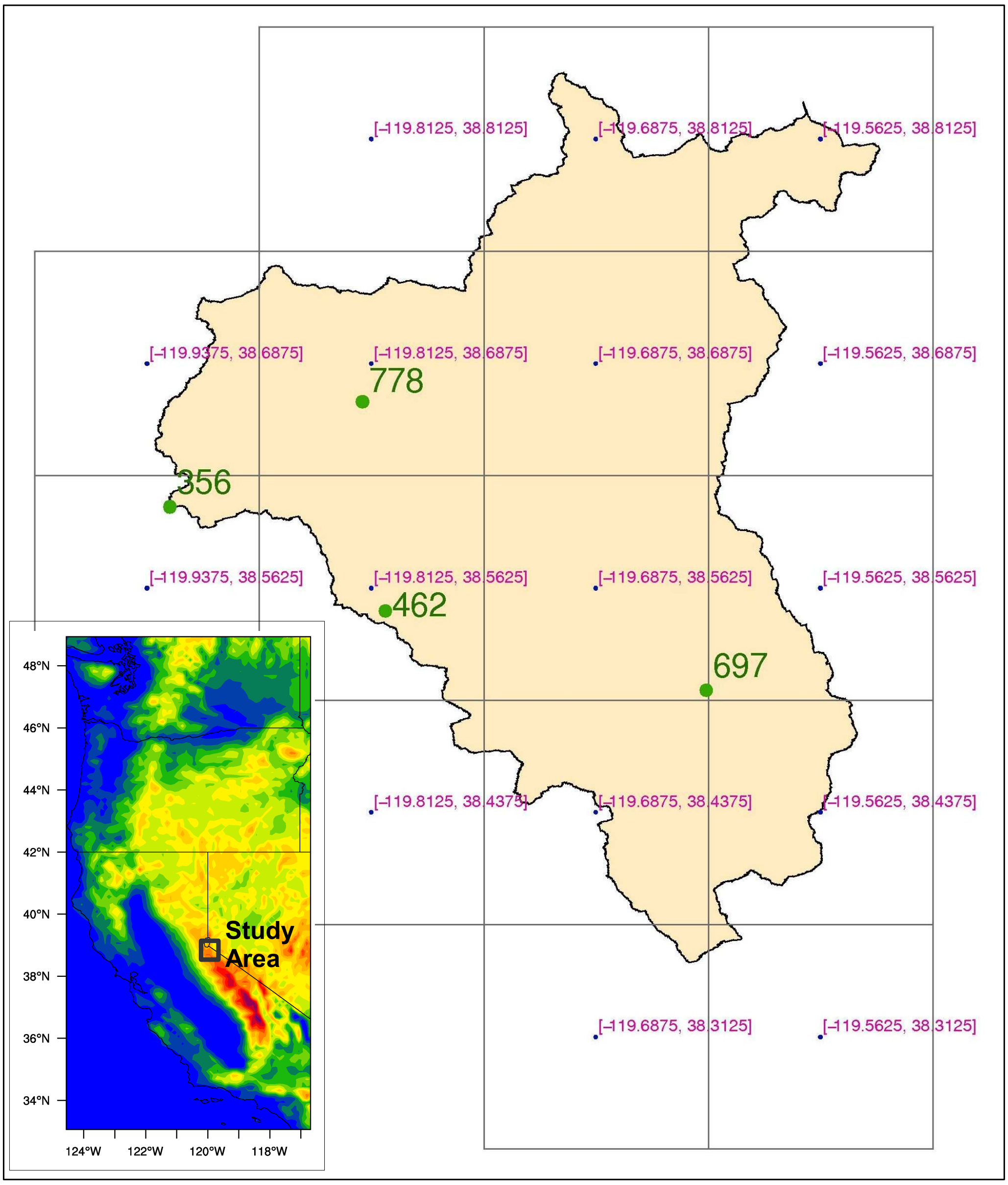

Figure 3.2: East Fork Carson River Basin and location of SNOTEL stations relevant to it. The coordinates inside brackets indicate the centers of model grid cells, and the numbers represent the SNOTEL station numbers.

Table 3.1: SNOTEL station information in the East Fork Carson River Basin. The unit in parentheses is meters.

Station	Lat / Lon	Elevation (ft)	SNOTEL ID
Blue Lakes	38.607800, -119.924433	8057 (2456)	356
Ebbetts Pass	38.549550, -119.804650	8765 (2672)	462
Poison Flats	38.505533, -119.626117	7736 (2358)	697
Spratt Creek	38.666250, -119.817550	6115 (1864)	778

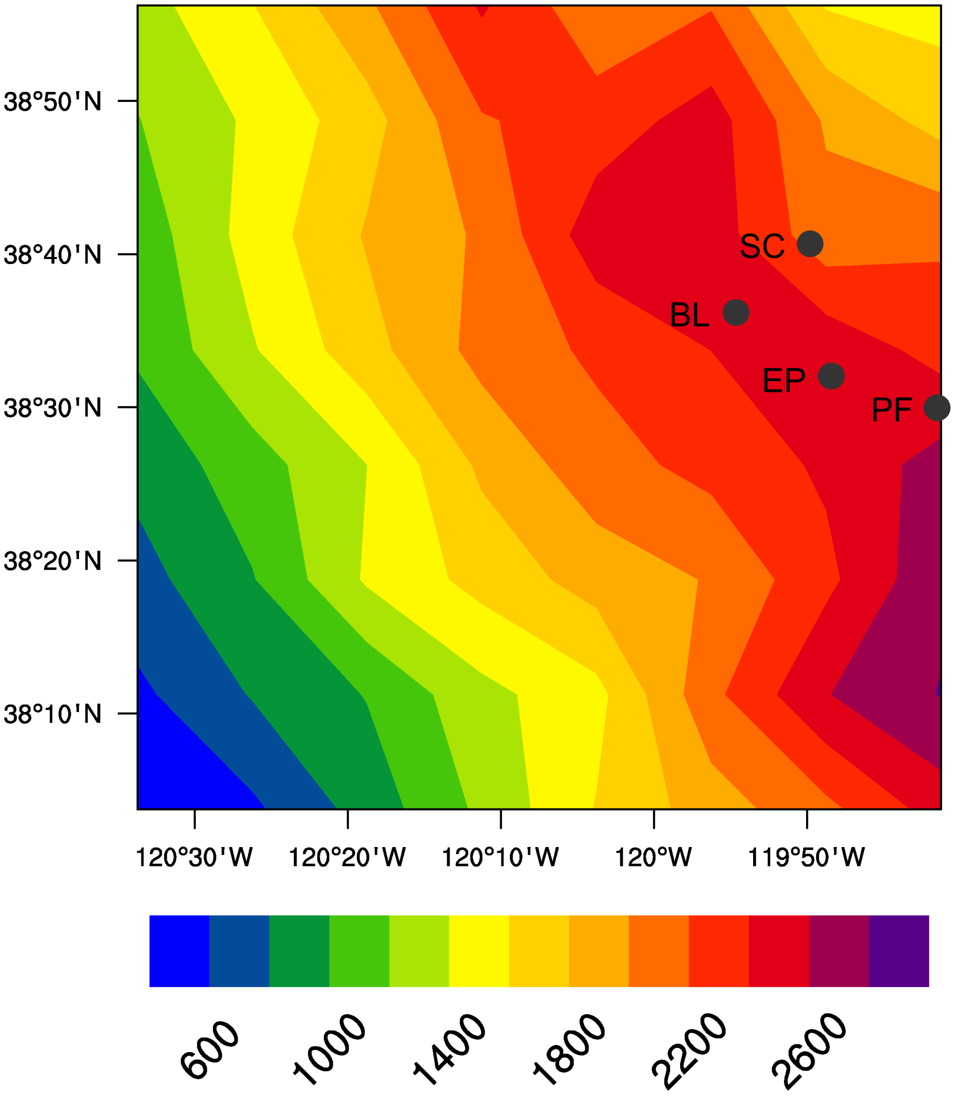

Figure 3.3: SNOTEL stations within the East Fork Carson River Basin on a elevation map. The elevation is interpolated based on the mean elevation of model grid cells within the rectangular boundary, and its unit is m. Points represent the Blue Lakes (BL), Ebbetts Pass (EP), Spratt Creek (SC), and Poison Flat (PF) stations.

3.4 Results and Discussion

3.4.1 Model Performance at the Shallow Snowpack Site

3.4.1.1 Snow water equivalent

Figure 3.4 shows SWE simulations by the M-L and 2-L models with observations. The results from both models do not show much difference overall. For these simulations, an emissivity of 1.0 and ten soil thermal layers were used. The simulations using a daily time step show that there is interannual variation in simulating SWE. For some years, both the models simulate SWE very well (e.g., water year 1969) or moderately well (e.g., water year 1970), while they overestimate SWE for other years (e.g., water year 1981). The interannual variability in model performance from Figure 3.4 has some implications of snow model validation that long-term simulations provide better understanding of model performance. The overestimation phenomenon of SWE in some of the Russian sites has also been reported in other literature including Sun et al. [51].

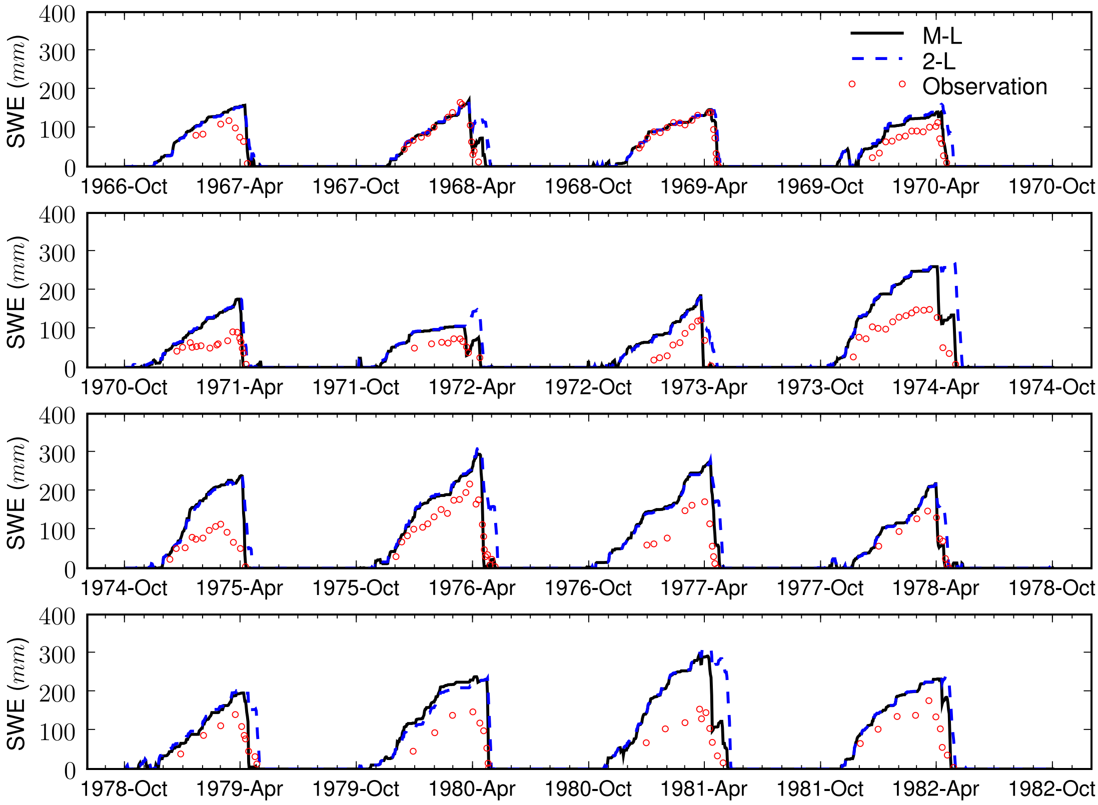

Figure 3.4: SWE comparison with emissivity of 1.0

As demonstrated by Nijssen et al. [35], there is more variability during the spring snowmelt period than the accumulation period. In fact, during the accumulation periods, both models behave similarly. For model sensitivity analysis, emissivity has been tested. Snow emissivity ranges from 0.82 for old snow to 0.99 for fresh snow [52]. We found that an emissivity of 0.94 gives the best results for our simulation. The results are shown in Figure 3.5. Even though the impact of emissivity changes varies depending on the water year, it noticeably improves the SWE simulation result for some years.

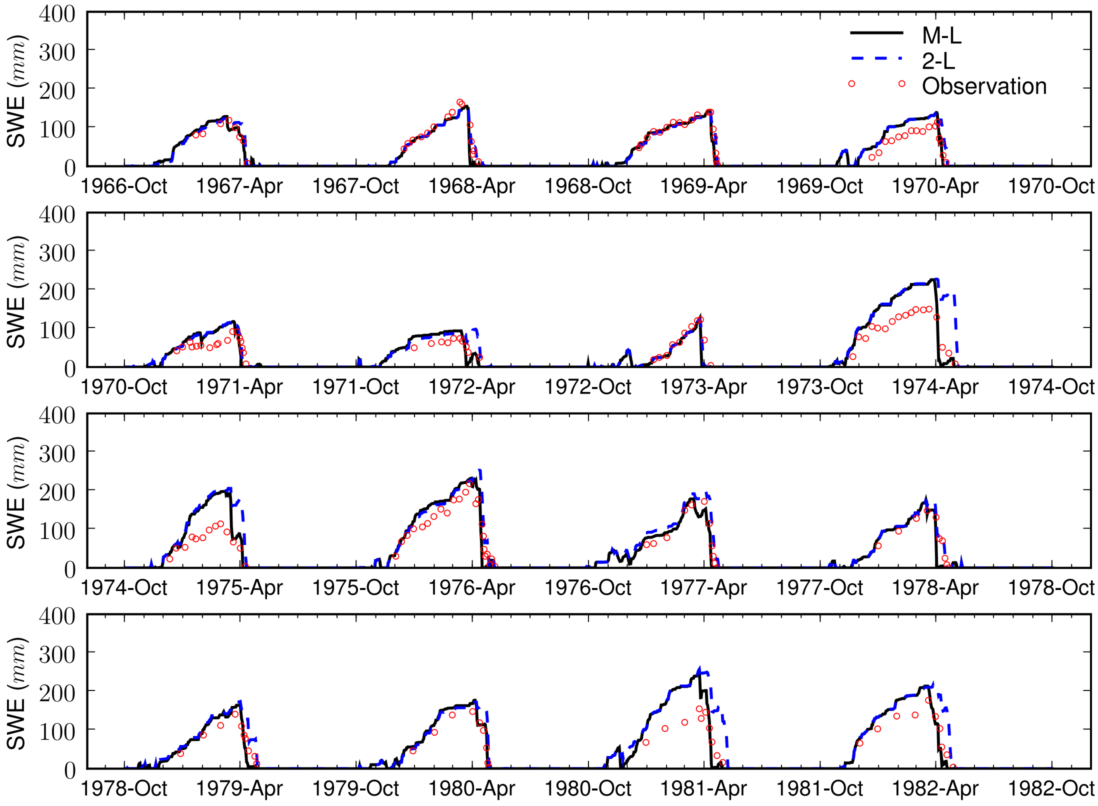

Figure 3.5: SWE comparison with emissivity of 0.94

For the case of emissivity 0.94, the M-L model captures the melting timing better than the 2-L model. But the overall performance shows the two models behave similarly to each other. Other relevant studies showed similar results. For example, the Snow-Atmosphere-Soil Transfer (SAST) model showed similar capability to that of SNTHERM by using three snow layers [34]. This result implies that snow models with less complexity can produce equivalent simulations to those that are complex although they need less computational requirements than complex models. One of the reasons for this result shown in our study is that ground heat flux, which benefits most from the multi-layered configuration, is smaller than the surface turbulent fluxes and radiative fluxes in magnitude. Moreover, the heat flux between soil and snow in mountainous environments tends to be relatively weak [20].

3.4.1.2 Snow depth

Another important snow state variable for snow model validation is snow depth. The Valdai station provides snow depth data for the Usad catchment. The simulations for snow depth in Figure 3.6 show similar results as those for SWE simulations. Snow depth is closely related to snow density in our model physics. In particular, for the M-L model SWE for each layer is computed based on the energy balance, density is updated as a result of SWE calculation, and then snow depth is updated. In Figure 3.6, the snow depth is the summation of the thickness of each layer for the M-L model. For the 2-L model, there is only one density ρ_{sl} $(kg\,m^{-3})$, which includes liquid water and solid snow, for the entire snowpack and snow depth D_z (m) is calculated in a similar way to Equation 3.50 as:

$$D_z = \frac{W_s \rho_w}{\rho_{sl}} \tag{3.74}$$

where W_s is snow water equivalent (m), and ρ_w is the intrinsic density of water $(kg\,m^{-3})$

Even though the methods for calculation of snow depth are different between the two models, the results for snow depth closely resemble each other. As in the results of SWE, the M-L model performs slightly better than the 2-L model during some of the melting seasons. For example, for the water years 1974 and 1981 the M-L model captures the melting timing correctly although there was overestimation during the accumulation period for both the models. The M-L model uses parameters for density calculation that need calibration. Among other density parameters, ρ_d in Equation 3.55 seems to play a relatively large role in the simulation of snow depth. According to Anderson [39], ρ_d is a constant to be calibrated and used to determine the fractional settling rate at 0 $°C$. For the result presented in Figure 3.6, we used 150 $kg\,m^{-3}$ based on Yen's finding [45] that the effect of snow settling is not significant for densities greater than 250 $kg\,m^{-3}$. To illustrate the effect of parameter ρ_d we tested a value of 100 $kg\,m^{-3}$ and this result is shown in Figure 3.7. The M-L model is sensitive to that parameter and overestimates snow depth mostly during the accumulation period compared to that of the 2-L model and the observations.

3.4.1.3 Ground surface temperature

Predicted ground surface temperature is a useful measure to determine the ability of snow models. The Valdai station provides ground surface temperature data for the Usad catchment. The surface temperature data in this station is the snow surface temperature for the snow season and soil surface temperature for the non-snow season. In the 2-L model the surface layer has a maximum depth of 12.5 cm in water equivalent, and this depth is maintained when there is enough snow on the ground. On the other hand, the M-L model uses 2 cm for the snow surface layer. Even with different configurations for the snow surface layer, both models simulate ground surface temperature very well compared to the observations as shown in Figures 3.8, 3.9, and 3.10. All of the values in these figures are daily averages. These results also support our findings from SWE simulations that there is not much difference in the model performance between the M-L model and the 2-L model.

3.4.1.4 Soil temperature

Soil temperature at different depths is another indicator used to evaluate snow model performance along with the ground surface temperature. When the simulation results for ground surface temperature from both models are well matched to the observations, analyzing soil temperature provides an opportunity to investigate model performances through a different

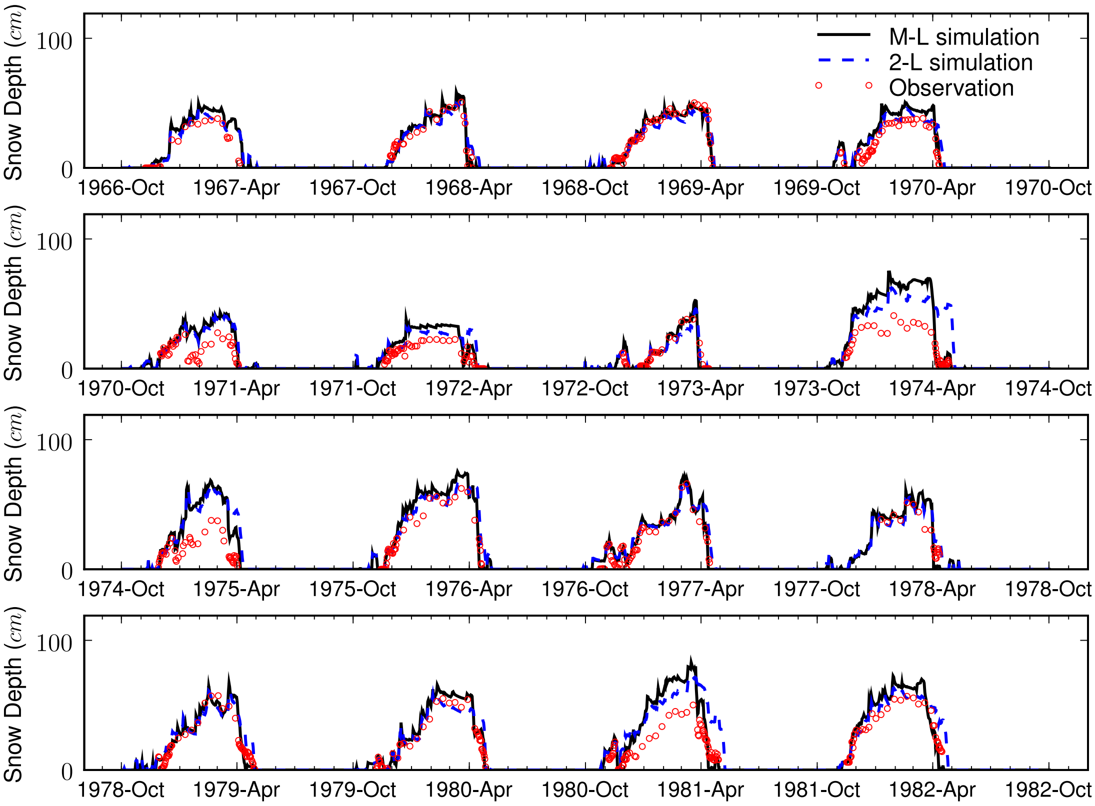

Figure 3.6: Snow depth with density parameter ρ_d of 150 $kg\ m^{-3}$.

angle. The 2-L snow model is also coupled with a frozen soil algorithm [38]. Even though the M-L soil-snow model uses a different numerical solution from the one in [38], its soil system structure is identical to the one used in the 2-L model. This is because we wanted to develop a new model respecting the overall framework of the VIC LSM. Moreover, as discussed previously this enables us to identify which physical process makes a difference in simulating snow variables.

Before we compare the results for soil temperature between the M-L model and the 2-L model, we describe the effect of the numerical scheme at the interface between soil and snow systems. In Section 3.2.3.5, a new scheme for the interface was introduced. This new scheme was developed based on [44] and applied because the original scheme did not perform well in terms of soil temperature at 20 cm below the soil surface compared to observations. In our new model configuration, this under-performance is possible due to the dissimilarity of heat conductivity between soil and snow. Recall that our new M-L model simulates the soil and snow systems as one. While implementing this numerical solution for the one soil-snow system, we use two distinct heat conductivities between soil and snow. Depending on the layer thickness, the numerical stability can be impaired due to a large difference in heat conductivity between the two media. When the snowpack is deep, the impaired calculation at the soil-snow interface may not affect the energy balance computation of the surface layer significantly. However, when the number of layers are small and the snowpack is not deep as in the Valdai station, the effect at the interface may be transferred to the surface layer, subsequently affecting the overall energy balance.

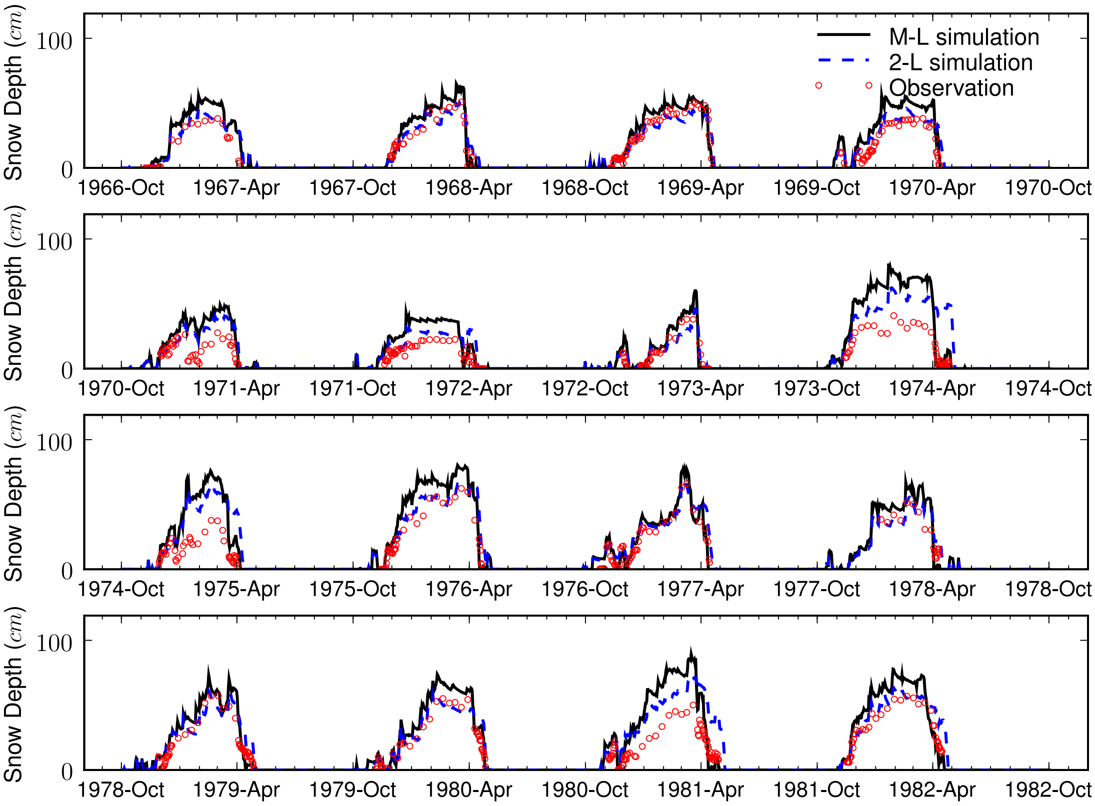

Figure 3.7: Snow depth with density parameter ρ_d of 100 $kg\ m^{-3}$.

Figure 3.12 shows simulations of soil temperature at 20 *cm* below the soil surface for the water years 1973 - 1975. As shown in the figure, the original normal scheme under-performs. In particular, note the snow accumulation period in the water year 1974. During the period of December through January, the normal interface scheme underestimates the soil temperature at 20 *cm* below the soil surface. This result reveals that when there is added complexity there are new factors to be considered. In addition, it also implies that there is a possible chance to improve simulations of soil temperature by using different schemes for the soil-snow interface. It is worth noting that even though we use the new soil-snow interface scheme, there is no significant difference in terms of SWE in this specific simulation condition (Figure 3.11). More accurate soil temperature profile estimates contribute to more precise predictions of ground heat flux. It is also true that the heat transfer process through the soil and snow layers itself affects the calculation of temperature profile. But this process is less important since ground heat flux is small in the energy balance.

Figures 3.13, 3.14, and 3.15 show simulated soil temperature and observed temperature at a depth of 20 *cm* for the years with observations. For the M-L model, the new soil-snow interface scheme has been used. The M-L model simulates soil temperature better than the 2-L model overall. In particular, during the melting season the M-L model's temperature is better matched to the observation. For example, for the water years 1974 and 1975 the M-L model captures the soil temperature more accurately compared to that of the 2-L model during the melting seasons. This accuracy is also reflected in the simulations of SWE and snow depth for

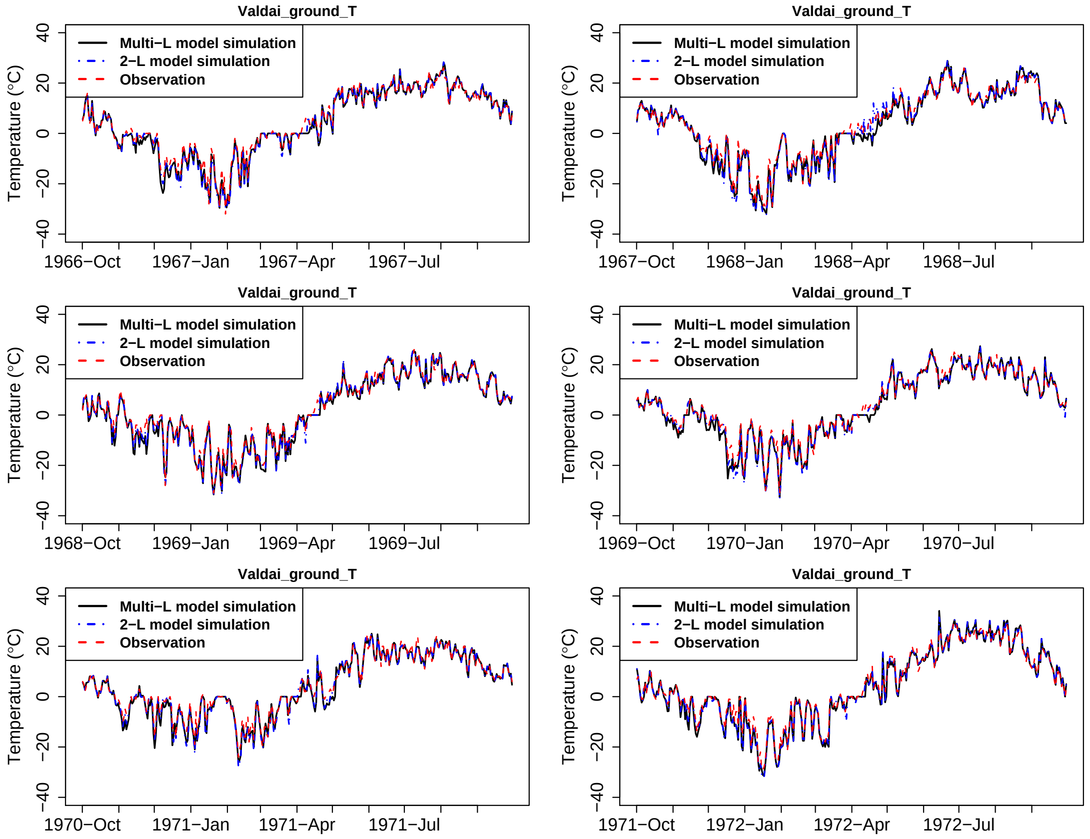

Figure 3.8: Ground surface temperature for the years 1967 - 1972.

the same years. See Figure 3.5 and Figure 3.6 for inter-comparison with SWE and snow depth, respectively.

3.4.2 Model Performance at Deep Snowpack Sites

The new M-L soil-snow model has also been evaluated in deep snowpack sites of the Sierra Nevada. Because we do not have various observed data as in the Valdai station, we validate using observed SWE. Unlike the Usad catchment in the Valdai station, which is small in size, there is a scale issue in the Sierra Nevada. While we run the models in grid cells with a size of 1/8th degree, observations are available at the point scale. For this reason, many studies (e.g., [53]) do not compare model simulated results at the grid cell scale with point-scale observations directly. However, this study compares model simulations with point-scale observations because we use quality DMIP2 precipitation and temperature data, which is presumably the best gridded data for our simulations. In Chapter 2 we have seen that DMIP2 temperature data are comparable to those of SNOTEL stations and the precipitation data are also interpolated using SNOTEL data.

Figure 3.16 shows the simulations of SWE for the corresponding grid cells to the four SNOTEL stations in the East Fork Carson River Basin. The conspicuous phenomenon is the difference in the state of SWE during the melting season at all of the four stations. In

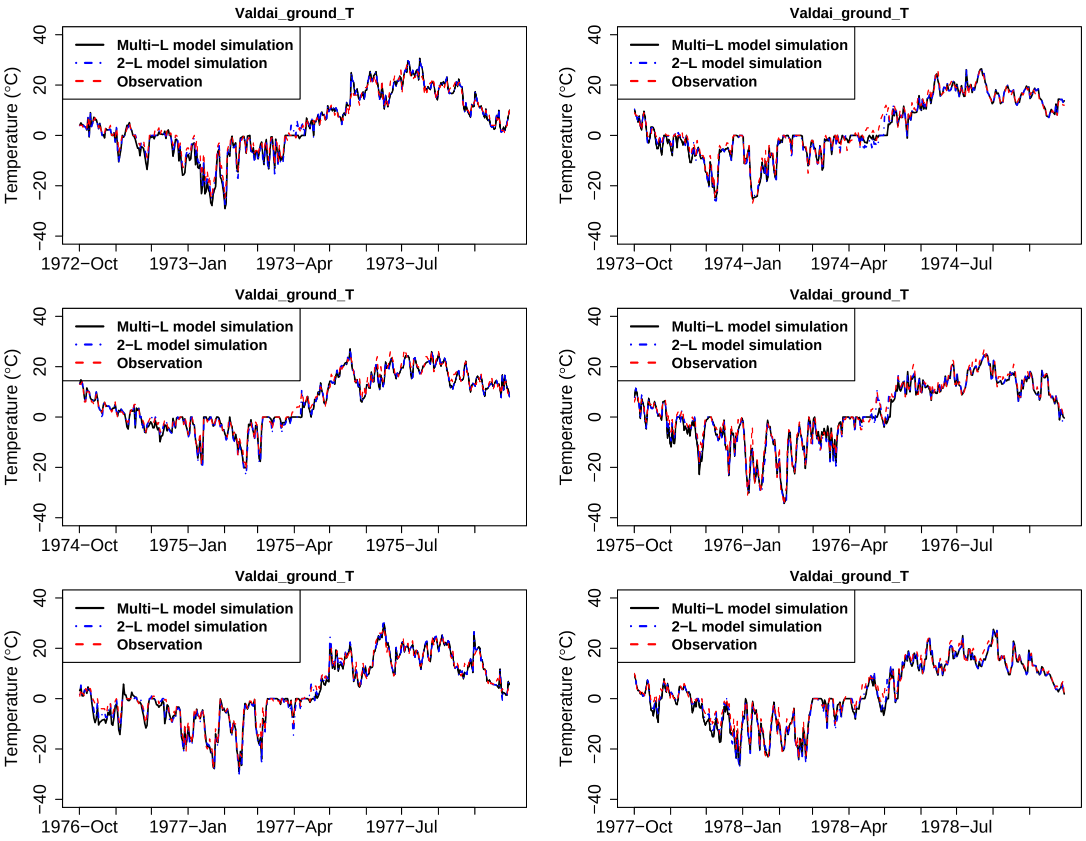

Figure 3.9: Ground surface temperature for the years 1973 - 1978.

particular, there is more discrepancy during the 2002 water year. During the accumulation periods, the M-L model and the 2-L model behave similarly as we have seen at the Valdai station. Considering that the boundary conditions of the two models at the snow surface are almost identical, this result shows that the effect of ground heat fluxes does not seem to be significant during the accumulation period. To verify this hypothesis, we compared the ground heat flux between the two models. In calculating ground heat flux, the 2-L model uses only the temperature gradient from the top soil layer or the top two layers, while iteratively solving the overall energy balance for the grid cell or the fraction of it. Since the M-L model solves the temperature simultaneously for the soil and snow layers, the calculation is different from that of the 2-L model. These details are presented in Appendix A. The results of simulated ground heat fluxes for the snow season are shown in Figures 3.17, 3.18, and 3.19 and the values are daily averages. There is no measurably large difference in the daily ground heat flux between the two models. In particular, in the middle of accumulation when the snowpack is deep, the ground heat flux does not show much variability in both the models. During the melting season, there are some differences between the two models, but the magnitude of the difference is not large compared to other fluxes such as net radiation.

Comparison of ground heat flux leads us to other possibilities responsible for the discrepancy in SWE during the melting season. Considering the magnitude of the difference in SWE between the two models, the cause is likely to come from the surface energy fluxes. As we have seen in the shallow Valdai station, the two models' ability to simulate the ground surface

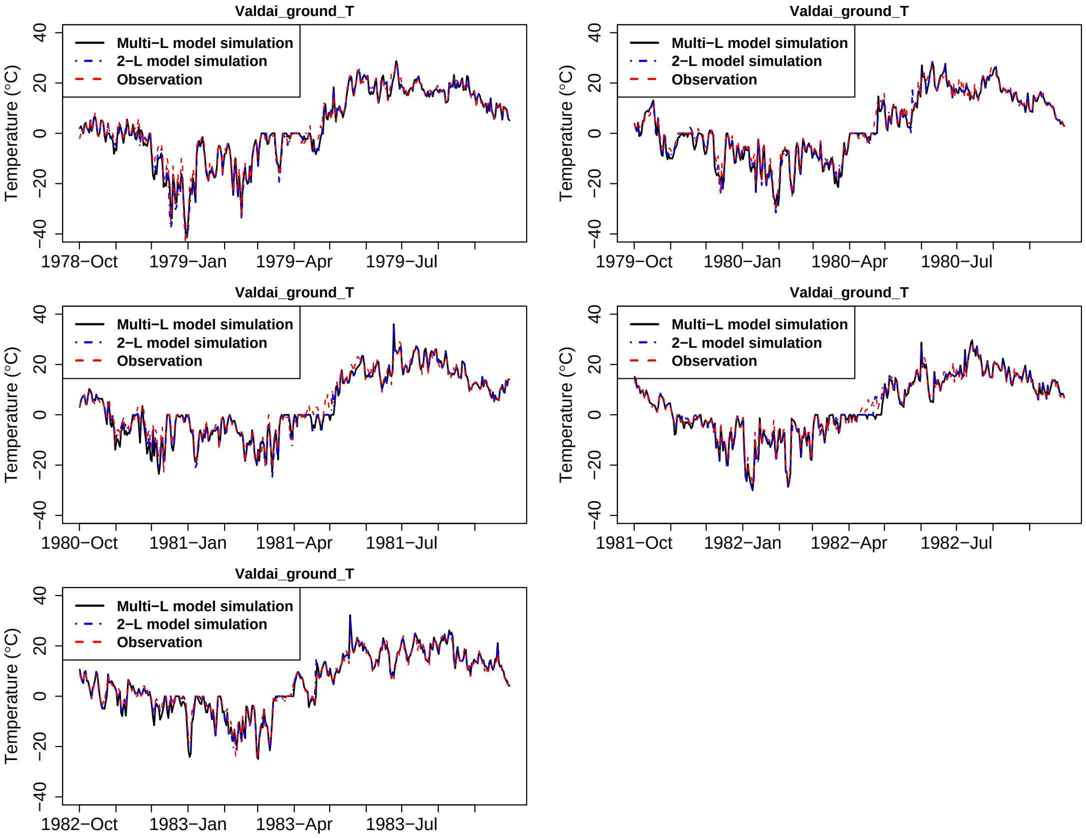

Figure 3.10: Ground surface temperature for the years 1979 - 1983.

temperature is very good and similar to each other. This fact implies that the latent heat fluxes and sensible heat fluxes are likely to be similar to each other. Because we use the same observed shortwave and longwave radiation fluxes for both models, these two fluxes do not contribute to the difference in the energy balance. Considering all these factors, the most probable cause of the SWE discrepancy during the melting season seems to be attributed to a dominant effect of albedo. Figures 3.20, 3.21 and 3.22 show comparison of albedo values between the 2-L and M-L models for the water years 2000, 2001, and 2002, respectively. As expected, there is fairly a large difference in albedo values between the models. The M-L model produces consistently low albedo values compared to that of the 2-L model. When there are melting events, the difference becomes larger. This low albedo in the M-L model leaves more energy available for melting in the snowpack. Therefore, either rapid melting or early melting occurs in the M-L model, causing the deviation of SWE from the 2-L model.

As discussed earlier, the 2-L model maintains a maximum thickness of 12.5 *cm* in water equivalent for the snow surface layer while the M-L model uses 2 *cm*. This inherent difference in the configuration of surface layer thickness did not affect the simulation of ground surface temperature significantly. However, the cold content, which is used to compute albedo, from these two different layers with incongruent maximum thickness creates some difference in albedo. From our results, the cold content from the top 2 *cm* seems to be error-prone under certain circumstances. Note that our original albedo scheme did not make a noticeable difference at the shallow Valdai station. But in the relative deep snowpack of the Sierra Nevada, the original

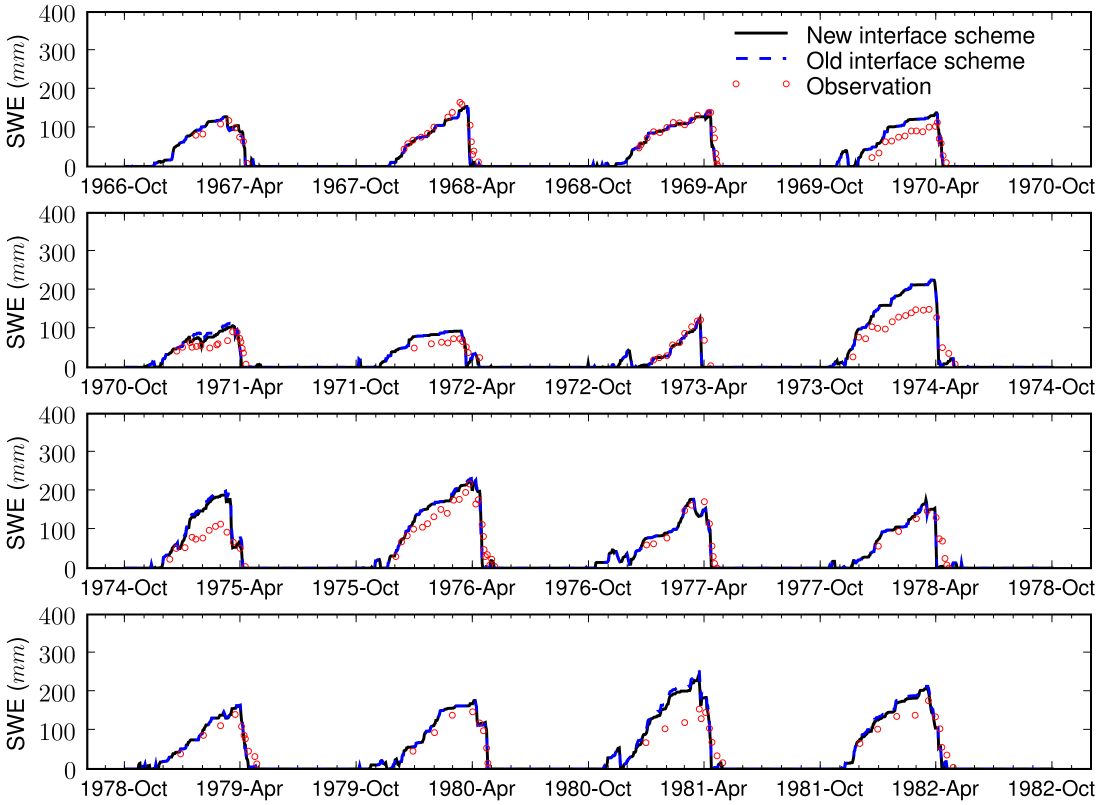

Figure 3.11: SWE comparison based on the new soil-snow interface scheme.

albedo scheme does not perform well. The quick solution to this problem would be to use the total cold content from several layers in calculating albedo. Instead of taking this approach, we implemented the albedo scheme from the Biosphere-Atmosphere Transfer Scheme (BATS) model [54] that is more applicable to the multi-layer structure. Details of the BATS albedo scheme are presented in Appendix H. The results using the BATS albedo scheme are shown in Figure 3.23. The M-L model based on the BATS albedo scheme captures the timing and magnitude of the 2-L model and shows more promising results for the Spratt Creek SNOTEL station. The Spratt Creek site is located at a lower elevation than the other stations (see Table 3.1 and Figure 3.3) and the maximum accumulation at the station is also lower than the others. Apart from the other stations, we see some overestimation for SWE at the station. Figure 3.24 compares the simulated SWE when both models used the BATS albedo scheme. That is, the 2-L model also used the BATS albedo scheme. In this figure, the 2-L model has slightly higher SWE during the melting period while the timing of the complete melting is unchanged. It is worth noting that there is no noticeable change during the accumulation season compared to the case of the original albedo scheme. Moreover, the 2-L model cannot capture the melting timing for the Spratt Creek station while the M-L model captures the melting timing for the 2002 water year and shows closer accumulation to the ground observation than the 2-L model for the 2001 water year.

The impact of albedo is relatively large compared to those of other physical processes in simulating SWE. The air temperature in the Sierra Nevada is higher than that of the Valdai

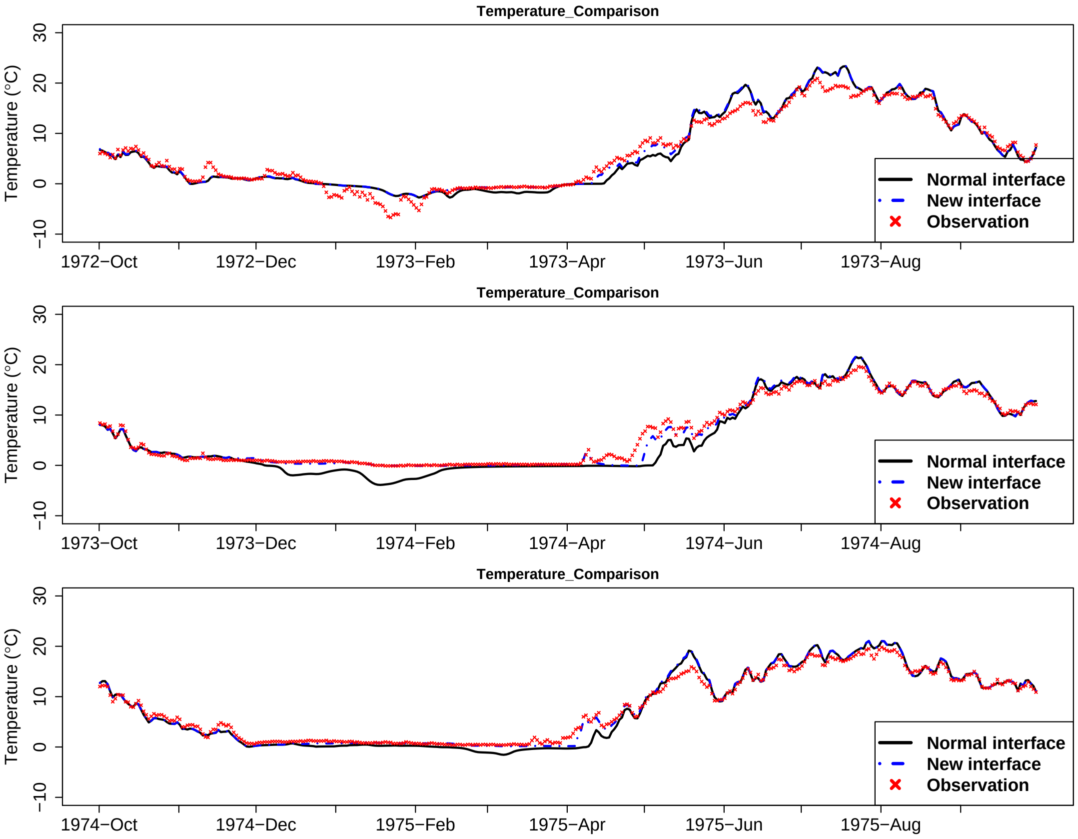

Figure 3.12: Soil temperature comparison at the depth of 20 *cm* for the water years 1973 - 1975 between the normal (original) and new schemes.

station. When the air temperature is high during the melting season, the impact of albedo seems to be more pronounced. Our results show that even though a better description of physical snow processes may not dramatically reduce the uncertainties due to forcing biases it contributes to improving simulations in some areas.

3.5 Conclusion

The complexity added to the 2-L snow model of the VIC LSM did not significantly change the way snow state variables are simulated. With the same boundary conditions at the snow-atmosphere interface as the 2-L model, the results by the new and more complex M-L model show that the impact of ground heat flux and its related processes are not very strong. In some cases, however, the M-L model outperformed the 2-L model. For example, the M-L model showed consistent improvements in capturing the timing of melting in the shallow snowpack site of the Valdai water balance research station. Emissivity and certain parameters (e.g., critical density for settling) for densification showed relatively high sensitivity in simulating snow variables. This study reveals that the added complexity involves more parameters and accurate descriptions of some processes. The additional treatment (e.g., more parameters in the density scheme) required by the new M-L model was found in soil temperature simulations using

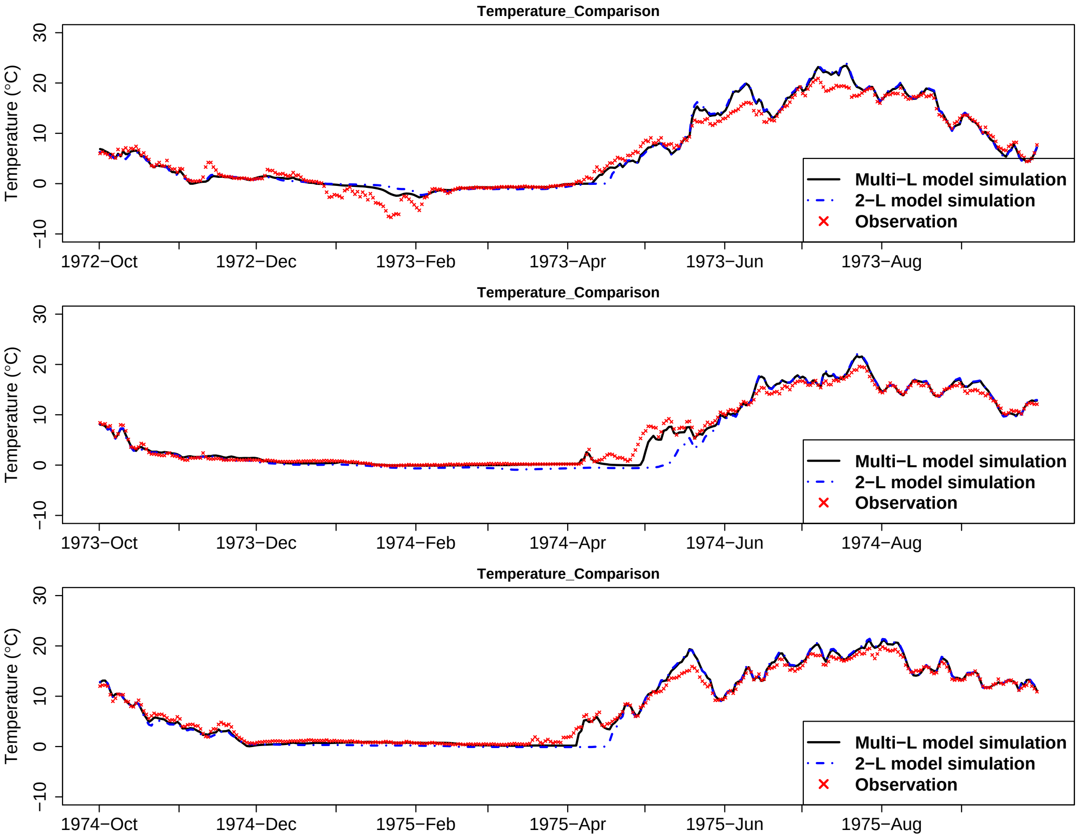

Figure 3.13: Soil temperature at the depth of 20 *cm* for the water years 1973 - 1975.

a new soil-snow interface scheme. In terms of numerical schemes, description of the soil-snow interface is required by the M-L model only due to added complexity in the model structure. Precise treatment of the soil-snow interface in the M-L model generated improvements to soil temperature simulations. In this regard, the M-L model can be applied to cases where more accurate simulations as in point-scale sensor validation are required and adjusting parameters is not expensive.

As we have seen from the results in the Sierra Nevada sites, the new M-L model did not overcome the dominant underestimation problem. As shown in other studies such as Pan et. al. [16] and Feng et. al. [22], underestimation is mainly attributed to low biases in precipitation data. The bias in precipitation forcing is also dominant in the uncertainty of SWE simulations in our study where the gridded areal mean temperature is well matched to the point-scale temperature. The M-L model performed in a similar way to the 2-L model, in particular for the accumulation season. However, application of a different snow albedo scheme (i.e., BATS albedo scheme) changed results to a large degree for a site located at relatively lower elevation. Snow albedo acts on the energy balance directly by changing the net radiation flux. The M-L model with the BATS albedo scheme showed a promising result for the Spratt Creek station. This result signals that processes directly related to energy fluxes such as albedo and emissivity have a large impact on snow state variables. Moreover, the process needs to be one that can be well integrated with the model's structure. Recall that the original albedo scheme showed a consistent low bias. As in the shallow snowpack site, the M-L model performed better than the

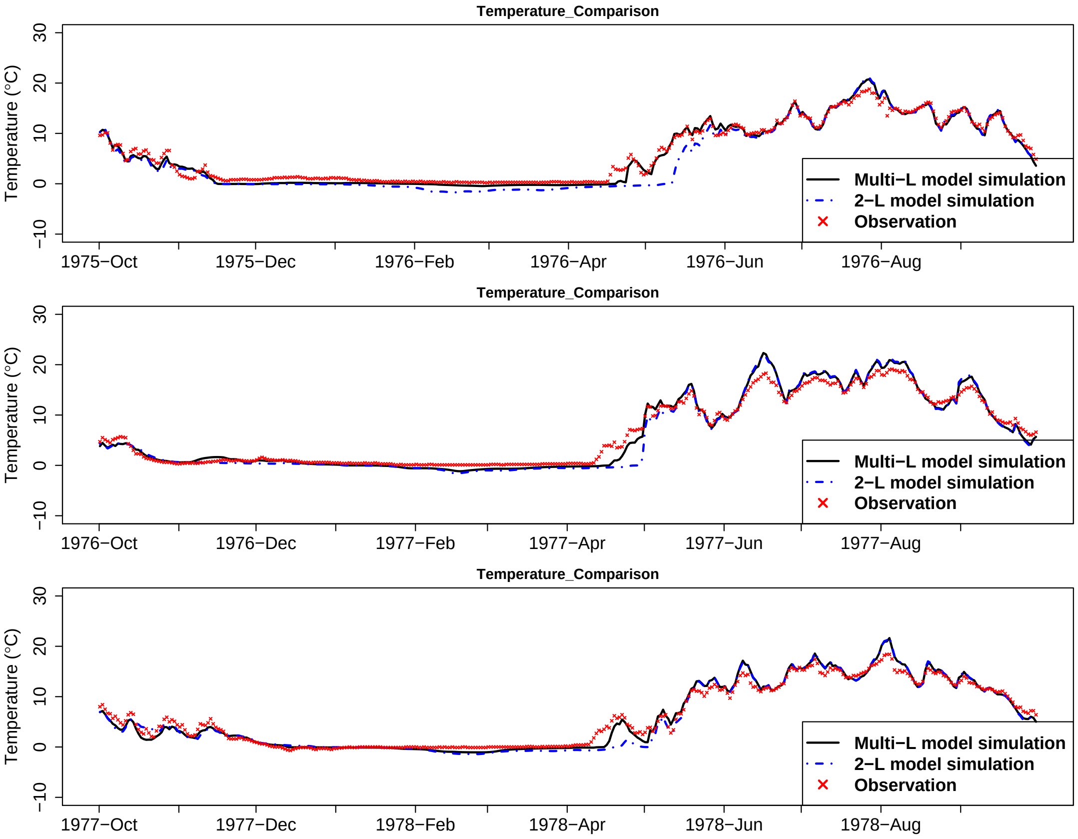

Figure 3.14: Soil temperature at the depth of 20 *cm* for the water years 1976 - 1978.

2-L model during the melting season. This ability of the M-L model can contribute to more accurate streamflow simulations by capturing melting timing and magnitude.

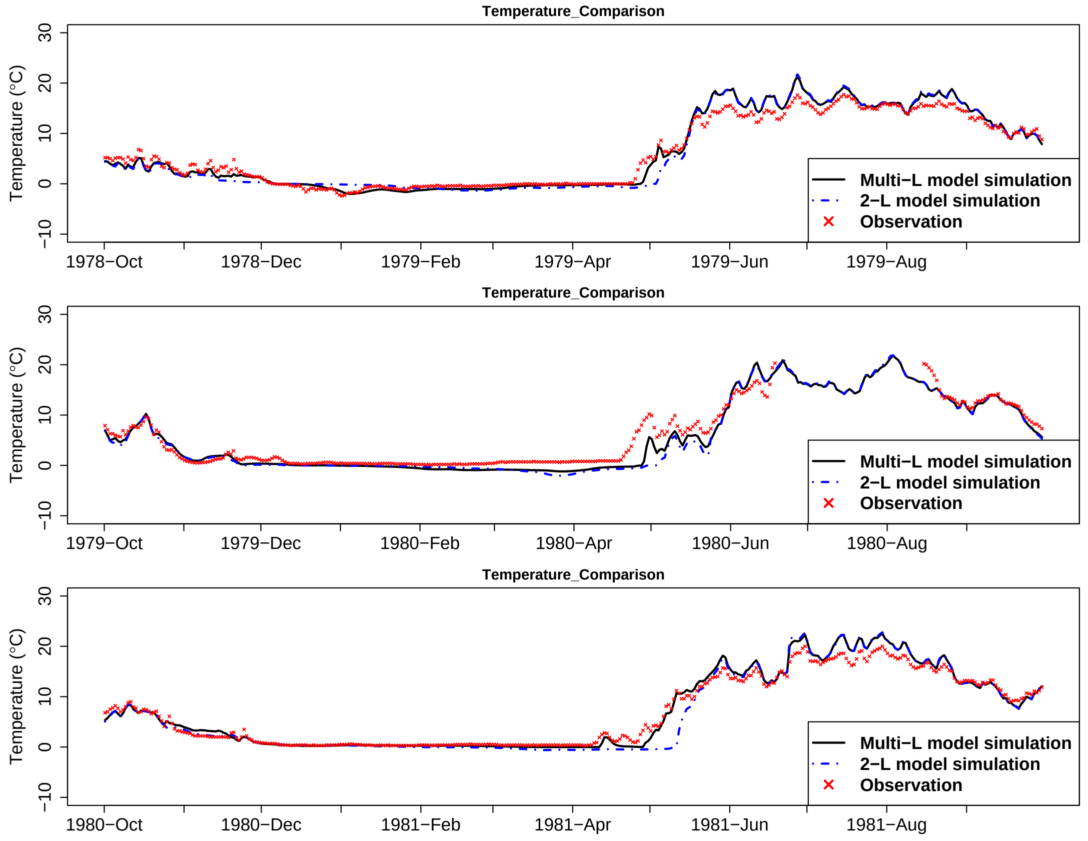

Figure 3.15: Soil temperature at the depth of 20 *cm* for the water years 1979 - 1981.

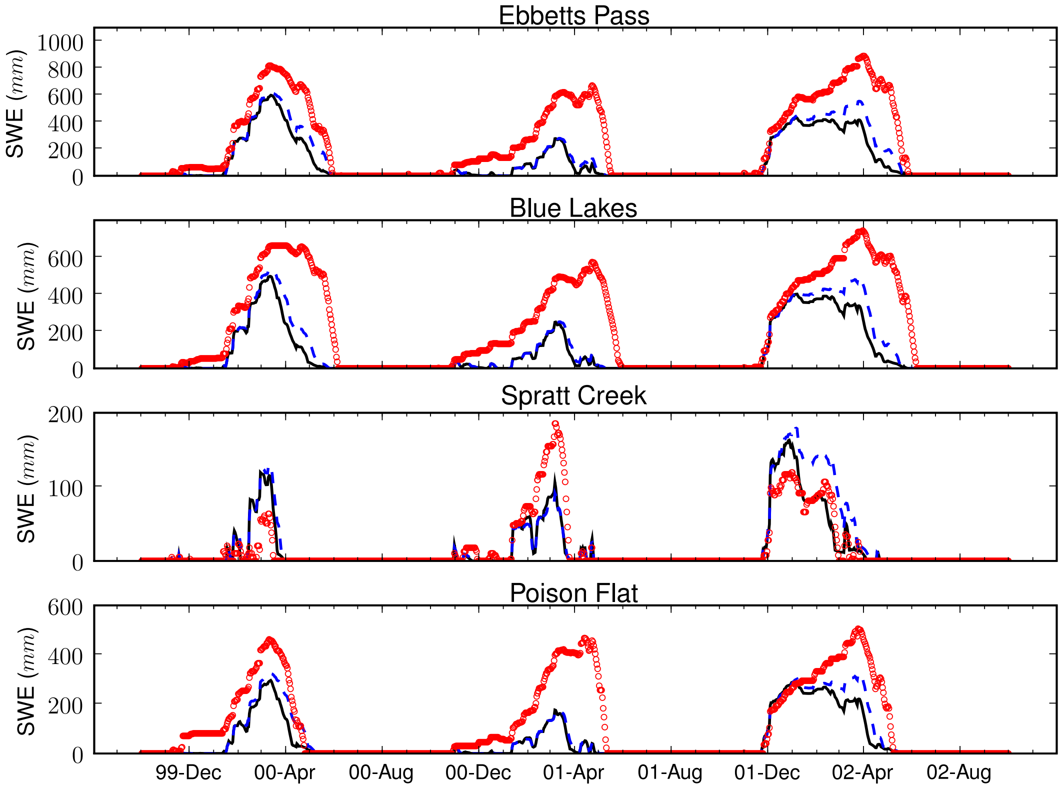

Figure 3.16: Comparison of SWE. The solid line is SWE from the M-L model, the dashed line the 2-L model, and the circle SNOTEL observation. Note the y-axis scale changes in each plot.

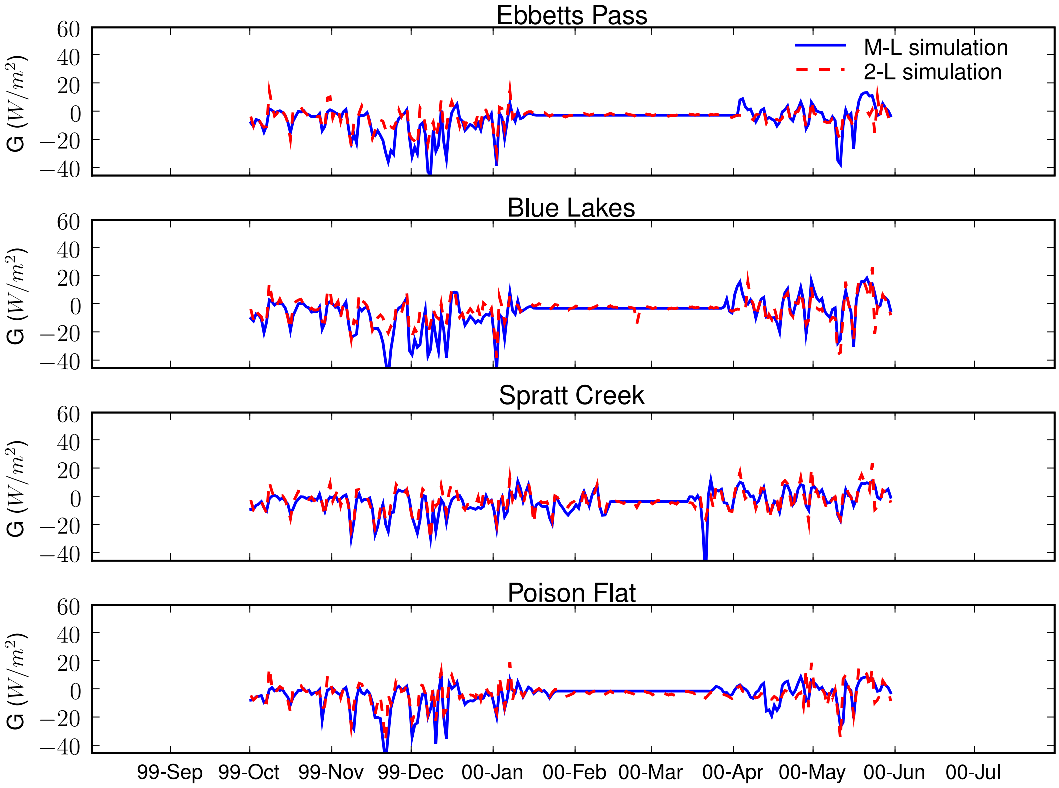

Figure 3.17: Comparison of ground heat flux between the M-L and 2-L models during the snow season of water year 2000.

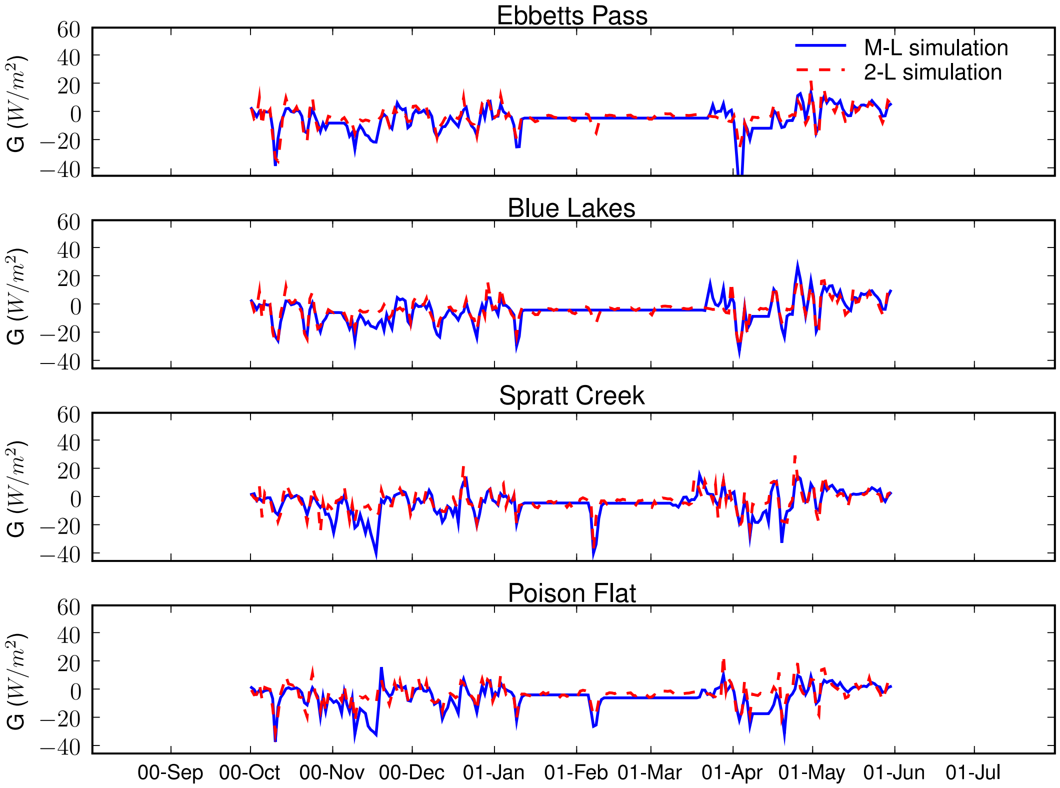

Figure 3.18: Comparison of ground heat flux between the M-L and 2-L models during the snow season of water year 2001.

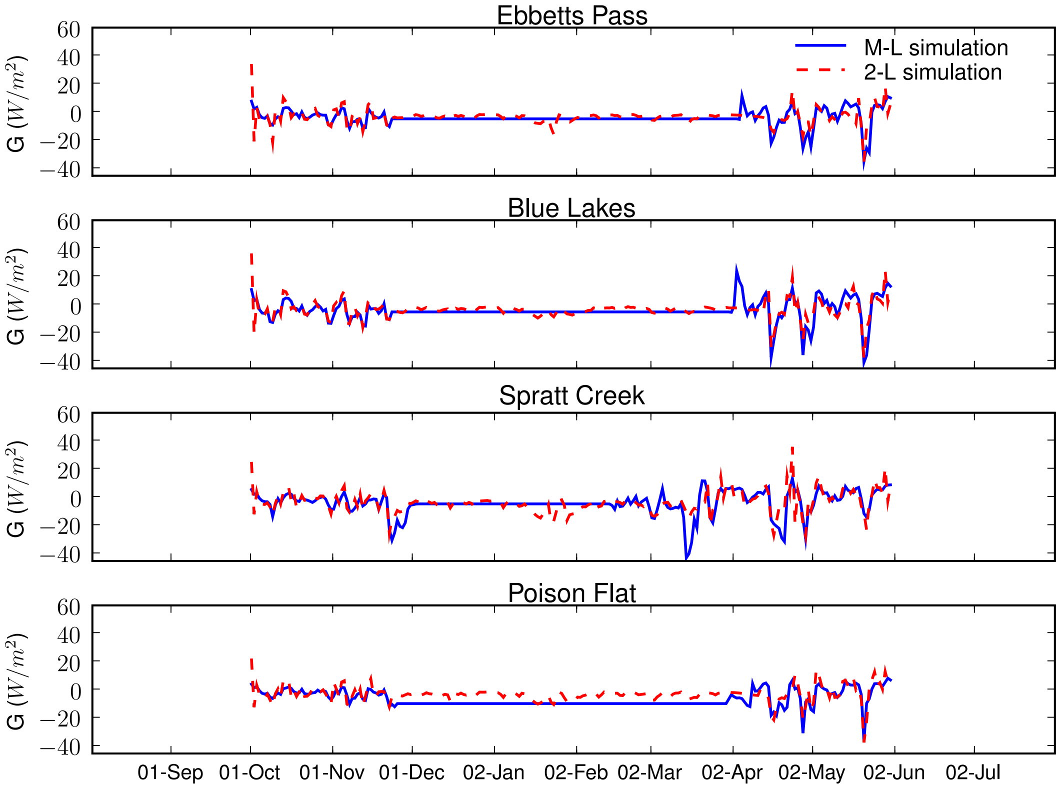

Figure 3.19: Comparison of ground heat flux between the M-L and 2-L models during the snow season of water year 2002.

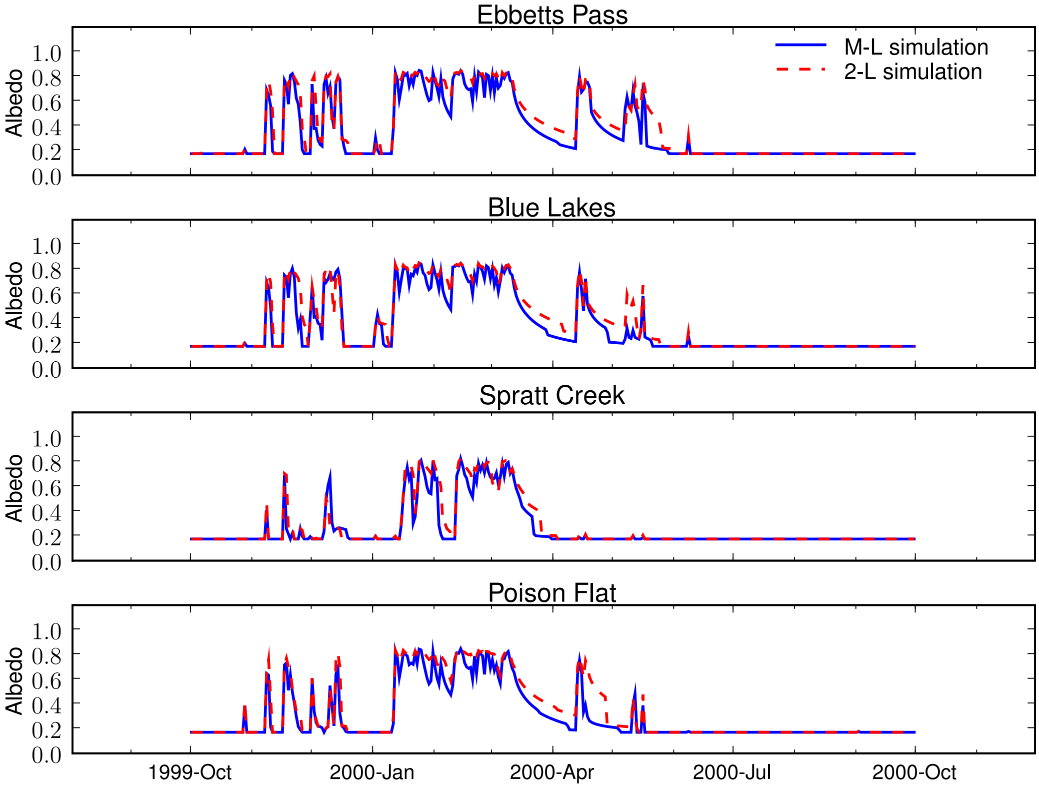

Figure 3.20: Comparison of albedo for the M-L model and 2-L model for the 2000 water year.

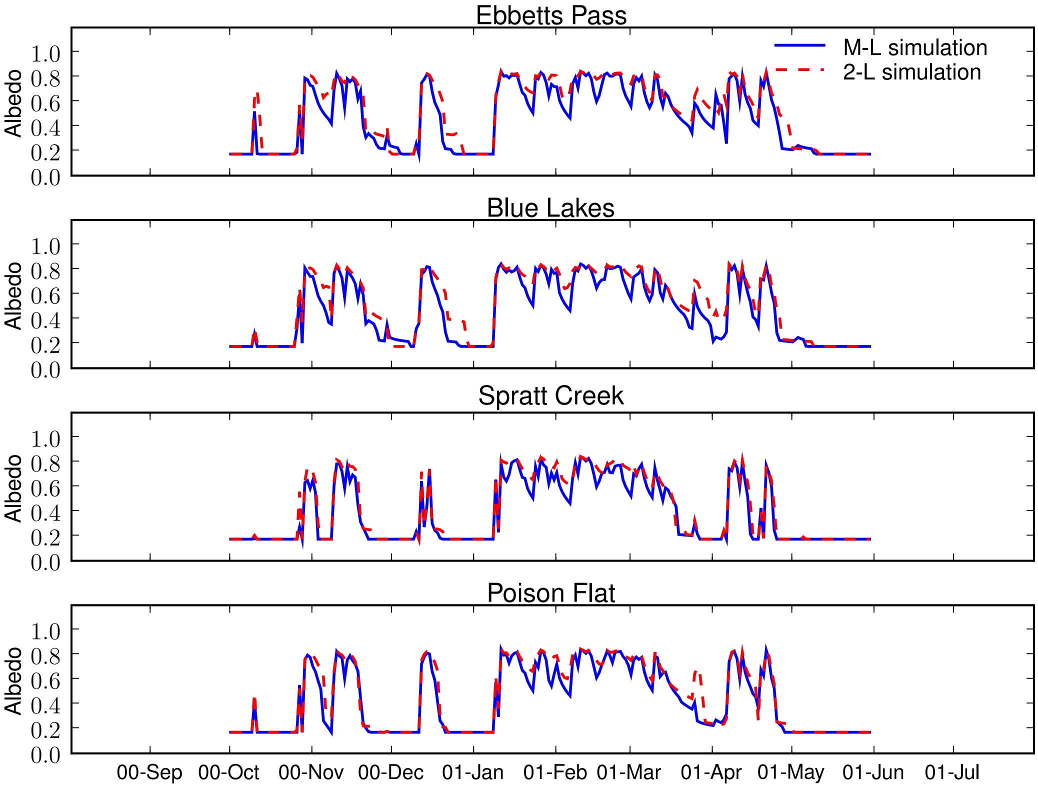

Figure 3.21: Comparison of albedo for the M-L model and 2-L model for the 2001 water year.

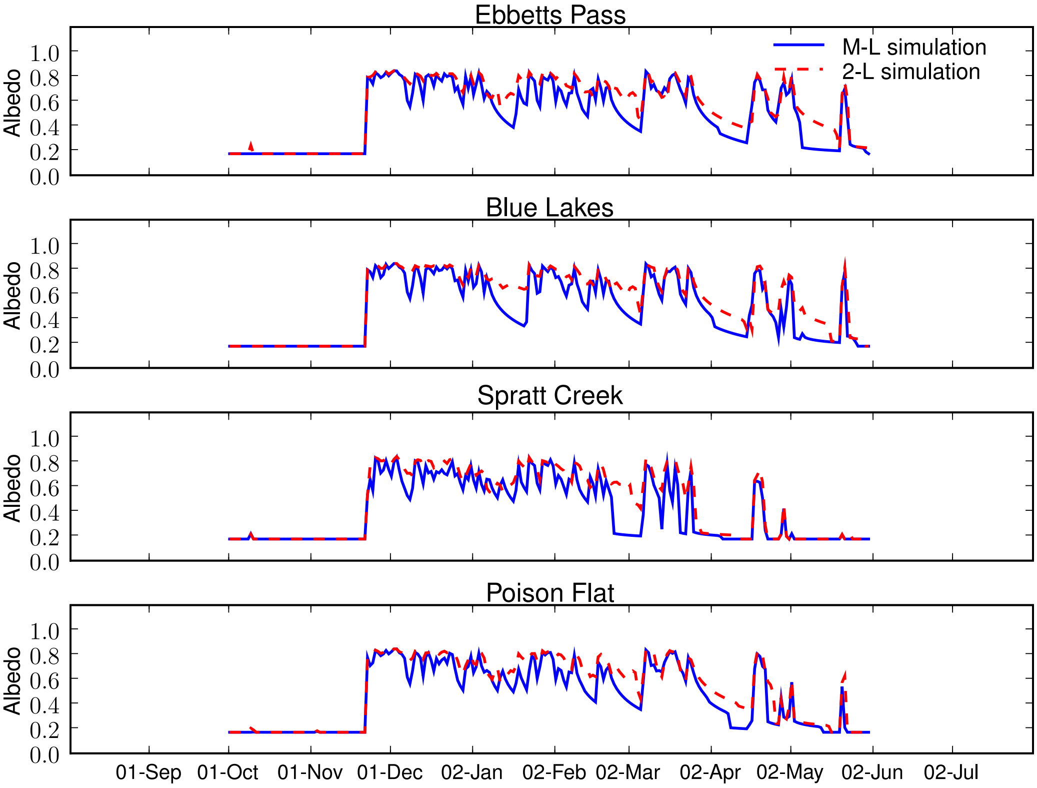

Figure 3.22: Comparison of albedo for the M-L model and 2-L model for the 2002 water year.

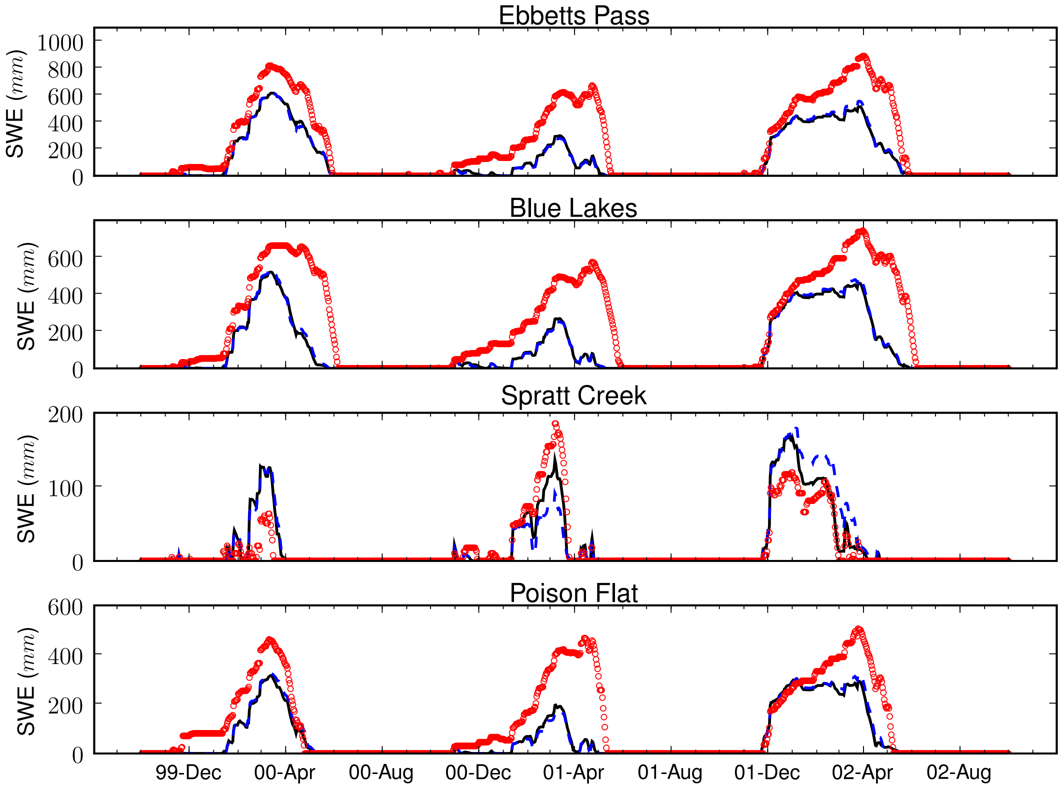

Figure 3.23: Comparison of SWE with the BATS albedo for the M-L model. The solid line is SWE from the M-L model, the dashed line the 2-L model, and the circle SNOTEL observation.

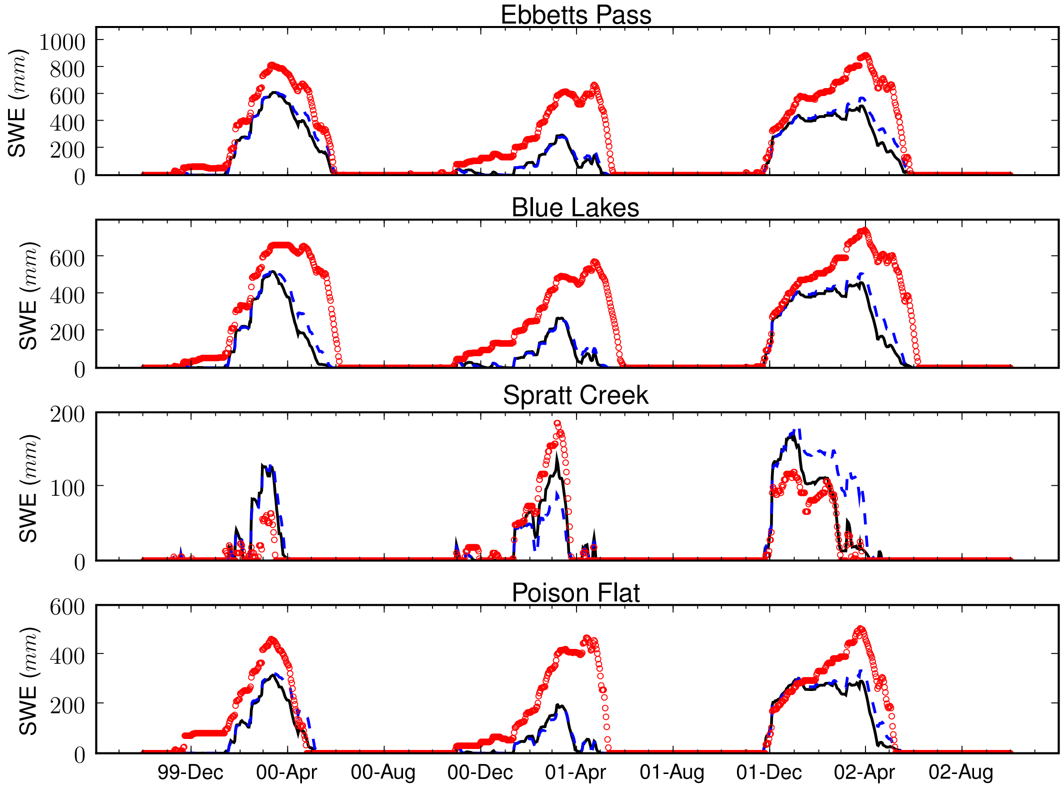

Figure 3.24: Comparison of SWE with the BATS albedo for both the M-L model and 2-L model. The solid line is SWE from the M-L model, the dashed line the 2-L model, and the circle SNOTEL observation.

Chapter 4

Multiscale Snow Data Assimilation

4.1 Introduction

The previous chapters showed that snow processes in high mountains such as the Sierra Nevada are difficult to simulate due to uncertainties associated with high spatial variations of landscape and steep spatial gradients of hydrologic variables (e.g., precipitation) with altitude [10]. In such a complex environment, simulation results may not represent the snow states of the simulation spatial domain correctly. There are many ways to characterize the uncertainty associated with snow modeling, depending on the modeling environment. For example, we can generate ensemble forcing data based on the available statistics of the modeling spatial domain to see the ensemble effect on the uncertainty of SWE simulations as in Shamir and Georgakakos [32] and in Chapter 2. When remotely sensed observations are considered in modeling snow processes, data assimilation is used widely either to reduce or to represent uncertainties in various ways [53].

Most of these studies related to uncertainty in snow modeling have focused on characterizing the uncertainty in the aspect of temporal evolution of the snow variable of interest. However, in high mountains where landscape and ground features vary sharply even over a small spatial domain, many factors that cause uncertainty are hidden in scale. Moreover, the modeling scales of snow processes are generally constrained by the scale of input forcing data [55]. This constraint is conspicuous in high mountains such as the Sierra Nevada where ground-based meteorological data are sparse and often affected by measurement errors [56].

In this regard, we present a method to relate the variable of interest at one scale to that at another in order to overcome the unfavorable conditions for physical snow models in high mountains with a particular application in the Sierra Nevada. We propagate the properties of snow states between fine scales and coarse scales using a multiscale data assimilation (MDA) scheme to reduce the uncertainty due to scaling and forcing errors. Uncertainties associated with snow processes in terms of model physics, scaling, and meteorological forcing data are explained by a multiscale perspective. The MDA scheme allows us to obtain estimates of snow variables at different scales by getting optimal parameters for the multiscale process. To understand the effect of scaling and data quality in observed data more thoroughly, we use an ensemble approach in the multiscale process.

4.2 Probabilistic Interpretation of Multiscale Process

The multiscale stochastic process in this study implements scale-recursive dynamics on trees [57]. In particular, the Gaussian process behaves in a similar way to the traditional Kalman filtering on tree structure. The multiscale process consists of two components: multiscale smoothing and optimal parameter estimation. Time-recursive state space models use “forward” and “backward” inference algorithms. The backward inference requires us to combine the forward recursion with it. This algorithm is known as the Rauch-Tung-Striebel (RTS) smoothing algorithm. For multiscale processes, the RTS algorithm is used on trees and is known as “sweep”. In this subsection, the fundamentals of the multiscale process are introduced based on probabilistic interpretation of it. In particular, derivations that are not explained in Chou et al. [58], Fieguth et al. [59], Luettgen and Willsky [60] and Parada and Liang [61] are presented.

4.2.1 Merge of Posterior Probabilities

The key probabilistic inference in a multiscale process is to calculate the probability of the current node given its child nodes. This inference process is to merge individual probabilities that relate the parent node with its each child node into one probability. Figure 4.1 shows the relationship between the parent node and its children in a graphical model. This graphical model accounts for only four child nodes under their parent node. In fact, this model will be used throughout the multiscale process in this dissertation. As shown in the graphical model, we assume that given the parent node, its children are conditionally independent and thus we can write it as:

$$p(y_1, y_2, y_3, y_3|x) = p(y_1|x)p(y_2|x)p(y_3|x)p(y_4|x) \tag{4.1}$$

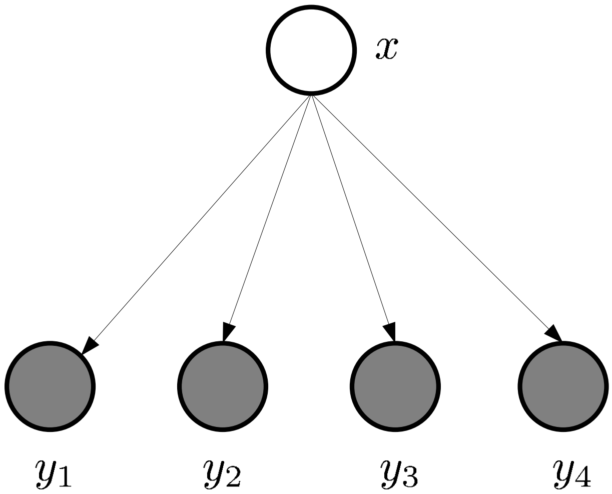

Figure 4.1: A graphical model for the relationship between the parent node and its children.

Noting each of the variable in Figure 4.1 is Gaussian, we can write the conditioning relationship for y_1 in the form of a linear function as:

$$y_1 = F_1 x + v_1 \tag{4.2}$$

where x $(0,\Sigma)$ and v has mean zero and covariance R. The generic linear function can be represented by:

$$y = Fx + v \tag{4.3}$$

The first step to compute the conditional probability between x and y is to obtain a joint distribution of the pair (x, y). If x has variance Σ, its joint distribution is summarized as:

$$\begin{bmatrix} 0 \\ \\ 0 \end{bmatrix}, \begin{bmatrix} \Sigma & \Sigma F^T \\ \\ F\Sigma & F\Sigma F^T + R \end{bmatrix}$$

where we calculated the covariance matrix as

$$\begin{aligned} Cov(x,y) &= E\left[(x-0)(y-E(y))^T\right] \\ &= E\left[x(Fx+v)^T\right] \\ &= E\left[xx^T F^T + xv^T\right] \\ &= \Sigma F^T \end{aligned} \tag{4.4}$$

Our goal is to calculate the posterior distribution $p(x|y_1, y_2, y_3, y_4)$. Letting $y = (y_1, y_2, y_3, y_4)$, the conditional distribution is then $p(x|y)$. In this Gaussian problem, we are interested in finding the conditional mean, $\hat{x}$, and the conditional covariance, P. Since we have the joint distribution, we can use the Gaussian conditioning formulas to calculate $\hat{x}$ and P.

Before calculating these quantity, we define F and R as:

$$F \triangleq \begin{bmatrix} F_1 \\ F_2 \\ F_3 \\ F_4 \end{bmatrix}, \text{ and } R \triangleq \begin{bmatrix} R_1 & 0 & 0 & 0 \\ 0 & R_2 & 0 & 0 \\ 0 & 0 & R_3 & 0 \\ 0 & 0 & 0 & R_4 \end{bmatrix} \tag{4.5}$$

The conditional mean is calculated as:

$$\begin{aligned} \hat{x} &= \left(\begin{bmatrix} F_1^T F_2^T F_3^T F_4^T \end{bmatrix} \begin{bmatrix} R_1^{-1} & 0 & 0 & 0 \\ 0 & R_2^{-1} & 0 & 0 \\ 0 & 0 & R_3^{-1} & 0 \\ 0 & 0 & 0 & R_4^{-1} \end{bmatrix} \begin{bmatrix} F_1 \\ F_2 \\ F_3 \\ F_4 \end{bmatrix} + \Sigma^{-1} \right)^{-1} \\ & \quad \left(\begin{bmatrix} F_1^T F_2^T F_3^T F_4^T \end{bmatrix} \begin{bmatrix} R_1^{-1} & 0 & 0 & 0 \\ 0 & R_2^{-1} & 0 & 0 \\ 0 & 0 & R_3^{-1} & 0 \\ 0 & 0 & 0 & R_4^{-1} \end{bmatrix} \begin{bmatrix} y_1 \\ y_2 \\ y_3 \\ y_4 \end{bmatrix} \right) \\ &= \left(F_1^T R_1^{-1} F_1 + F_2^T R_2^{-1} F_2 + F_3^T R_3^{-1} F_3 + F_4^T R_4^{-1} F_4 + \Sigma^{-1})^{-1}\right)^{-1} \\ & \quad \left(F_1^T R_1^{-1} y_1 + F_2^T R_2^{-1} y_2 + F_3^T R_3^{-1} y_3 + F_4^T R_4^{-1} y_4\right) \\ &= \left(P_1^{-1} - \Sigma^{-1} + P_2^{-1} - \Sigma^{-1} + P_3^{-1} - \Sigma^{-1} + P_4^{-1} - \Sigma^{-1} + \Sigma^{-1}\right) \\ & \quad \left(P_1^{-1}\hat{x}_1 + P_2^{-1}\hat{x}_2 + P_3^{-1}\hat{x}_3 + P_4^{-1}\hat{x}_4\right) \\ &= \left(P_1^{-1} + P_2^{-1} + P_3^{-1} + P_4^{-1} - 3\Sigma^{-1}\right) \\ & \quad \left(P_1^{-1}\hat{x}_1 + P_2^{-1}\hat{x}_2 + P_3^{-1}\hat{x}_3 + P_4^{-1}\hat{x}_4\right) \end{aligned} \tag{4.6}$$

In fact, in Equation 4.6 we have the expression for the overall conditional covariance P, which is:

$$\left(P_1^{-1} + P_2^{-1} + P_3^{-1} + P_4^{-1} - 3\Sigma^{-1}\right)$$

Therefore the overall conditional mean $\hat{x}$ can be written as:

$$\hat{x} = P\left(P_1^{-1}\hat{x}_1 + P_2^{-1}\hat{x}_2 + P_3^{-1}\hat{x}_3 + P_4^{-1}\hat{x}_4\right) \tag{4.7}$$

Because we now have the overall conditional mean and covariance for $p(x|y)$, we can use these in our upward and downward calculations.

4.2.2 Dynamic Equation for Upward Sweep

The equations for merging posterior probabilities in the previous subsection requires us to obtain an inverse form of the dynamics in scale. In a similar way to the traditional time-recursive Kalman filtering, we can write a forward equation for multiscale processes, which is called "downward sweep." In Figure 4.1, we interpreted the tree structure in terms of conditional probabilities. Now we introduce a state space model for the evolution in scale as:

$$\begin{aligned} x(s) &= A(s)x(\gamma s) + w(s) && (4.8)\\ y(s) &= C(s)x(s) + v(s) && (4.9) \end{aligned}$$

where $x(s)$ is the state of the process at node s, γs denotes the parent of node s. $w(s)$ is independent and identically distributed (i.i.d.), independent of $x(0)$ and has distribution $N(0, Q(s))$. $v(s)$ is also i.i.d. and has distribution $N(0, R(s))$. Figure 4.2 shows how the evolution in scale is related to the time-recursive process. In this graphical model, $x(s)$ is a linear function of the conditioning variable, $x(\gamma s)$. The inverse dynamics may be expressed as:

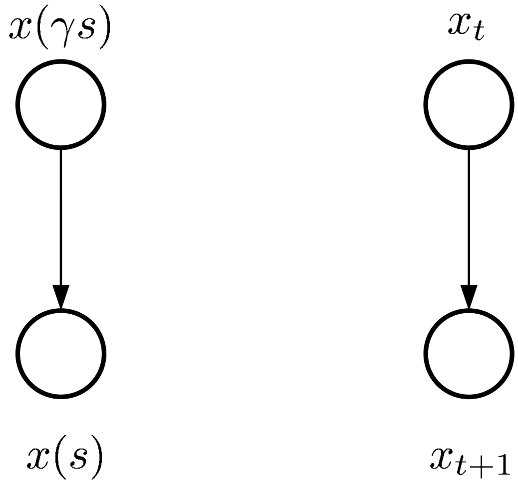

Figure 4.2: A graphical model for comparison between scale-recursive (left) and time-recursive (right) processes

$$x(\gamma s) = Fx(s) + \bar{w}(s) \tag{4.10}$$

where F is a matrix that relates scale s to scale γs and $\bar{w}(s)$ is white noise as usual.

Our goal is to find the expressions for F and $\bar{w}(s)$. Once we find expressions for these quantities, the remaining process is similar to that of the traditional Kalman filtering as shown in Chou et al. [58], Fieguth et al. [59], Luettgen and Willsky [60] and Parada and Liang [61]. This subsection presents the derivation of these quantities in detail. First we need to get the joint distribution of the pair $(x(\gamma s), x(s))$, which is summarized as:

$$\begin{bmatrix} \Sigma(\gamma s) & \Sigma(\gamma s)A(s)^T \\ A(s)\Sigma(\gamma s) & \Sigma(s) \end{bmatrix}$$

where $\Sigma(s) = A(s)\Sigma(\gamma s)A(s)^T + Q(s)$ by the Lyapunov equation. We also calculated the covariance between $x(\gamma s)$ and $x(s)$ as:

$$\begin{aligned} Cov(x(\gamma s), x(s)) &= E\left[(x(\gamma s) - \hat{x}(\gamma s))(x(s) - \hat{x(s)})^T\right] \\ &= E\left[(x(\gamma s))(A(s)x(\gamma s) + w(s))^T\right] \end{aligned} \tag{4.11}$$

where we assumed that $E(x(s)) = 0$. If $E(x(s))$ is not zero, the mean needs to be subtracted.

The backwards Markovian property shows:

$$E\left[w(x)|x(s), \ldots, x(S)\right] = E\left[w(s)|x(s)\right] \tag{4.12}$$

where S is the index for the finest node.

Given the property of $w(s)$, we need to compute $E\left[w(s)|x(s)\right]$. As usual, calculation of this quantity requires the joint distribution of $w(s)$ and $x(s)$:

$$\begin{bmatrix} 0 \\ \\ 0 \end{bmatrix}, \begin{bmatrix} E\left[w(s)w(s)^T\right] & E\left[w(s)x(s)^T\right] \\ \\ E\left[x(s)w(s)^T\right] & E\left[x(s)x(s)^T\right] \end{bmatrix}$$

From the definition, $E\left[w(s)w(s)^T\right] = Q(s)$. We also define:

$$E\left[x(s)x(s)^T\right] = \Sigma(s) \tag{4.13}$$

From this joint distribution, we can express the conditional distribution in Equation 4.12 as:

$$\begin{aligned} E\left[w(s)|x(s)\right] &= E\left[w(s)(A(s)x(\gamma s) + w(s))^T\right] \cdot \\ &\quad E\left[(A(s)x(\gamma s) + w(s))(A(s)x(\gamma s) + w(s))^T\right]^{-1} x(s) \\ &= E\left[w(s)w(s)^T\right] \cdot \\ &\quad E\left[A(s)x(\gamma s)x(\gamma s)^T A^T(s) + w(s)w(s)^T\right]^{-1} x(s) \\ &= Q(s)\left[A(s)\Sigma(\gamma s)A^T(s) + Q(s)\right]^{-1} x(s) \\ &= Q(s)\Sigma^{-1}(s)x(s) \end{aligned} \tag{4.14}$$

On the other hand, $w(s)$ can be decomposed into $E\left[w(s)|x(s), x(s+1), \ldots, x(S)\right]$ and a remaining error $\tilde{w}(s)$ as:

$$\begin{aligned} w(s) &= E\left[w(s)|x(s), x(s+1), \ldots, x(S)\right] + \tilde{w}(s) \\ &= E\left[w(s)|x(s)\right] + \tilde{w}(s) \end{aligned} \tag{4.15}$$

where we used the Markovian property in Equation 4.12. Using Equation 4.14, the remaining error term can be written as:

$$\tilde{w}_s = w(s) - Q(s)\Sigma^{-1}(s)x(s) \tag{4.16}$$

with covariance $\tilde{Q}(s)$, which is represented as:

$$\begin{aligned}
E\left[\tilde{x}(s)\tilde{x}^T(s)\right] &= Var[\tilde{w}(s)] \\
&= Var\left[w(s) - Q(s)\Sigma^{-1}(s)x(s)\right] \\
&= Q(s) - Var\left[Q(s)\Sigma^{-1}(s)x(s)\right] \\
&= Q(s) - Q(s)\Sigma^{-1}(s)Var[x(s)](Q(s)\Sigma^{-1}(s))^T \\
&= Q(s) - Q(s)\Sigma^{-1}(s)Q(s)
\end{aligned}$$

Here we recall our original model:

$$x(s) = A(s)x(\gamma s) + w(s)$$

Direct reversing of this equation yields:

$$x(\gamma s) = A^{-1}(s)x(s) - A^{-1}(s)w(s) \tag{4.17}$$

If we substitute the result from Equation 4.16 into Equation 4.17, we find:

$$x(\gamma s) = \left(A^{-1}(s) - A^{-1}(s)Q(s)\Sigma^{-1}(s)\right)x(s) - A^{-1}(s)\tilde{w}(s) \tag{4.18}$$

If we compare Equation 4.18 with the inverse dynamics equations defined in Equation 4.10 we find:

$$F(s) = A^{-1}(s) - A^{-1}(s)Q(s)\Sigma^{-1}(s) \tag{4.19}$$

$$\bar{w}(s) = -A^{-1}(s)\tilde{w}(s) \tag{4.20}$$

We use these expressions for the inverse (upward) dynamics on tree, and other details such as the EM algorithm is presented in Kannan et al. [57] and Parada and Liang [61].

4.3 Multiscale Assimilation Methods and Data

4.3.1 Method

This subsection describes the method to apply the fundamentals of multiscale assimilation introduced in the previous subsection to the Sierra Nevada site. The VIC LSM [42] is coupled with the MDA scheme. We use two physical snow models within the VIC LSM to consider the uncertainty in model physics more thoroughly: 2-layer (2-L) snow model [38] and multi-layer (M-L) snow model [62], which was introduced in Chapter 3. The NLDAS forcing data [50] are used to run the two snow models. Using a macro-scale LSM and forcing data available on the public domain, we perform our experiment for the environment where observed forcing data are sparse and error-prone and for the case where the physical model scale is limited by such input forcing data [55].

We use the SWE variables from two independent sources, one for a fine resolution and the other for a coarse resolution. For the fine resolution data, the SNODAS product from the National Operational Hydrologic Remote Sensing Center (NOHRSC) is used [63]. The NOHRSC SNODAS product has been reported to well represent the hydrologic system of interest [64].

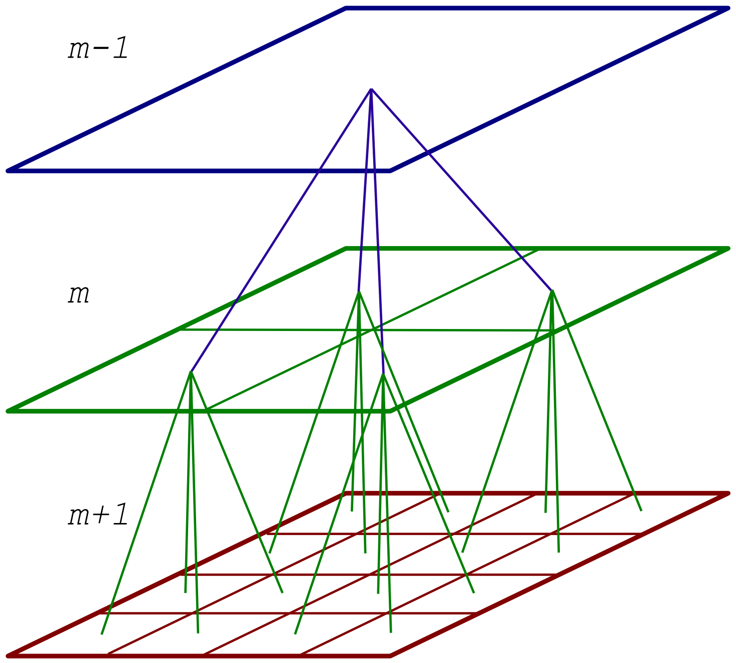

Figure 4.3: Multiscale structure on tree. Collective index m includes scale index s, and location index (i, j).

SNODAS SWE data are archived at 1 km resolution and aggregated into 1/64th degrees for the experiment. For the coarse resolution, we use the AMSR-E daily SWE product [65]. AMSR-E SWE data are provided in 25 km resolution. Due to the known problems such as the saturation effect [66], AMSR-E SWE data are used only during the early snow season.

The SWE data or indirect observations of them (e.g., brightness temperature) that we can use for data assimilation are often available at different scales from that of model predictions. Therefore, following Chou et al. [58], Fieguth et al. [59], Luettgen and Willsky [60] and Parada and Liang [61], we can define the model to describe the multiscale process in a tree structure as:

$$x(s) = A(s)x(\gamma s) + w(s) \tag{4.21}$$

where $x(s)$ is the Gaussian multiscale hidden state vector at node s, and γs denotes the parent of node s. The process noise $w(s)$ is white and independent of $x(s_0)$ and has a distribution $N(0, Q(s))$. s is the node index, and s_0 represents the root node. As in the traditional Kalman filter, the Gaussian process x and its noisy observation y can be related as:

$$y(s) = C(s)x(s) + D(s) + v(s) \tag{4.22}$$

where $y(s)$ is a noisy measurement vector, $D(s)$ is a matrix for an exogenous input, and $v(s)$ is white and independent of $x(s_0)$ and $w(s)$ and has a distribution $N(0, R(s))$.

From Equations 4.21 and 4.22, our parameter set θ to be optimized for every assimilation time can be written as:

$$\theta = \{\hat{x}(s_0), P(s_0), Q(s), R(s) | s \in S_T\} \tag{4.23}$$

where $x(s_0)$ is the unconditional mean for the root node, $P(s_0)$ is the unconditional covariance matrix for the root node, and S_T is the set of all the nodes in the tree. It is important to note that we set $C(s)$ as 1 because we use direct SWE observations in this experiment. Also, we set $A(s)$ to be 1 to conserve the mean SWE value across the scale. The time-varying parameter set θ determines the uncertainty that is attributed to observations and model predictions. We use the expectation-maximization (EM) algorithm to estimate θ when independent SWE data (e.g., SNODAS data) are available [57] [61]. In our MDA scheme, SWE from SNODAS, AMSR-E, and the snow models are all considered as independent observations to obtain the unknown state $x(s)$ in Equation 4.21.

We further investigate the effect of scaling and data quality of independent observations on multiscale data assimilation using an ensemble approach. To examine the effect of observation data uncertainty, we are required to generate an ensemble of SNODAS datasets with different degrees of uncertainty. To avoid using arbitrary uncertain parameters in generating ensemble noisy data, we focus on posterior density of a state space model as shown in Chapter 2.

Since SWE from SNODAS during a given water year shows a rather simple behavior with both increasing and decreasing trends, we model the SWE state as:

$$x_{t+1} = Ax_t + w_t \tag{4.24}$$

$$y_t = Cx_t + v_t \tag{4.25}$$

where t is time index, x_t and y_t are the state and observation at time t, respectively, A and C are linear operators, $w_t \sim N(0, Q)$ and $v_t \sim N(0, R)$. As usual, we assume that v_t and w_t are white and independent of the state x_t. Note that C is 1 since we are modeling the same state variable as the observation.

From the Markov property and the Bayes rule, the posterior density can be expressed as:

$$\begin{aligned}
p(x_{t+1}|y_{t+1}, y_0, ..., y_t) &\propto p(y_{t+1}|x_{t+1}, y_0, ..., y_t)p(x_{t+1}|y_0, ..., y_t) \\
&= p(y_{t+1}|x_{t+1})p(x_{t+1}|y_0, ..., y_t) \\
&= p(y_{t+1}|x_{t+1}) \int p(x_{t+1}, x_t|y_0, ..., y_t)dx_t \\
&= p(y_{t+1}|x_{t+1}) \int p(x_{t+1}|x_t, y_0, ..., y_t)p(x_t|y_0, ..., y_t)dx_t \\
&= p(y_{t+1}|x_{t+1}) \int p(x_{t+1}|x_t)p(x_t|y_0, ..., y_t)dx_t \qquad (4.26)
\end{aligned}$$

where $p(\cdot)$ is a general Gaussian density function and we used conditional independences from the Markov property to convert the integrand into an easy form for integrating out x_t.

Following the definition and result in Chapter 2, the posterior density can be written as:

$$x_{t+1}|y_{t+1}, y_0, ..., y_t \sim N(\hat{x}_{t+1|t+1}, P_{t+1|t+1}) \tag{4.27}$$

with

$$\begin{aligned}
\hat{x}_{t+1|t+1} &= \hat{x}_{t+1|t} + K_{t+1}(y_{t+1} - \hat{x}_{t+1|t}) \qquad (4.28) \\
P_{t+1|t+1} &= P_{t+1|t} - K_{t+1}CP_{t+1|t} \qquad (4.29)
\end{aligned}$$

where K_{t+1} is the quantity known as Kalman gain.

Perturbed observations are generated based on the posterior distribution whose parameters are obtained for each SNODAS grid cell independently using the EM algorithm. For data with a coarse scale, we aggregate the SNODAS data from 1/64th degrees (i.e., Scale 4) to 1/4th degrees (i.e., Scale 0) and use this coarse scale data as equivalent observations to AMSR-E data. Using this aggregated SNODAS data and the original SNODAS data we conduct multiscale assimilation experiments for two representative cases. In Case I, we perturb the aggregated SNODAS data at Scale 0 to generate ensemble observations at this scale and use these data to run the MDA system with the original SNODAS data. In Case II, we perturb SNODAS data at Scale 4 only along with the aggregated SNODAS data at Scale 0, which is not perturbed.

The experiment using the coupled MDA system is conducted in a 25 $km \times 25$ km domain in the East Fork Carson River Basin of the Sierra Nevada. We use data from the Ebbetts Pass and Blue Lakes SNOTEL stations, the elevation of each of which is 2,672 m and 2,456 m, respectively. We chose these two stations because they well represent the modeling grid cells at 1/8th degrees. We use five different scales from Scale 0 to Scale 4 to match the AMSR-E data, VIC LSM output and SNODAS data. For example, Scale 0 is set as 1/4th degrees ($\sim 25 \times 25$ km^2), which corresponds to the AMSR-E data, Scale 1 as 1/8th degrees corresponding to the VIC LSM scale, and Scale 4 as 1/64th degrees corresponding to the SNODAS data (Figure 4.4).

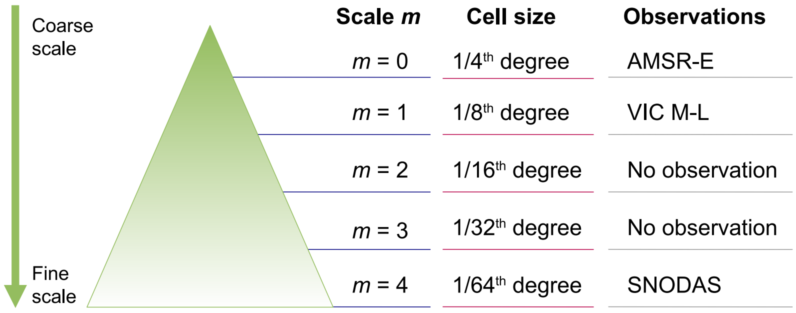

Figure 4.4: Design scales where $m = (s, i, j)$.

4.4 Results

The time series in Figures 4.5 and 4.6 show SWE assimilation results with SNODAS data, model simulations at grid cells corresponding to the Blue Lakes SNOTEL station, and the SWE observations at the station. Figures 4.7 and 4.8 show the same results for the Ebbetts Pass SNOTEL station. When the MDA system is applied, the SWE values are close to the SNOTEL observation at all scales, removing most of the uncertainty in the simulations of SWE by the 2-L snow model and M-L snow model of the VIC LSM. These figures also show that the uncertainty due to model physics is much smaller than that of meteorological forcing data. Even though there are certain differences in the physical description of snow processes (e.g., layer structure) between the 2-L and M-L models, their impact was much smaller than that of forcing data in our experiment setting. Similar results were reported by Pan et al. [16] where all SWE simulations by the three snow models had large low biases. In our experiment, most of the low biases are removed by the data assimilation that uses independent SWE data at a fine scale in a multiscale perspective.

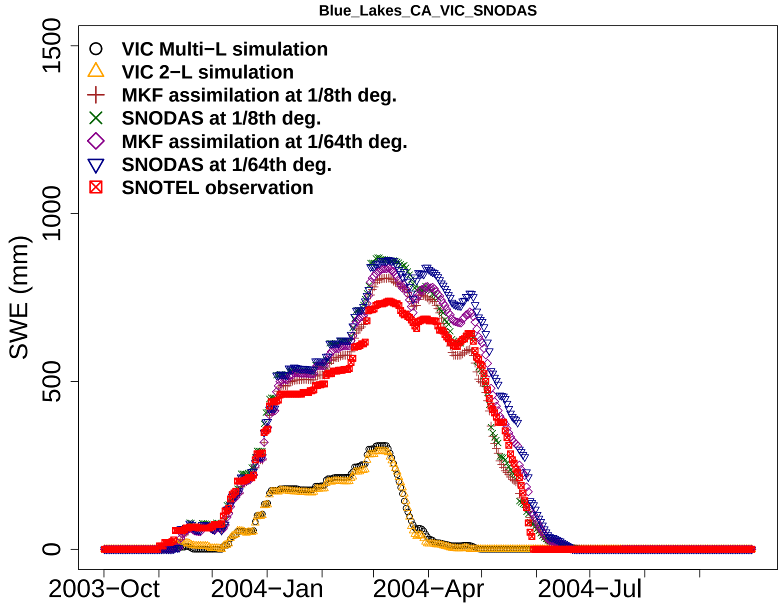

Figure 4.5: Assimilation results at the grid cell corresponding to/including the Blue Lakes SNOTEL station with SNODAS only for the 2004 water year.

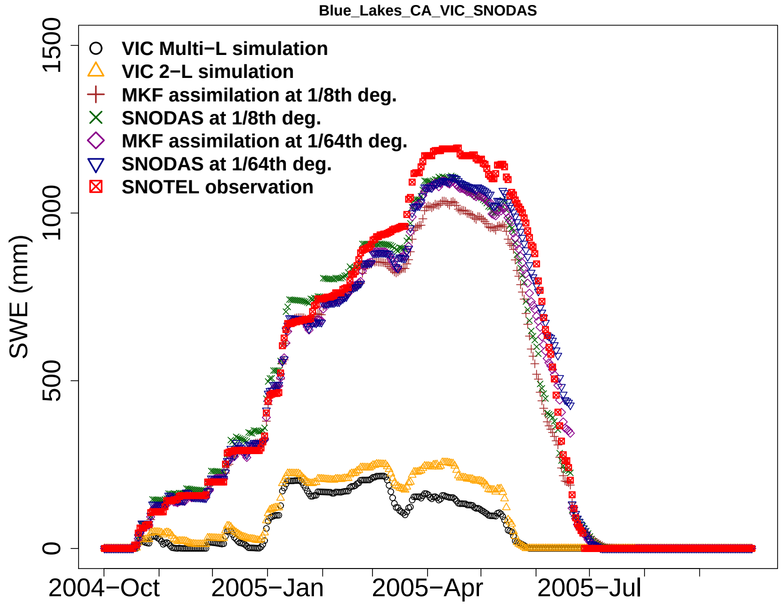

Figure 4.6: Assimilation results at the grid cell corresponding to/including the Blue Lakes SNOTEL station with SNODAS only for the 2005 water year.

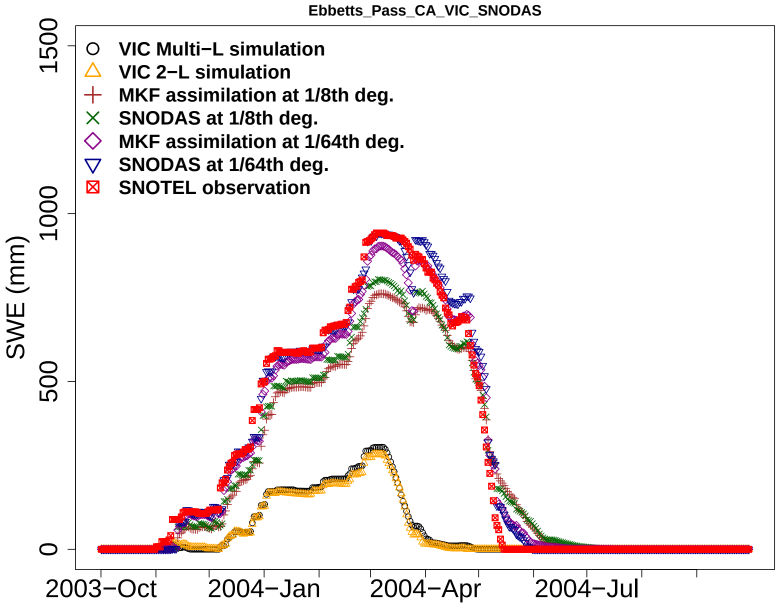

Figure 4.7: Assimilation results at the grid cell corresponding to/including the Ebbetts Pass SNOTEL station with SNODAS only for the 2004 water year.

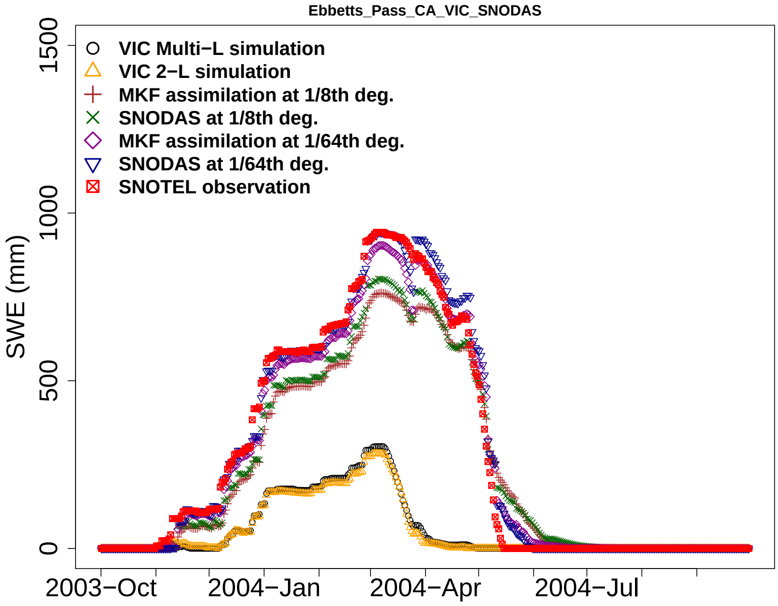

Figure 4.8: Assimilation results at the grid cell corresponding to/including the Ebbetts Pass SNOTEL station with SNODAS only for the 2005 water year.

We also need to examine the effect of observations with coarse resolution because they have their own characteristics in scaling. For this purpose we use the AMSR-E daily SWE product along with the SNODAS product. Figure 4.9 and Figure 4.10 show the time series of assimilated SWE when AMSR-E SWE data were used with SNODAS data for the Blue Lake SNOTEL station. Figure 4.11 and Figure 4.12 show the time series of assimilated SWE when AMSR-E SWE data were used with SNODAS data for the Ebbetts Pass SNOTEL station. Due to reported problems with AMSR-E data in high mountains with deep snowpack [66] [53], only data during the early snow season are used. When AMSR-E data are assimilated, variability in the posterior SWE increased as shown in the early snow season (e.g., December), not improving the assimilation results. This result shows that errors in the AMSR-E data reported by Andreadis and Lettenmaier [53] are also reflected in our multiscale process experiment.

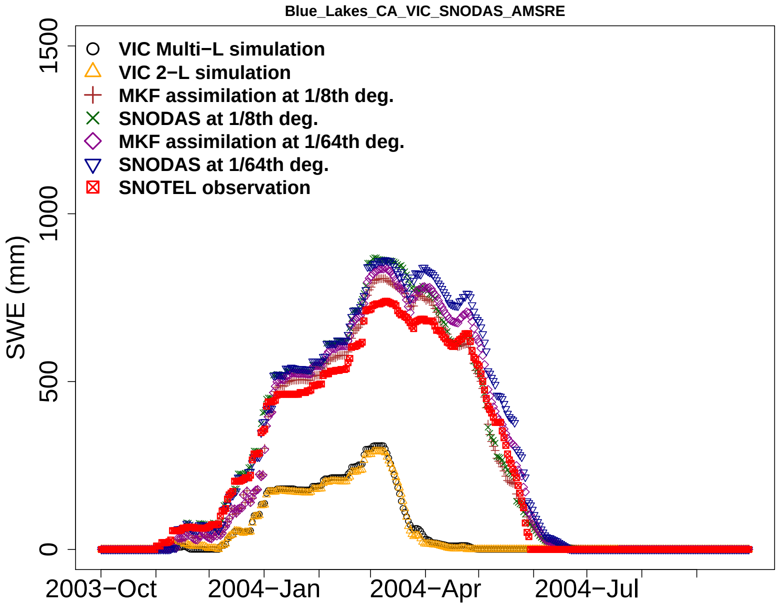

Figure 4.9: Assimilation results at the grid cell corresponding to/including the Blue Lakes SNOTEL station with SNODAS and AMSR-E for the 2004 water yea.

Spatial distribution of the assimilated SWE in Figure 4.13, in which only SNODAS data are assimilated, shows a similar result to what we have seen in the temporal evolution of SWE. As the scale becomes finer, the spatial distribution of SWE is better captured in the domain while we see the spatially averaged effect as the scale becomes coarser. When assimilated with SNODAS data, it results in a considerable improvement in the spatial structure of SWE at the model scale. Not only do we have better estimates of the mean field of SWE at the modeling scale (i.e., 1/8th degrees), but we can also describe the system of the domain at its sub-grid scale whether an observation is available for the fine scale or not.

We have shown how the MDA scheme reduced the uncertainty in simulating SWE based on one assimilation event. To better understand the uncertainty associated with forcing data and independent SWE data, we performed the MDA runs using an ensemble-based approach. As described in Section 4.3, the ensemble assimilation is conducted by generating ensemble members for the SNODAS SWE data. Figure 4.14 shows the ensemble generation of SNODAS data based on the state space model discussed earlier, and Figure 4.15 shows the difference between the original SNODAS data and ensemble members. The simulations in both figures use variance $\Sigma_p = 4P_{t+1|t+1}$.

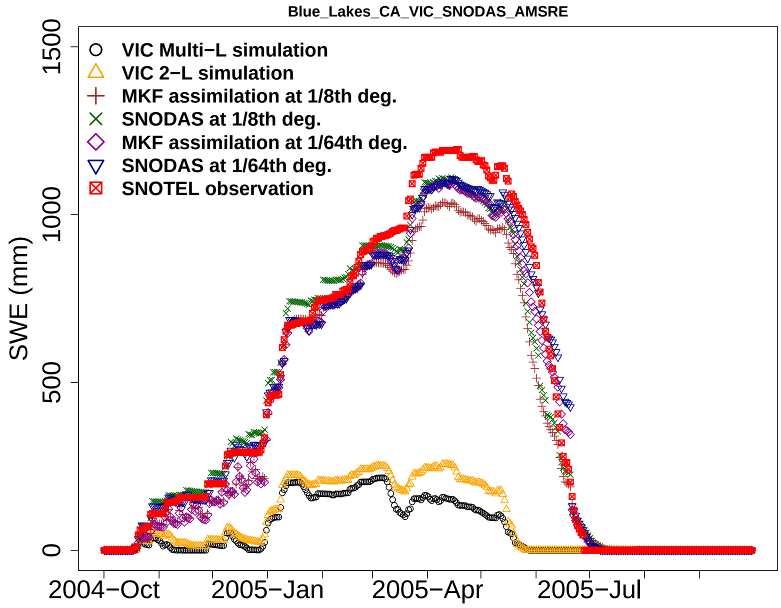

Figure 4.10: Assimilation results at the grid cell corresponding to/including the Blue Lakes SNOTEL station with SNODAS and AMSR-E for the 2005 water year.

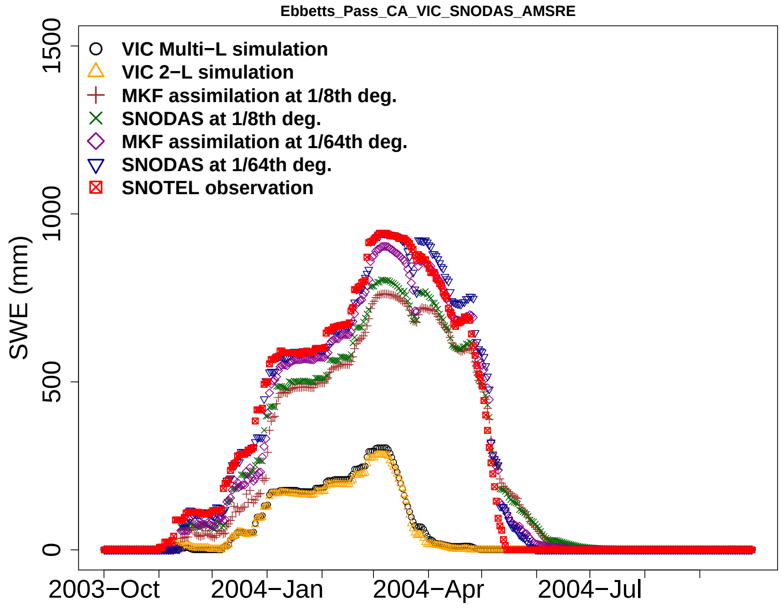

Figure 4.11: Assimilation results at the grid cell corresponding to/including the Ebbetts Pass SNOTEL station with SNODAS and AMSR-E for the 2004 water year.

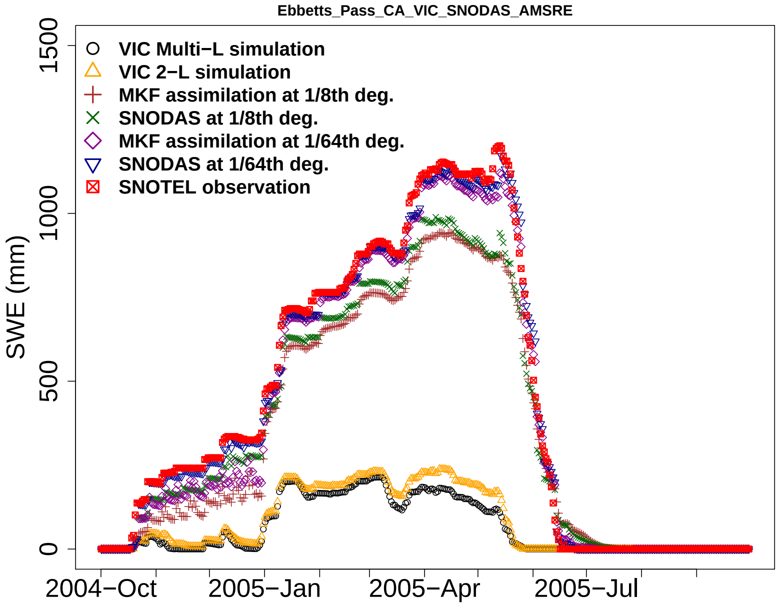

Figure 4.12: Assimilation results at the grid cell corresponding to/including the Ebbetts Pass SNOTEL station with SNODAS and AMSR-E for the 2005 water year.

Figures 4.16 and 4.17 show the snapshots of differences in SWE between the assimilation without perturbation and the 50 perturbed ensemble assimilations at Scale 1 and Scale 4, respectively. For the snapshot at each scale, the SWE differences are presented under Cases I and II. We used the M-L snow model only for the assimilation. Figure 4.16 also shows the range of differences (dashed line) between the original unperturbed SNODAS data and 50 perturbed data, which are the inputs for the MDA runs, for Cases I and II. That is, the range shows the maximum and minimum differences in the time series. For both cases, we generated the perturbed SNODAS data using the posterior variances $P_{t+1|t+1}$ and $4P_{t+1|t+1}$ to introduce a range of uncertainty degrees. In the figure, only the uncertainty range of the perturbed SNODAS SWE for $4P_{t+1|t+1}$ is shown as a reference.

This ensemble-based multiscale process provides a few important pieces of information related to snow modeling and data assimilation. First, in both Cases I and II, the independent SWE data with the larger posterior variance (i.e., $4P_{t+1|t+1}$) resulted in a lager uncertainty range than those with the smaller posterior variance. However, the range of uncertainties is still relatively small considering the magnitude of the ground observations at the SNOTEL stations. For example, in Figure 4.16 (right panel) where the snapshot is viewed at Scale 1, we have much smaller uncertainty range of the ensemble posterior SWE compared to that of the perturbed SNODAS data. Note that the uncertainty range generated by the perturbed 50 SNODAS datasets is presented in dashed line. This result is because the uncertainty (e.g., data quality) of SNODAS SWE data at Scale 4 is alleviated at Scale 1 through the MDA scheme. It is assumed that a reasonable range of uncertainties was provided to SNODAS SWE data by the posterior variances. In Figure 4.16 (right panel), for example, when $\Sigma p = 4P_{t+1|t+1}$ the maximum uncertainty range (dashed line) at Scale 4 is approximately 30 mm in SWE difference from the original SNODAS data. Even with this range (i.e., about 30 mm) of uncertainty in observations at Scale 4, the assimilated results at Scale 1 (i.e., model scale) have not changed significantly. These results imply that we will see more significant change in the simulation of SWE at Scale 1 by changing the forcing data at Scale 1 rather than by changing SNODAS data

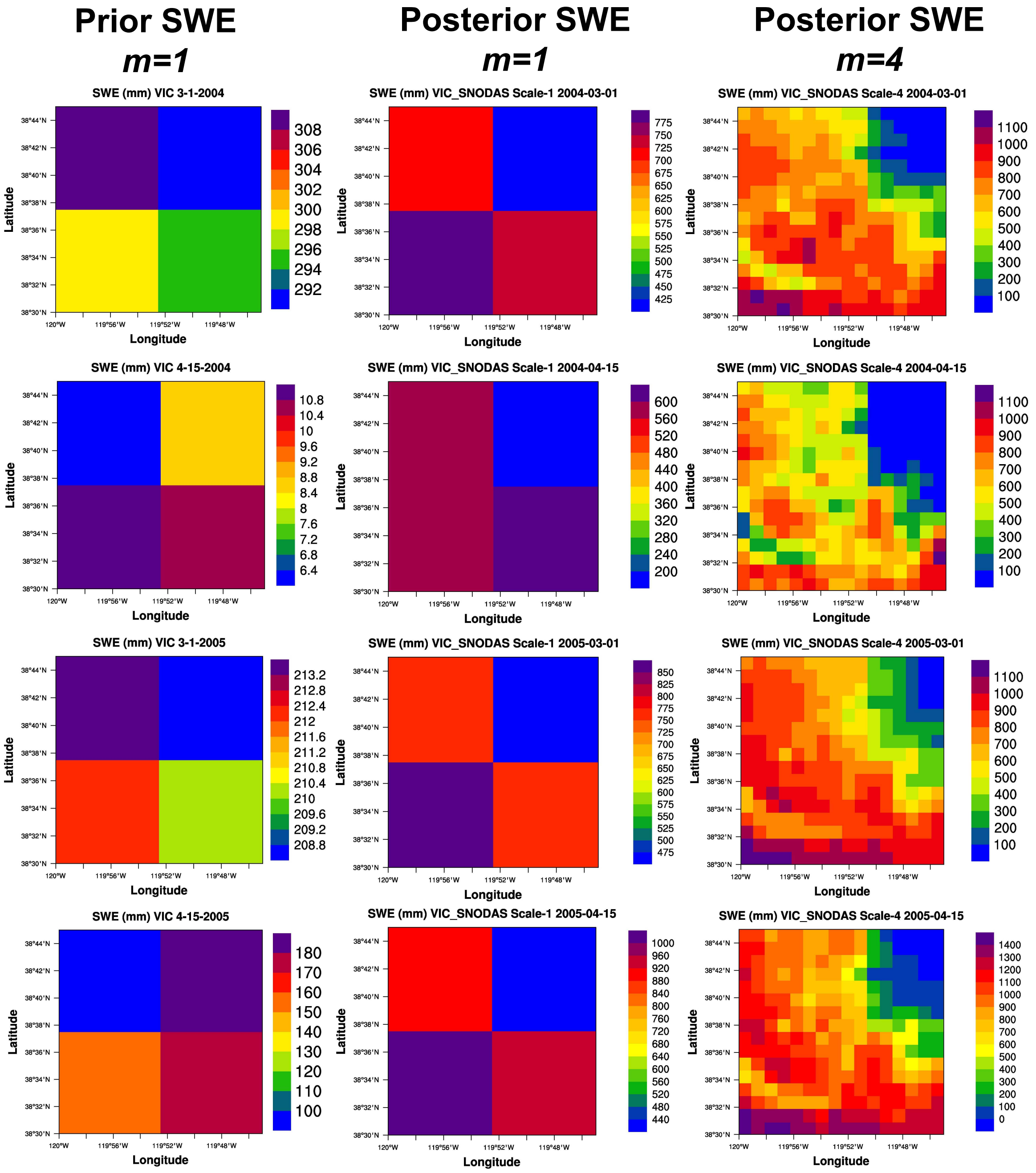

Figure 4.13: Assimilation results with SNODAS data at different scales (only results with m = 1 and m = 4 are shown). Prior SWE denotes VIC M-L snow model prediction for the current time given previous assimilations at scale m = 1, and Posterior SWE the assimilation results for the current time step at a given scale, which belongs to {0, 1, 2, 3, 4} in this experiment. The first row shows results for March 1, 2004, the second row for April 15, 2004, the third row for March 1, 2005, and the fourth row for April 15, 2005.

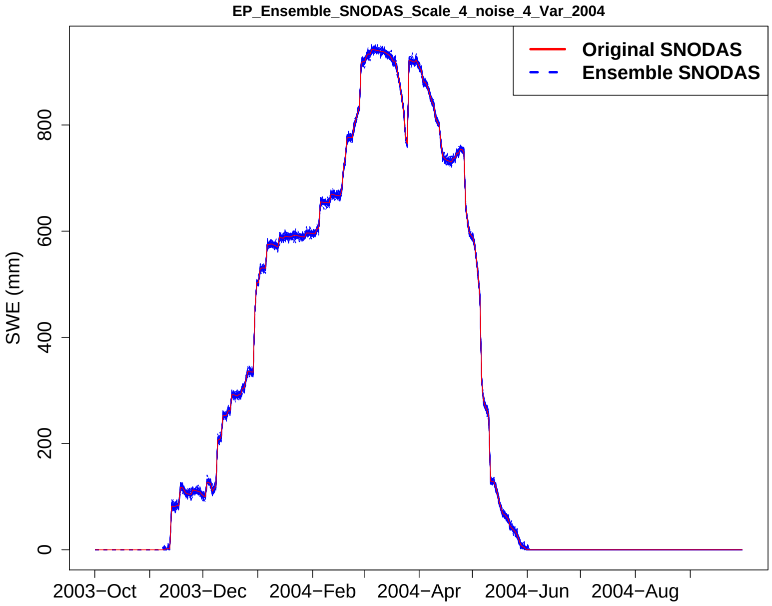

Figure 4.14: 50 perturbed SNODAS data using $\Sigma_p = 4P_{t+1|t+1}$ at the grid cell corresponding to the Ebbetts Pass SNOTEL station for the 2004 water year.

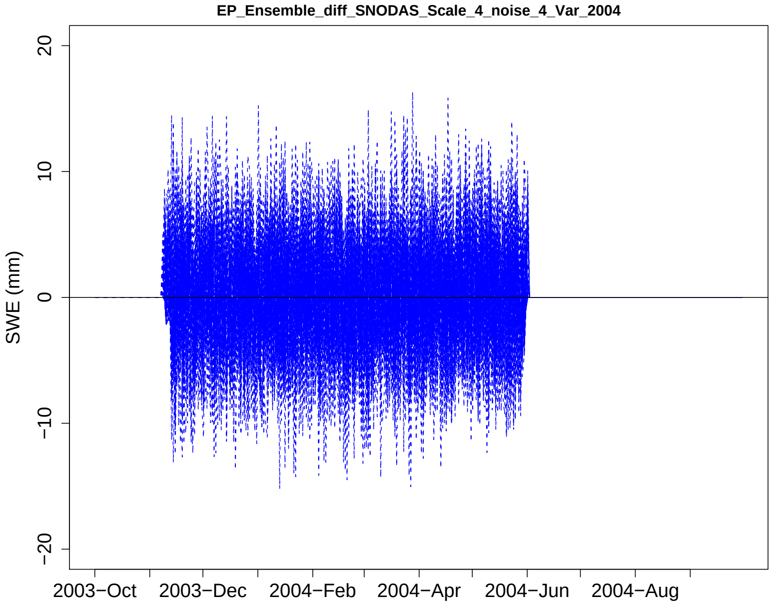

Figure 4.15: Difference between the original SNODAS data and 50 perturbed SNODAS data using $\Sigma_p = 4P_{t+1|t+1}$ at the grid cell corresponding to the Ebbetts Pass SNOTEL station for the 2004 water year.

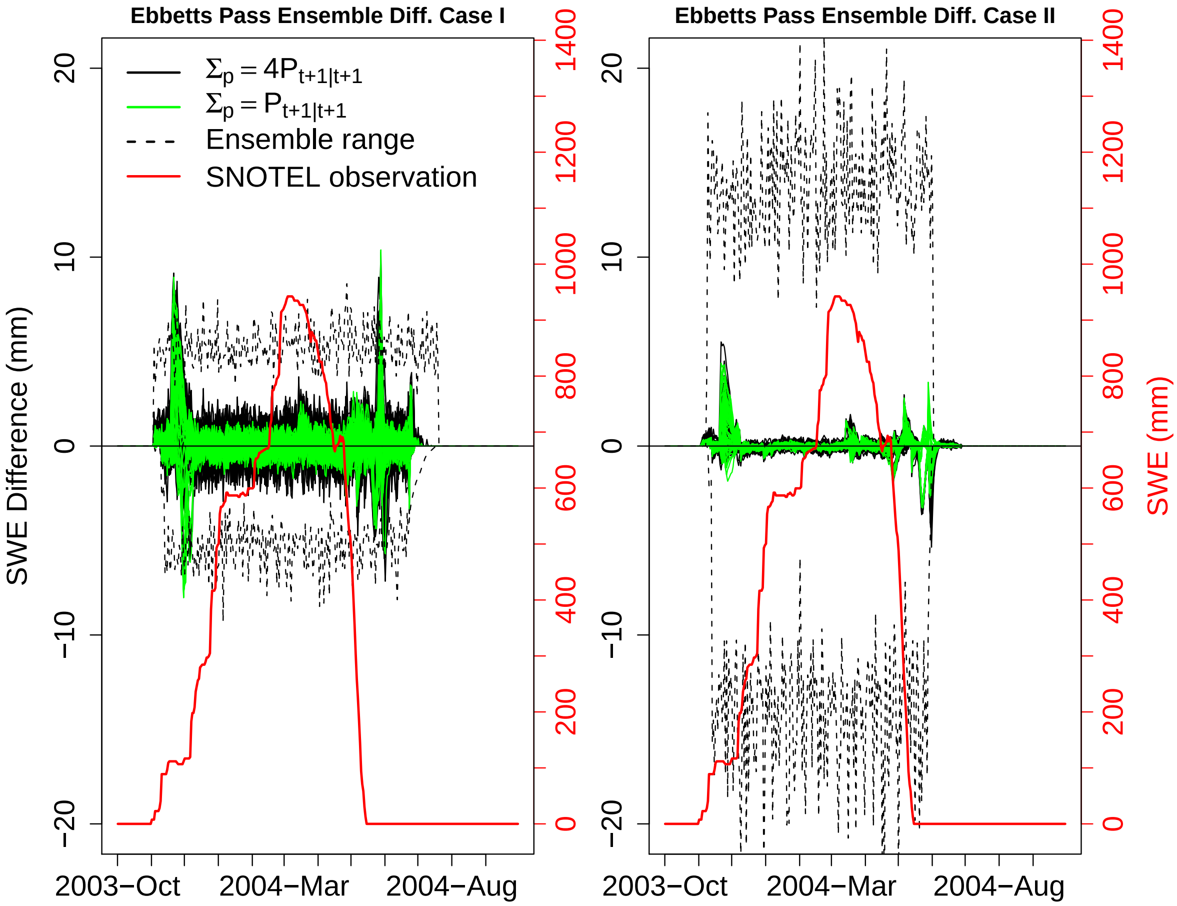

Figure 4.16: SWE differences at Scale 1 between the normal unperturbed assimilation and 50 perturbed ensemble assimilations for Case 1 (left) and Case II (right) at the Ebbetts Pass SNOTEL station for the 2004 water year. The SNOTEL observation (red) is shown as a reference and the dashed line indicates the range of differences between the original SNODAS data and the 50 perturbed ensemble data.

(i.e., observation) at Scale 4.

When the differences in the assimilated SWE are compared between Case I and II at the VIC LSM modeling scale (i.e., Scale 1), the impact of uncertainty in the SNODAS data on the ensemble assimilation is larger in Case I than in Case II, as shown in Figure 4.16. This result means that the assimilation at Scale 1 is more sensitive to observed data at its parent scale (i.e., Scale 0) than those at Scale 4. More specifically, the result implies that if the quality of data at Scale 0 is good, it can be used to improve the assimilation results at Scale 1. Currently, most of remotely sensed SWE products (e.g., AMSR-E SWE) are available at coarser scale than our modeling scale (i.e., Scale 1). Even though our experiment with the AMSR-E SWE product did not show improvement in multiscale processes, our ensemble-based results show that there are still potential benefits of using quality data with coarse resolution.

The result in Figure 4.16 also shows that the range of uncertainty in both cases expands rapidly when melting occurs. This snapshot at Scale 1 gives us a different angle than the one at Scale 4 shown in Figure 4.17. This result clearly shows that the uncertainty in snow modeling is relatively high during the melting process whether the melting occurs during the accumulation season or the melting season. For example, a large uncertainty range is shown during the period

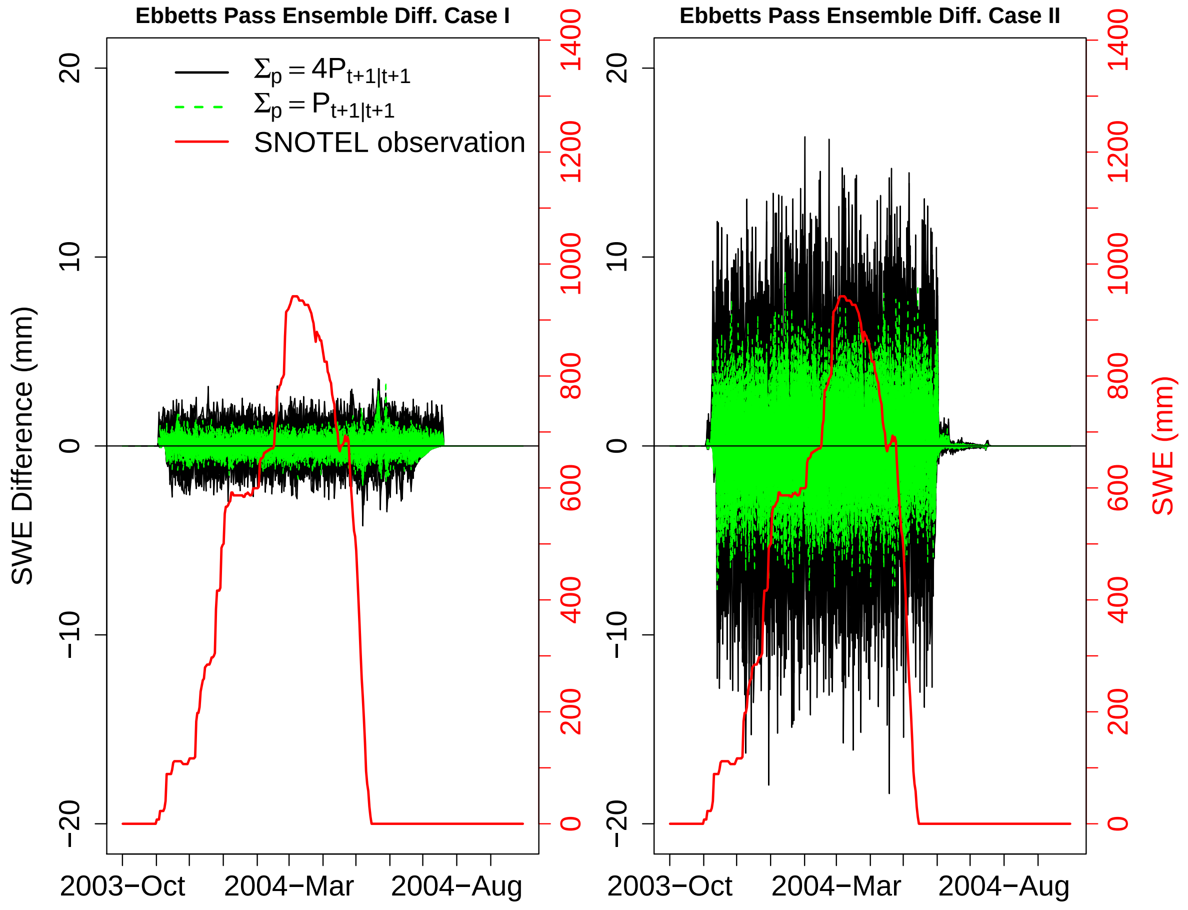

Figure 4.17: SWE differences at Scale 4 between the normal unperturbed assimilation and 50 perturbed ensemble assimilations for Case 1 (left) and Case II (right) at the Ebbetts Pass SNOTEL station for the 2004 water year. The SNOTEL observation (red) is shown as a reference.

of mid-November to early December in Figure 4.16. This large range at Scale 1 appears to be the effect of the snow model, rather than the ensemble effect, noting that the distribution of the drawn SWE samples shows much less fluctuation than the uncertainty range by the assimilated ensemble SWE. For the distribution of the generated SWE samples, in Figure 4.16 we present the maximum deviations of the 50 drawn ensemble members from the unperturbed value for each observation time based on the posterior distribution. Even though the effect of the different model physics between our 2-L model and M-L model is small in temporal evolution of SWE (e.g., Figure 4.5), different representations of liquid water can still cause a difference in melting time by several days as shown by Rutter et al. [67]. Our ensemble-based assimilation results provide a similar evidence that the model uncertainty during the melting period can be large.

Figure 4.18 shows the root mean square errors (RMSE) across the scale (i.e., Scales 0 to 4). The figure uses the SNOTEL SWE observations as the reference data in computing RMSE without perturbation of SNODAS data. The assimilated SWE results at all scales show a large improvement in RMSE. In addition, the RMSE decreases as the resolution becomes finer, reflecting that there is a spatial averaging effect, which was also observed in the spatial distribution of SWE in Figure 4.13. Spatial averaging alters the mean value of each grid cell at a scale by aggregating values at a smaller scale to a larger target scale. However, the RMSE values by the posterior SWE at all assimilation scales are much smaller than that of the prior SWE. This result informs us that the uncertainty due to the forcing data is larger than that of the spatial averaging effect, considering that the model physics plays a relatively small role in our uncertainty experiment. In some cases, SNOTEL may not represent the mean value of the corresponding model grid cell. However, their correlation was reported to be high in areas with persistent snow cover [64].

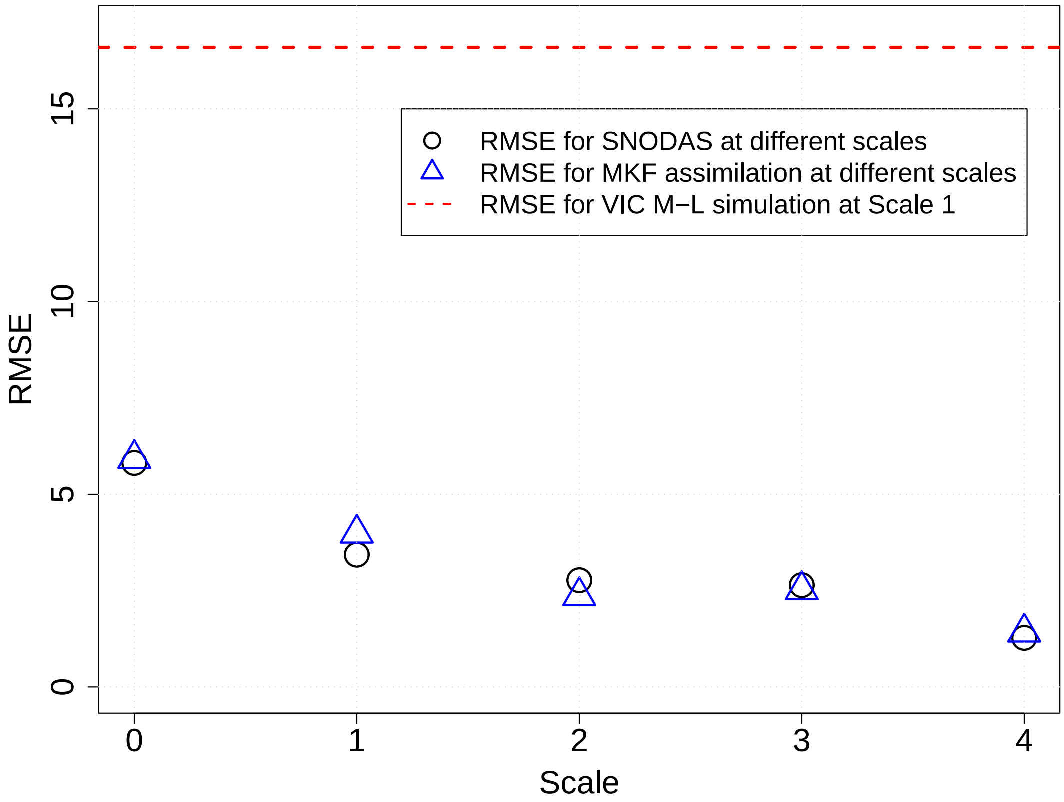

Figure 4.18: Root mean square error (RMSE) at different scales at the Ebbetts Pass SNOTEL station for water years 2004-2005

Figure 4.19 shows the average of ensemble RMSE for each scale. For each scale we calculated 50 RMSE's using the unperturbed assimilated SWE as the reference data instead of the SNOTEL observation. Then we took the average of the RMSE's to obtain the average ensemble RMSE for each scale. For Case I, only the SNODAS data at Scale 0 was perturbed using the posterior variances $P_{t+1|t+1}$ and $4P_{t+1|t+1}$. Therefore, the average RMSE decreases towards Scale 4 overall. On the contrary, for Case II, the average RMSE increases towards Scale 4 since the SNODAS SWE at Scale 4 was perturbed. This overall linear behavior in the average RMSE summarizes how the uncertainties in independent SWE data propagate through the multiscale linear process. However, we observe a different behavior in the average RMSE for Scale 1. For instance, under Case II the average RMSE shows increase for Scale 1 rather than decrease. This behavior seems to reflect the effect of model-simulated SWE at Scale 1. We did not perturb the model-simulated SWE by giving noise either to the forcing or the model parameters. But for Case I we see the largest average RMSE at Scale 1. This result suggests that at Scale 1 the assimilation is affected by the model simulation uncertainty as we have seen the difference between the snapshots at Scale 1 and Scale 4 from Figures 4.16 and 4.17 . The uncertainty from model simulation at Scale 1 is smoothed at Scale 4 while propagating through the scale nodes.

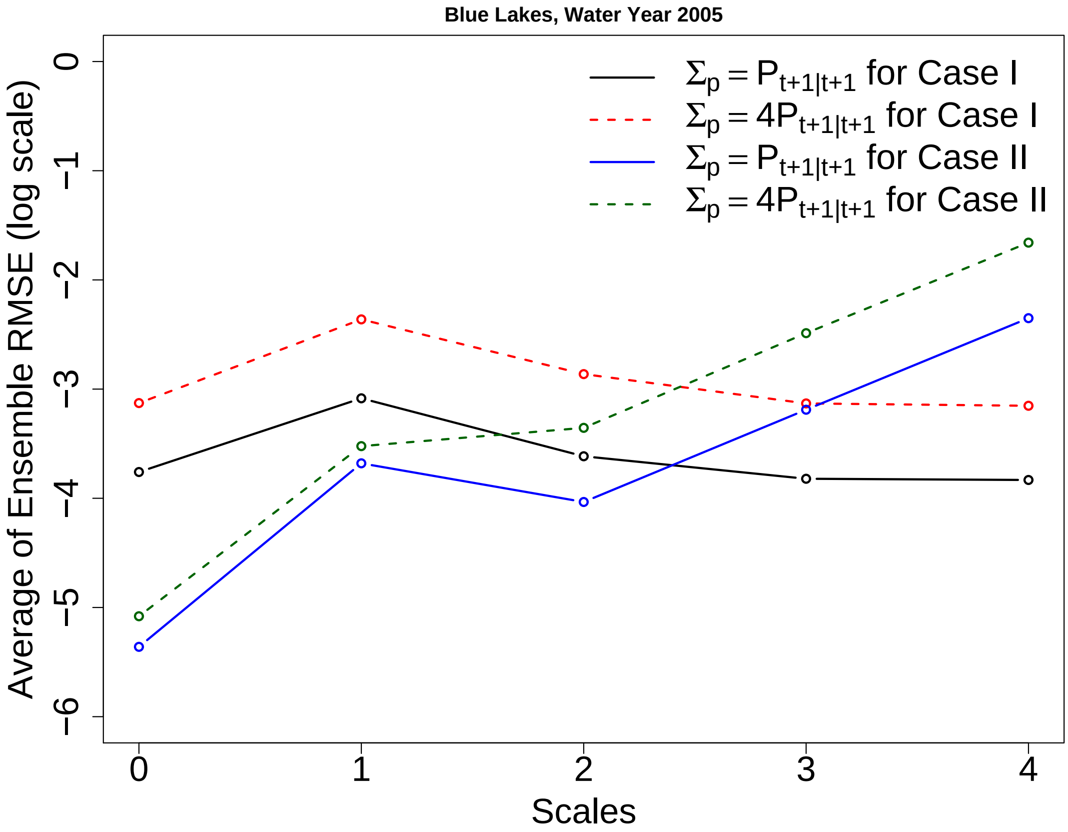

Figure 4.19: Average of ensemble RMSE for each scale at the Blue Lakes station for the 2005 water year.

4.5 Conclusion

High mountains are scale-sensitive areas where the spatial gradient of hydrologic variables is sharp. However, there is not much support for distributed snow modeling to consider such scale sensitivity due to sparse and error-prone forcing data. The presented data assimilation framework showed a new paradigm where a land surface model fully embeds an assimilation scheme for multiscale processes to address such issues in the alpine environment. The results show that the forcing data play a much bigger role in the uncertainty of SWE simulations than the scaling effect due to aggregation or the model physics. The assimilation scheme removes most of the uncertainty in the simulation of SWE. Without regard to scale, all assimilated results show similar states of SWE to the ground SNOTEL observations. Our ensemble-based experiment provides various angles to examine the scaling issue and the effect of observed data quality. In particular, the ensemble-based assimilation showed that the range of uncertainty increases when melting occurs. Also, the ensemble results showed that information from observations with close resolution to the model resolution affects the assimilation result with more sensitivity.

Chapter 5

Data Assimilation at Regional Scale

5.1 Introduction

This chapter extends the application of the multiscale process in Chapter 4 to a regional scale. We implemented a multiscale data assimilation experiment for a small area in the previous chapter to study uncertainties associated with snow processes. This chapter not only extends this work's spatial domain, but also investigates the impacts of a multiscale-based snow data assimilation framework on snow processes, energy budget, and streamflow simulations in the West Coast region. Hydrologic processes such as streamflow in the western United States are dominated by snow accumulation and ablation processes [4]. However, predictions of snow processes in the region are greatly affected by uncertainties associated with precipitation and temperature due to complex terrain and high altitudes. Proper forcing data at fine spatial scales are rarely available in mountainous regions. Consequently, the accuracy of streamflow simulations in mountainous regions is significantly deteriorated [17]. Mitchell et al. [18] showed that all the participating land surface models in NLDAS underestimate the mean annual runoff in the northern Rocky Mountains. This underestimation is primarily attributed to systematic precipitation biases [68]. Systematic precipitation biases result from complex terrain and gauge measurement errors, mainly due to wind-blowing [13]. But the question is how to remove the systematic uncertainty in streamflow simulations and related hydrologic processes maintaining key physical process information and computational complexity. This chapter focuses on answering this research question at the regional and watershed scales.

As discussed in the previous chapters, local adjustments of biased forcing data can be performed to improve simulation results. Alternatively, forcing data with fine resolutions that represent the spatial characteristics of the study domain can be used to improve simulation results. However, simulations at a large scale like this study are not easy to conduct due to lack of fine-scale forcing data, in particular for mountainous areas. Also, local scale forcing adjustments are only possible for small scale studies due to local data availability. Therefore, we take a data assimilation approach in which SWE observations are directly assimilated into the snow model based on the methodology in the previous chapter. The multiscale process used in this dissertation can be expanded to assimilate observed forcing data when they are available. This extended capability will be the subject of future research following this dissertation study.

As an extension of the study in Chapter 4, the same methodology is used except the size of the domain under study. However, this chapter is more interested in learning the impacts of data assimilation at regional and subregional scales. The impacts of data assimilation are studied for SWE, snow covered area, energy fluxes, and streamflow both temporally and spatially. SWE data from SNODAS and AMSR-E are used at fine and coarse scales, respectively, in the data assimilation process. Results indicate that the assimilation reduces large low biases in simulating SWE and improves the spatial distribution of SWE in mountainous areas, which contributes to more accurate estimates of early summer streamflow in both timing and magnitude.

5.2 Data and Methods

5.2.1 Study domain

The study domain at the regional scale includes Washington, Oregon, California, and part of Nevada. Within this region, a subregional scale study is also conducted. This subregion has fourteen SNOTEL stations, and is used to evaluate the impact of multiscale data assimilation. The study domain in the West Coast is shown in Table 5.1. Figure 5.1 shows a spatial map that defines the spatial domain. The entire study domain has been divided into 128 subregional units, and the multiscale process is conducted for each assimilation unit independently. Figure 5.2 shows an elevation map for the entire spatial study domain. This map was generated from NLDAS mean elevation data with a resolution of 1/8th degree.

Table 5.1: Study domain for data assimilation in the West Coast region (in degrees)

North boundary	49.0
South boundary	33.0
East boundary	-116.625
West boundary	-124.625

For in-depth study of the impact of data assimilation, a subregion has been selected at the assimilation unit scale. Unit 85 is used for this purpose, and most of this unit is covered with snow during the winter season. This subregion has fourteen SNOTEL stations as shown in Figure 5.3. We have selected two watersheds for streamflow simulations. Figure 5.4 and Figure 5.5 show the basin boundaries and streamflow and SWE gages for the Upper Merced River Basin with drainage area 321 square miles and the East Fork Carson River Basin with drainage area 356 square miles, respectively.

5.2.2 Data

We use hourly meteorological forcing data from NLDAS. This dataset includes precipitation, temperature, wind speed, and other secondary forcing such as downward solar radiation and pressure. For observation data with fine and coarse resolutions, the same sources as in

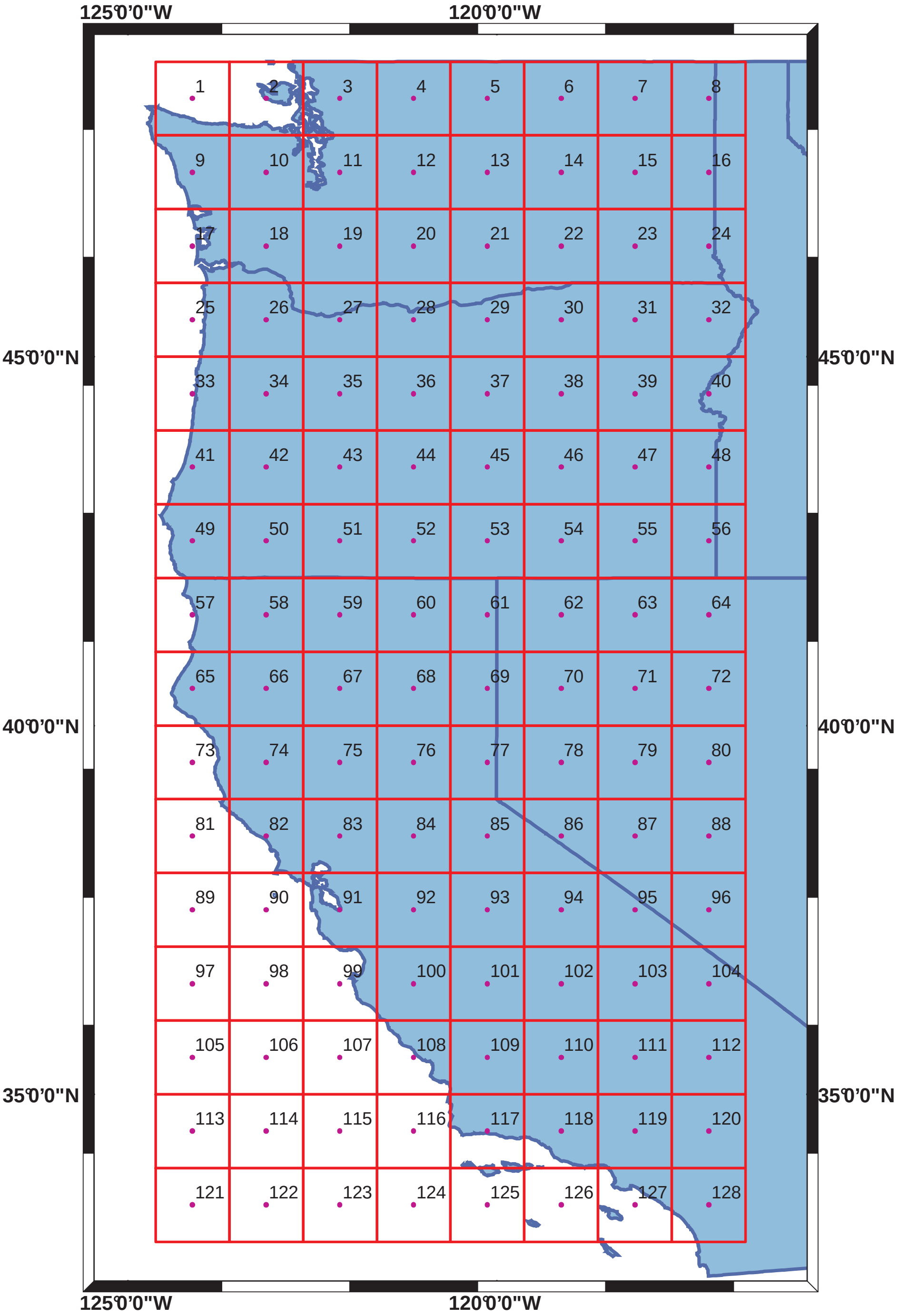

Figure 5.1: Study domain for multiscale data assimilation in the western US and 128 assimilation units. The number for each unit indicates assimilation unit number for identification.

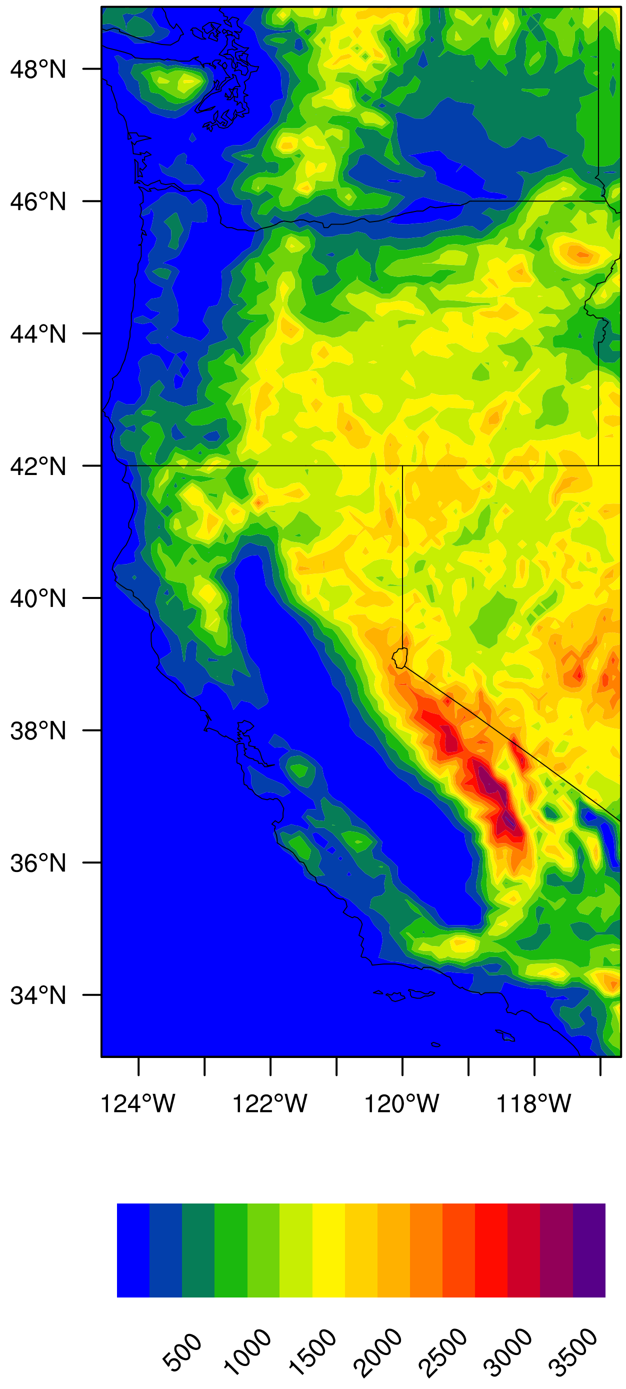

Figure 5.2: Elevation (m) in the study domain

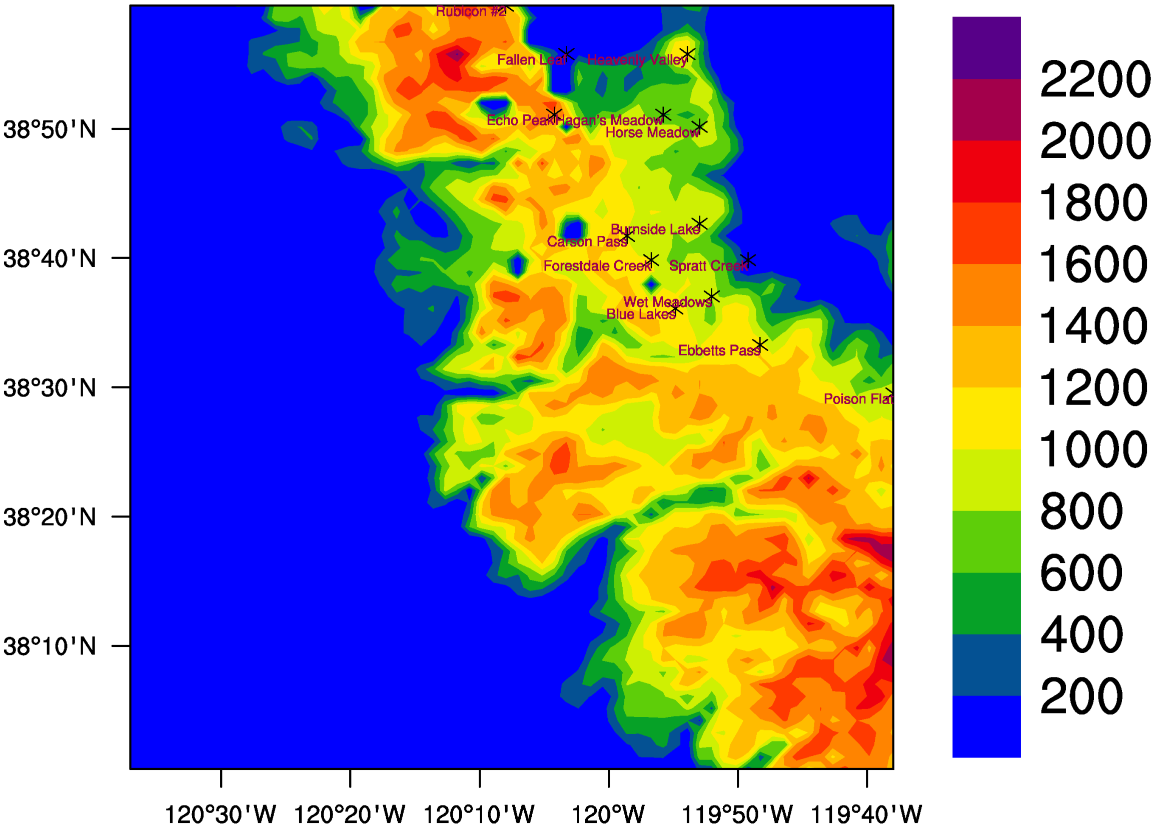

Figure 5.3: A subregional study area with fourteen SNOTEL stations in the Sierra Nevada. The background image represents SNODAS data for April 15, 2005.

Chapter 4 are used. For the fine resolution data, the SNODAS product from NOHRSC is used [63]. SNODAS SWE data are archived at 1 km resolution and aggregated into 1/64th degree as in Chapter 4. For the coarse resolution, the AMSR-E daily SWE product [65], which is provided in 25 km resolution, is used. Due to the known problems such as the saturation effect [66] and the results we have seen in Chapter 4, AMSR-E SWE data are used only during the early snow season, October through December.

To study the impacts of data assimilation, this chapter compares snow covered area (SCA) from data assimilation with that of the Moderate Resolution Imaging Spectroradiometer (MODIS) remote sensing product. MODIS has higher spatial and spectral resolution, and thus has a better ability to detect cloud and snow under vegetation canopies compared to products from the Geostationary Orbiting Environmental Satellite (GOES) [69]. The dataset used in this study is MOD10A1, which is a daily gridded snow cover data product at a resolution of 500 m. To fit with the scaling shown in Table 5.2, the 500 m product was regridded into 1/64th degree according to the method described in Appendix D.

5.2.3 Assimilation Scales

The design of assimilation scaling depends on the scales of available data and model output and the domain size to be assimilated. In Chapter 4 only four different scales were used. In this

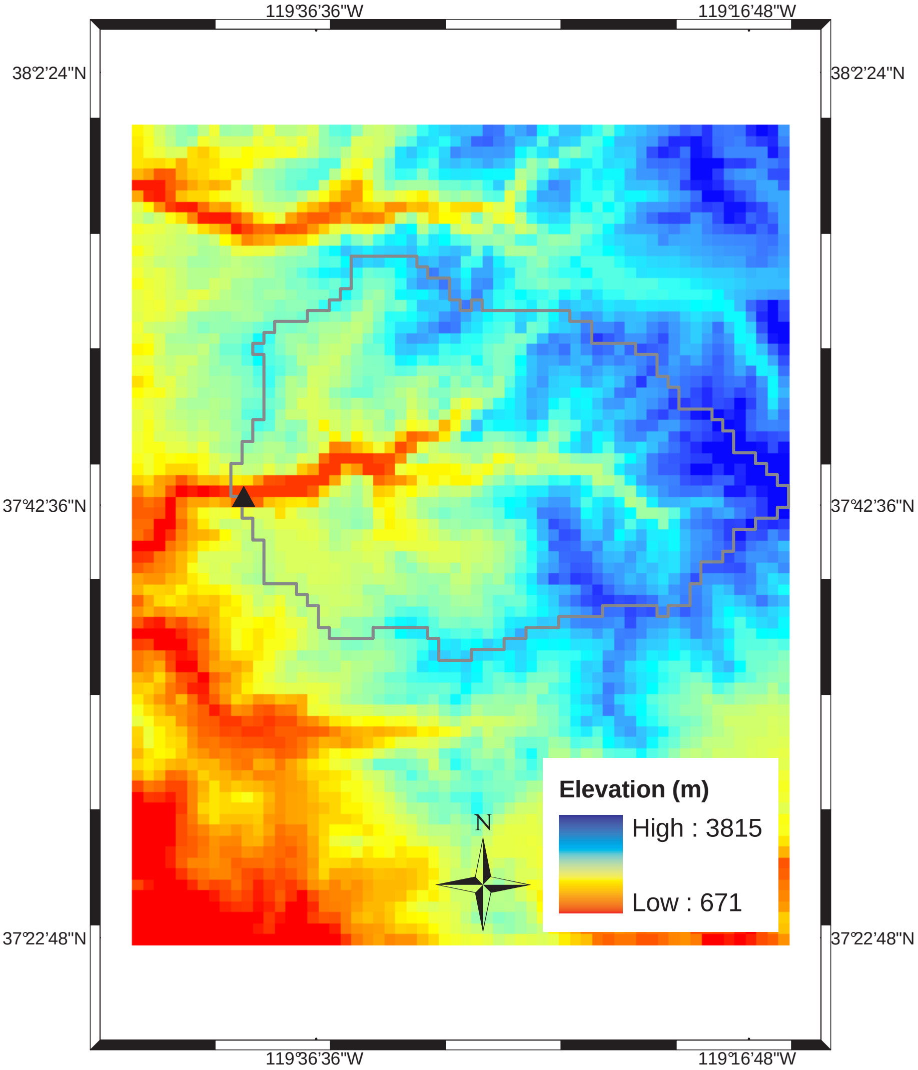

Figure 5.4: Upper Merced River Basin boundary. The triangle indicates USGS streamflow station at the Pohono Bridge.

regional study, the spatial domain is so large that it needs to be divided into appropriate units. The assimilation scheme is very efficient, and it can be coupled with the VIC LSM seamlessly. But for a large area like this study domain, the input and output processes of data limit the size of unit. For this reason, we use a unit size of 1 degree × 1 degree, which produces 128 assimilation units for the entire domain. High performance computing resources can be used to provide favorable unit size configurations at a range of scales. Table 5.2 shows the appropriate configuration of scales for the 1 degree × 1 degree assimilation unit.

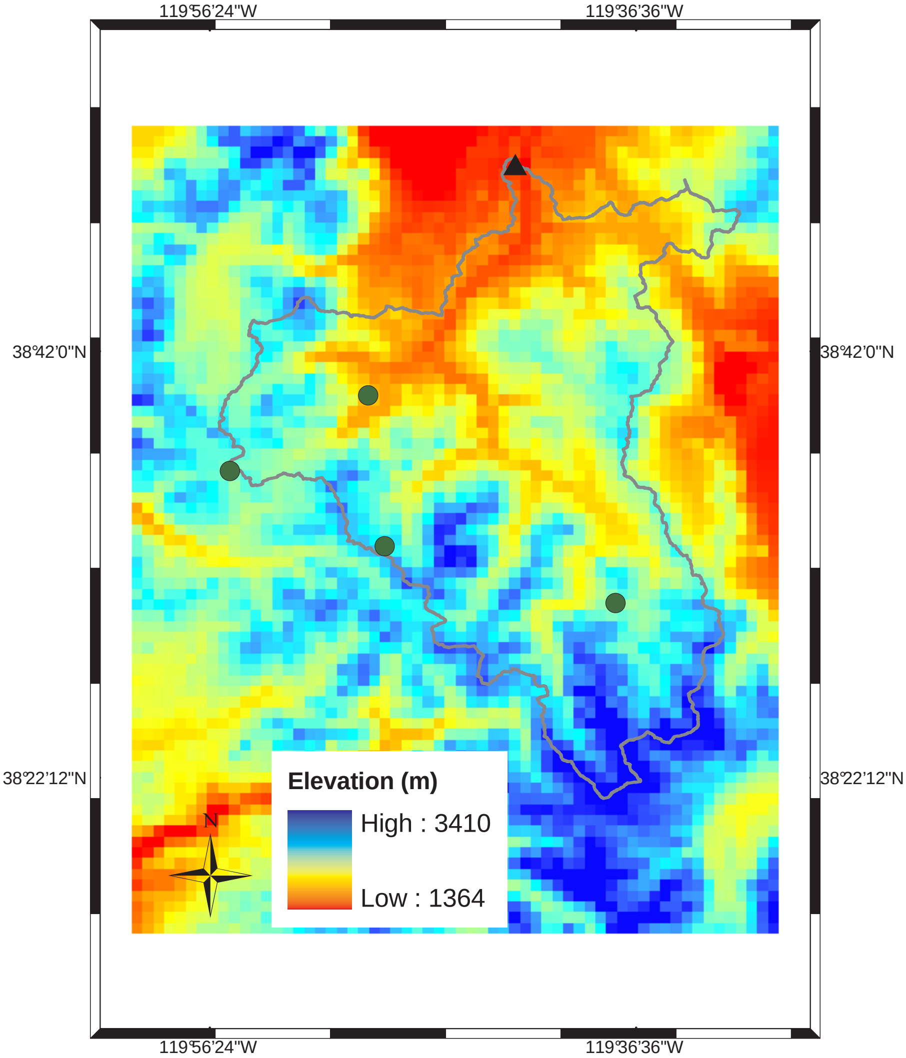

Figure 5.5: East Fork Carson River Basin boundary. The triangle indicates USGS streamflow station near Gardnerville. The circles represent SNOTEL stations.

Table 5.2: Assimilation scales.

Scale	Resolution (degrees)	Cell size
0	1	1 x 1
1	1/2	2 x 2
2	1/4	4 x 4
3	1/8	8 x 8
4	1/16	16 x 16
5	1/32	32 x 32
6	1/64	64 x 64

5.3 Results

5.3.1 Spatial Distribution of Snow Variables

5.3.1.1 Regional scales

This subsection presents spatial distributions of SWE based on the multiscale data assimilation. Spatial distributions of SWE at a large spatial domain show how the multiscale process affects the snow variable in magnitude and spatial extent. In the West Coast region, the spatial distribution of SWE closely follows the altitudinal gradient. Figures 5.6 and 5.7 show the spatial distributions of SWE at different scales over the study domain for April 1, 2005 and April 1, 2006, respectively. These results are produced using the SNODAS product only, as results with both SNODAS and AMSR-E products will be discussed later. The posterior distribution at both Scales 3 and 6 shows more snow-covered area as well as more accumulation of SWE. Based on the results in Chapter 4, we presume that this posterior distribution represents the SWE state of the study domain. The verification of this presumption will be provided later in this chapter. Figures 5.8 and 5.9 show the spatial distribution of SWE for April 1, 2007 and April 1, 2008, respectively. These spatial distributions for the water years 2007 and 2008 show the state of drought in the West Coast region, in particular the Sierra Nevada. They show contraction both in magnitude of SWE accumulation and in snow covered area, presenting the ability of the multiscale assimilation scheme to capture interannual variability affected by regional climate conditions.

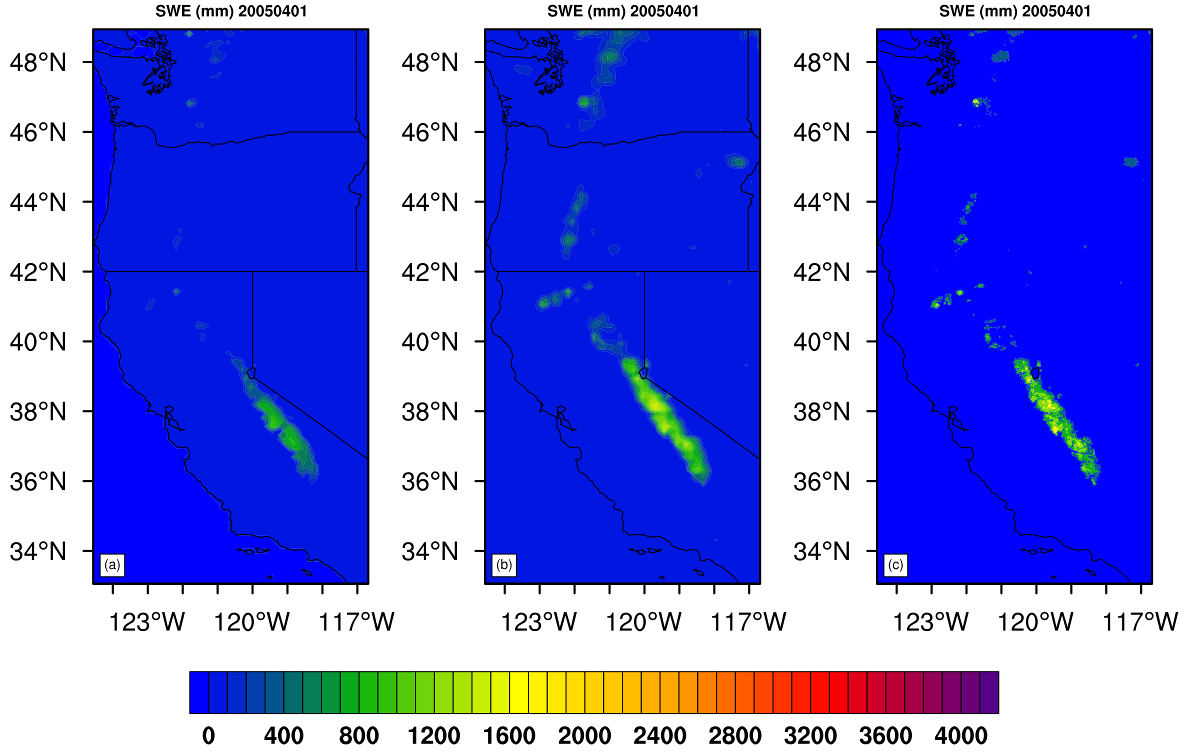

Figure 5.6: Spatial distribution of prior SWE at Scale 3 (a), posterior SWE at Scale 3 (b), and posterior SWE at Scale 6 (c) on April 1, 2005.

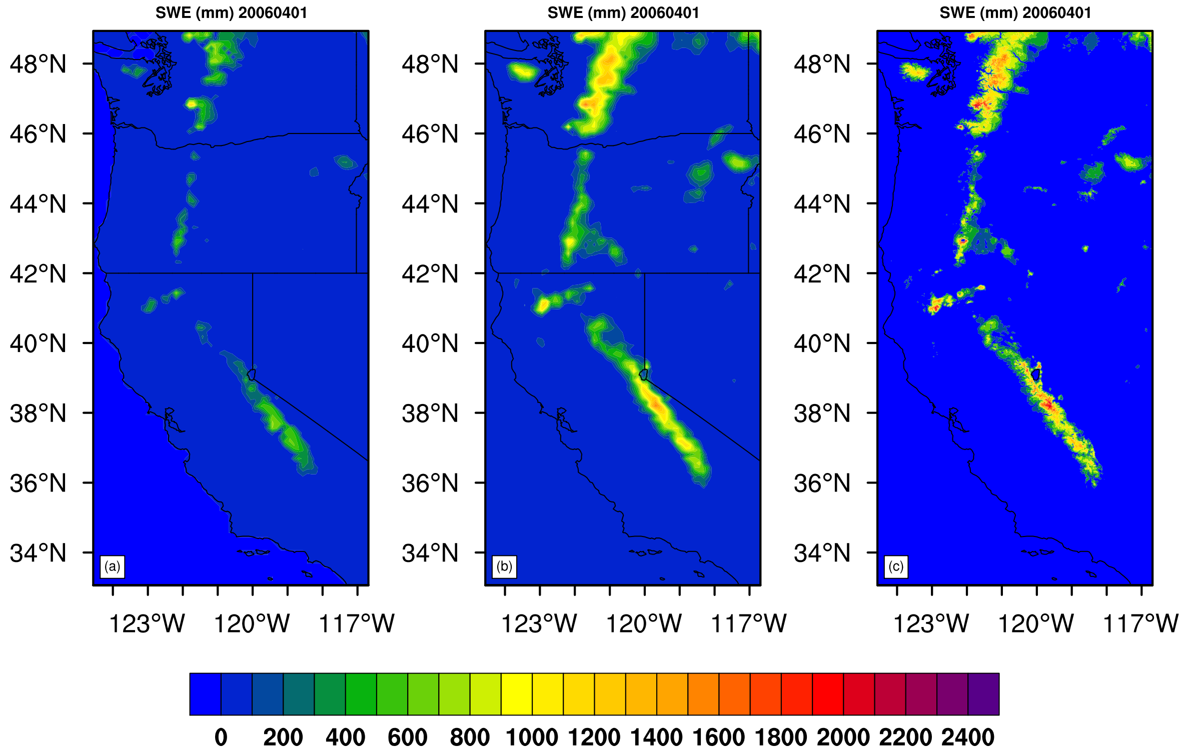

Figure 5.7: Spatial distribution of prior SWE at Scale 3 (a), posterior SWE at Scale 3 (b), and posterior SWE at Scale 6 (c) on April 1, 2006.

As in Chapter 4, the SWE product from AMSR-E has also been used for a coarse resolution, which is 1/4th degree or Scale 2. Because of measurement quality problems in forests and deep snowpacks, AMSR-E SWE data are used only at the beginning of the snow season. An example of AMSR-E SWE map is shown in Figure 5.10. It captures the overall spatial distribution of snow over the study domain, but shows low biases, in particular on high elevations. For comparison with posterior SWE values, see Figures 5.11 and 5.12 where posterior SWE maps are shown for assimilation cases with and without the AMSR-E SWE product. Note that for the case without the AMSR-E product we use only the SNODAS product for assimilation. When AMSR-E data are used, SWE values on high mountains tend to be reduced due to the low bias of AMSR-E SWE. On the other hand, assimilation with AMSR-E SWE predicts more snow for some parts at low elevations. For example, as shown in Figure 5.11 assimilation with AMSR-E SWE shows more snow accumulation in the eastern part of Oregon where the elevation ranges from 1000 m to 1500 m. Even though we have seen some noisy behaviors when assimilated with AMSR-E data in Chapter 4, this result reveals that there is the possibility that assimilation with AMSR-E data performs better than the case with only SNODAS assimilation for low-lying regions.

5.3.1.2 Sub-regional scales

This subsection views the assimilation results at a subregional scale, which is assimilation unit 85. This assimilation unit has fourteen SNOTEL stations (see Figure 5.3). The elevation of the snow-covered area in this assimilation unit ranges from 1600 m to over 2600 m. Figures 5.14, 5.15, 5.16, and 5.17 show the spatial distribution of SWE over assimilation unit 85 on

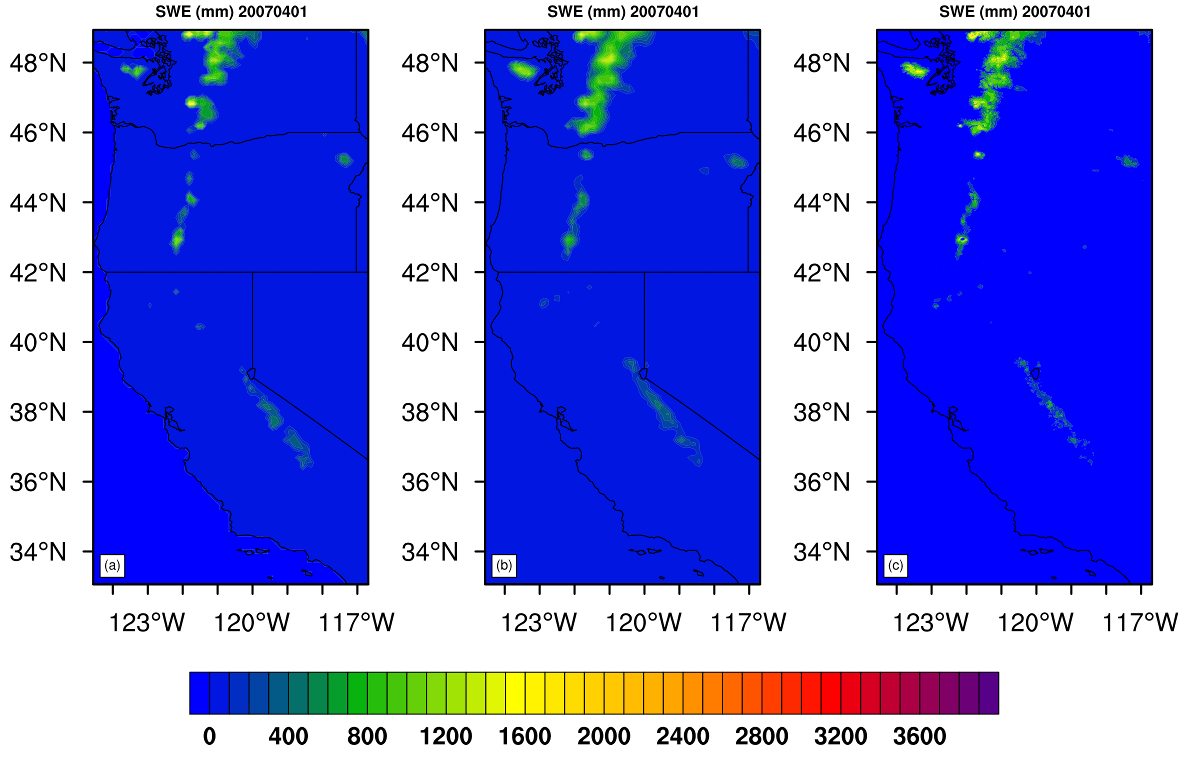

Figure 5.8: Spatial distribution of prior SWE at Scale 3 (a), posterior SWE at Scale 3 (b), and posterior SWE at Scale 6 (c) on April 1, 2007

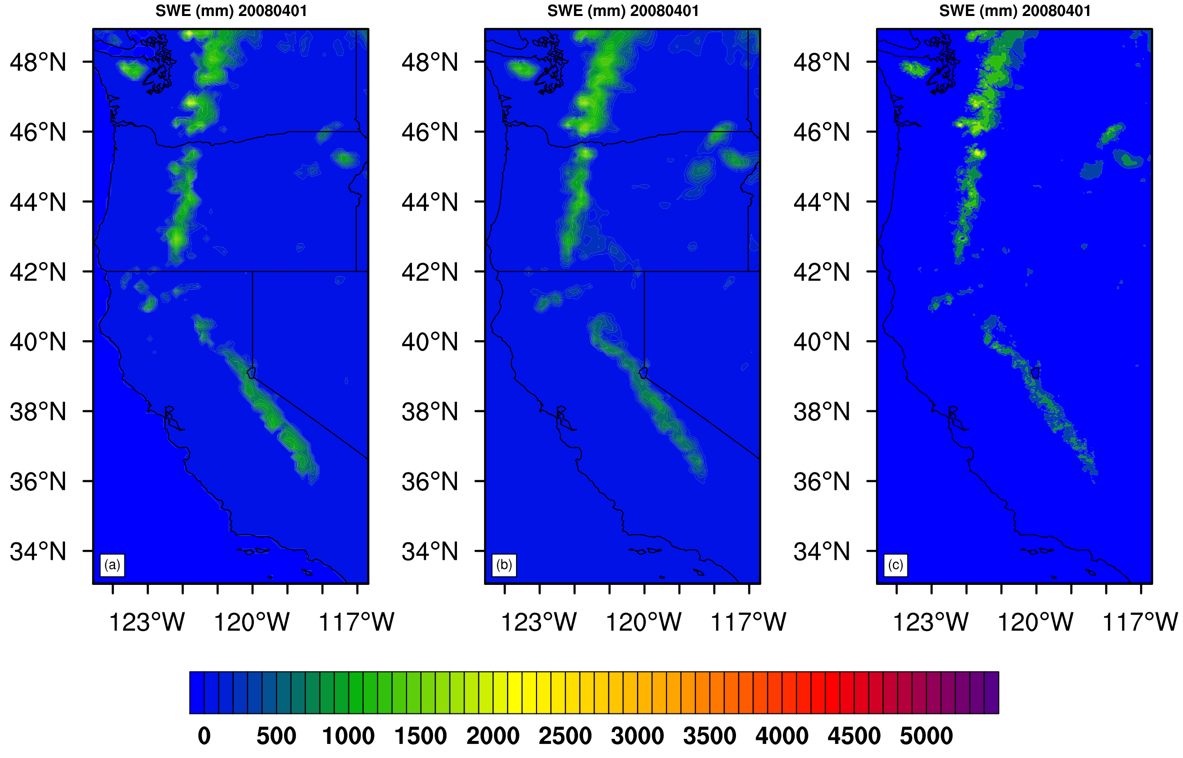

Figure 5.9: Spatial distribution of prior SWE at Scale 3 (a), posterior SWE at Scale 3 (b), and posterior SWE at Scale 6 (c) on April 1, 2008

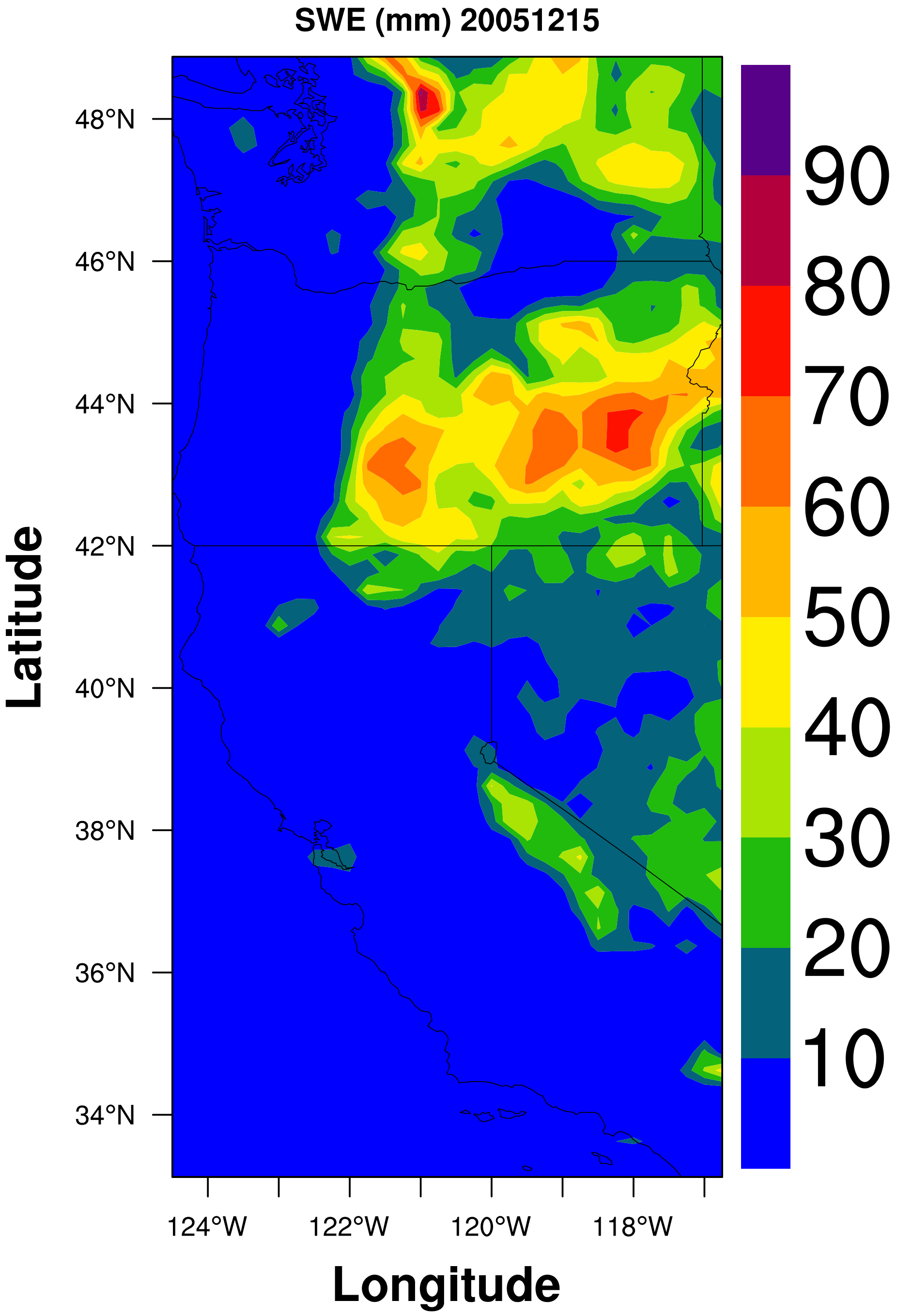

Figure 5.10: An example map of SWE from the AMSR-E product on December 15, 2005.

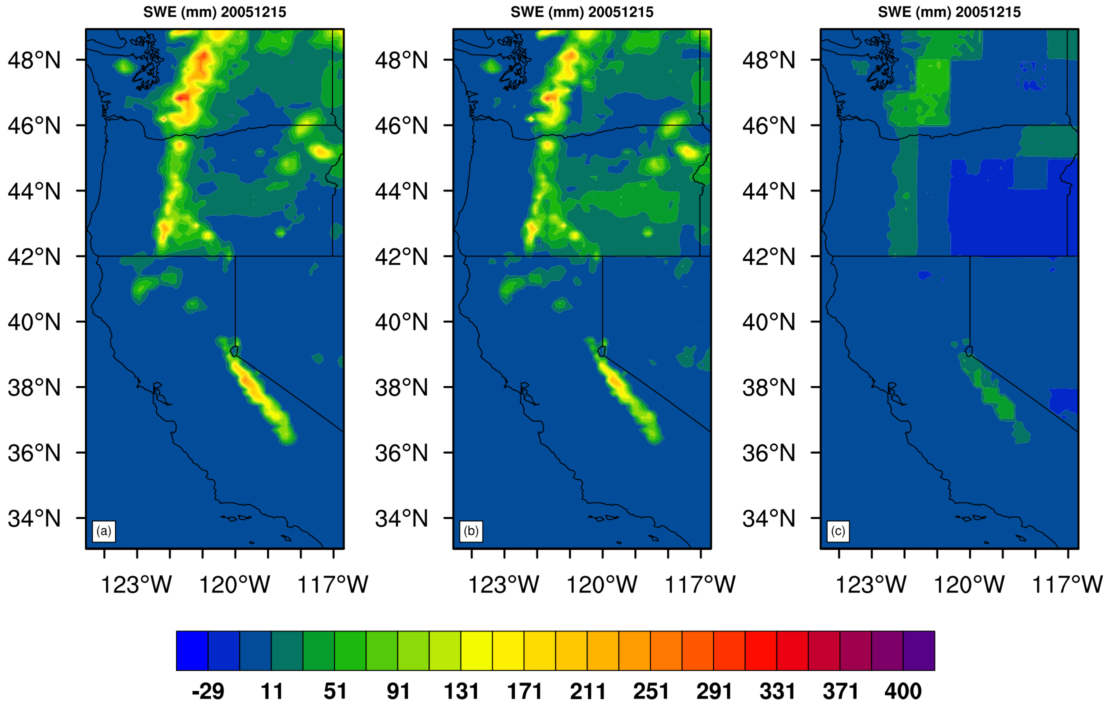

Figure 5.11: Comparison of posterior SWE between without AMSR-E data (a), with AMSR-E data (b), and the difference (c) for December 15, 2005.

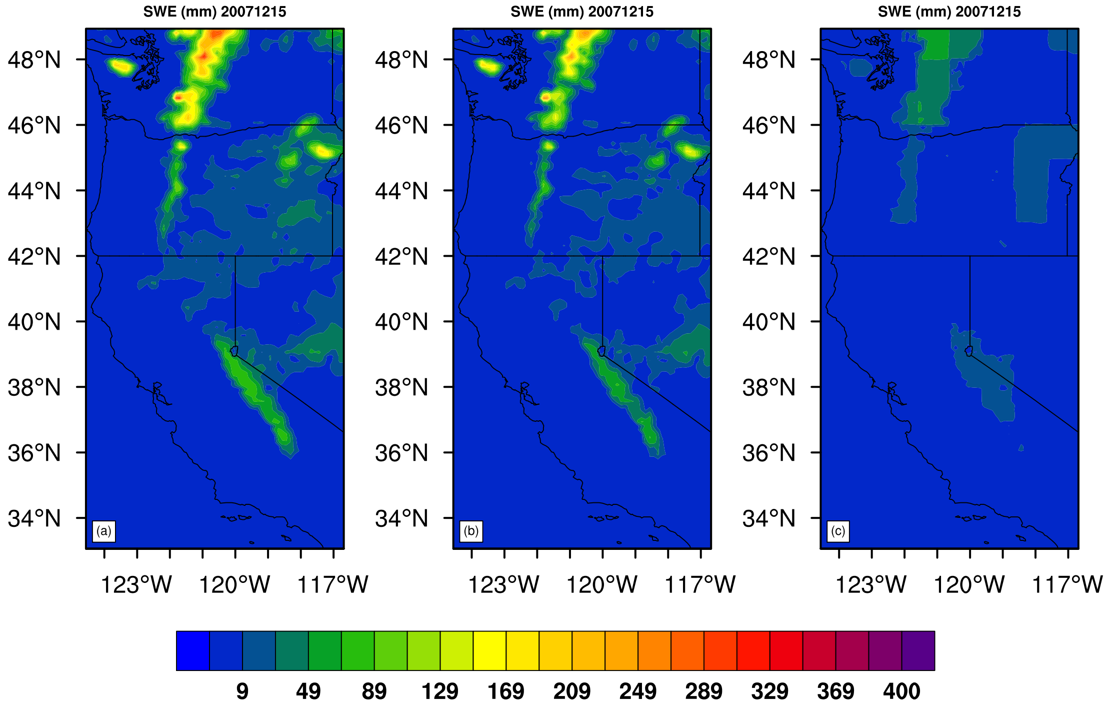

Figure 5.12: Comparison of posterior SWE between without AMSR-E data (a), with AMSR-E data (b), and the difference (c) for December 15, 2007.

April 15th of the water years 2005, 2006, 2007, and 2008, respectively. In this high mountain area, there is a large difference in magnitude and spatial distribution between the prior and posterior SWE values. This discordant spatial distribution is large for the water years 2005, 2006, and 2007. However, for the 2008 water year, prior SWE shows more accumulation than posterior SWE at Scale 3 (see Figure 5.17). This difference results from using the version 2 product from NLDAS for the 2008 simulation. This new product shows some improvements for precipitation data. The improved behavior of the new NLDAS product is shown in the temporal evolution of SWE (e.g., see Figure 5.23). This result supports our consistent argument that the forcing, particularly precipitation, is a dominant factor in the simulation of snow variables in high mountains.

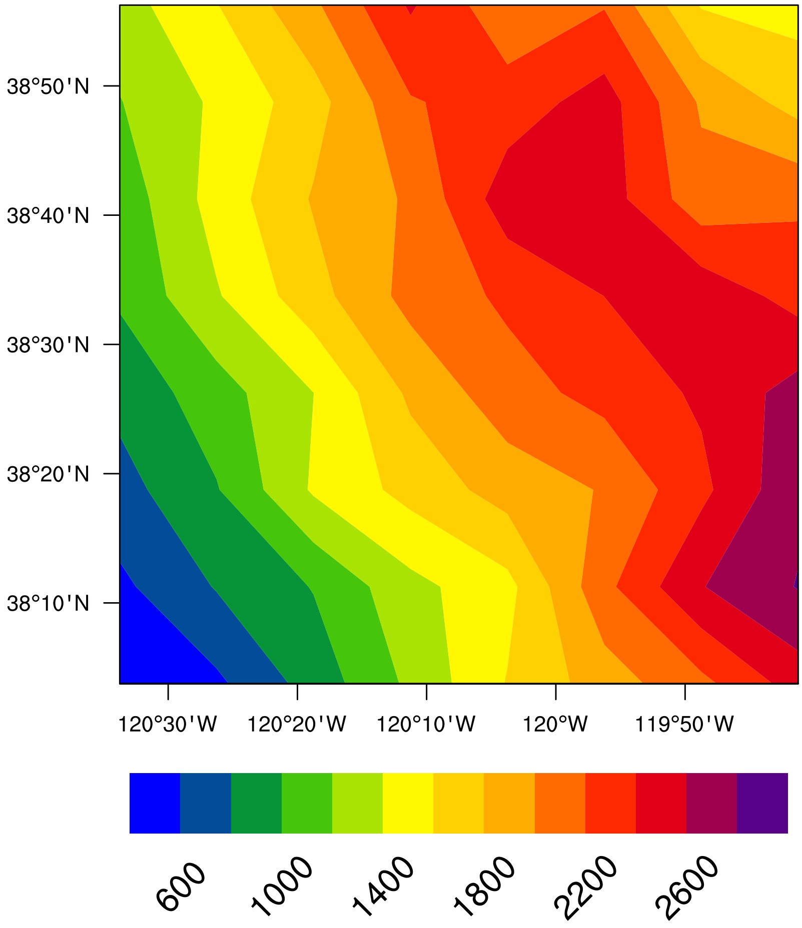

Figure 5.13: Elevation (m) of assimilation unit 85.

To evaluate the results of the assimilation scheme, we use the MODIS snow covered area (SCA) product. Figures 5.18, 5.19, 5.20, and 5.21 show comparisons between the posterior SWE at Scale 6 and MODIS SCA. All these figures compare output for around April 15 where the accumulation in this subregion is known to be the highest (see the time series plots later). Because the MODIS SCA was regridded into 1/64th degree, it is also at Scale 6 for pixel to pixel comparison. The numbers in the parentheses indicate the matching rate in percentage between the two methods. The matching rate was calculated using a threshold of 20 % SCA in fraction. Thus, if a pixel is covered with snow by 20 % or more in fraction and the corresponding posterior SWE pixel has snow, it is classified as 1. Otherwise it is classified as 0, which means

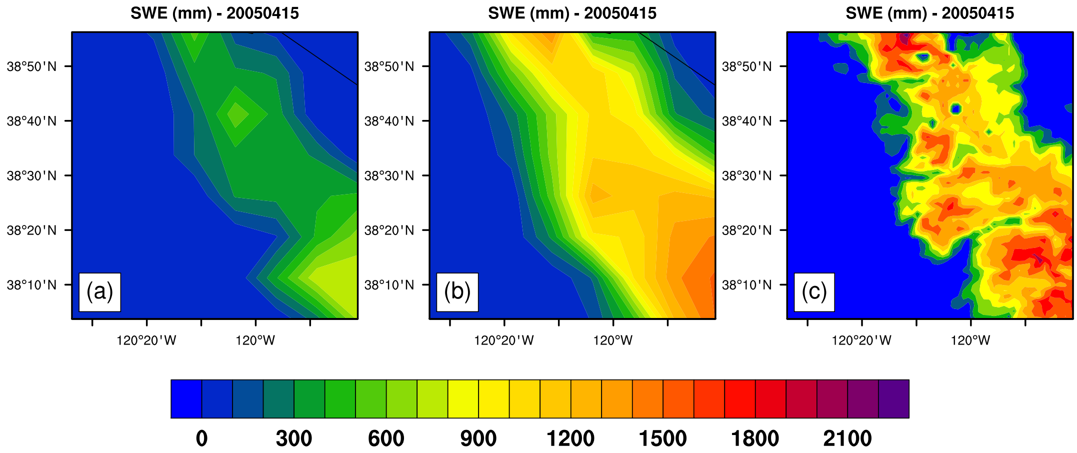

Figure 5.14: Spatial distribution of prior SWE at Scale 3 (a), posterior SWE at Scale 3 (b), and posterior at Scale 6 (c) in the Sierra Nevada where 14 SNOTEL stations are located.

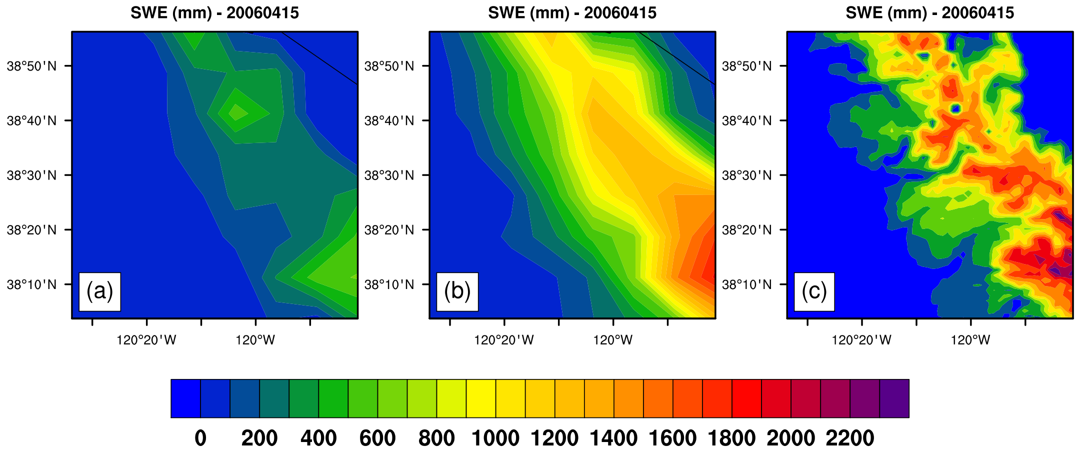

Figure 5.15: Spatial distribution of prior SWE at Scale 3 (a), posterior SWE at Scale 3 (b), and posterior at Scale 6 (c) in the Sierra Nevada where 14 SNOTEL stations are located.

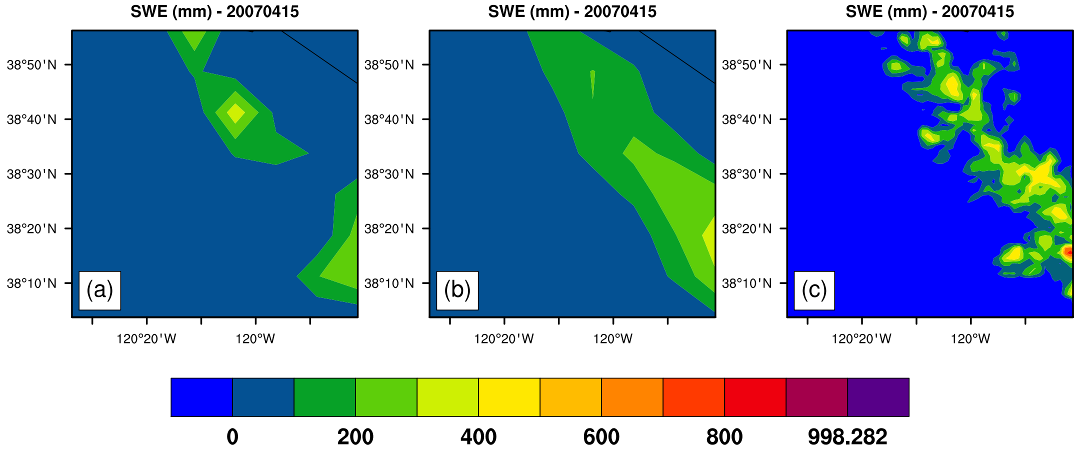

Figure 5.16: Spatial distribution of prior SWE at Scale 3 (a), posterior SWE at Scale 3 (b), and posterior at Scale 6 (c) in the Sierra Nevada where 14 SNOTEL stations are located.

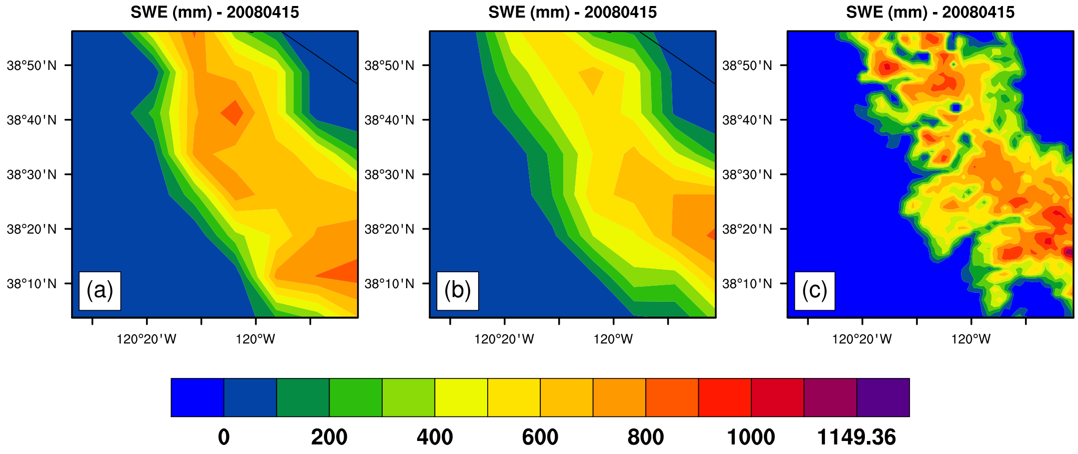

Figure 5.17: Spatial distribution of prior SWE at Scale 3 (a), posterior SWE at Scale 3 (b), and posterior at Scale 6 (c) in the Sierra Nevada where 14 SNOTEL stations are located

they do not match. Overall, the posterior SWE at Scale 6 is well matched to the MODIS SCA. The matching rate is high in places where elevations are high and snow accumulation is also high. Edge areas are not matched well between the two datasets. In addition, the two datasets agree well during the snow accumulation period while during the melting period the matching rate is not high (figures are not shown). As we have seen in the figures for comparison between prior and posterior spatial distribution, the MODIS data also show a large contraction of SCA during the dry water year of 2007. For the 2008 water year, SWE accumulation has been reduced compared to the 2005 and 2006 water years, but SCA has not contracted by as much as the 2007 water year. This phenomenon is shown from both assimilated results and MODIS observations. Figure 5.22 shows the matching rate in time series for the snow season of the 2006 water year. This figure shows results only from days without clouds blocking MODIS measurements. As shown in the figure, the matching rate is low during the melting period.

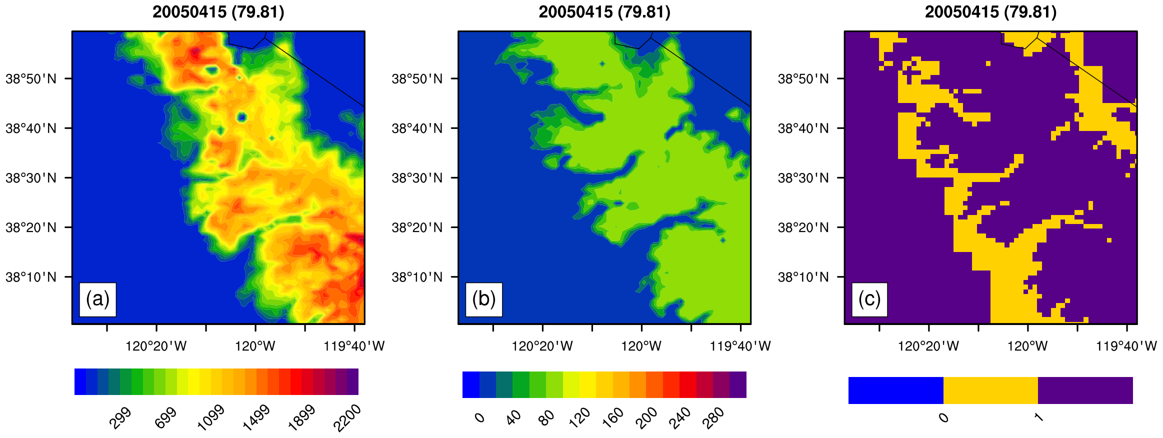

Figure 5.18: Comparison of snow covered area: posterior SWE at Scale 6 (a), MODIS SCA at Scale 6 (b), and matching map (c).

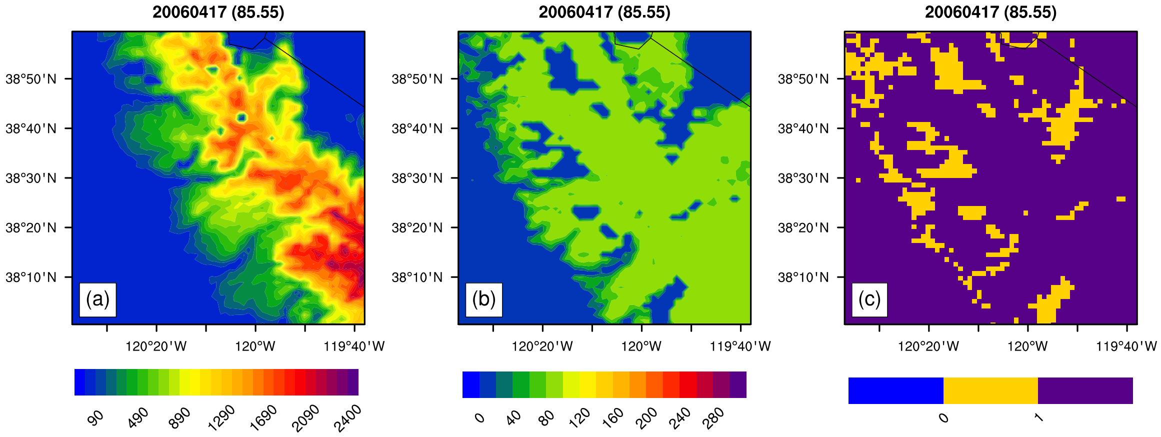

Figure 5.19: Comparison of snow covered area: posterior SWE at Scale 6 (a), MODIS SCA at Scale 6 (b), and matching map (c).

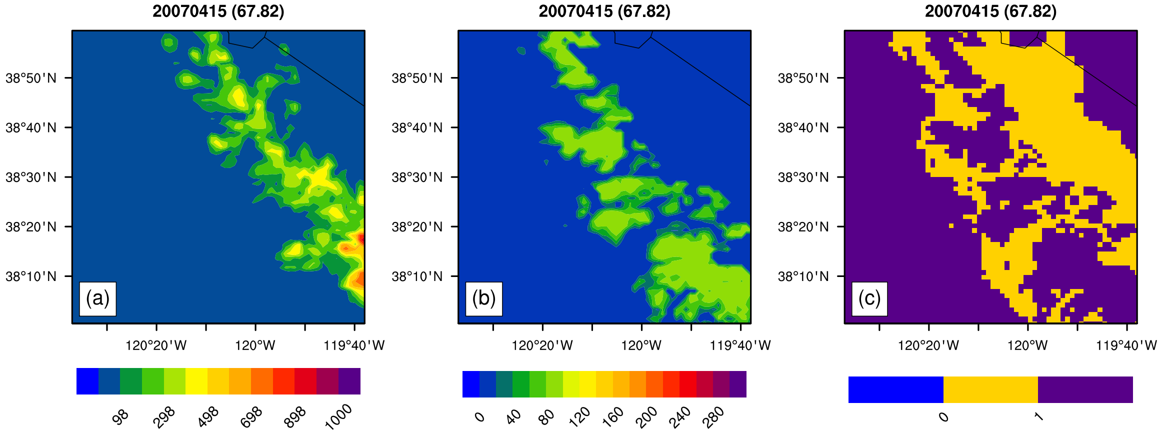

Figure 5.20: Comparison of snow covered area: posterior SWE at Scale 6 (a), MODIS SCA at Scale 6 (b), and matching map (c).

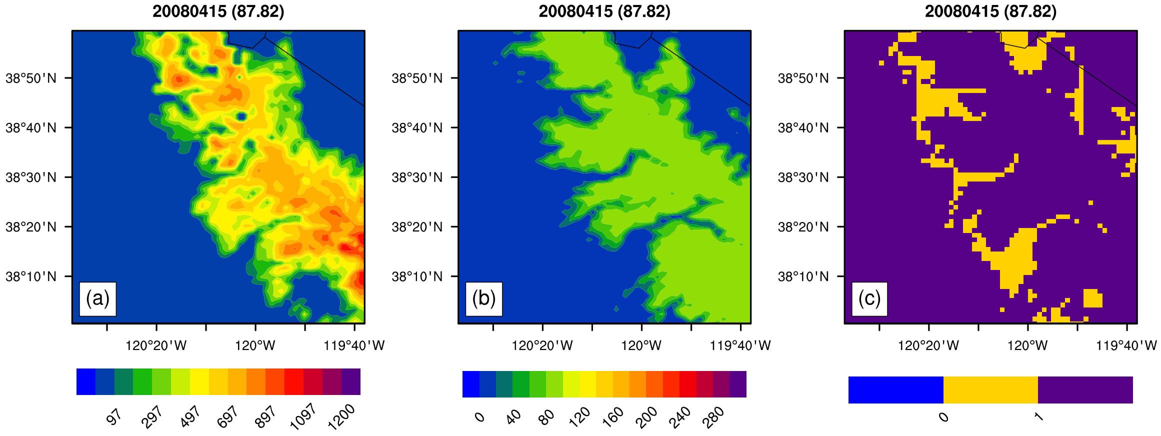

Figure 5.21: Comparison of snow covered area: posterior SWE at Scale 6 (a), MODIS SCA at Scale 6 (b), and matching map (c).

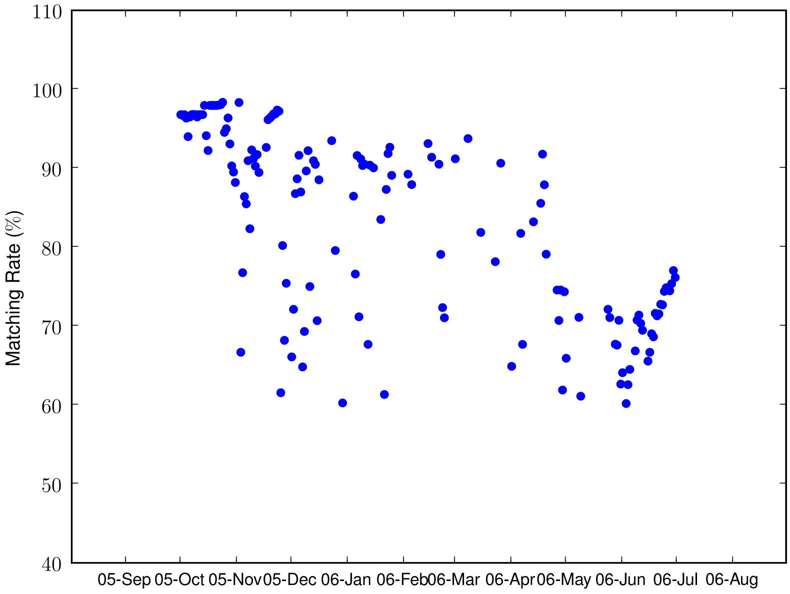

Figure 5.22: Matching rate between the MODIS-derived SCA and posterior SWE at Scale 6.

5.3.2 Temporal Evolution of SWE

It is often hard to analyze simulation results over a large area. In particular, when the study is done in mountain environments where observations are limited, it is necessary to investigate a subregion of the study domain. In this subsection, temporal evolution of SWE based on the multiscale process is presented in assimilation unit 85 as in the spatial study. We use observed SWE data from the SNOTEL stations belonging to the subregion (i.e., unit 85) shown in Figure 5.3. This one unit is composed of 64 grid cells of 1/8th degree. Table 5.3 show grouping of the SNOTEL stations in the subregion, and this information is used to interpret the results of the temporal evolution of SWE.

The assimilation results show promise in comparison with the SNOTEL observations overall. The posterior SWE values at Scale 3 for the corresponding grid cells to the Ebbetts Pass and Blue Lakes station match the ground observations well as shown in Figures 5.23 and 5.27, respectively. These results are similar to those we have seen in Chapter 4 for these stations. Note that in Chapter 4 we used only 4 grid cells of 1/8th degree while here we use 64 grid cells of the same resolution. This comparison implies that the multiscale process presented in this dissertation shows some independence from the number of scales used. In Chapter 4, we used four different scales whereas we use seven different scales as shown in Table 5.2.

The first feature of the assimilation results is that the multiscale process removes most of the low bias in the mountainous area. In particular, for the 2005 - 2006 water years, prior SWE shows large underestimates, and these values are recovered in posterior SWE. For the 2007 water year, underestimation by the prior simulation is much less than that of the previous two years. This result reveals that when accumulation of snow is small due to drought the uncertainty also decreases. This phenomenon is consistently shown in all ten stations presented in these figures.

Table 5.3: Group of SNOTEL stations in the subregional domain by elevation. Only ten stations are shown.

Station Name	Elevation (ft)	Group
Ebbetts Pass	8700	A
Horse Meadow	8557	A
Carson Pass	8353	A
Burnside Lake	8139	A
Blue Lakes	8000	A
Echo Peak	7800	B
Poison Flat	7736	B
Rubicon #2	7500	B
Fallen Leaf	6300	C
Spratt Creek	6200	C

Even though the overall performance of the multiscale process scheme is encouraging, there are some differences in performance depending on the location. The comparison between stations at high elevations and their corresponding model grid cells show better results than those at low elevations. That is, comparison at stations marked as Group A in Table 5.3 present better results among the groups. At the stations belonging to Group B the multiscale process scheme also produces good results. However, there is overestimation at the Poison Flat station belonging to Group B. This overestimation is attributed to overestimates from the SNODAS product. In Figure 5.33, we included the aggregated values of posterior SWE into Scale 3, supporting our analysis that the SNODAS product at Scale 6 is overestimated. This aggregated value for each day in the time series is the average of 64 grid cells at 1/64th degree, which are equivalent to one 1/8th grid cell. The aggregation into Scale 3 shows similar results to the posterior SWE at Scale 3. This overestimation result implies that the quality of data at the fine scale greatly affects posterior results at a coarse scale.

The stations at low elevations are located at the edge of snow dominated areas. Therefore, the gradient of snow state variables at the edge with altitude is relatively large while high mountain sites have deep snowpack with less gradients. For example, as shown in Figure 5.14, the fringe area has a larger gradient of SWE over elevation. This result also implies that SNOTEL stations at this fringe area may not well represent the areal mean value of a corresponding grid cell. The Fallen Leaf (Figure 5.31) and Spratt Creek (Figure 5.32) stations are located at this fringe area (see Figure 5.3) whose elevation is relatively low. These stations show poor comparison results relative to the stations in high elevations. As shown in Figure 5.33, overestimates from SNODAS add difficulty in this type of point to grid cell comparison.

5.3.3 Impacts on Energy Fluxes

This section investigates the impact of snow data assimilation on energy fluxes over the study domain. Sensible heat and latent heat fluxes are studied for this purpose. When snow cover exists, the surface albedo changes rapidly, reducing the surface temperature. This reduced temperature causes the outgoing longwave radiation to be smaller, leading to less sensible heat flux from the snow surface. Therefore, the existence of snow cover on the ground surface directly

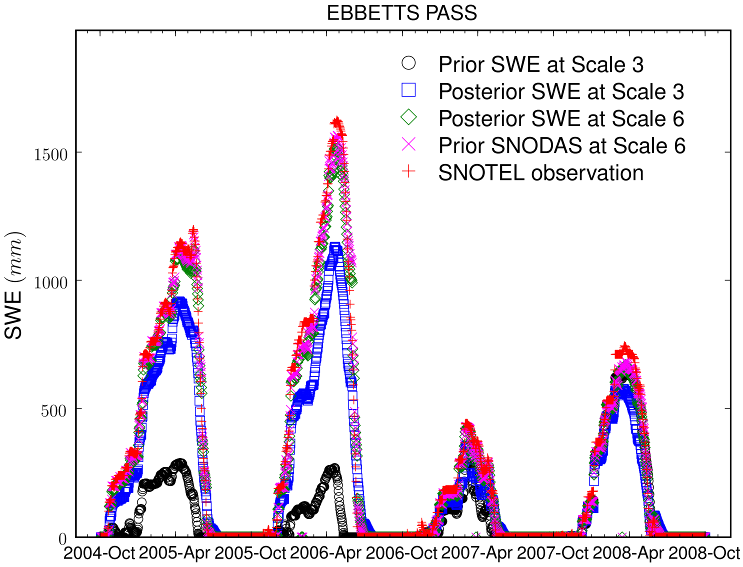

Figure 5.23: Temporal evolution of prior and posterior SWE at the Ebbetts Pass station.

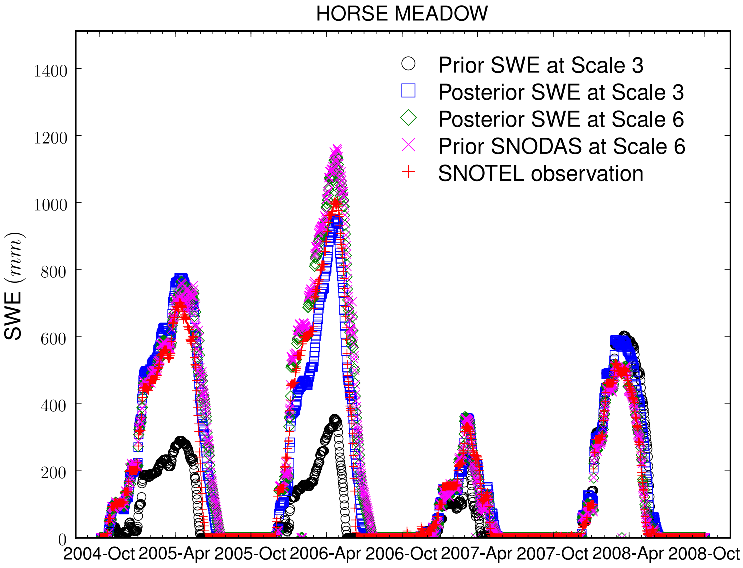

Figure 5.24: Temporal evolution of prior and posterior SWE at the Horse Meadow station.

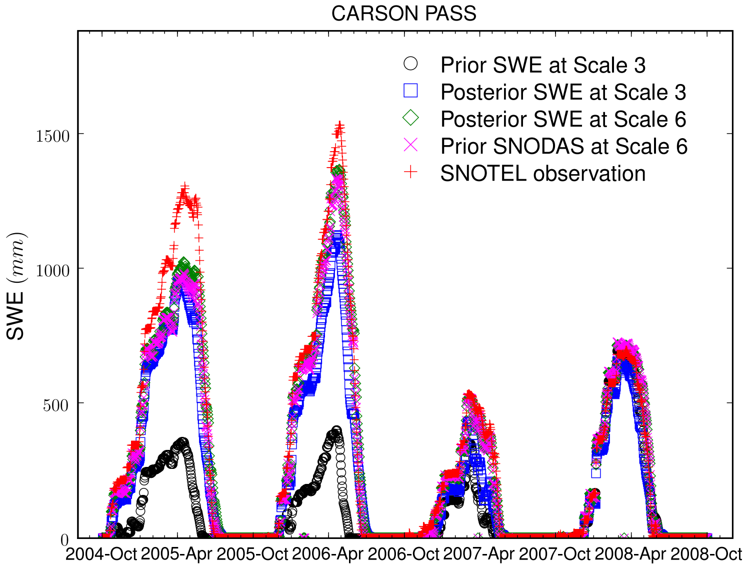

Figure 5.25: Temporal evolution of prior and posterior SWE at the Carson Pass station.

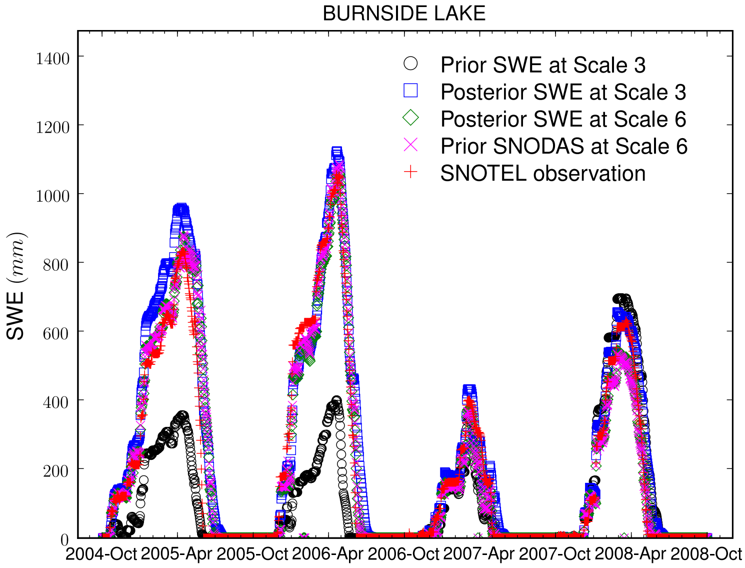

Figure 5.26: Temporal evolution of prior and posterior SWE at the Burnside Lakes station.

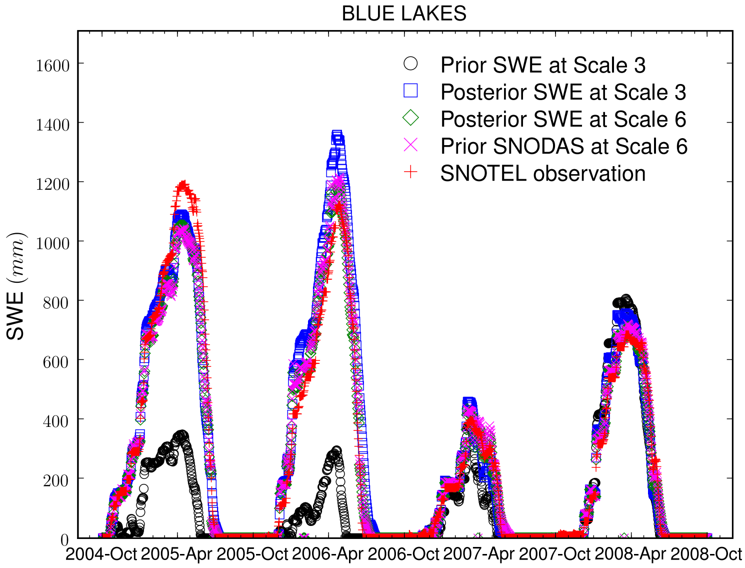

Figure 5.27: Temporal evolution of prior and posterior SWE at the Blue Lakes station.

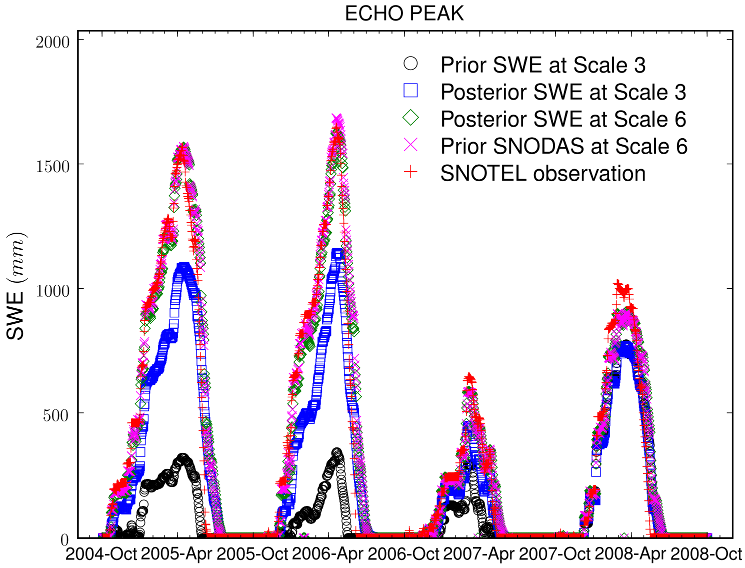

Figure 5.28: Temporal evolution of prior and posterior SWE at the Echo Peak station.

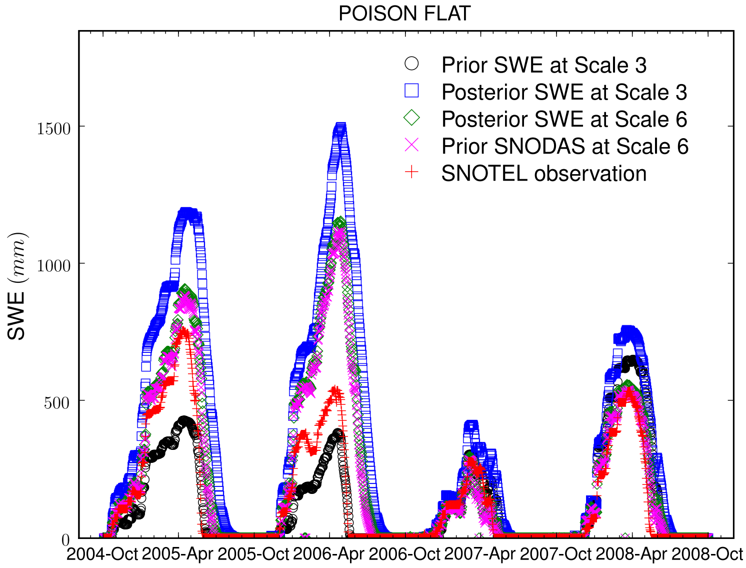

Figure 5.29: Temporal evolution of prior and posterior SWE at the Poison Flat station.

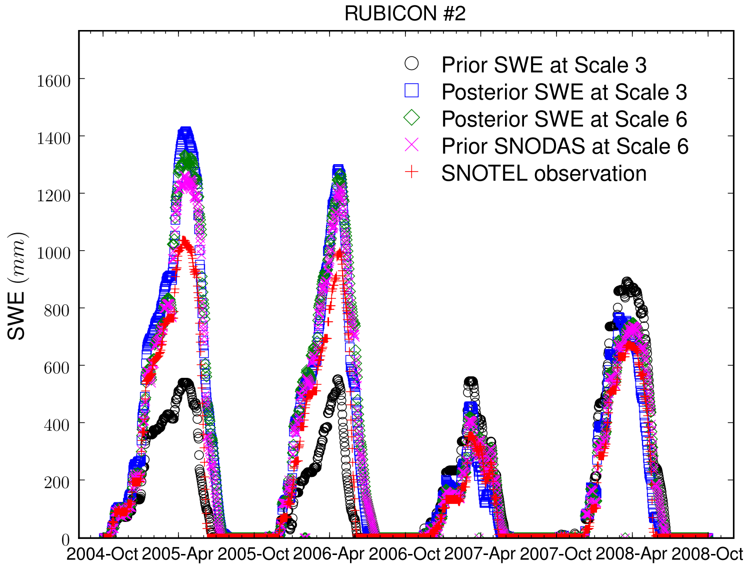

Figure 5.30: Temporal evolution of prior and posterior SWE at the Rubicon #2 station.

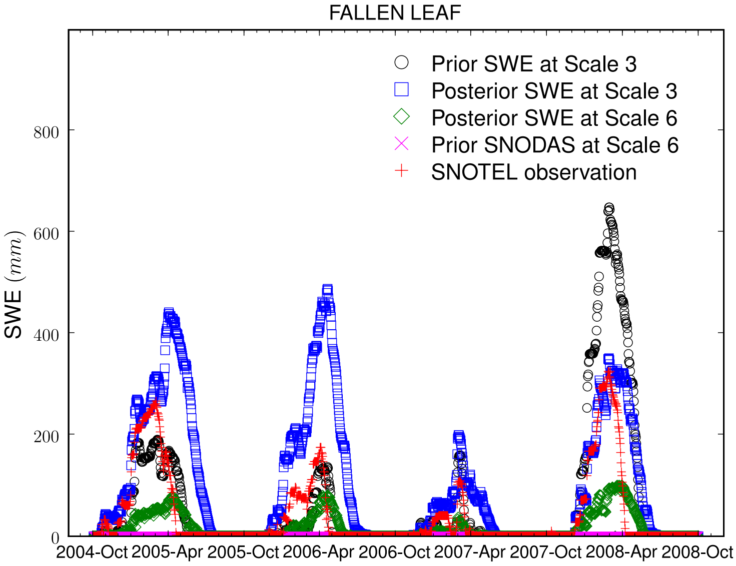

Figure 5.31: Temporal evolution of prior and posterior SWE at the Fallen Leaf station.

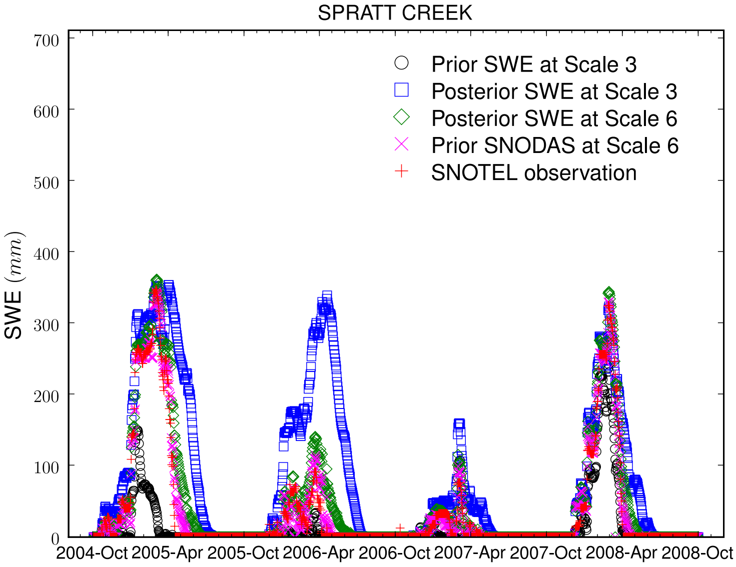

Figure 5.32: Temporal evolution of prior and posterior SWE at the Spratt Creek station.

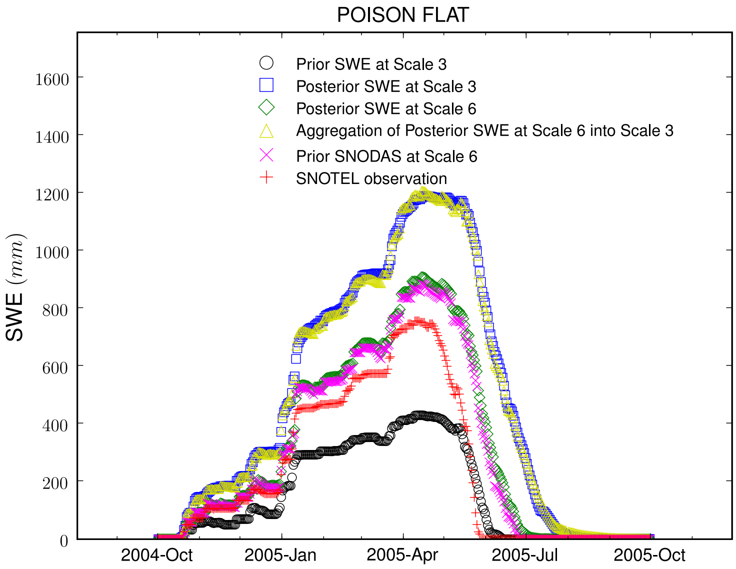

Figure 5.33: Temporal evolution of prior and posterior SWE at the Spratt Creek station.

affects the turbulent heat fluxes. Our assimilation results show this general phenomenon during the cold season. Figure 5.34 shows the spatial distribution of sensible heat for April 15, 2005, when snow accumulation is high in the region while Figure 5.35 for June 15, 2005, which is one of the melting days. During the melting period, the sensible heat flux is higher than during the accumulation period as shown in the figures due to increased temperature. These figures also show the difference between posterior and prior simulations. The difference occurs mostly due to the snow-covered areas. This difference can easily be identified by comparing the sensible heat flux distribution with the SWE distribution in Figures 5.36 and 5.37. When melting occurs, the difference in sensible heat between prior and posterior simulations increases due to the difference in snow covered area between the prior and the posterior.

Latent heat flux distributions are shown in Figures 5.38 and 5.39. As in sensible heat flux, there is stronger latent heat flux during the melting season (i.e., June 15) than during the accumulation season. The strong latent heat flux occurs in most of the study domain except the high elevations in the Sierra Nevada where snow covered areas still remain. In California, the Central Valley region and the coastal region show high latent heat in April, because active evaporation is induced by stored soil moisture from winter storms. In particular, strong latent heat flux is shown at the foot of the Sierra Nevada due to early melting snow at low elevations. This strong latent heat at the foot of the Sierra Nevada is more apparent during the melting season in Figure 5.39. This figure also shows more latent heat flux in the eastern part of Oregon for which the posterior simulation shows more snow than the prior. Note that there is little difference in latent heat flux in the region along the coast between the posterior and the prior.

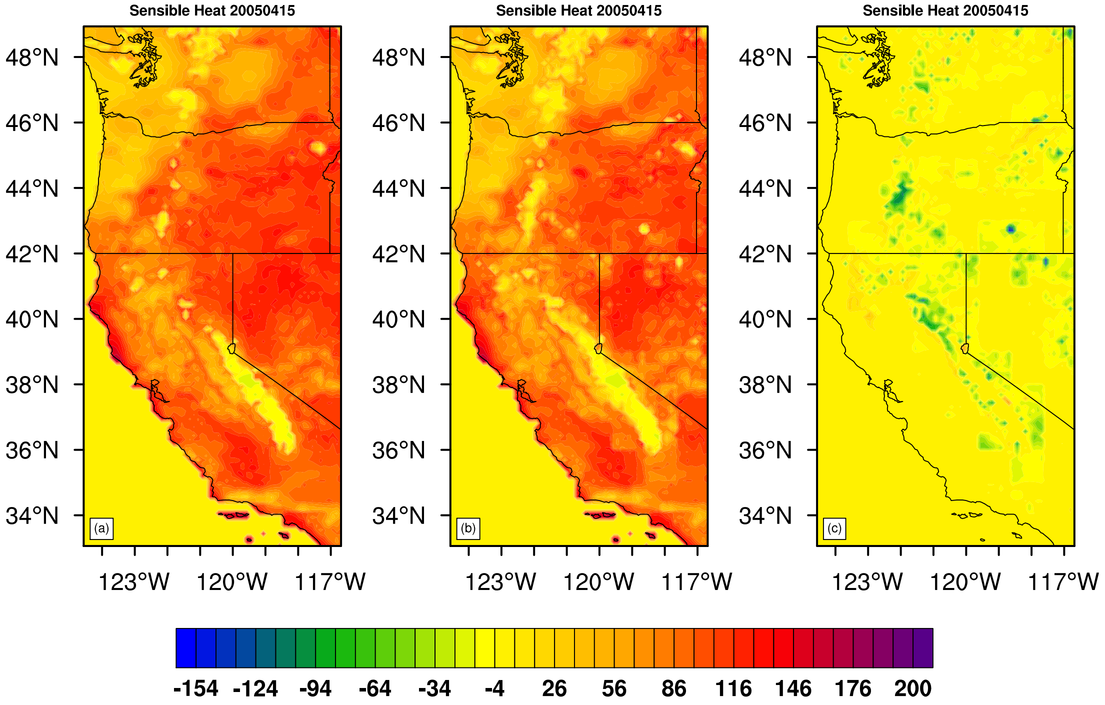

Figure 5.34: Comparison of daily average sensible heat flux (W/m^2) for April 15, 2005: prior at Scale 3 (a), posterior at Scale 3 (b), posterior minus prior (c).

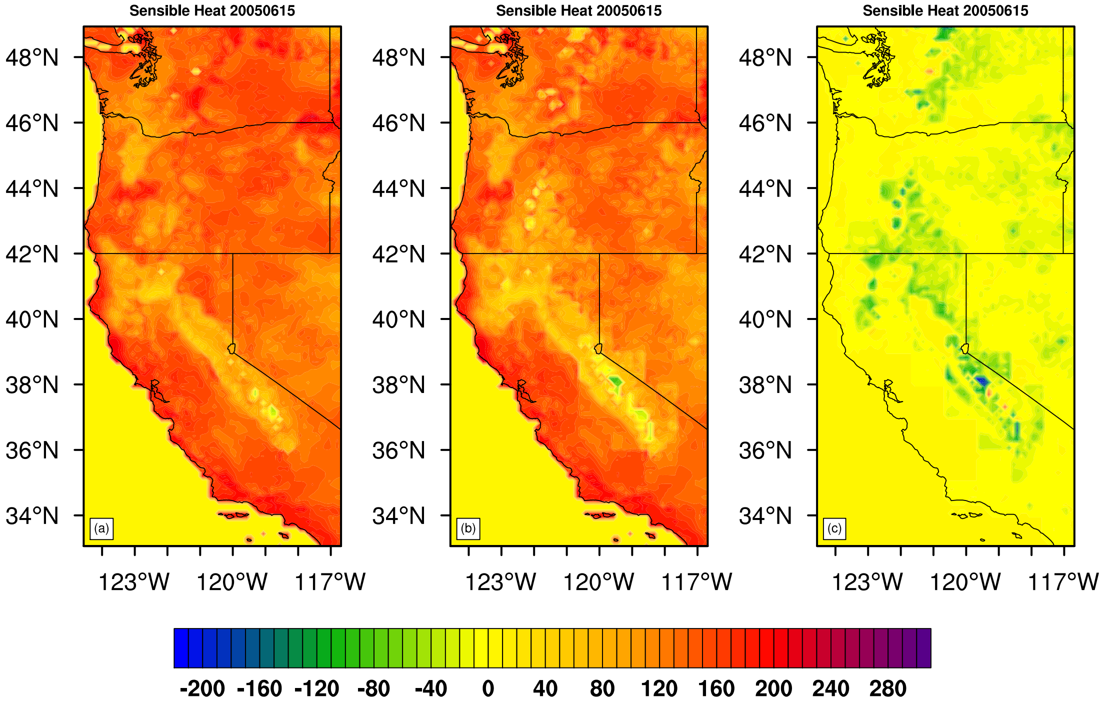

Figure 5.35: Comparison of daily average sensible heat flux (W/m^2) for June 15, 2005: prior at Scale 3 (a), posterior at Scale 3 (b), posterior minus prior (c).

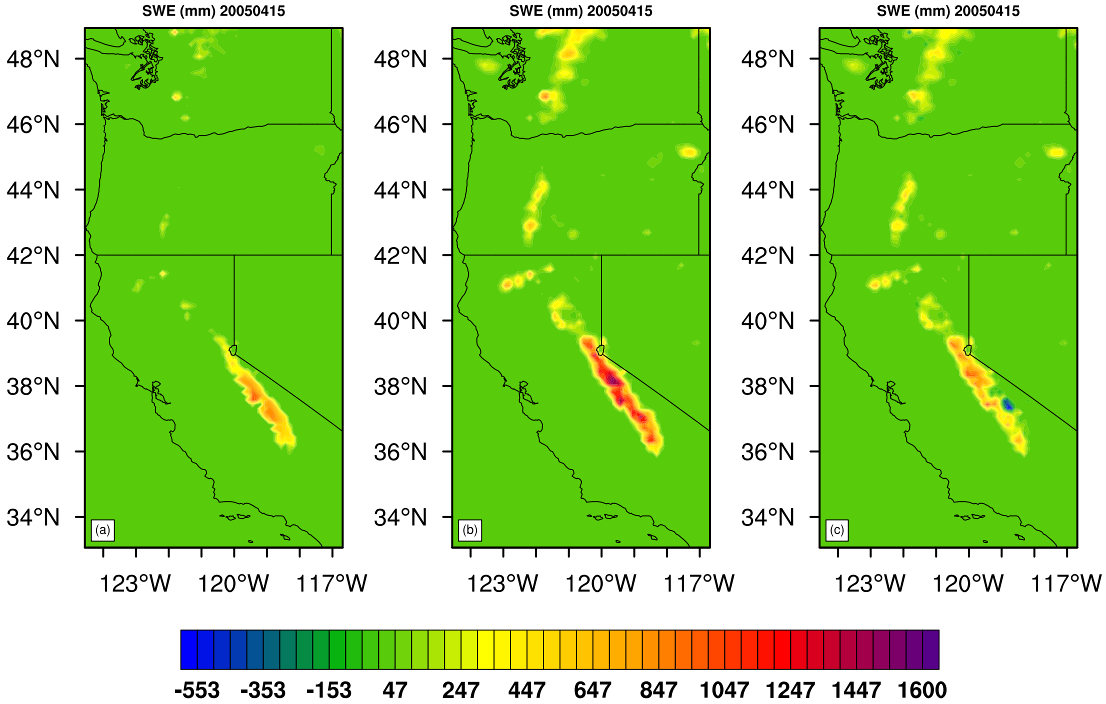

Figure 5.36: Comparison of daily average SWE (mm) for April 15, 2005: prior at Scale 3 (a), posterior at Scale 3 (b), posterior minus prior (c).

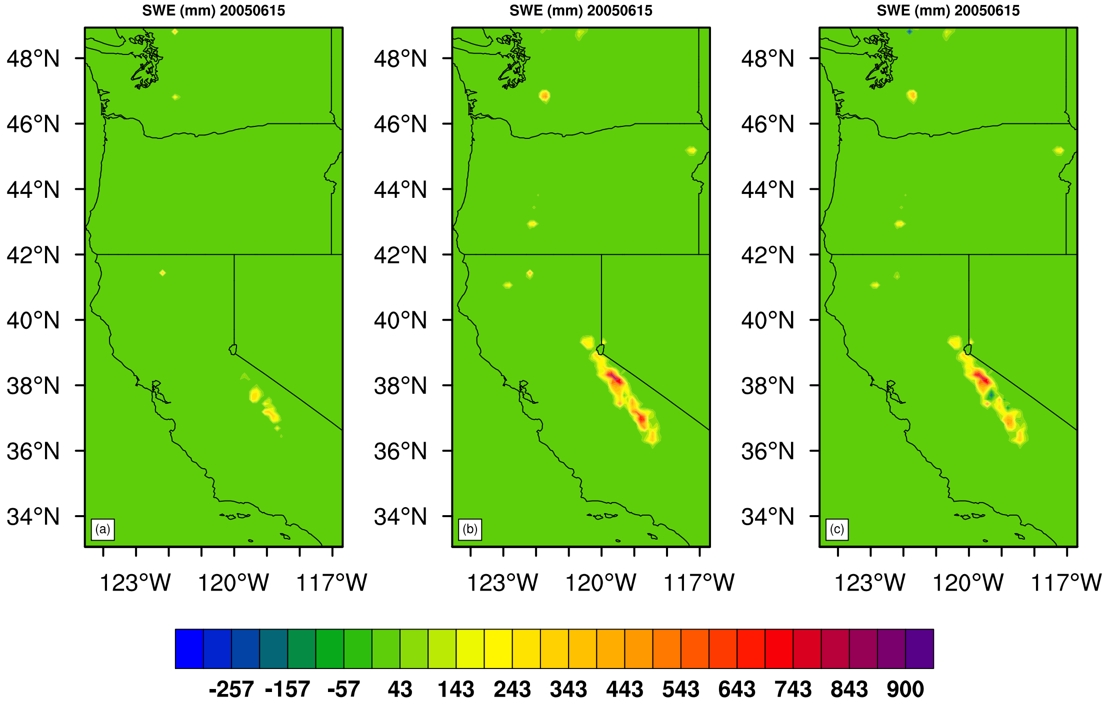

Figure 5.37: Comparison of daily average SWE (mm) for June 15, 2005: prior at Scale 3 (a), posterior at Scale 3 (b), posterior minus prior (c).

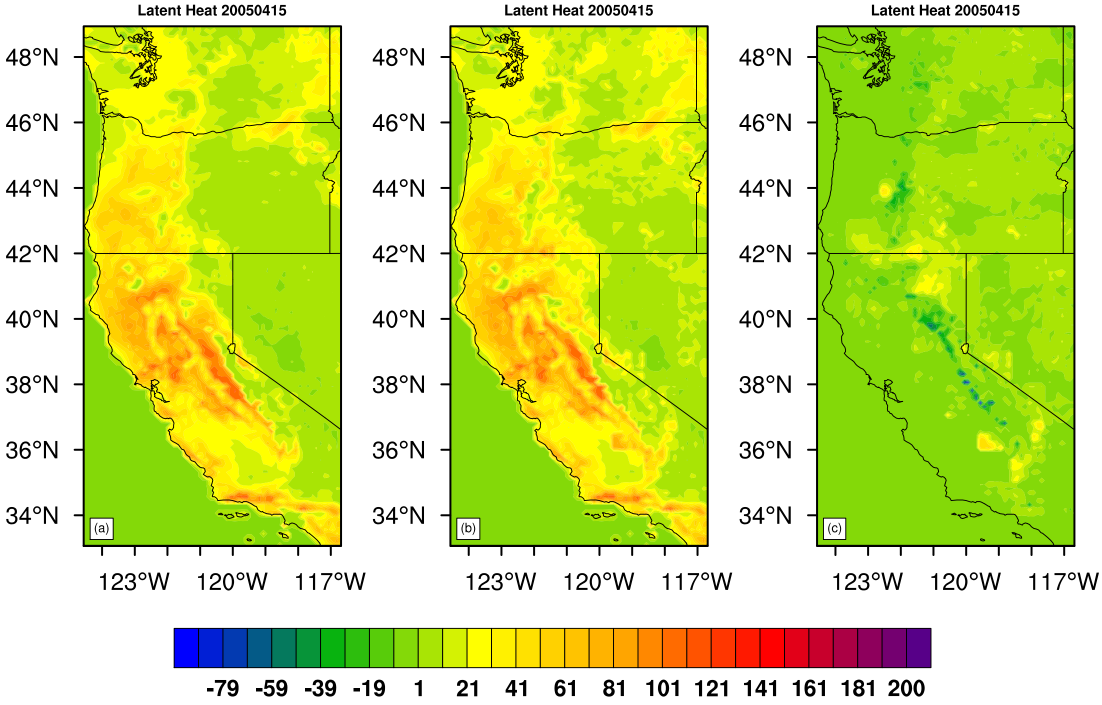

Figure 5.38: Comparison of daily average latent heat flux (W/m^2) for April 15, 2005: prior at Scale 3 (a), posterior at Scale 3 (b), posterior minus prior (c).

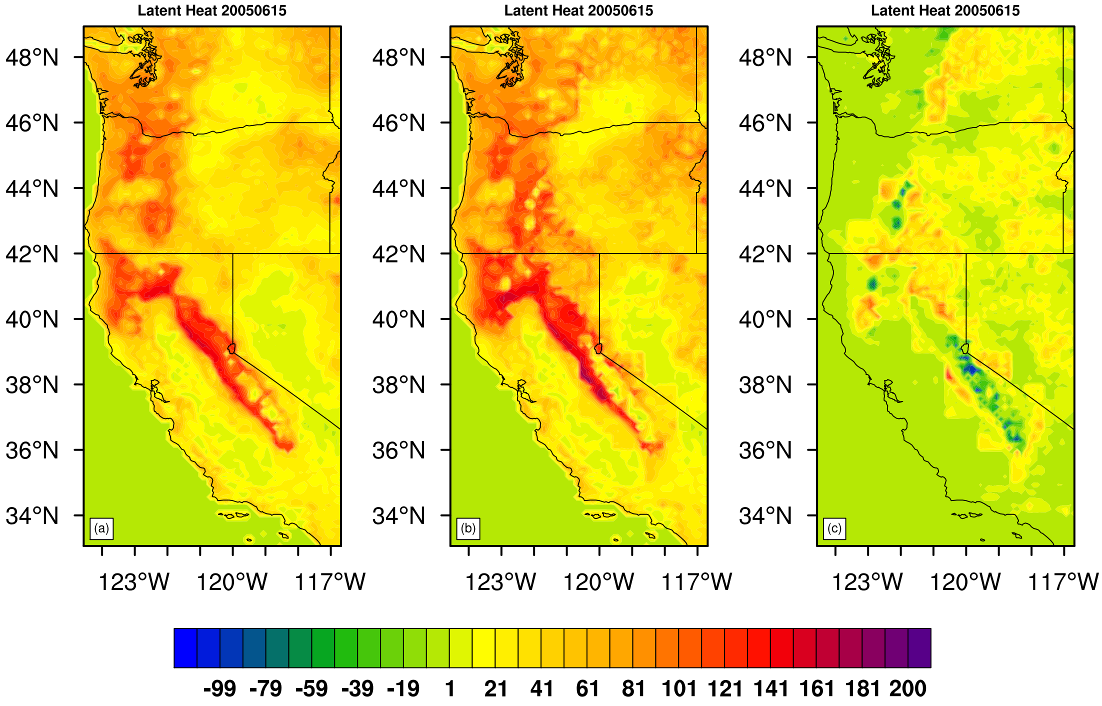

Figure 5.39: Comparison of daily average latent heat flux (W/m^2) for June 15, 2005: prior at Scale 3 (a), posterior at Scale 3 (b), posterior minus prior (c).

5.3.4 Impacts on Streamflow Simulation

Streamflow represents the composite effect of a watershed and is one of the most important variables used to validate hydrological simulations. This subsection examines the impact of the multiscale data assimilation on streamflow simulations. While we have studied SWE and energy fluxes over the large study domain, we conduct streamflow simulations in two small basins in the Sierra Nevada (see Figures **??** and 5.5). These basins are located in high elevations, where forcing uncertainty was dominant as we have seen previously. Because this study focuses on the impact of multiscale assimilation on streamflow, we do not calibrate model parameters.

Figure 5.40 shows the simulated daily streamflow with the observation at the East Fork Carson River Basin near Gardnerville, NV. Streamflow based on the posterior simulation shows promise during the 2005 and 2006 water years. As we have seen in the simulation of SWE, there has been large underestimation during these two years, and our posterior results recover this low bias. For the 2007 and 2008 water years, the posterior simulation shows some overestimation. This overestimation is attributed to SWE overestimates in the posterior simulation at Scale 6. The result in the Poison Flat belonging to the East Fork Carson River Basin, for example, shows overestimates of SWE for the 2007 and 2008 water years (Figure 5.29). The discrepancy between the simulated streamflow and the observation for the 2005 and 2006 water years is so large that it is not easy to remove the uncertainty in streamflow without considering snow accumulation and melting. Figure 5.41 shows the monthly streamflow simulation for the 2005 - 2008 water years. This monthly average also shows a similar result to that of the daily one. During the 2007 water year, the drought in the Sierra Nevada caused an abrupt decrease in streamflow. As a result, the under-catch of precipitation, which usually occurs in the mountain basin, did not contribute to the low bias in streamflow. For the 2008 water year, drought in the Sierra Nevada and improved precipitation data from NLDAS generate a good result in the streamflow simulation.

The simulation in the Upper Merced River Basin also shows promise (Figures 5.42 and 5.43). For the daily comparison between the prior and the posterior, the posterior improves streamflow simulation results by removing underestimation by the prior during the 2005 and 2006 water years. On the other hand, during the 2007 and 2008 water years, the posterior reduces overestimation by the prior. Similar results are found in the monthly simulations (Figure 5.43). These results show the ability of the multiscale process used in this dissertation to represent the subscale variability for areas where streamflow is dominated by snow accumulation and ablation processes.

5.4 Conclusion

This chapter showed how multiscale assimilation of SWE affects other hydrological variables. The existence of snow on the land surface changes the energy balance on it, in particular by altering albedo. The results in this chapter also showed such changes in the surface energy balance. The posterior predicted the state of snow on the ground more accurately than the prior in both volume and extent. In many cases, the posterior predicted the existence of snow for the areas where the prior predicted no snow. The existence of snow changed surface temperature and albedo, and subsequently brought changes to sensible and latent heat fluxes. In addition, we compared the snow covered area by the model with MODIS SCA. The results

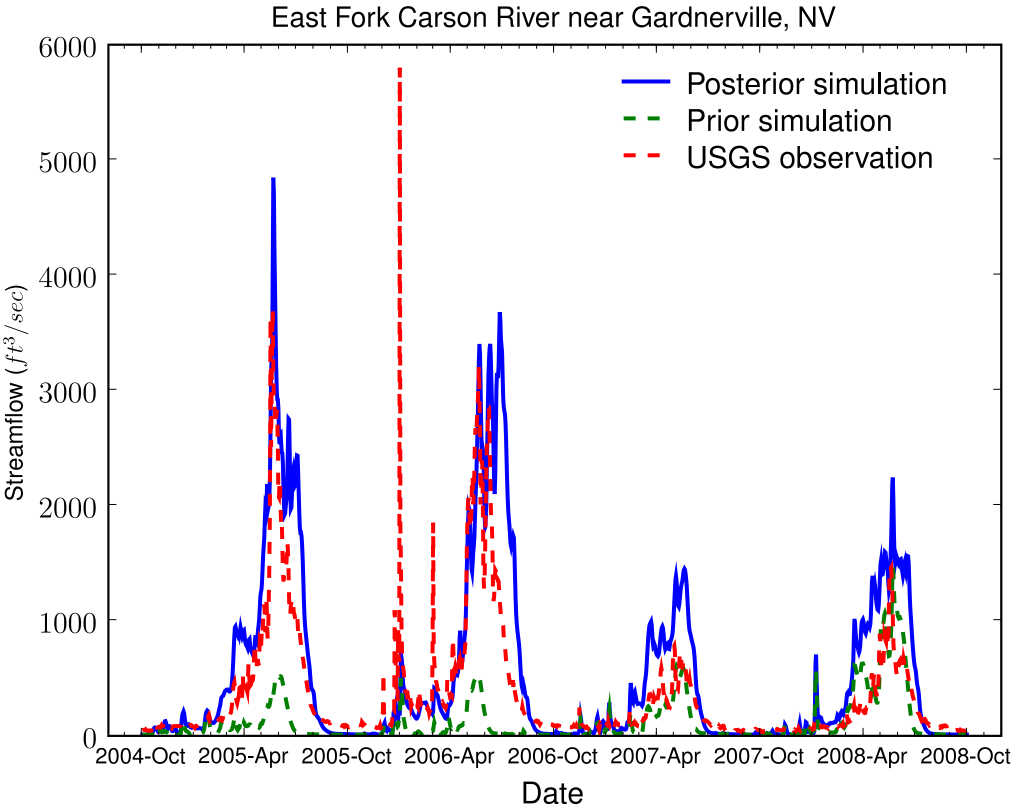

Figure 5.40: Comparison of daily simulated streamflow with the observation for the water years 2005 - 2008.

are promising and showed similarity between the assimilation and MODIS observations. To evaluate the impact of the proposed assimilation method at the basin scale, we compared simulated streamflow and observations. The assimilation scheme improved streamflow simulations by removing uncertainties associated with model forcing and physics in a complex mountain environment. In particular, the approach employed in this dissertation show how one can use snow data assimilation to generate more accurate streamflow simulations.

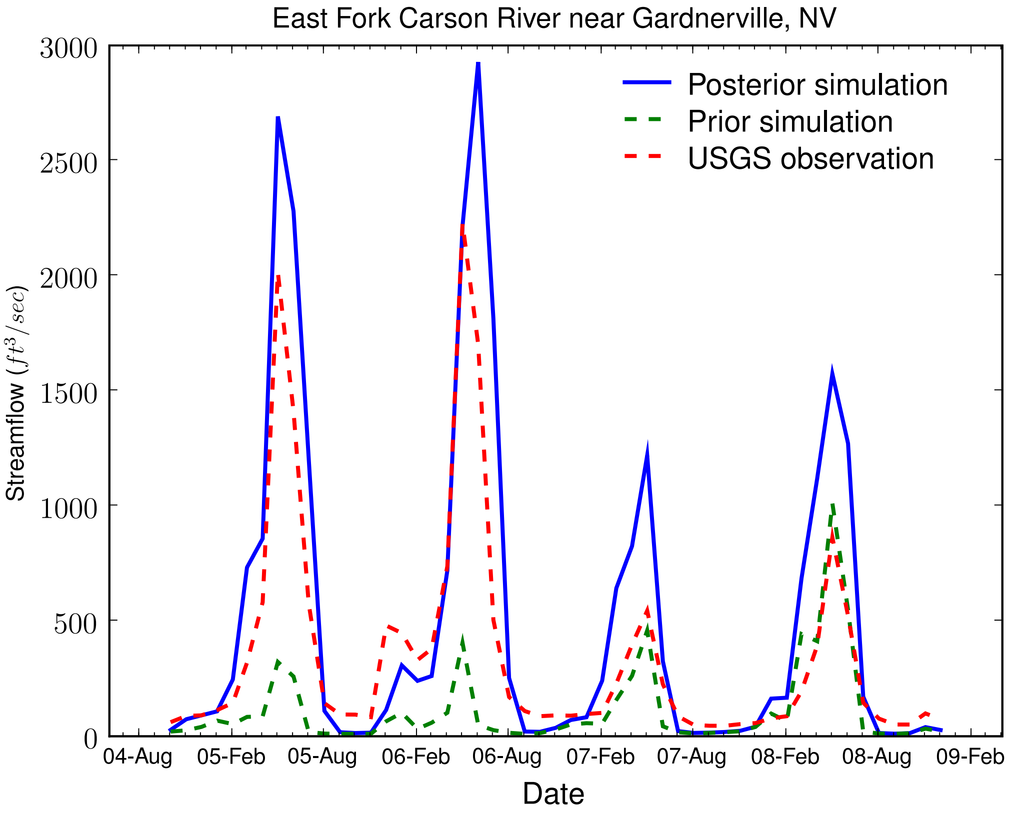

Figure 5.41: Comparison of monthly simulated streamflow with the observation for the water years 2005 - 2008.

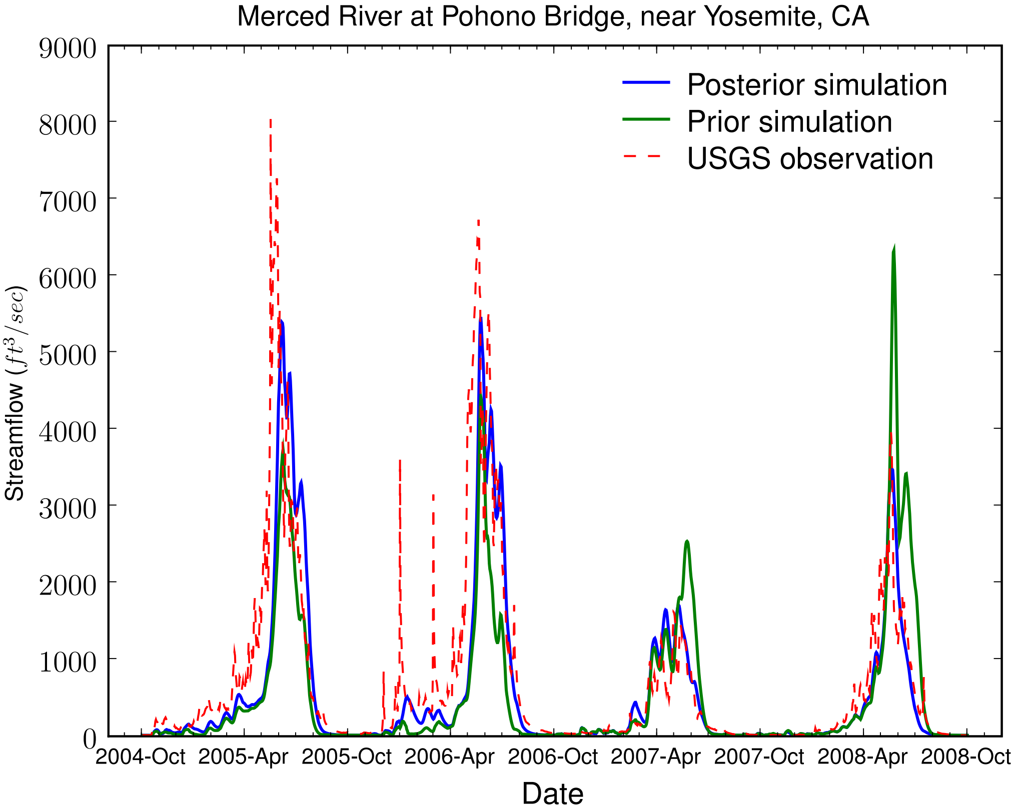

Figure 5.42: Comparison of daily simulated streamflow with the observation for the water years 2005 - 2008.

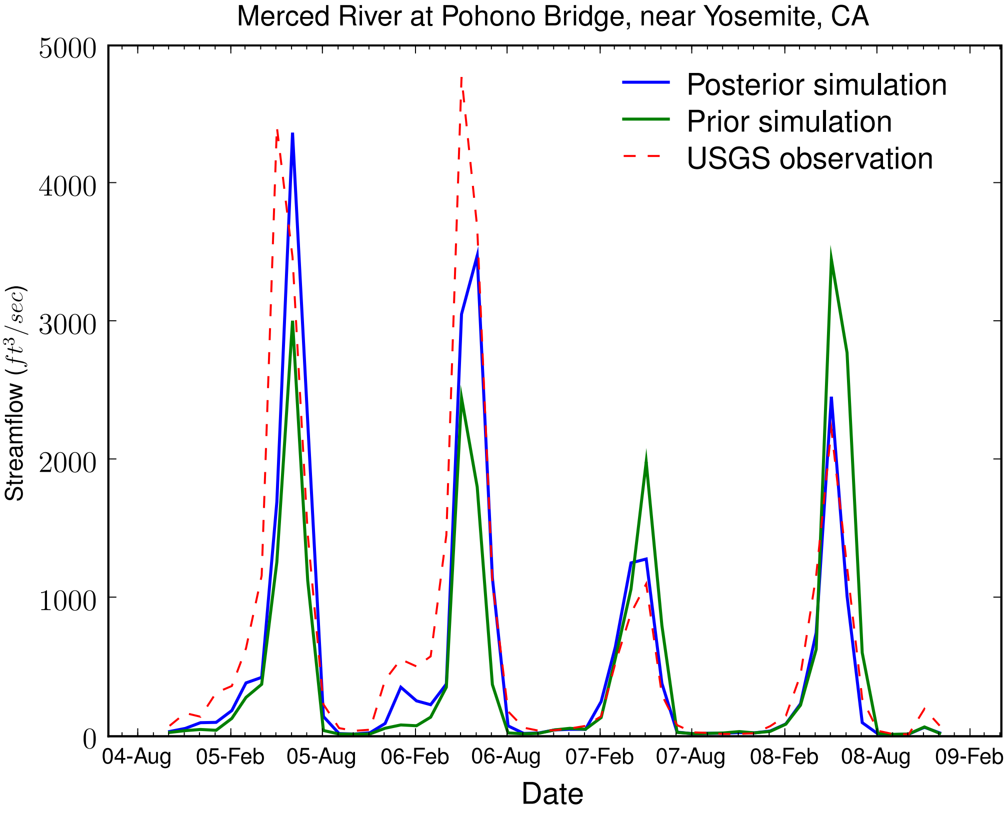

Figure 5.43: Comparison of monthly simulated streamflow with the observation for the water years 2005 - 2008.

Chapter 6

Conclusions

Mountain hydrology is by nature a complex field due to the complicated terrains and highly diverse land surface environments it encompasses. The distinct problem in mountain hydrology is that it is very difficult to accurately simulate hydrological variables [10]. This dissertation thoroughly examines hydrological processes in mountainous areas with a particular focus on simulating snow processes and related energy exchanges. The complete investigation of mountain snow processes in this dissertation includes: (1) understanding behavior of meteorological forcing data in high mountains, (2) development of a complex soil-snow model, and (3) study of a method to reduce uncertainties related to snow processes. Therefore this dissertation covers data, model physics, and a solution to improving uncertainty, and so comprises a full study set of snow processes.

Chapter 2 presented why forcing data in high mountains are problematic and how they affect the model simulation. To define the degree of uncertainties associated with model forcing data, this study employed an ensemble approach. We used the gridded precipitation and temperature data from the DMIP2 product that represents the grid cell very well. We added noise to these DMIP2 data to assign uncertainties. The results from ensemble simulations showed that perturbed forcing data with reasonable uncertainty could not remove the low-bias in SWE. One of the reasons was that the DMIP2 dataset has less solid precipitation than observed by SNOTEL, which led to underestimation of SWE in the model simulations. Among the forcing variables used, the effect of precipitation uncertainty was the largest. Temperature followed precipitation and other secondary forcing variables were smaller than these two. It is likely that DMIP2 precipitation and temperature data are the most accurate ones we could use for distributed modeling. However, our results imply that there are still undercatch problems in the raw precipitation data (e.g., cooperative rain gage data) on which the DMIP2 precipitation product is based. This situation led us to raise questions of how snow model physics can contribute to solving this problem. We need to learn how new snow parameterizations could change the underestimation problem with quality forcing data such as DMIP2 precipitation and temperature to fully understand the uncertain processes of snow.

In Chapter 3, we developed a new multilayer (M-L) soil-snow model and investigated its impact on simulating snow states. The complexity added to the 2-L snow model of the VIC LSM did not significantly change the simulation results while the M-L model showed consistent improvements in capturing the timing of melting in the shallow snowpack site of the Valdai station compared to the 2-L model. Emissivity and certain parameters (e.g., critical density for settling) for densification showed relatively high sensitivity in simulating snow variables. In terms of numerical schemes, description of the soil-snow interface occurs in the M-L model due to the added complexity of its model structure. Precise treatment of the soil-snow interface in the M-L model generated improvements to soil temperature simulations. In this regard, the M-L model can be applied to cases where more accurate simulations as in point-scale sensor validation are required and adjusting parameters is not expensive.

As we have seen from the results in the Sierra Nevada sites, the new M-L model did not overcome the dominant underestimation problem. The bias in precipitation forcing was dominant in the uncertainty of SWE simulations in our study where the gridded areal mean temperature is well matched to the point-scale temperature. The M-L model performed in a similar way to the 2-L model, in particular for the accumulation season. However, application of a different snow albedo scheme (i.e., BATS albedo scheme) changed results to a large degree during the melting season. The M-L model with the BATS albedo scheme showed a promising result for a site located at relatively lower elevation. This result implies that processes directly related to energy fluxes such as albedo and emissivity have a large impact on snow state variables.

Chapter 4 builds upon the research from the previous chapters. This chapter showed a method to reduce the uncertainty in simulating snow states. Quality meteorological forcing data, preferably with a fine resolution, tend to generate reasonable estimates of snow states. This phenomenon was shown in the 2008 year simulations in Chapter 5. However, it is very difficult to obtain quality forcing data for mountainous areas due to lack of gages and complex terrains. When we understand that high mountains are scale-sensitive areas, there is not much support for scale sensitivity from the traditional approach. Instead of using quality forcing data, we assimilated snow data from other sources with different scales into the model. The presented data assimilation framework showed a new paradigm where a land surface model fully embeds an assimilation scheme for multiscale processes to address such issues in the alpine environment. The assimilation scheme removed most of the uncertainty in the simulation of SWE. The results also showed that the forcing data play a much bigger role in the uncertainty of SWE simulations than the scaling effect due to aggregation or the model physics. Without regard to scale, all assimilated results showed similar states of SWE to the ground SNOTEL observations.

All work in the previous chapters are applied and expanded in Chapter 5. The new soil-snow model and multiscale data assimilation method are used to simulate various hydrological variables. As in Chapter 4, SWE data from the SNODAS and AMSR-E products are assimilated into the new model to investigate the impact of data assimilation on hydrological variables. The results of the multiscale assimilation of SWE changed energy fluxes on the land surface. The assimilated result, the posterior, predicted the state of snow on the ground more accurately than the prior in both volume and extent. In many cases, the posterior predicted the existence of snow for the areas where the prior predicted no snow. The existence of snow changed surface temperature and albedo, and subsequently brought changes to sensible and latent heat fluxes. In addition, we compared the snow covered area by the model with the one that was derived from the MODIS product. For this comparison, we used various data processing techniques for data with different scales. The results are promising and showed similarity between the assimilation and MODIS observations. To evaluate the impact of the proposed assimilation method at the basin scale, we compared simulated streamflow and observations. This dissertation showed how the multiscale assimilation scheme for snow reduced uncertainties in streamflow simulations. The assimilation scheme improved streamflow simulations by removing uncertainties associated with model forcing and physics in a complex mountain environment.

This dissertation study should be useful to hydrological scientists and water resources planners in several ways. First, it provides a baseline of support for interpreting snow states and available water resources in mountainous areas. As we have seen in Chapter 5 the prediction of snow states in mountain basins dominated by snow accumulation and ablation determines the accuracy of streamflow simulations. By more greatly understanding the data (e.g., precipitation) that are provided to a physical model as an input, researchers can analyze estimates of snow states and other related hydrological variables. Second, this dissertation contributes to understanding the physical processes of snow by describing snow models with different complexity levels. As we have seen, a complex model does not necessarily guarantee better results. This dissertation provided a measure to evaluate snow models with different treatments of snow processes that affect simulation results. Third, this dissertation proposed a data assimilation framework that can be deployed in the real-time prediction of hydrological variables including streamflow. Our data assimilation scheme is very efficient and can be run with a normal model simulation environment of the VIC LSM without special treatment of numerical methods. As we have seen in the streamflow simulations, the posterior results showed large improvements in estimating streamflow values. When the developed multilayer soil-snow model is refined more in conjunction with the multiscale assimilation scheme, it is expected that more accurate prediction of snow states in mountainous areas will be achieved.

Bibliography

[1] B.L. Loth, H-F. Graf, and J.M. Oberhuber. Snow cover model for global climate simulations. *J. Geophys. Res.*, 98:10451–10464, 1993.

[2] TP Barnett, L. D
”umenil, U. Schlese, E. Roeckner, and M. Latif. The Effect of Eurasian Snow Cover on Regional and Global Climate Variations. *Journal of Atmospheric Sciences*, 46:661–686, 1989.

[3] D.L. Verseghy. CLASS-A Canadian land surface scheme for GCMS. I: Soil model. *Int. J. Climatol.*, 11:111–133, 1991.

[4] B. Balk and K. Elder. Combining Binary Decision Tree and Geostatistical Methods to Estimate Snow Distribution in a Mountain Watershed. *Water Resources Research*, 36(1):13–26.

[5] M.C. Serreze, M.P. Clark, R.L. Armstrong, D.A. McGinnis, and R.S. Pulwarty. Characteristics of the western United States snowpack from snowpack telemetry (SNOTEL) data. *Water Resour. Res.*, 35(7):2145–2160, 1999.

[6] A.F. Hamlet, P.W. Mote, M.P. Clark, and D.P. Lettenmaier. Effects of temperature and precipitation variability on snowpack trends in the western united states. *J. Climate*, 18:4545–4561, 2005.

[7] SR Fassnacht, KA Dressler, and RC Bales. Snow water equivalent interpolation for the Colorado River Basin from snow telemetry (SNOTEL) data. *Water Resources Research*, 39(8):1208, 2003.

[8] C. Derksen, AE Walker, BE Goodison, and JW Strapp. Integrating in situ and multiscale passive microwave data for estimation of subgrid scale snow water equivalent distribution and variability. *IEEE Transactions on Geoscience and Remote Sensing*, 43(5):960–972, 2005.

[9] P.A. Houser. Assimilation of land surface data. In R. Swinank, editor, *Data assimilation for the earth system*. Kluwer Academic Publishers, Netherlands, 2003.

[10] R.C. Bales, N.P. Molotch, T.H. Painter, M.D. Dettinger, R. Rice, and J. Dozier. Mountain hydrology of the western united states. *Water Resour. Res.*, 42:W08432, doi:10.1029/2005WR004387, 2006.

[11] B. Nijssen and D.P. Lettenmaier. Effect of precipitation sampling error on simulated hydrological fluxes and states: Anticipating the Global Precipitation Measurement satellites. *Journal of Geophysical Research-Atmospheres*, 109(D2):D02103, 2004.

[12] E. Shamir and K.P. Georgakakos. Distributed snow accumulation and ablation modeling in the american river basin. *Adv. in Water Resour.*, 29:558570, 2006.

[13] J.C. Adam and D.P. Lettenmaier. Adjustment of global gridded precipitation for systematic bias. *J. Geophys. Res.*, 108(D9):4257, doi:10.1029/2002JD002499, 2003.

[14] D.M. Schultz, W.J. Steenburgh, R.J. Trapp, J. Horel, D.E. Kingsmill, L.B. Dunn, W.D. Rust, L. Cheng, A. Bansemer, J. Cox, et al. Understanding Utah winter storms: The intermountain precipitation experiment. *Bulletin of the American Meteorological Society*, 83(2):189–210, 2002.

[15] P.C.D. Milly and K.A. Dunne. Macroscale water fluxes 1. quantifying errors in the estimation of basin mean precipitation. *Water Resour. Res.*, 38(10):1205, doi:10.1029/2001WR000759, 2002.

[16] M. Pan, J. Sheffield, E.F. Wood, K.E. Mitchell, P.R. Houser, J.C. Schaake, A. Robock, D. Lohmann, B. Cosgrove, Q. Duan, L. Luo, R.W. Higgins, R.T. Pinker, and J.D. Tarpley. Snow process modeling in the north american land data assimilation system (nldas): 2. evaluation of model simulated snow water equivalent. *J. Geophys. Res.*, 108(D22):8850, doi:10.1029/2003JD003994, 2003.

[17] D. Lohmann, K.E. Mitchell, P.R. Houser, E.F. Wood, J.C. Schaake, A. Robock, B.A. Cosgrove, J. Sheffield, Q. Duan, L. Luo, et al. Streamflow and water balance intercomparisons of four land surface models in the North American Land Data Assimilation System project. *J. Geophys. Res.*, 109(D7):D07S91, 2004.

[18] K.E. Mitchell. The multiinstitution north america land data assimilation system (nldas): Utilizing multiple gcip products and partners in a continental distributed hydrological modeling system. *J. Geophys. Res.*, 109:D07S90, doi:10.1029/2003JD003823, 2004.

[19] F. Mesinger, G. Dimego, E. Kalnay, K. Mitchell, P.C. Shafran, W. Ebisuzaki, D.A. Jovi, J. Woollen, E. Rogers, E.H. Berbery, et al. North American Regional Reanalysis. *Bulletin of the American Meteorological Society*, 87:343–360, 2006.

[20] P. Etchevers, E. Martin, R. Brown, C. Fierz, Y. Lejeune, E. Bazile, A. Boone, Y. Dai, R. Essery, A. Fernandez, Y. Gusev, R. Jordan, V. Koren, E. Kowalczyk, N.O. Nasonova, R.D. Pyles, A. Schlosser, A.B. Shmakin, T.G. Smirnova, U. Strasser, D. Verseghy, T. Yamazaki, and Z. Yang. Validation of the energy budget of an alpine snowpack simulated by several snow models (snowmip project). *Ann. Glaciol.*, 38:150–158, 2004.

[21] L.C. Bowling and Coauthors. Simulation of high-latitude hydrological processes in the TorneKalix basin: PILPS Phase 2(e) 1: Experiment description and summary intercomparisons. *Glob. Planet. Change*, 38:1–30, 2003.

[22] X. Feng, A. Sahoo, K. Arsenault, P. Houser, Y. Luo, and T.J. Troy. The impact of snow model complexity at three clpx sites. *J. Hydrometeor.*, 9:1464–1480, 2008.

[23] Y. Hong, K. Hsu, H. Moradkhani, and S. Sorooshian. Uncertainty quantification of satellite precipitation estimation and Monte Carlo assessment of the error propagation into hydrologic response. *Water resources research*, 42(8):8421, 2006.

[24] F. Moreda, S. Cong, J. Schaake, and M. Smith. Gridded rainfall estimation for distributed modeling in western mountainous areas. *AGU Spring Meeting Abstracts*, May 2006.

[25] D.R. Greene and M.D. Hudlow. Hydrometeorological grid mapping procedures. In *International Symposium on Hydrometeorology*, Denver, Colorado, 14-17 June 1982. American Water Resources Associations.

[26] AP Dempster, NM Laird, and DB Rubin. Maximum Likelihood from Incomplete Data via the EM Algorithm. *Journal of the Royal Statistical Society. Series B (Methodological)*, 39(1):1–38, 1977.

[27] B.J.N. Blight. Recursive solutions for the estimation of a stochastic parameter. *J. American Statistical Association*, 69(346):477–481, 1974.

[28] B. Sinopoli, L. Schenato, M. Franceschetti, K. Poolla, M.I. Jordan, and S.S. Sastry. Kalman filtering with intermittent observations. *IEEE Trans. Automat. Contr.*, 49(9):1453–1464, 2004.

[29] A.T.C. Chang and L.S. Chiu. Nonsystematic errors of monthly oceanic rainfall derived from SSM/I. *Monthly Weather Review*, 127(7):1630–1638, 1999.

[30] M. Steiner, T.L. Bell, Y. Zhang, and E.F. Wood. Comparison of two methods for estimating the sampling-related uncertainty of satellite rainfall averages based on a large radar dataset. *Journal of Climate*, 16(22):3759–3778, 2003.

[31] R.H. Shumway and D.S. Stoffer. *Time Series Analysis and Its Applications: With R Examples.* Springer, 2nd edition, 2006.

[32] E. Shamir and K.P. Georgakakos. Distributed snow accumulation and ablation modeling in the American River basin. *Adv. in Water Resour.*, 29(4):558–570, 2006.

[33] C.A. Schlosser and Coauthors. Simulations of a boreal grassland hydrology at Valdai, Russia: PILPS Phase 2(d). *Mon. Wea. Rev.*, 128:301–321, 2000.

[34] J. Jin, X. Gao, Z.-L. Yang, R.C. Bales, S. Sorooshian, and R.E. Dickinson. Comparative analysis of physically based snowmelt model for climate simulations. *J. Climate*, 12:2643–2657, 1999.

[35] B. Nijssen and Coauthors. Simulation of high latitude hydrological processes in the TorneKalix basin: PILPS Phase 2(e) 2: Comparison of model results with observations. *Glob. Planet. Change*, 38:31–53, 2003.

[36] A. Boone and P. Etchevers. An intercomparison of three snow schemes of varying complexity coupled to the same land surface model: local-scale evaluation at an alpine site. *J. Hydrometeor.*, 2:374–393, 2001.

[37] R. Jordan. A one-dimensional temperature model for a snow cover. Special Report 91-16, US Army Corps of Engineers, Cold Regions Research and Engineering Laboratory, 1991. pp. 49.

[38] K.A. Cherkauer and D.P. Lettenmaier. Hydrologic effects of frozen soils in the upper mississipi river basin, j. geophys. res., 104 (d16), 19599 - 19610. *J. Geophys. Res.*, 104(D16):19599–19610, 1999.

[39] E.A. Anderson. A point energy and mass balance model for a snow cover. NOAA Tech. Rep. NWS 19, U.S. Dept. of Commer., Washington, D.C., 1976.

[40] X. Liang, D.P. Lettenmaier, and E.F. Wood. Surface soil moisture parameterization of the VIC-2L model: Evaluation and modification. *Global Planet. Change*, 13:195206, 1996.

[41] G.N. Flerchinger and K.E. Saxton. Simultaneous heat and water model of a freezing snow-residue-soil system, I, Theory and development. *Trans. ASAE*, 32:565–571, 1989a.

[42] X. Liang, D.P. Lettenmaier, E.F. Wood, and S.J. Burges. A simple hydrologically based model of land surface water and energy fluxes for general circulation models. *J. Geophys. Res.*, 99:14415–14428, 1994.

[43] R.L. Bras. *Hydrology: An Introduction to Hydrologic Science*. Addison-Wesley, 1990.

[44] M. Lynch-Stieglitz. The Development and Validation of a Simple Snow Model for the GISS GCM. *Journal of Climate*, 7(12):1842–1855, 1994.

[45] Y.-C. Yen. Recent studies on snow properties. In V.T. Chow, editor, *Advances in Hydroscience*, pages 173 – 214. Academic Press, New York, 1969.

[46] K. Kojima. Densification of Seasonal Snow Cover. In *Proceedings of International Conference on Low Temperature Science-Sapporo*, volume 1, pages 929–952, Sapporo, Japan, 1967. Institute of Low Temperature Science, Hokkaido University.

[47] M. Mellor. Properties of snow. In *Cold Regions Science and Engineering Monograph*, volume III-A1, page 105 pp. Cold Regions Research and Engineering Laboratory, Hanover, N.H., 1964.

[48] C.F. Bohren and B.R Barkstrom. Theory of the optical properties of snow. *J. Geophys. Res.*, 79(30):4527 – 4535, 1974.

[49] C.A. Schlosser, A. Robock, Y. Vinnikov, N.A. Speranskaya, and Y. Xue. 18-year land-surface hydrology model simulations for a midlatitude grassland catchment in valdai, russia. *Mon. Wea. Rev.*, 125:3279–3296, 1997.

[50] B.A. Cosgrove, D. Lohmann, K.E. Mitchell, P.R. Houser, E.F. Wood, J.C. Schaake, A. Robock, C. Marshall, J. Sheffield, Q. Duan, L. Luo, R.W. Higgins, R.T. Pinker, J.D. Tarpley, and J. Meng. Real-time and retrospective forcing in the north american land data assimilation system (nldas) project. *J. Geophys. Res.*, 108(D22):8842, doi:10.1029/2002JD003118, 2003.

[51] S. Sun, J. Jin, and Y. Xue. A simple snow-atmosphere-soil transfer model. *Journal of Geophysical Research-Atmospheres*, 104(D16):19587–19598, 1999.

[52] T.R. Oke. *Boundary Layer Climates.* Methuen, London and New York, 2nd edition, 1987.

[53] K. Andreadis and D. Lettenmaier. Assimilating remotely sensed snow observations into a macroscale hydrology model. *Adv. Water Resour.*, 29(6):872–886, 2006.

[54] R.E. Dickinson, A. Henderson-Sellers, P.J. Kennedy, and M. F. Wilson. Biosphere-atmosphere transfer scheme (bats) version 1e as coupled to community climate model. NCAR Tech. Note NCAR/TN-387+STR, NCAR, 1993.

[55] G. Blschl. Scaling issues in snow hydrology. *Hydrol. Processes*, 13:2149–2175, 1999.

[56] P.Y.Groisman and D.R. Legates. The accuracy of United States precipitation data. *Bull. Amer. Meteor. Soc.*, 75:215–227, 1994.

[57] A. Kannan, M. Ostendorf, W.C. Karl, DA Castanon, R.K. Fish, N. Commun, and M. Park. ML parameter estimation of a multiscale stochastic process usingthe EM algorithm. *IEEE Trans. Signal Processing*, 48(6):1836–1840, 2000.

[58] K.C. Chou, A.S. Willsky, and A. Benveniste. Multiscale recursive estimation, data fusion, and regularization. *IEEE Trans. Autom. Control*, 39:464–478, 1994.

[59] P.W. Fieguth, W.C. Karl, A.S. Willsky, and C. Wunsch. Multiresolution optimal interpolation and statistical analysis of TOPEX/POSEIDON satellite altimetry. *IEEE Trans. Geosci. Remote Sens.*, 33:280–292, 1995.

[60] M.R. Luettgen and A.S. Willsky. Multiscale smoothing error models, ieee trans. autom. control, 40, 173175. *IEEE Trans. Automat. Contr.*, 40:173–175, 1995.

[61] L.M. Parada and X. Liang. Optimal multiscale kalman filter for assimilation of near-surface soil moisture into land surface models. *J. Geophys. Res.*, 109:D24109, doi:10.1029/2004JD004745, December 2004.

[62] S. Jeong, X. Liang, and J.A. Dracup. A new multiple-layer snow model for land surface models. *Eos Trans. AGU*, 88(52):Fall Meet. Suppl., Abstract H21B–0512, 2007.

[63] National Operational Hydrologic Remote Sensing Center. *Snow Data Assimilation System (SNODAS) data products at NSIDC.* National Snow and Ice Data Center, Boulder, CO, digital media edition, 2004.

[64] N.P. Molotch and R.C. Bales. Scaling snow observations from the point to the grid element: Implications for observation network design. *Water Resour. Res.*, 41:W11421, doi:10.1029/2005WR004229, 2005.

[65] R.E. J. Kelly, A.T.C. Chang, J.L. Foster, and M. Tedesco. *AMSR-E/Aqua Daily L3 Global Snow Water Equivalent EASE-Grids, October 2003 to September 2005.* National Snow and Ice Data Center, Boulder, Colorado USA, 2004. Digital media.

[66] R.E. Kelly, A.T. Chang, L. Tsang, and J.L. Foster. A prototype AMSR-E global snow area and snow depth algorithm. *IEEE Transactions on Geoscience and Remote Sensing*, 41(2):230–242, 2003.

[67] N. Rutter, D. Cline, and L. Li. Evaluation of the nohrsc snow model (nsm) in a one-dimensional mode. *J. Hydrometeor.*, 9:695–711, 2008.

[68] Y. Xia. Optimization and uncertainty estimates of wmo regression models for the systematicbias adjustment of nldas precipitation in the united states. *J. Geophys. Res.*, 111:D08102, doi:10.1029/2005JD006188, 2006.

[69] D.K. Hall, G.A. Riggs, V.V. Salomonson, N.E. DiGirolamo, and K.J. Bayr. MODIS snow-cover products. *Remote Sensing of Environment*, 83(1-2):181–194, 2002.

Appendix A

Ground and Snow Heat Flux

A.1 Introduction

The structure of the VIC LSM for cold season processes has been changed by incorporating a multi-layer soil-snow model. Therefore, the way ground heat and snow fluxes are computed has also changed. This appendix shows how to calculate these fluxes.

A.2 Ground Heat Flux

A.2.1 Governing Equation

The ground heat flux, which is the heat flux across the ground surface, is calculated using the first two layers of the soil system.

The governing equations above can be solved numerically using the following finite difference approximation

$$
\begin{aligned}
C_s \frac{\partial T}{\partial t} &= -\frac{\partial G}{\partial z} + \rho_i L_f (\frac{\partial W_i}{\partial t}) && \text{(A.1)} \\
G &= -\kappa \frac{\partial T}{\partial z} && \text{(A.2)}
\end{aligned}
$$

where G is the soil heat flux in the z direction, C_s is the volumetric specific heat of soil ($Jm^{-3}K^{-1}$), κ is the soil thermal conductivity ($Wm^{-1}K^{-1}$), ρ_i is the density of ice (kgm^{-3}), L_f is the latent heat of fusion (Jkg^{-1}), and W_i is the ice content of the layer (m^3m^{-3}). In the above equation each term has a unit of Wm^{-3}.

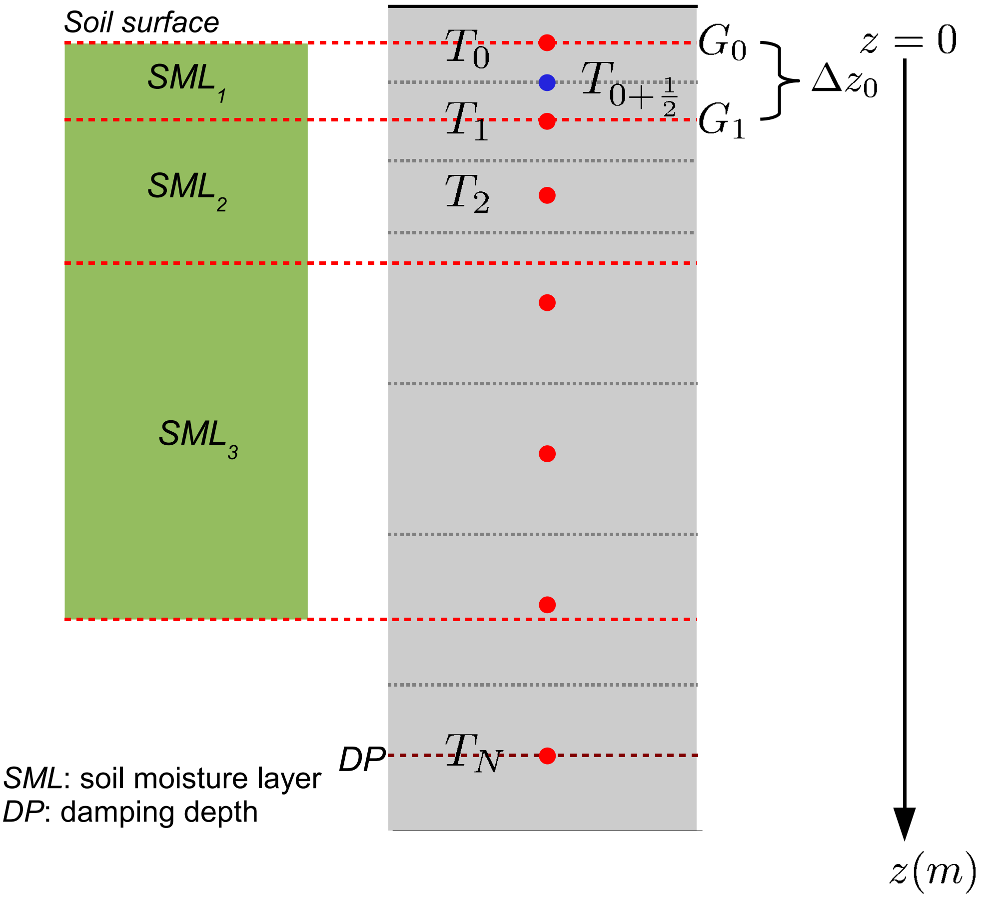

Figure A.1: An example of layering scheme for ground heat flux. The top three layers (i.e., $j = 0, 1, 2$) are fixed and the rest layers can vary depending on the number of soil thermal layers.

A.2.2 Solution

Because we are interested in the heat flux at the ground surface, we can rewrite the Equation A.2 as:

$$\begin{aligned} C_s \frac{T^{n+1}_{0+\frac{1}{2}} - T^{n}_{0+\frac{1}{2}}}{\Delta t} &= -\frac{G_1 - G_0}{\Delta z_0} + \rho_i L_f \left(\frac{(W_i)^{n+1}_{0+\frac{1}{2}} - (W_i)^{n}_{0+\frac{1}{2}}}{\Delta t} \right) \\ &= -\frac{1}{\Delta z_0} G_1 + \frac{1}{\Delta z_0} G_0 + \rho_i L_f \left(\frac{(W_i)^{n+1}_{0+\frac{1}{2}} - (W_i)^{n}_{0+\frac{1}{2}}}{\Delta t} \right) \qquad \text{(A.3)} \end{aligned}$$

If we solve for G_0, we have:

$$G_0 = G_1 + \frac{\Delta z_0}{\Delta t} C_s (T^{n+1}_{0+\frac{1}{2}} - T^{n}_{0+\frac{1}{2}}) - \rho_i L_f \left(\frac{(W_i)^{n+1}_{0+\frac{1}{2}} - (W_i)^{n}_{0+\frac{1}{2}}}{\Delta t} \right) \qquad \text{(A.4)}$$

In our simultaneous calculation of soil and snow temperature, the temperature for the next time step has already been calculated. We only need to recalculate the ground heat flux using those known temperatures. Now, we need the expression for G_1, which is the flux at the interface corresponding to T_1 as shown in Figure A.1. G_1 can be calculated as

$$G_1 = 0.5\left(-\kappa_{01}\frac{T_1^{n+1} - T_0^{n+1}}{z_1 - z_0} - \kappa_{12}\frac{T_2^{n+1} - T_1^{n+1}}{z_2 - z_1}\right) \tag{A.5}$$

where κ_{01} is the average heat conductivity between z_0 and z_1, and in the same way κ_{12} between z_1 and z_2. Therefore we use the average of the upper and lower fluxes of the interface corresponding to T_1 to reduce numerical errors.

In Figure A.1, we are using the temperature at the midpoint between z_0 and z_1, which is expressed as $T_{0+\frac{1}{2}}$. Assuming the linear relationship between layers 0 and 1, we can write as

$$T_{0+\frac{1}{2}} = \frac{T_0 + T_1}{2} \tag{A.6}$$

In the same way, the ice content between z_0 and z_1 can be calculated as the average of $(W_i)_0$ and $(W_i)_1$ yielding

$$(W_i)_{0+\frac{1}{2}} = \frac{(W_i)_0 + (W_i)_1}{2} \tag{A.7}$$

A.3 Snow Heat Flux

Figure A.2 shows a layering scheme for the snow system, which depends on the number of layers. In a similar way to the calculation of ground heat flux, snow heat flux is the flux at the interface between the first layer and the second layer, which is denoted as $F_{0+\frac{1}{2}}$ in Figure A.2.

We use an equation for the flux at the interface between layer $j = 0$ and layer $j = 1$ following [44]:

$$F_{0+\frac{1}{2}} = -(DK_e)_{0,1}(T_1 - T_0) \tag{A.8}$$

where $(DK_e)_{0,1}$ can be expressed as

$$(DK_e)_{0,1} = \frac{1}{\left(\frac{\Delta z_0}{2} + \frac{\Delta z_1}{2}\right)}\left(\frac{\Delta z_0 + \Delta z_1}{\frac{\Delta z_0}{(K_e)_0} + \frac{\Delta z_1}{(K_e)_1}}\right) \tag{A.9}$$

In our solution to the temperature of the soil-snow system, we use the Crank-Nicholson method. In the same context, we can write the snow flux as

$$F_{0+\frac{1}{2}} = \theta F_{0+\frac{1}{2}}^{n+1} + (1-\theta)F_{0+\frac{1}{2}}^{n} \tag{A.10}$$

where n denotes the previous time as usual. Therefore, we have

$$F_{0+\frac{1}{2}}^{n} = -(DK_e)_{0,1}^{n}(T_1 - T_0) \tag{A.11}$$

$$(DK_e)_{0,1}^{n} = \frac{1}{\left(\frac{\Delta z_0^n}{2} + \frac{\Delta z_1^n}{2}\right)}\left(\frac{\Delta z_0^n + \Delta z_1^n}{\frac{\Delta z_0^n}{(K_e)_0^n} + \frac{\Delta z_1^n}{(K_e)_1^n}}\right) \tag{A.12}$$

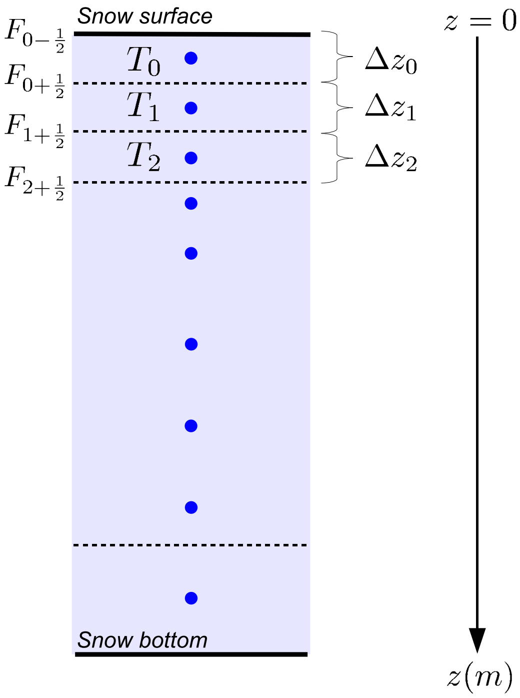

Figure A.2: An example of layering scheme for the snow system.

Appendix B

Matrix Equations for Netwon-Raphson Solutions

B.1 Introduction

Computing soil and snow state variables simultaneously requires a fast solution in the new macro-scale model for cold season processes. Therefore, we use the Newton-Raphson (NR) method in a multi-dimensional way. This appendix shows how to set up the matrix to apply the multi-dimensional NR method.

B.2 Matrix of Equations

$$\begin{bmatrix}
\left.\frac{\partial(f_0)}{\partial x_0}\right|_{\mathbf{x}_i} & \left.\frac{\partial(f_0)}{\partial x_1}\right|_{\mathbf{x}_i} & 0 & 0 & 0 & 0 \\
\left.\frac{\partial(f_1)}{\partial x_0}\right|_{\mathbf{x}_i} & \left.\frac{\partial(f_1)}{\partial x_1}\right|_{\mathbf{x}_i} & \left.\frac{\partial(f_1)}{\partial x_2}\right|_{\mathbf{x}_i} & 0 & 0 & 0 \\
0 & \left.\frac{\partial(f_2)}{\partial x_1}\right|_{\mathbf{x}_i} & \left.\frac{\partial(f_2)}{\partial x_2}\right|_{\mathbf{x}_i} & \left.\frac{\partial(f_2)}{\partial x_3}\right|_{\mathbf{x}_i} & 0 & 0 \\
0 & 0 & \left.\frac{\partial(f_3)}{\partial x_2}\right|_{\mathbf{x}_i} & \left.\frac{\partial(f_3)}{\partial x_3}\right|_{\mathbf{x}_i} & \left.\frac{\partial(f_3)}{\partial x_4}\right|_{\mathbf{x}_i} & 0 \\
0 & 0 & 0 & \left.\frac{\partial(f_4)}{\partial x_3}\right|_{\mathbf{x}_i} & \left.\frac{\partial(f_4)}{\partial x_4}\right|_{\mathbf{x}_i} & \left.\frac{\partial(f_4)}{\partial x_5}\right|_{\mathbf{x}_i} \\
0 & 0 & 0 & 0 & \left.\frac{\partial(f_5)}{\partial x_4}\right|_{\mathbf{x}_i} & \left.\frac{\partial(f_5)}{\partial x_5}\right|_{\mathbf{x}_i}
\end{bmatrix}$$

$$\begin{bmatrix} (x_0)_{i+1} \\ (x_1)_{i+1} \\ (x_2)_{i+1} \\ (x_3)_{i+1} \\ (x_4)_{i+1} \\ (x_5)_{i+1} \end{bmatrix}$$

$$= \begin{bmatrix} (RHS_0)_i \\ (RHS_1)_i \\ (RHS_2)_i \\ (RHS_3)_i \\ (RHS_4)_i \\ (RHS_5)_i \end{bmatrix}$$

where $\frac{\partial(f_0)}{\partial x_0}\Big|_{\mathbf{x}_i}$ is the derivative of the equation for layer $j = 0$ with respect to x_0 evaluated with the value of $\mathbf{x}_i$. Layer equation f_j is shown in Chapter 3. $\mathbf{x}_i$ is a vector that contains the solutions from the ith iteration. Note that we are solving for solutions at the $(i+1)$th iteration.

B.3 New Mass Fraction

This section shows how to solve the new snow mass fraction (i.e., $(f_s)_j^{n+1}$) when the layer temperature for the new time step (i.e., T_j^{n+1}) is equal to 0 $°C$. We have the following equation for the snow surface:

$$\begin{aligned}(f_0)_i \;=\;& H_0^{n+1} - H_0^n - \theta\frac{\Delta t}{\Delta z_{j=0}}F_{0-\frac{1}{2}}^{n+1} - (1-\theta)\frac{\Delta t}{\Delta z_{j=0}}F_{0-\frac{1}{2}}^{n} \\ &+\theta\frac{\Delta t}{\Delta z_{j=0}}F_{0+\frac{1}{2}}^{n+1} + (1-\theta)\frac{\Delta t}{\Delta z_{j=0}}F_{0+\frac{1}{2}}^{n} \\ &+\frac{\Delta t}{\Delta z_{j=0}}(R_s)_{0+\frac{1}{2}}^{n} \end{aligned} \tag{B.1}$$

where $H = C_v(T - 273.15) - f_sL_f\rho_{sl}$. The definition for each term is presented in Chapter 3.

We need to solve Equation B.1 for $(f_s)_j^{n+1}$ at the surface layer with T_j^{n+1} being 273.15 K. The result can be written as

$$\begin{aligned}(f_s)_0^{n+1} \;=\;& \frac{1}{L_f\rho_{sl}}\left(-H_0^n - \theta\frac{\Delta t}{\Delta z_{j=0}}F_{0-\frac{1}{2}}^{n+1} - (1-\theta)\frac{\Delta t}{\Delta z_{j=0}}F_{0-\frac{1}{2}}^{n}\right) \\ &+\frac{1}{L_f\rho_{sl}}\left(\theta\frac{\Delta t}{\Delta z_{j=0}}F_{0+\frac{1}{2}}^{n+1} + (1-\theta)\frac{\Delta t}{\Delta z_{j=0}}F_{0+\frac{1}{2}}^{n}\right) \\ &+\frac{1}{L_f\rho_{sl}}\left(\frac{\Delta t}{\Delta z_{j=0}}(R_s)_{0+\frac{1}{2}}^{n}\right) \end{aligned} \tag{B.2}$$

where $H_0^{n+1} = -(f_s)_0^{n+1}L_f\rho_{sl}$ when $T_0^{n+1} = 273.15K$.

The only term that contains the solid fraction of snow f_s is the heat content H (Jm^{-3}). The derivative of H with respect to $(f_s)_j^{n+1}$ is written as:

$$\begin{aligned} \left[H_j^n\right]_{(f_s)_j^{n+1}} &= 0 && \text{(B.3)} \\ \left[H_j^{n+1}\right]_{(f_s)_j^{n+1}} &= -L_f(\rho_{sl})_j^n && \text{(B.4)} \end{aligned}$$

Thus the following holds:

$$[f_j]_{(f_s)_j^{n+1}} = -L_f(\rho_{sl})_j^n \tag{B.5}$$

$$\begin{bmatrix} \left.\frac{\partial(f_0)}{\partial x_0}\right|_{\mathbf{x}_i} & 0 & 0 & 0 & 0 & 0 \\ 0 & \left.\frac{\partial(f_1)}{\partial x_1}\right|_{\mathbf{x}_i} & 0 & 0 & 0 & 0 \\ 0 & 0 & \left.\frac{\partial(f_2)}{\partial x_2}\right|_{\mathbf{x}_i} & 0 & 0 & 0 \\ 0 & 0 & 0 & \left.\frac{\partial(f_3)}{\partial x_3}\right|_{\mathbf{x}_i} & 0 & 0 \\ 0 & 0 & 0 & 0 & \left.\frac{\partial(f_4)}{\partial x_4}\right|_{\mathbf{x}_i} & 0 \\ 0 & 0 & 0 & 0 & 0 & \left.\frac{\partial(f_5)}{\partial x_5}\right|_{\mathbf{x}_i} \end{bmatrix}$$

$$\begin{bmatrix} (x_0)_{i+1} \\ (x_1)_{i+1} \\ (x_2)_{i+1} \\ (x_3)_{i+1} \\ (x_4)_{i+1} \\ (x_5)_{i+1} \end{bmatrix}$$

$$= \begin{bmatrix} (RHS_0)_i \\ (RHS_1)_i \\ (RHS_2)_i \\ (RHS_3)_i \\ (RHS_4)_i \\ (RHS_5)_i \end{bmatrix}$$

The right-hand side RHS can be written as:

$$(RHS_j)_i = -(f_j)_i + (x_j)_i \left.\frac{\partial(f_j)}{\partial x_j}\right|_{\mathbf{x}_i} \tag{B.6}$$

where $(x_j)_i$ is the ith (i.e., previous) iteration result for the unknown of layer j (i.e., $(f_s)_j$). Note that only the jth component of the vector $\mathbf{x}_i$ is used for the jth layer equation.

Appendix C

Verification of the Proposed Numerical Solution

C.1 Introduction

The challenge for the proposed numerical method is to solve two unknown variables using only one equation. That is, for each snow layer, we have only one equation, but need to solve two unknowns: temperature and water content. Therefore, temperature profile and water content profile consist of $2 \times N$ unknown variables while we have N equations. Recall the governing equations and their solutions in Chapter 3. We use an independent non-linear solver to evaluate and verify the proposed numerical scheme. We use *fsolve*, which implements the *minpack* package (*http://www.netlib.org/minpack/*).

C.2 Comparison with *fsolve*

Figure C.1 shows the comparison result between the proposed NR solution and the *fsolve* (*minpack*) solver.

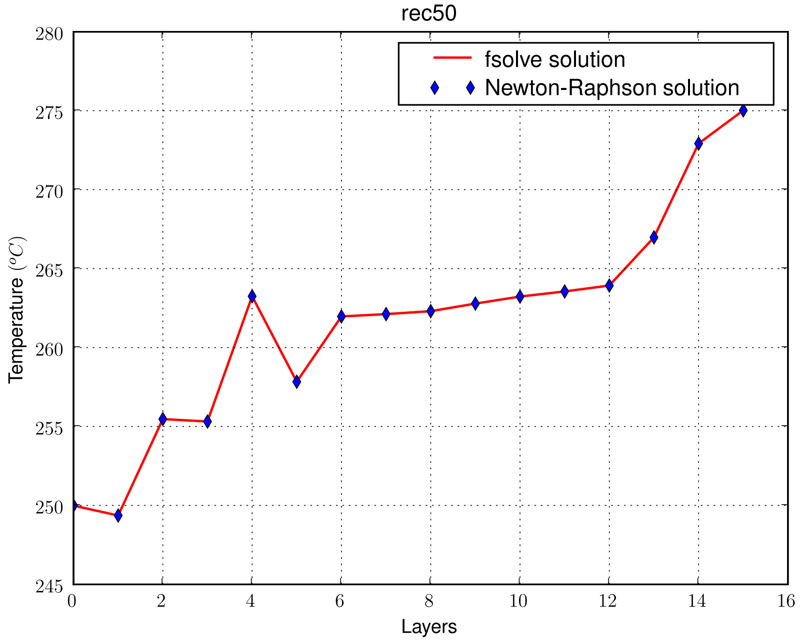

Figure C.1: Comparison of temperature profile between the proposed Newton-Raphson solution and the *minpack* package

Appendix D

Algorithm for Spatial Aggregation and Resampling

D.1 Introduction

This appendix describes the algorithm to aggregate and resample remotely sensed data used in this dissertation. The goal of resampling or spatial aggregation is to obtain areal mean values for grid cells corresponding to the model simulation domain. In this dissertation, two sources of remotely sensed data were used: MODIS for fine resolution and AMSR-E for coarse resolution. This dissertation uses a conservative approach to resampling. In particular, for AMSR-E, which has a 25 km × 25 km resolution, we have found that resampling is sensitive to the resampling algorithm. For example, when we resample the original level 3 AMSR-E snow water equivalent product to the model grid cell with a resolution of 1/4th degrees, the simplest way to represent the model grid cell is to use the value of the AMSR-E grid cell nearest to the center of the target model grid cell. However, since the spatial variation of AMSR-E is high from grid cell to grid cell, using one nearest cell value is not accurate. We have found that our approach produced a very different set of data compared to this simple method.

D.2 Algorithm

Even though there are many methods to avoid this resampling problem, we developed a weighted averaging algorithm. As shown in Figure D.1, we first convert remotely sensed data into the same projection as the target grid cell, for which we are calculating areal mean values. In Figure D.1, the dashed blue rectangle is the target grid cell, and other rectangles are grid cells for remotely sensed data. Then, we calculate the relative contributing area to the target grid cell using various computational geometry techniques (e.g., convex hull technique). Once the relative areas are calculated, these are used as weights for the corresponding grid cells. Figure D.2 shows an example of processing MODIS snow cover data with a resolution of 500 m, where the coordinate system is sinusoidal. The thick polygons in Figure D.2 are the computed relative areas that fall within the target grid cell, which has a resolution of 1/64th degree.

This method is computationally expensive compared with the method to select one or several values without weighting to represent the target grid cell. One efficient way of using the weighting algorithm is to compute the weights once for all and reuse them. Reusing the weights becomes a simple matrix calculation.

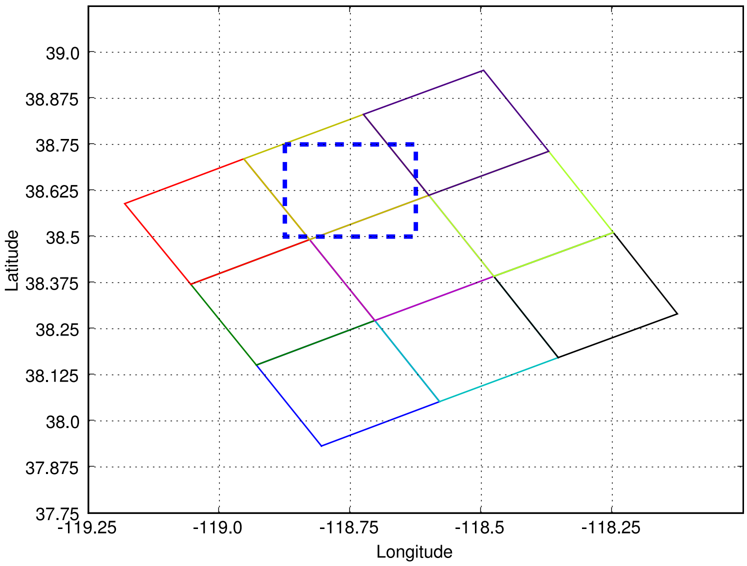

Figure D.1: Coordinate conversion of EASE grids to geographic for calculation of contributing areas to the target grid cell.

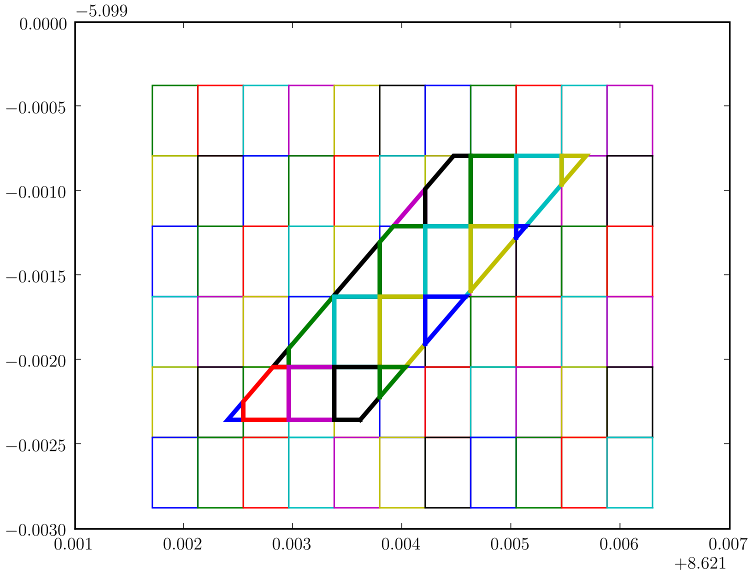

Figure D.2: Calculation of weighted area relative to the target grid cell.

Appendix E

Error Time Series

E.1 Introduction

This appendix describes the lag-one autoregressive model that was used to generate the precipitation error time series in Chapter 2.

E.2 Error Time Series Model

In order to produce one hundred samples of input data, the errors of hourly precipitation are modeled as lag-one autoregressive (i.e., AR (1)) random sequences. The AR(1) model can be expressed by:

$$\epsilon_t = \phi \epsilon_{t-1} + \theta \lambda_t \tag{E.1}$$

where ϵ_t is the error time series, ϕ and θ are the AR (1) coefficients, and λ_t is a normal random number with mean of zero and variance of one.

Following the notation in Shumway and Stoffer [31] Equation E.1 can also be written as:

$$\epsilon_t = \phi \epsilon_{t-1} + w_t \tag{E.2}$$

where w_t is the white noise with zero mean and variance σ_w. Therefore, w_t can expressed in terms of λ_t as:

$$w_t = \theta \lambda_t \tag{E.3}$$

The AR(1) coefficients can be estimated based on the method of moments estimators. The Yule-Walker equations in Shumway and Stoffer [31] are given by:

$$\begin{aligned} \gamma(h) &= \phi_1 \gamma(h-1) + \cdots + \phi_p \gamma(h-p),\ h = 1, 2, \ldots, p && \text{(E.4)} \\ \sigma_w^2 &= \gamma(0) - \phi_1 \gamma(1) - \cdots - \phi_p \gamma(p) && \text{(E.5)} \end{aligned}$$

where $\gamma(h)$ is autocovariance function with lag of h. Note that σ_w is the standard deviation of the white noise in Equation E.2.

For AR(1), Equations E.4 and E.5 can be written as:

$$\begin{aligned} \gamma(1) &= \phi_1\gamma(0) = \phi\gamma(0) && \text{(E.6)} \\ \sigma_w^2 &= \gamma(0) - \phi_1\gamma(1) = \gamma(0) - \phi\gamma(1) && \text{(E.7)} \end{aligned}$$

where ϕ_1 is now replaced by ϕ.

Using the method of moments, it is possible to replace $\gamma(h)$ with $\gamma(\hat{h})$. Also, it can be sometimes more convenient to use the sample autocorrelation function (ACF) ρ. If $\gamma(0)$ is factored in Equations E.6 and E.7, these equations become:

$$\begin{aligned} \rho(\hat{1}) &= \hat{\phi} && \text{(E.8)} \\ \hat{\sigma}_w^2 &= \hat{\gamma}(0) - \hat{\phi}\hat{\gamma}(1) = \hat{\gamma}(0)[1 - \hat{\phi}\hat{\rho}(1)] = \hat{\gamma}(0)[1 - \hat{\rho}(1)^2] && \text{(E.9)} \end{aligned}$$

Since the first coefficient of the AR(1) model is obtained from Equation E.8, the second coefficient needs to be represented in terms of the sample lag-one ACF. From Equation E.3, the following holds:

$$Var(w_t) = \sigma_w^2 = \theta^2 Var(\lambda_t) = \theta^2 \tag{E.10}$$

Therefore, using the result in Equation E.9, the second coefficient

$$\hat{\theta} = \hat{\sigma}_w = \left(\hat{\gamma}(0)[1 - \hat{\rho}(1)^2]\right)^{\frac{1}{2}} = \left(\hat{\sigma}_\epsilon^2[1 - \hat{\rho}(1)^2]\right)^{\frac{1}{2}} \tag{E.11}$$

where $\hat{\sigma}_\epsilon^2 = \hat{\gamma}(0)$, which is the variance of the error time series.

Appendix F

Posterior Distribution of a State Space Model

F.1 Introduction

We describe the posterior density of a state space model to represent uncertainty of observed data (e.g., SNODAS data) used in this dissertation.

F.2 Equation

We model as:

$$x_{t+1} = Ax_t + w_t \tag{F.1}$$

$$y_t = Cx_t + v_t \tag{F.2}$$

Uncertainty simulation requires an ensemble of datasets (e.g., noisy SNODAS data). But there is no straight-forward way of generating ensemble data. Unless we use arbitrary noise parameters, we should know certain parameters for a given domain (e.g., variance). But in most cases, those parameters are not available. The alternative is to obtain a distribution from the available data. A state space model provides underlying signals of the data with certain degree of uncertainty. Therefore we use a posterior density of a state space model (i.e., Kalman filter) to generate ensemble noisy data using a Bayesian approach. Even though the parameters in the proposed state space model are estimated using the expectation-maximization (EM) algorithm, this method is purely based on data, not requiring known domain parameters.

We derive a posterior distribution of the Kalman equation given in Equations F.1 and F.2 (The EM algorithm and details of the model are not included here).

Following Blight [27] we use the following notation for a multivariate normal distribution:

$$\{x; \mu, \Sigma\} = e^{-\frac{1}{2}(x-\mu)^T \Sigma^{-1} (x-\mu)} \tag{F.3}$$

When β is a square nonsingular matrix, we have:

$$\{x;\alpha+\beta\mu,\Sigma\}=\{\mu;\beta^{-1}(x-\alpha),\beta^{-1}\Sigma(\beta^{-1})^T\} \tag{F.4}$$

Also, using the definition it can be derived as:

$$\begin{aligned}\{x;\mu_1,\Sigma_1\}\{x;\mu_2,\Sigma_2\} &= \{x;(\Sigma_1^{-1}+\Sigma_2^{-1})^{-1}(\Sigma_1^{-1}\mu_1+\Sigma_2^{-1}\mu_2),\\ &\quad (\Sigma_1^{-1}+\Sigma_2^{-1})^{-1}\}\{\mu_1;\mu_2,\Sigma_1+\Sigma_2\} \end{aligned}\tag{F.5}$$

The density we are interested in is:

$$p(x_{t+1}|y_{t+1},y_0,...,y_t) \tag{F.6}$$

where $p(\cdot)$ is a general Gaussian density function.

Noting that this is a posterior distribution, as usual we can write the posterior as

$$posterior \propto likelihood \times prior \tag{F.7}$$

From the Markov property and the Bayes rule, this density can be expressed as

$$\begin{aligned} p(x_{t+1}|y_{t+1},y_0,...,y_t) &\propto p(y_{t+1}|x_{t+1},y_0,...,y_t)p(x_{t+1}|y_0,...,y_t)\\ &= p(y_{t+1}|x_{t+1})p(x_{t+1}|y_0,...,y_t)\\ &= p(y_{t+1}|x_{t+1})\int p(x_{t+1},x_t|y_0,...,y_t)dx_t\\ &= p(y_{t+1}|x_{t+1})\int p(x_{t+1}|x_t,y_0,...,y_t)p(x_t|y_0,...,y_t)dx_t\\ &= p(y_{t+1}|x_{t+1})\int p(x_{t+1}|x_t)p(x_t|y_0,...,y_t)dx_t \end{aligned}\tag{F.8}$$

where we used the conditional independences in the state space model represented by Equations F.1 and F.2. For example, conditioning on the state x_t the outputs y_s and y_u can be written as

$$p(y_u|x_t,y_s)=p(y_u|x_t), s<t<u \tag{F.9}$$

Using Equation F.3, we can write the first term in Equation F.8 as

$$p(y_{t+1}|x_{t+1})=\{y_{t+1};x_{t+1},R\} \tag{F.10}$$

where we calculate the conditional mean using Equation F.2

$$E[y_{t+1}|x_{t+1}] = E[x_{t+1}+v_t|x_{t+1}] \tag{F.11}$$

$$= x_{t+1} \tag{F.12}$$

where we noted the previous assumption that x_t is independent of v_t. The conditional variance can be calculated in a similar way.

Also, the first term of the integrand can be written as

$$p(x_{t+1}|x_t)=\{x_{t+1};Ax_t,Q\} \tag{F.13}$$

But we need to express this distribution by regarding x_t as a random quantity. To do that, we use Equation F.4 as

$$\{x_{t+1};Ax_t,Q\}=\{x_t;A^{-1}x_{t+1},A^{-1}Q(A^{-1})^T\} \tag{F.14}$$

The second term in the integrand can be simplified using the following definition

$$\begin{aligned} \hat{x}_{t|t} &\equiv E[x_t|y_0, ..., y_t] && \text{(F.15)} \\ P_{t|t} &\equiv E[(x_t - \hat{x}_{t|t})(x_t - \hat{x}_{t|t})^T|y_0, ..., y_t] && \text{(F.16)} \end{aligned}$$

as

$$p(x_t|y_0, ..., y_t) = \{x_t; \hat{x}_{t|t}, P_{t|t}\} \tag{F.17}$$

Combining the three terms yields

$$\begin{aligned} p(x_{t+1}|y_{t+1}, y_0, ..., y_t) \;\propto\; & \{y_{t+1}; x_{t+1}, R\} \\ & \int \{x_t; A^{-1}x_{t+1}, A^{-1}Q(A^{-1})^T\}\{x_t; \hat{x}_{t|t}, P_{t|t}\}dx_t \end{aligned} \tag{F.18}$$

To calculate the integration, if we apply Equation F.5 to the integrand of Equation F.18, we have

$$\begin{aligned} \{x_t; A^{-1}x_{t+1}, A^{-1}Q(A^{-1})^T\}\{x_t; \hat{x}_{t|t}, P_{t|t}\} \;=\; & \{x_t; \mu_{x_t}, \Sigma_{x_t}\} \\ & \{A^{-1}x_{t+1}; \hat{x}_{t|t}, A^{-1}Q(A^{-1})^T + P_{t|t}\} \end{aligned} \tag{F.19}$$

where

$$\begin{aligned} \mu_{x_t} &= \left((A^{-1}Q(A^{-1})^T)^{-1} + P_{t|t}^{-1}\right)^{-1} \left((A^{-1}Q(A^{-1})^T)^{-1}A^{-1}x_{t+1} + P_{t|t}^{-1}\hat{x}_{t|t}\right) \\ \Sigma_{x_t} &= \left((A^{-1}Q(A^{-1})^T)^{-1} + P_{t|t}^{-1}\right)^{-1} \end{aligned}$$

Now the posterior density is

$$\begin{aligned} p(x_{t+1}|y_{t+1}, y_0, ..., y_t) &\propto \{y_{t+1}; x_{t+1}, R\} \\ &\quad \int \{x_t; \mu_{x_t}, \Sigma_{x_t}\}\{A^{-1}x_{t+1}; \hat{x}_{t|t}, A^{-1}Q(A^{-1})^T + P_{t|t}\}dx_t \\ &= \{y_{t+1}; x_{t+1}, R\} \\ &\quad \{A^{-1}x_{t+1}; \hat{x}_{t|t}, A^{-1}Q(A^{-1})^T + P_{t|t}\} \int \{x_t; \mu_{x_t}, \Sigma_{x_t}\}dx_t \\ &= \{y_{t+1}; x_{t+1}, R\}\{A^{-1}x_{t+1}; \hat{x}_{t|t}, A^{-1}Q(A^{-1})^T + P_{t|t}\} \\ &= \{x_{t+1}; y_{t+1}, R\}\{\hat{x}_{t|t}; A^{-1}x_{t+1}, A^{-1}Q(A^{-1})^T + P_{t|t}\} \end{aligned} \tag{F.20}$$

At the last line of Equation F.20, we used

$$\{x; \mu, \Sigma\} = \{\mu; x, \Sigma\} \tag{F.21}$$

The second term of the right-hand side of Equation F.20 can be manipulated further using Equation F.4 as

$$\begin{aligned} \{\hat{x}_{t|t}; A^{-1}x_{t+1}, A^{-1}Q(A^{-1})^T + P_{t|t}\} &= \{x_{t+1}; A\hat{x}_{t|t}, A(A^{-1}Q(A^{-1})^T + P_{t|t})A^T\} \\ &= \{x_{t+1}; A\hat{x}_{t|t}, Q + AP_{t|t}A^T\} \end{aligned} \tag{F.22}$$

Now the posterior distribution takes the following form

$$p(x_{t+1}|y_{t+1}, y_0, ..., y_t) \quad \propto \quad \{x_{t+1}; y_{t+1}, R\}\{x_{t+1}; A\hat{x}_{t|t}, Q + AP_{t|t}A^T\}$$

and applying Equation F.5 one more time yields

$$p(x_{t+1}|y_{t+1}, y_0, ..., y_t) \propto \{x_{t+1}; \hat{x}_{t+1|t+1}, P_{t+1|t+1}\} \tag{F.23}$$

where

$$\begin{aligned} \hat{x}_{t+1|t+1} \quad = \quad & \left(R^{-1} + (Q + AP_{t|t}A^T)^{-1}\right)^{-1} \\ & \left(R^{-1}y_{t+1} + (Q + AP_{t|t}A^T)^{-1}A\hat{x}_{t|t}\right) \end{aligned} \tag{F.24}$$

$$P_{t+1|t+1} = \left(R^{-1} + (Q + AP_{t|t}A^T)^{-1}\right)^{-1} \tag{F.25}$$

From this, we can express the posterior density of the state space model as

$$x_{t+1}|y_{t+1}, y_0, ..., y_t \sim N(\hat{x}_{t+1|t+1}, P_{t+1|t+1}) \tag{F.26}$$

Now, we want to express the mean and covariance matrix in a convenient form. Equation F.25 can also be rearranged to yield

$$\begin{aligned} (P_{t+1|t+1})^{-1} \quad &= \quad R^{-1} + (Q + AP_{t|t}A^T)^{-1} \\ (Q + AP_{t|t}A^T)^{-1} \quad &= \quad (P_{t+1|t+1})^{-1} - R^{-1} \end{aligned} \tag{F.27}$$

Using Equation F.25, Equation F.24 can be written as

$$\hat{x}_{t+1|t+1} = P_{t+1|t+1}\left(R^{-1}y_{t+1} + \left((P_{t+1|t+1})^{-1} - R^{-1}\right)A\hat{x}_{t|t}\right) \tag{F.28}$$

Before we rewrite this equation in a convenient form, we define

$$\begin{aligned} \hat{x}_{t+1|t} \quad &\equiv \quad A\hat{x}_{t|t} && \text{(F.29)} \\ P_{t+1|t} \quad &\equiv \quad AP_{t|t}A^T + Q && \text{(F.30)} \\ K_{t+1} \quad &\equiv \quad P_{t+1|t}(P_{t+1|t} + R)^{-1} \\ &= \quad P_{t+1|t+1}R^{-1} && \text{(F.31)} \end{aligned}$$

where K_{t+1} is the quantity called Kalman gain.

Finally we have

$$\begin{aligned} \hat{x}_{t+1|t+1} \quad &= \quad P_{t+1|t+1}R^{-1}y_{t+1} + \hat{x}_{t+1|t} - P_{t+1|t+1}R^{-1}\hat{x}_{t+1|t} \\ &= \quad K_{t+1}y_{t+1} + \hat{x}_{t+1|t} - K_{t+1}\hat{x}_{t+1|t} \\ &= \quad \hat{x}_{t+1|t} + K_{t+1}(y_{t+1} - \hat{x}_{t+1|t}) \end{aligned} \tag{F.32}$$

Appendix G

EM Algorithm for a State Space Model

G.1 Introduction

This section describes the EM algorithm for the state space model used in Chapters 2 and 4. The model is shown in Figure G.1. In this appendix we focus on the complete log likelihood, which is the first step of the EM algorithm. The rest step is just to take derivative of the matrix equation.

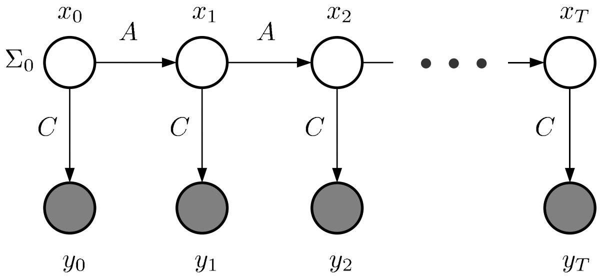

$$x_{t+1} = Ax_t + Gw_t$$

$$y_t = Cx_t + v_t$$

Figure G.1: A graphical model for the state space model. x is the hidden state and y is the observation.

G.2 Complete Log Likelihood

The complete log likelihood for the state space model in Figure G.1 can be written as:

$$\begin{aligned} l(A, C, Q, R|x, y) &= log \prod_{t=0}^{T} p(x_t|x_{t-1})p(y_t|x_t) \\ &= logp(x_0) + \sum_{t=0}^{T-1} logp(x_{t+1}|x_t) + \sum_{t=0}^{T} logp(y_t|x_t) \end{aligned} \tag{G.1}$$

As an example, if we include the term for the matrix A, the partial likelihood can be written as:

$$\begin{aligned} l(Q, A|x) &= log \left(\prod_{t=0}^{T-1} p(x_{t+1}|x_t) \right) \\ &= \sum_{t=0}^{T-1} log\left(p(x_{t+1}|x_t)\right) \\ &= \sum_{t=0}^{T-1} log\left(\frac{1}{(2\pi)^{d/2}}\right) \\ &\quad +log|GQG^T|^{-\frac{1}{2}} - \frac{1}{2}(x_{t+1} - Ax_t)^T(GQG^T)^{-1}(x_{t+1} - Ax_t) \qquad \text{(G.2)} \\ &= \sum_{t=0}^{T-1} \left(log\left(\frac{1}{(2\pi)^{d/2}}\right)\right) + \\ &\quad \sum_{t=0}^{T-1} \left(-\frac{1}{2}log|GQG^T| - \frac{1}{2}(x_{t+1} - Ax_t)^T(GQG^T)^{-1}(x_{t+1} - Ax_t)\right) \\ &= \sum_{t=0}^{T-1} \left(log\left(\frac{1}{(2\pi)^{d/2}}\right)\right) + \\ &\quad \sum_{t=0}^{T-1} -\frac{1}{2}log|GQG^T| - \sum_{t=0}^{T-1} \frac{1}{2}(x_{t+1} - Ax_t)^T(GQG^T)^{-1}(x_{t+1} - Ax_t) \\ &= const + \sum_{t=0}^{T-1} -\frac{1}{2}log|GQG^T| \\ &\quad - \sum_{t=0}^{T-1} \frac{1}{2}(x_{t+1} - Ax_t)^T(GQG^T)^{-1}(x_{t+1} - Ax_t) \end{aligned}$$

Based on the above complete log likelihood, we take the derivative with respect to A and obtain an updated estimate:

$$A^{(n+1)} = \left(\sum_{t=0}^{T-1} E[x_{t+1}x_t^T|y, \theta^{(n)}] \right) \left(\sum_{t=0}^{T-1} E[x_t x_t^T|y, \theta^{(n)}] \right)^{-1} \tag{G.3}$$

where $\theta^{(n)}$ is the parameter from the previous iteration.

Other parameters can be derived in a similar way.

Appendix H

BATS Snow Albedo Scheme

H.1 Introduction

The snow albedo in BATS model depends on a spectral mix of the incident radiation, solar zenith angle, soot loading of the snow, snow depth, and grain size [54].

H.2 Albedo Scheme

Depending on the wavelength of the radiation, λ, the scheme has different albedos:

$$\alpha_V = \alpha_{VD} + 0.4f(\theta_Z)[1 - \alpha_{VD}] \tag{H.1}$$

$$\alpha_{IR} = \alpha_{IRD} + 0.4f(\theta_Z)[1 - \alpha_{IRD}] \tag{H.2}$$

where α_V is the albedo for $\lambda < 0.7\ \mu m$, α_{IR} is the albedo for $\lambda > 0.7\ \mu m$, θ_Z is the solar zenith angle, $f(\theta_Z)$ is the increase of snow visible albedo due to solar zenith angle exceeding 60°, and the subscript D denotes diffuse albedos given by

$$\alpha_{VD} = [1 - C_S f_\tau]\alpha_{VN} \tag{H.3}$$

$$\alpha_{IRD} = [1 - C_N f_\tau]\alpha_{IRN} \tag{H.4}$$

$$C_S = 0.2 \tag{H.5}$$

$$C_N = 0.5 \tag{H.6}$$

where α_{VN} is the albedo for visible radiation incident on new snow with solar zenith angle less than 60° and taken as 0.95, α_{IRN} is the albedo of new snow for near-infrared solar radiation with solar zenith angle less than 60° and taken as 0.65, and f_τ is the fractional decrease of snow albedo due to snow aging.

$f(\theta_Z)$ is parameterized as

$$f(\theta_Z) = \frac{1}{b}\left[\frac{b+1}{1+2b\ C(\theta_Z)} - 1\right] \tag{H.7}$$

$$f(\theta_Z) = 0,\ if\ C(\theta_Z) > 0.5 \tag{H.8}$$

where $C(\theta_Z)$ is the cosine of solar zenith angle.

Equation H.7 becomes 0 when $C(\theta_Z) = 0.5$ for all b, and 1 when $C(\theta_Z) = 0$ (i.e., sun on the horizon). b is adjustable, but set as 2.0.

Snow albedo decreases because snow grain size increases over time. Also it decreases when dirt and soot accumulate. The snow aging factor, f_τ is parameterized as

$$f_\tau = \frac{\tau_S}{1 + \tau_S} \tag{H.9}$$

where τ_S is the non-dimensional age of snow and can be calculated as

$$\frac{\Delta \tau_S}{\Delta t} = \frac{1}{\tau_0}(r_1 + r_2 + r_3) \tag{H.10}$$

where τ_0 is 10^6 s and Δt is the model time step (s). The three parameters, r_1, r_2, r_3, can be calculated as

$$\begin{aligned} r_1 &= e^{5000\left(\frac{1}{273.16} - \frac{1}{T_s}\right)} && \text{(H.11)} \\ r_2 &= r_1^{10} \leq 1 && \text{(H.12)} \\ r_3 &= \begin{cases} 0.01 & \textit{over Antarctica,} \\ 0.3 & \textit{elsewhere} \end{cases} && \text{(H.13)} \end{aligned}$$

where T_s is the snow surface temperature in K.

The parameter r_1 represents the effect of grain growth due to vapor diffusion. r_2 reflects the additional effect near and at the freezing point of melt water and r_3 the effect of dirt and soot. Note that the effect of dirt and soot is represented only by one parameter value. In our simulation, we use 0.3 for r_3.

A snow water equivalent of 0.01 m is assumed to restore the snow surface albedo to that of new snow. Since the precipitation in one model time step is usually less than that required to restore the surface albedo, the snow age is reduced by a factor depending on the amount of the fresh snow in m, ΔP_s, as follows:

$$\tau_S^{n+1} = (\tau_S^n + \Delta\tau_S)(1 - 100\Delta P_s),\ \tau_S > 0 \tag{H.14}$$

Note that if we use the unit mm for ΔP_s, we multiply it by 0.1 instead of 100.